Investigating the theranostic properties of apoA-I-linked porphyrin-lipid nanoparticles in atherosclerosis

VICTORIA ANN NANKIVELL

A thesis submitted to The University of Adelaide in candidature for the degree of Doctor of Philosophy in the School of Medicine, Faculty of Health and Medical Sciences

September 2022

School of Medicine
Faculty of Health and Medical Sciences
The University of Adelaide
South Australia
&
Vascular Research Centre
Lifelong Health Theme
South Australian Health & Medical Research Institute
South Australia

Table of Contents

List of Figures ix

List of Tables xiii

Abstract xiv

Declaration xvi

Acknowledgements xvii

Conference Presentations xix

Abbreviations xxi

CHAPTER 1 1

Introduction 1

1.1 Burden of cardiovascular disease 2

1.2 Cardiovascular system and vessel structure 3

1.3 Coronary artery disease 6

1.4 Atherosclerosis 6

1.5 The role of macrophages in atherosclerosis 9

1.5.1 Classification of macrophage subtypes 10

1.5.2 Macrophage foam cells and lipid metabolism 11

1.6 CAD Treatments 15

1.6.1 Percutaneous Coronary Intervention (PCI) 15

1.7 PCI complications - mechanisms of restenosis 20

1.7.1 Neointimal hyperplasia (NIH) 20

1.7.2 Stent thrombosis (ST) 20

1.7.3 In-stent neoatherosclerosis 21

1.7.3.1 Morphological features of neoatherosclerosis 21

1.7.3.2 Potential mechanisms of neoatherosclerosis 22

1.7.3.3 Preclinical models of neoatherosclerosis post-stent implantation 25

1.8 Imaging atherosclerosis 30
1.9 Use of nanotechnology and nanoparticles in atherosclerosis 32
1.10 High Density Lipoprotein 34
1.11 HDL-like nanoparticles for atherosclerosis 35
1.11.1 Examples of theranostic HDL-like nanoparticle therapies targeted to macrophages in atherosclerosis 35
1.12 Porphyrin-lipid nanoparticles 37
1.12.1 Porphyrin chemistry 37
1.12.2 Photodynamic therapy from porphyrin compounds 38
1.12.3 Fluorescence/ metal chelation properties of porphyrin compounds 41
1.12.4 Porphysomes 41
1.12.5 HDL-like apoA-I linked porphyrin-lipid nanoparticles 42
1.12.6 Theranostic applications of porphyrin-lipid based nanoparticles in preclinical models 44
1.12.7 ApoA-I mimetic peptide R4F 50
1.12.8 Targeting of SR-BI by HDL-like nanoparticles 51
1.13 Translating theranostic nanoparticles: cancer to atherosclerosis 51
1.14 Applications of porphyrin-lipid based nanoparticles in cardiovascular disease 52
1.15 Hypothesis and aims 53
CHAPTER 2 55
General Methods 55
2.1 Porphysome nanoparticles 56
2.1.1 Porphysome nanoparticle synthesis 56
2.1.2 Porphysome composition 56
2.1.3 ^{64}Cu-labelling of porphysome nanoparticles 59
2.2 Preparation of discoidal reconstituted HDL 59
2.2.1 Reconstitution of apoA-I 59

2.2.2 Complexing apoA-I with PLPC....59

2.3 Animal methods....60

2.3.1 Animal care....60

2.3.2 Positron Emission Tomography (PET)....60

2.3.3 Magnetic Resonance Imaging (MRI)....61

2.3.4 Micro-Computed Tomography (microCT)....61

2.3.5 IVIS fluorescence imaging of *ex vivo* tissues/ organs....61

2.3.6 Blood processing....61

2.3.7 Plasma lipid analysis....62

2.4 Histology....62

2.4.1 OCT Embedding of fresh frozen tissues....62

2.4.2 Hematoxylin and eosin (H&E) staining....63

2.4.3 Oil red O staining....63

2.4.4 Masson’s Trichrome staining....64

2.4.5 Alpha-smooth muscle actin immunohistochemistry....64

2.4.6 CD68 immunofluorescence staining....65

2.4.7 Microscopy of tissue sections....65

2.5 Image analysis....65

2.6 Statistical Analysis....66

CHAPTER 3....67

Anti-atherosclerotic effects of apoA-I-linked porphysome nanoparticles *in vitro*....67

3.1 Introduction....68

3.2 Methods....70

3.2.1 Immortalised bone marrow derived macrophages cell culture....70

3.2.2 Inflammatory stimulation of iBMDMs....70

3.2.3 Real time-qPCR....71

3.2.4 Cell media sample preparation 71

3.2.5 Nuclear protein extraction 72

3.2.6 Whole cell protein extraction 72

3.2.7 Western Blotting 72

3.2.8 ELISAs 73

3.2.8.1 IL-1β ELISA 73

3.2.8.2 CCL5 ELISA 74

3.2.8.3 CCL2 ELISA 74

3.2.8.4 Caspase-1 ELISA 75

3.2.9 Cholesterol efflux assay 75

3.2.10 Flow cytometry of iBMDMs 76

3.2.11 Fluorescence/ Confocal microscopy of cultured cells 76

3.3 Results 78

3.3.1 Porphysome nanoparticles are internalised by macrophages *in vitro* 78

3.3.2 Porphysomes promote cholesterol efflux from macrophages *in vitro* 81

3.3.3 Porphysome nanoparticles inhibit the expression of pro-inflammatory cytokines *Il-1β* and *Il-18* 84

3.3.4 Porphysome nanoparticles inhibit the expression of pro-inflammatory chemokine CCL5 88

3.3.5 The effect of porphysome nanoparticles on expression of pro-inflammatory chemokine CCL2 in macrophages 91

3.3.6 Porphysome nanoparticles did not affect pro-inflammatory cytokine *Il-6* expression in macrophages 94

3.3.7 Effect of porphysomes on levels of p65-NFκB mRNA and nuclear protein in macrophages 97

3.3.8 Porphysome nanoparticles suppress some components of the NLRP3 inflammasome in macrophages 100

3.3.9 Porphysome nanoparticles have no effect on Caspase-1 expression in macrophages 103

3.3.10 Porphysome nanoparticles suppress inflammation in macrophages independently of passive cholesterol efflux 106

3.4 Discussion 110

CHAPTER 4 121

Theranostic properties of apoA-I-linked porphysome nanoparticles in stable atherosclerosis 121

4.1 Introduction 122

4.2 Methods 124

4.2.1 *In vivo* stable atherosclerosis model protocols 124

4.2.1.1 *Apoe*$^{-/-}$ mice for PET/MRI, IVIS fluorescence imaging and flow cytometry 124

4.2.1.2 *Apoe*$^{-/-}$ mice for histological analysis of the aortic sinus 125

4.2.2 ^{64}Cu-porphysome gamma (γ-) counting in organs/tissues 125

4.2.3 Sectioning of the aortic sinus 126

4.2.4 Image analysis of the aortic sinus 126

4.2.5 Flow cytometry of the descending aorta 126

4.3 Results 129

4.3.1 Porphysome nanoparticles localise to the aortic arch region in HCD fed *Apoe*$^{-/-}$ mice, detected by IVIS fluorescence imaging 130

4.3.2 Porphysome nanoparticle detection *ex vivo* in the organs of *Apoe*$^{-/-}$ mice 134

4.3.3 Determination of the biodistribution of 30 mol % porphysomes using ^{64}Cu-radiolabelling 137

4.3.4 The biodistribution of 30 mol % ^{64}Cu-radiolabelled porphysome NPs in *Apoe*$^{-/-}$ mice fed a HCD for 32 weeks indicates increase in uptake in heart but not liver 140

4.3.5 PET/MRI imaging reveals some increase in signal in the heart region of mice fed a HCD compared to chow fed mice for 11 weeks 143

4.3.6 Porphysomes reduce body weight but have no effect on plasma lipids in HCD fed *Apoe*$^{-/-}$ 146

4.3.7 Fluorescent porphyrin-lipid detection in aortic cells of *Apoe*$^{-/-}$ mice by flow cytometry 151

4.3.8 Aortic cells from HCD fed *Apoe*$^{-/-}$ mice uptake porphysomes with a higher proportion of porphyrin-lipid cells in aortic macrophages 154

4.3.9 Porphysome detection in CD68^{+} macrophage regions of plaque in the aortic sinus of *Apoe*$^{-/-}$ mice administered porphysomes 157

4.3.10 ^{64}Cu-Porphysomes can be longitudinally imaged in the heart region of *Apoe*$^{-/-}$ mice 160

4.3.11 Porphysome treatment did not affect aortic sinus plaque size, collagen, lipid, α-SMA^{+} smooth muscle cells or CD68^{+} macrophage content in HCD fed *Apoe*$^{-/-}$ mice 163

4.3.12 Changes in aortic cell types observed in *Apoe*$^{-/-}$ mice treated with porphysome NPs compared to PBS control mice 166

4.4 Discussion 169

CHAPTER 5 176

Theranostic properties of apoA-I-linked-porphysome nanoparticles in a model of atherosclerotic plaque instability 176

5.1 Introduction 177

5.2 Methods 179

5.2.1 Carotid artery tandem stenosis procedure in *Apoe*$^{-/-}$ mice 179

5.2.2 Nanoparticle administration in *Apoe*$^{-/-}$ mice post-tandem stenosis surgery 179

5.2.3 Sectioning and histological analysis of tandem stenosis carotid Segment I 179

5.2.4 TER-119 immunohistochemistry 180

5.3 Results 181

5.3.1 Porphysomes are detected by PET imaging *in vivo* and IVIS fluorescence imaging *ex vivo* in unstable plaque 181

5.3.2 Porphysome fluorescence is detected in CD68$^+$ macrophage regions of unstable plaque in TS Segment I 184

5.3.3 Effect of porphysome nanoparticles on unstable atherosclerotic plaque area in the tandem stenosis model of plaque instability 187

5.3.4 No change in the inner vessel area (vessel size) of TS Segment I carotid sections 190

5.3.5 Porphysomes decrease unstable plaque collagen content, with no change in lipid content in TS Segment I 193

5.3.6 Porphysome have no effect on plaque smooth muscle cell, erythrocyte or macrophage content in the tandem stenosis model of plaque instability 196

5.3.7 Reduced bodyweight and lower plasma triglycerides observed following treatment with porphysomes in the tandem stenosis model of unstable plaque 199

5.4 Discussion 202

CHAPTER 6 208

Development of a murine in-stent neoatherosclerosis model 208

6.1 Introduction 209

6.2 Methods 211

6.2.1 Stented aorta-carotid interposition grafting procedure 211

6.2.2 In-stent neoatherosclerosis model and nanoparticle administration 212

6.2.3 JB-4 resin embedding of stented aortas 212

6.2.4 Sectioning, staining and immunohistochemistry of JB-4 resin embedded stented aortas 213

6.2.5 Analysis of neointimal area and strut to lumen distance in stented aortas 214

6.2.6 Sectioning and staining of grafted aortas without stent deployment 214

6.3 Results 215

6.3.1 In-stent neoatherosclerosis model optimisation in *Apoe*$^{-/-}$ mice fed HCD for 6 weeks 215

6.3.2 In-stent neoatherosclerosis model revealed a high rate of in-stent occlusion 220

6.3.3 Neoatherosclerotic area and stent strut to lumen distance measures from in-stent neoatherosclerosis model 223

6.3.4 Stented aortas that maintained patency model some features of in-stent neoatherosclerosis in PBS and porphysome treated groups 226

6.3.5 Grafted aortas with no stent had varied morphological features in *Apoe*$^{-/-}$ mice fed HCD 229

6.3.6 Porphysomes could be detected by PET and IVIS fluorescence imaging in mice with implanted stent in HCD fed *Apoe*$^{-/-}$ mice 232

6.4 Discussion 235

CHAPTER 7 243

General Discussion 243

7.1 General Discussion 244

7.2 Future directions 260

References 267

List of Figures

Figure legend 1.1: Schematic of the structure and components of blood vessels; the three main layers. 5

Figure legend 1.2: The process of atherosclerotic plaque formation. 14

Figure legend 1.3: Schematic of the process of percutaneous coronary intervention to implant a stent at the atherosclerotic plaque site. 19

Figure legend 1.4: Potential mechanisms underlying in-stent neoatherosclerosis development 29

Figure legend 1.5: Chemical and structural diagrams of porphyrin-lipid based nanoparticles. 40

Figure legend 1.6: Multimodal imaging of ^{64}Cu-labelled porphysomes in prostate cancer model 47

Figure legend 1.7: Tumour-specific uptake and multimodal imaging of apoA-I-linked porphylipoprotein (PLP) in an orthotopic prostate cancer model 49

Figure legend 2.1: Summary of porphyrin-lipid/ HDL mimetic nanoparticles. 58

Figure legend 3.1: Fluorescence detection of porphysome nanoparticles in macrophages *in vitro* 80

Figure legend 3.2: Porphysome nanoparticles efflux cholesterol from macrophages 83

Figure legend 3.3: Discoidal and spherical porphysomes inhibit expression of cytokines *Il-1β* and *Il-18* in macrophages in response to inflammatory stimulation 87

Figure legend 3.4: Porphysomes inhibit the expression of CCL5 in macrophages following inflammatory stimulation 90

Figure legend 3.5: The effect of porphysome nanoparticles on expression of CCL2 in macrophages following inflammatory stimulation 93

Figure legend 3.6: Porphysome nanoparticles have no effect on the expression of *Il-6* mRNA in macrophages following inflammatory stimulation..96

Figure legend 3.7: Porphysomes suppress p65-NFκB mRNA and nuclear protein in macrophages 99

Figure legend 3.8: Porphysome nanoparticles decrease *Asc* and *Nlrp3* expression in macrophages following inflammatory stimulation..102

Figure legend 3.9: Effect of porphysome nanoparticles on Caspase-1 expression in macrophages following inflammatory stimulation..105

Figure legend 3.10: The anti-inflammatory properties of porphysomes occur independently of cholesterol efflux 109

Figure legend 4.1: Gating strategy for flow cytometry analysis of aortic cell types. ...129

Figure legend 4.2: Porphysome nanoparticles can be detected using fluorescence imaging *ex vivo* in *Apoe*$^{-/-}$ mice and localise to the aortic arch....................................133

Figure legend 4.3: Biodistribution of porphysome nanoparticles in organs of chow and HCD fed mice detected ex vivo using fluorescence. 136

Figure legend 4.4: Overall biodistribution of ^{64}Cu-radiolabelled porphysomes in chow or HCD fed *Apoe*$^{-/-}$ mice using γ-counting 139

Figure legend 4.5: ^{64}Cu-radiolabelled porphysomes in *Apoe*$^{-/-}$ mice fed either chow diet or HCD..142

Figure legend 4.6: PET/MRI imaging of ^{64}Cu-porphysomes in *Apoe*$^{-/-}$ mice fed chow or HCD..145

Figure legend 4.7: Schematic of the treatment and imaging regime for *Apoe*$^{-/-}$ mice to study the theranostic properties of apoA-I linked porphysomes in stable atherosclerosis 148

Figure legend 4.8: Weight and plasma lipid measures from *Apoe*$^{-/-}$ mice fed a HCD administered PBS or porphysome nanoparticles 150

Figure legend 4.9: Flow cytometry can be used to detect the porphyrin-lipid from porphysomes in aortic cells from porphysome treated HCD fed *Apoe*$^{-/-}$ mice 153

Figure legend 4.10: Flow cytometric analysis of the descending aorta of HCD fed *Apoe*$^{-/-}$ mice reveals higher proportion of uptake of porphyrin-lipid in macrophages compared to other aortic cell types 156

Figure legend 4.11: Representative fluorescence images of plaque in the aortic sinus of HCD fed *Apoe*$^{-/-}$ mice shows detection of porphyrin-lipid in CD68^{+} macrophage regions in mice administered porphysomes.. 159

Figure legend 4.12: Longitudinal PET/MRI imaging of ^{64}Cu-porphysomes in HCD fed *Apoe*$^{-/-}$ mice at week 7 and week 11 162

Figure legend 4.13: Histological analysis of stable atherosclerotic lesions in the aortic sinus of *Apoe*$^{-/-}$ mice fed a HCD for 13 weeks 165

Figure legend 4.14: Flow cytometry to determine changes in proportion of aortic cell types in PBS and porphysome treated HCD fed *Apoe*$^{-/-}$ mice 168

Figure legend 5.1: PET and IVIS fluorescence imaging of porphysomes in the *Apoe*$^{-/-}$ tandem stenosis murine model of plaque instability.. 183

Figure legend 5.2: Detection of porphyrin-lipid fluorescence and CD68^{+} macrophages in unstable plaque of TS segment I.. 186

Figure legend 5.3: Unstable plaque area changes between PBS and porphysome groups in TS Segment I 189

Figure legend 5.4: Inner vessel area measurements of TS segment I following treatment with PBS or porphysomes.. 192

Figure legend 5.5: Decrease in collagen but not lipid content in TS segment I of *Apoe*$^{-/-}$ mice treated with porphysomes in the tandem stenosis model of plaque instability....195

Figure legend 5.6: Porphysomes have no effect on SMC, erythrocyte, or macrophage content in TS Segment I...198

Figure legend 5.7: Bodyweight and plasma lipid changes following tandem stenosis surgery in *Apoe*$^{-/-}$ mice administered PBS or porphysomes 201

Figure legend 6.1: Murine in-stent neoatherosclerosis model with stent deployment and carotid interposition grafting surgical procedure in *Apoe*$^{-/-}$ mice 217

Figure legend 6.2: Pilot testing of the murine neoatherosclerosis model in *Apoe*$^{-/-}$ mice reveals features of plaque development...219

Figure legend 6.3: Representative images of stented aortas grafted into *Apoe*$^{-/-}$ mice fed a HCD for 6 weeks: Evidence of significant vessel occlusion 222

Figure legend 6.4: No change in neoatherosclerotic area and strut to lumen distance between PBS and porphysome treated *Apoe*$^{-/-}$ mice fed a HCD..................................225

Figure legend 6.5: Morphological features of neoatherosclerosis in stented aortas from mice fed HCD 228

Figure legend 6.6: Grafted control aorta with balloon injury but no stent develop plaque-like features in *Apoe*$^{-/-}$ mice fed a HCD..231

Figure legend 6.7: Representative images of porphysomes detected in stented aorta graft region with *in vivo* PET and *ex vivo* IVIS fluorescence imaging 234

Figure legend 7.1: Diagram summarising the therapeutic and diagnostic properties of apoA-I-linked porphysome nanoparticles in macrophages *in vitro.*.............................249

Figure legend 7.2: Summary of the work described in Chapters 3-6 of this thesis representing the some of the theranostic properties of apoA-I-linked porphysomes in atherosclerosis...259

List of Tables

Table 2.1 0.3% Porphyrin-lipid nanoparticle composition (0.3 mol % porphyrin-lipid/total lipid) 57

Table 2.2 30% Porphyrin-lipid nanoparticle composition (30 mol % porphyrin-lipid/total lipid) 57

Table 2.3 Discoidal R4F HDL mimetic nanoparticle composition (0 mol % porphyrin-lipid/total lipid) 57

Table 3.1: RT-qPCR conditions and primer sequences used to measure gene changes in treated murine iBMDMs. 77

Table 4.1: Flow cytometry antibodies and reagents 128

Abstract

In an era following advances in lipid-lowering therapies for atherosclerotic cardiovascular disease (CVD), an unacceptably high number of patients still experience cardiovascular events. Atherosclerosis is an inflammatory process involving accumulation of lipid laden plaque in the blood vessel wall. In the coronary arteries, occlusion caused by atherosclerosis can lead to a myocardial infarction. Subsequent percutaneous intervention to revascularise the heart can involve the deployment of a stent. Despite substantial improvements in preventing restenosis in stented regions, concerns remain around complications of an accelerated form of atherosclerosis within the stented region, known as in-stent neoatherosclerosis. Furthermore, current imaging techniques are unable to identify the molecular characteristics of atherosclerosis at a sufficient resolution that impedes accurate prediction of the risk of clinical events. This highlights the need for novel strategies that better identify and prevent atherosclerosis for the improved management of CVD.

Nanotechnologies are promising candidates. ApoA-I-linked porphyrin-lipid nanoparticles (apoA-I porphysomes) incorporate theranostic, therapeutic and diagnostic, properties. Porphysomes consist of an outer layer of a fluorescent porphyrin-lipid conjugate with excellent fluorescence imaging capabilities and can be radiolabelled for positron emission tomography (PET) imaging. Also in the outer layer is the apoA-I mimetic peptide R4F that enables diagnostic and therapeutic targeting via binding to the SR-BI receptor, highly expressed in plaque macrophages. Porphysomes have been previously investigated as theranostic nanoparticles for applications in cancer but have not been explored as yet in atherosclerotic models. Accordingly, the objective of this thesis was to investigate the therapeutic and diagnostic capabilities of apoA-I porphysomes in atherosclerotic CVD.

Through experimental approaches utilising both *in vitro* and *in vivo* atherosclerosis models, this thesis describes the first studies of apoA-I porphysome nanoparticles as a theranostic in atherosclerotic CVD. *In vitro* studies revealed that porphysomes exhibited anti-atherosclerotic properties in macrophages including inhibiting inflammation and promoting cholesterol efflux. We also demonstrated that apoA-I porphysomes could be internalised by macrophages *in vitro*, as detected by confocal microscopy of the fluorescent porphyrin-lipid. *In vivo* studies in *Apoe*$^{-/-}$ mouse models of stable and unstable plaque found that apoA-I-porphysomes localised to the site of plaque deposition and could be detected with both PET and fluorescence imaging modalities. Flow cytometric and histological analysis suggested that uptake in atherosclerotic plaque *in vivo* was primarily co-localised with macrophages. Overall, the therapeutic effects of porphysome on plaque development were modest, however, a significant reduction in plaque size occurred in the unstable model. Finally, we made the first foray into the development of a novel mouse model of in-stent neoatherosclerosis with some histopathological changes reminiscent of neoatherosclerosis observed within the stented regions. Further optimisation of the model is required, however, to ensure the patency of the stented vessels are retained consistently.

In summary, this thesis explores the highly novel application of apoA-I porphysomes in atherosclerosis to establish as a new potential theranostic for CVD. These studies provide a stepping stone for future development of porphyrin-lipid based nanoparticles into a clinical application for atherosclerotic CVD.

Declaration

I certify that this work contains no material which has been accepted for the award of any other degree or diploma in my name, in any university or other tertiary institution and, to the best of my knowledge and belief, contains no material previously published or written by another person, except where due reference has been made in the text. In addition, I certify that no part of this work will, in the future, be used in a submission in my name, for any other degree or diploma in any university or other tertiary institution without the prior approval of the University of Adelaide and where applicable, any partner institution responsible for the joint-award of this degree.

I give permission for the digital version of my thesis to be made available on the web, via the University's digital research repository, the Library Search and also through web search engines, unless permission has been granted by the University to restrict access for a period of time.

I acknowledge the support I have received for my research through the provision of an Australian Government Research Training Program Scholarship.

………………………………….
Victoria Ann Nankivell
………………………………….

Date: 2/09/22

Acknowledgements

I would like to thank all the important people who helped me along the way during this PhD journey. This has been one of the most challenging but also rewarding times of my life, made better by all the extraordinary people that I have had the pleasure to work with over the years.

First and foremost, thank you to my parents Anna and Brenton, you have encouraged and supported me throughout all my studies and for that I am forever grateful. To Emma and Nate, you are some of the best siblings anyone could have and were always willing to listen when things went wrong. Thank you to Nathan, you have always been there during the hard times despite the distance, you always put a smile on my face and I'm hoping we can spend more time together in the future.

Thank you to my primary supervisor A/Prof Christina Bursill, your determination and resilience in your work has always inspired me and you have taught me so much about how to tackle so many of the challenges that arise in the life of a scientist. Thank you to my co-supervisor Dr. Joanne Tan you have always been a great support and I really appreciate all the constructive advice that you have given me over the years. Thank you so much to both of you for having belief in me especially when I had doubts about my own abilities.

I would like to thank not only those who have helped me in the lab, but for making working at SAHMRI enjoyable. A big thank you to the past and present members of the Vascular Research Centre at SAHMRI: Emma S, Khalia, Ben, Zahra, Jocelyn, Emma A, Sanuja, Anna, Sanuri, Nathan, Laura, Jarrad, Thalia, Lauren, Mia, Ayla, Achini, Jake and Mohammad (sorry if I missed anyone!). A special mention to Lauren, you really go above and beyond in your work, I could not have completed the incredibly difficult surgical

procedures without your support. I would also like to thank Laura Vanags for taking the time to teach me the carotid interposition grafting surgery, this is the most difficult experimental techniques I have ever attempted, and I am grateful that you made the trip to Adelaide to share your incredible technical skills. Thank you to William Tieu for the radiolabelling of the nanoparticles and Wick Lakshantha for assistance with the preclinical imaging procedures, this was integral to the completion of this project. A special mention to Chien Hung and Steve Wise from the University of Sydney for advice on resin embedding and for the sectioning of the resin-embedded stented aortas.

To all who made this thesis possible, thank you.

Conference Presentations

2019 Nankivell, V., Vidanapathirana A., Rajora, M., Zheng, G., Bursill, C. *Theranostic properties of apoA-I porphysome nanoparticles in cardiovascular disease*. Student finalist oral presentation. Australian Atherosclerosis Society (Melbourne, Australia).

Nankivell, V., Vidanapathirana A., Rajora, M., Zheng, G., Bursill, C. *Theranostic properties of apoA-I porphysome nanoparticles in cardiovascular disease*. Oral presentation. Centre for Nanoscale Biophotonics Annual Conference (Adelaide, Australia)

2020 Nankivell, V., Vidanapathirana A., Rajora, M., Tieu, W., Zheng, G., Bursill, C. *Theranostic properties of porphysome nanoparticles in cardiovascular disease*. Oral presentation. Centre for Nanoscale Biophotonics Mid-year Conference (Online).

Nankivell, V., Vidanapathirana A., Rajora, M., Tan, J., Tieu, W., Zheng, G., Bursill, C. *Theranostic properties of porphysome nanoparticles in cardiovascular disease*. Poster presentation. Australian Society for Medical Research (Online).

2021 Nankivell, V., Vidanapathirana A., Rajora, M., Psaltis, P., Tan, J., Tieu, W., Zheng, G., Bursill, C. *Theranostic properties of porphysome nanoparticles in cardiovascular disease*. Oral presentation. Australian Society for Medical Research (Adelaide, Australia).

2022 Nankivell, V., Vidanapathirana A., Rajora, M., Psaltis, P., Tan, J., Tieu, W., Zheng, G., Bursill, C. *Theranostic properties of porphysome nanoparticles in cardiovascular disease*. PhD awards session oral presentation. Australian Society for Medical Research (Adelaide, Australia)

Nankivell, V., Vidanapathirana A., Rajora, M., Psaltis, P., Tan, J., Tieu, W., Zheng, G., Bursill, C. *Theranostic properties of porphysome nanoparticles in atherosclerotic cardiovascular disease. Abstract number 13112*. Abstract accepted. American Heart Association (Chicago, USA).

Abbreviations

^{64}Cu	Copper 64
aa	Amino acid
ABCA1	ATP-Binding cassette transporter sub-family A member 1
ABCG1	ATP-Binding cassette transporter sub-family G member 1
ANOVA	Analysis of variance
AP	Alkaline phosphatase
Apo	Apolipoprotein
apoA-I	Apolipoprotein A-I
ApoE	Apolipoprotein E
Apoe$^{-/-}$	Apolipoprotein E deficient mice
ASC	Apoptosis-associated speck-like protein containing a CARD
BCA	Bicinchoninic acid
BMDM	Bone marrow derived macrophage
BMS	Bare metal stent
CABG	Coronary artery bypass grafting
CAD	Coronary artery disease
CCL2	Chemokine (C-C motif) ligand 2
CCL5	Chemokine (C-C motif) ligand 5
CD	Cluster of Differentiation
cDNA	Complementary deoxyribonucleic acid
CO	Cholesteryl oleate
CT	Computed tomography
CVD	Cardiovascular disease

DAB	3,3'-Diaminobenzidine
DAPI	4',6-diamidino-2-phenylindole
DAPT	Dual anti-platelet therapy
DES	Drug eluting stent
DMPC	1,2-Dimyristoyl-sn-glycero-3-phosphocholine
ECL	Enhanced chemiluminescence
EDTA	Ethylenediaminetetraacetic acid
ELISA	Enzyme-linked immunosorbent assay
FBS	Fetal bovine serum
FMT	Florescence molecular tomography
g	Gram
h	Hour
H&E	Hematoxylin and eosin
HCAEC	Human coronary artery endothelial cell
HCASMC	Human coronary artery smooth muscle cell
HCD	High cholesterol diet
HDL	High density lipoprotein
HRP	Horseradish peroxidase
iBMDM	Immortalised bone marrow derived macrophage
ICAM- 1	Intercellular adhesion molecule-1
ID	Injected dose
IFN-γ	Interferon-gamma
IgG	Immunoglobulin G
IL-18	Interleukin-18

IL-1β	Interleukin-1 beta
IL-6	Interleukin-6
IVIS	In vivo imaging system
kDa	Kilodalton
kg	Kilogram
L	Litre
LDL	Low density lipoprotein
LPS	Lipopolysaccharide
M	Molar
MBq	Megabecquerel
mCi	Millicurie
MI	Myocardial infarction
min	Minute
mL	Millilitre
MMP	Matrix metalloproteinase
mol %	Mole percent
MRI	Magnetic resonance imaging
mRNA	Messenger ribonucleic acid
MT	Masson’s Trichrome
mTOR	Mammalian target of rapamycin
MβCD	Methyl-β-cyclodextrin
NF-κB	Nuclear factor kappa B
ng	Nanogram
NIH	Neointimal hyperplasia

NIR	Near infrared
NLRP3	NOD-, LRR- and pyrin domain-containing protein 3
nm	Nanometer
NP	Nanoparticle
OCT	Optical coherence tomography
ORO	Oil red O
PAI-1	Plasminogen activator inhibitor-1
PBS	Phosphate buffered saline
PBST	Phosphate-buffered saline with Tween 20
PCI	Percutaneous coronary intervention
PEG	Polyethylene glycol
PET	Positron emission tomography
PFA	Paraformaldehyde
pg	Picogram
PLPC	1-palmitoyl-2-linoleoyl-phosphatidylcholine
qPCR	Quantitative polymerase chain reaction
RCT	Reverse cholesterol transport
rHDL	Reconstituted HDL
RNA	Ribonucleic acid
ROS	Reactive oxygen species
Rplp0	Ribosomal protein large P0
rpm	Revolutions per minute
RT	Room temperature
s	Second

SD	Standard deviation
SMC	Smooth muscle cell
sr	Steradian
SR-A1	Scavenger receptor-A1
SR-BI	Scavenger receptor class B type I
STEMI	ST-segment elevation MI
TBP	TATA-binding protein
TBS	Tris buffered saline
TBST	Tris buffered saline with Tween
TNF-α	Tumour necrosis factor alpha
TREM2	Triggering receptor expressed on myeloid cells 2
Tris	Tris(hydroxymethyl)aminomethane
TS	Tandem stenosis
v/v	Volume/ volume
VCAM-1	Vascular cell adhesion molecule-1
VLDL	Very low density lipoprotein
w/v	Weight/ volume
wk	Week
WT	Wildtype
α-SMA	Alpha-smooth muscle actin
µCi	microcurie
µg	Microgram
µL	Microlitre
µm	Micrometre

μM	Micromolar
μmol	Micromole

CHAPTER 1

Introduction

1.1 Burden of cardiovascular disease

According to the World Health Organization (WHO), cardiovascular disease (CVD) still retains the status as the leading cause of mortality worldwide, with an estimated 17.9 million deaths in 2019 accounting for 32% of deaths globally [1]. The underlying pathophysiology of cardiovascular disease is atherosclerosis. The athero-occlusions caused by atherosclerotic plaques result in luminal narrowing or thrombus formation in the affected artery. When this disease is present in the coronary arteries of the heart it is called coronary artery disease (CAD), which may cause significant clinical outcomes such as sudden cardiac death or acute myocardial infarction (MI) [2].

Atherosclerosis develops over a lifetime and is the process of a plaque forming in arterial blood vessels subsequently occluding blood flow as a result of plaque rupture and thrombosis. Atherosclerotic lesions start as fatty streaks that are composed of macrophages engorged with cholesterol (foam cells) in the sub-endothelial layer, eventually leading to the formation of complex plaques as more foam cells accumulate. Smooth muscle cells from the vessel wall (media) start to migrate to the edge of expanding plaques and deposit extracellular matrix in an effort to form a stabilising cap. However, with ongoing lipid uptake from the circulation and other destabilising factors, the integrity of the cap may become compromised [3, 4]. There is increasing evidence that atherosclerosis is not only caused by dysfunctional lipid metabolism but is also a chronic inflammatory disease, developing over a lifetime [4-6]. Current therapies for atherosclerosis primarily rely on lipid lowering medications (e.g. statins) as both a primary and secondary prevention strategy. Interventional techniques are also used to revascularise vessels using coronary artery bypass grafting (CABG) surgery or percutaneous coronary interventions (PCI), often with stent deployment [7]. However, the inherent complexities of atherosclerotic plaque development makes it difficult to identify and treat culprit cells within the lesion [8, 9]. Interestingly individuals without the major conventional cardiovascular risk factors of hypertension, diabetes, hypercholesterolemia and smoking, can still develop sub-clinical atherosclerosis from cardiovascular events [10]. This illustrates the need for the continuing exploration of the mechanisms underlying atherosclerosis so that novel therapies and diagnostic tools can be developed that can help reduce the health and economic impact of CVD.

1.2 Cardiovascular system and vessel structure

The cardiovascular system is made up of a network of arteries and veins through which blood is pumped by the heart to sustain a continuous supply of blood throughout the body and organs. There are several important functions that the cardiovascular system provides including the delivery of nutrients, removal of waste, circulation of hormones, thermoregulation, and oxygenation of tissues. Oxygenated blood is circulated through the body via arteries and the exchange of materials occurs in the capillaries. Deoxygenated blood then flows through the veins back to the heart to be transported to the lungs for re-oxygenation [11, 12].

All blood vessels, excluding the smallest ones, have a common structure that consist of three layers (or tunics) that surround the inner space through which blood flows, called the lumen (Fig 1.1). The innermost layer of the blood vessels is the tunica intima that contains the endothelium, a layer of endothelial cells (ECs) that minimises friction as blood moves through and provides a barrier to the outer layers. In most larger vessels (>1mm diameter) there is a subendothelial layer that consists of connective tissue and a basement membrane that acts to support the endothelial layer. In addition, the internal elastic lamina makes up the outermost layer of the tunica intima [11].

The middle layer is the tunica media that is made up of circumferentially arranged smooth muscle cells and elastin fibers and is surrounded by the external elastic lamina. The tunica media is responsible for responding to the sympathetic nervous system by either vasoconstricting or vasodilating. The tunica media is therefore critical for the regulation of hemodynamics and in arteries is important for the maintenance of circulation and blood pressure [11].

The outermost layer of the vessel wall is known as the tunica adventitia, and the structure is composed of loosely woven collagen fibers which act to protect and provide support, anchoring it to the surrounding tissue. In addition, the tunica adventitia also contains lymphatic vessels and nerve fibers. In some larger blood vessels, the tunica adventitia can contain a vasa vasorum, a system of small blood vessels that supply blood to the outer layers of the vessel [11].

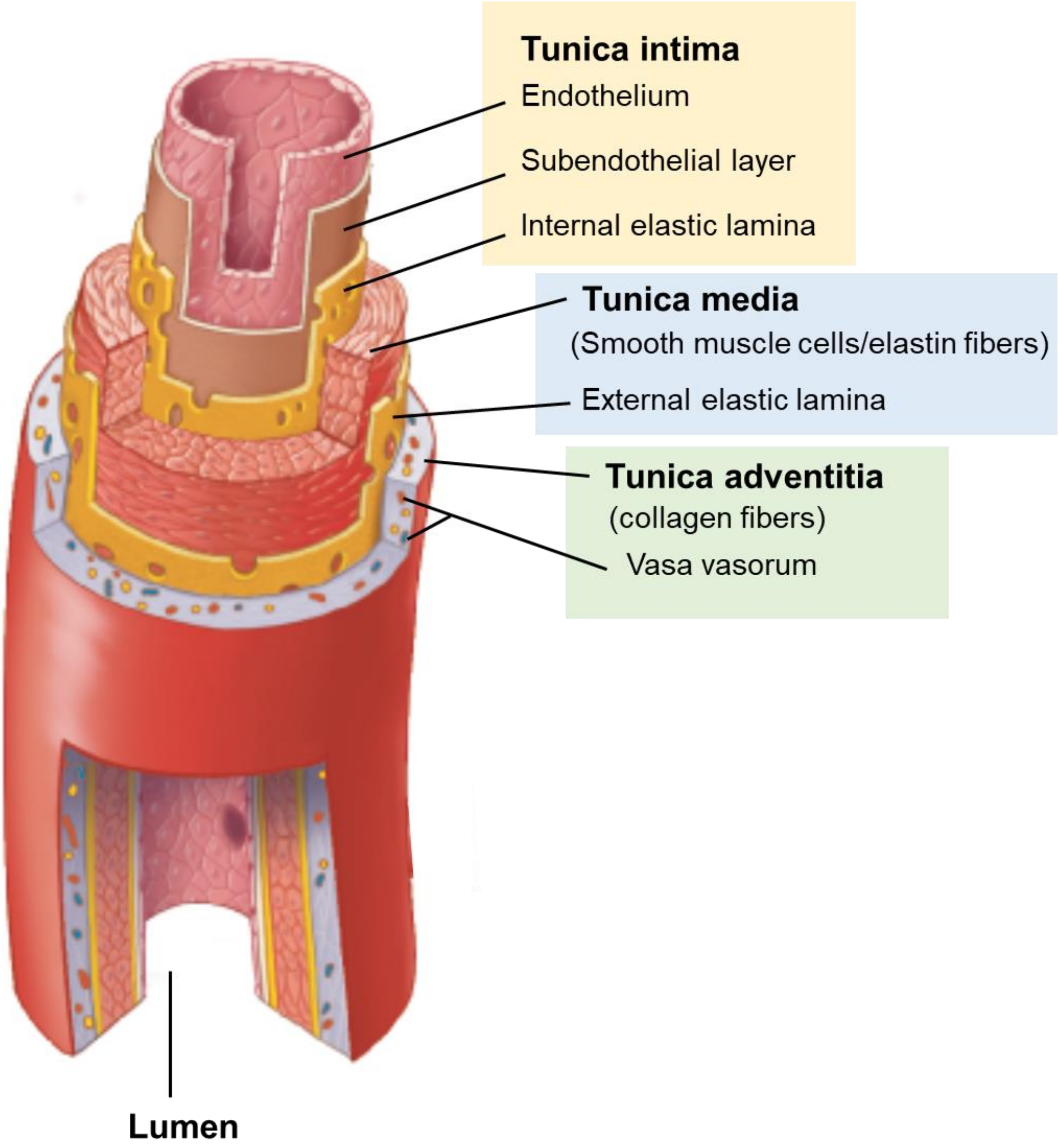
Tunica intima
Endothelium
Subendothelial layer
Internal elastic lamina
Tunica media
(Smooth muscle cells/elastin fibers)
External elastic lamina
Tunica adventitia
(collagen fibers)
Vasa vasorum
Lumen

Figure legend 1.1: Schematic of the structure and components of blood vessels; the three main layers.

Diagram modified from Marieb and Hoehn [11].

1.3 Coronary artery disease

The heart is the organ that pumps blood through the body, but the myocardium (heart muscle) also requires blood supply. This blood supply is provided by the left and right coronary arteries that originate from the base of the aorta [12]. Coronary artery disease (CAD) occurs when blood supply through these arteries is compromised due to a blockage. If the blockage is significant and remains for a prolonged period of time, a myocardial infarction (MI) may occur that causes extensive myocardial cell death due to tissue ischemia. Atherosclerosis, a process that results in the build-up of lipid and cellular debris in the arterial wall, is the cause of these blockages [4, 12].

1.4 Atherosclerosis

Atherosclerosis is initiated when low density lipoprotein (LDL) accumulates in the intimal layer. Entry of LDL into the intima is typically prevented by an intact endothelium, however, damage to this protective layer allows for LDL infiltration. The integrity of the endothelium can be compromised by increased blood pressure, shear stress with increases in blood flow turbulence, high LDL, VLDL or glucose levels, smoking or pollution [2, 13].

LDL particles are normally protected by antioxidants in the plasma, however, when LDL particles enter the subintimal space of the vessel they are exposed, unprotected, to oxidants. This causes LDL to become oxidised (ox-LDL), which is pro-inflammatory and pro-atherogenic. Circulating monocytes are attracted to these sites of ox-LDL deposition in the arteries. Monocytes are initially pulled out of the circulation and recruited to the endothelium via the increased expression of adhesion (VCAM-1 and ICAM-1) and chemoattractant molecules (chemokines/ cytokines) [3, 4]. Once localised and based in the intima, monocytes differentiate into macrophages as reparative actor to remove accumulated lipoproteins. These macrophages express scavenger receptors that enable uptake of deposited lipoproteins and, with time and increased lipoprotein uptake, turn into lipid-laden macrophage foam cells. T-cell lymphocytes also enter the intima, in which they help to regulate the responses of immune, endothelial, and smooth muscle cells (SMCs) [2, 4, 5].

As atherosclerosis progresses, SMCs migrate from the media into the intima and contribute to the production of extracellular matrix (ECM) molecules which include collagen, elastin, proteoglycans and glycosaminoglycans. The accumulation of these extracellular macromolecules can ensnare and trap lipoproteins leading to an increased accumulation of lipid in the intima. T-cell lymphocytes found in the atherosclerotic plaque can also release factors, such as IFN-γ, that promote atherosclerosis by impairing the ability of SMCs to produce interstitial collagen that is essential for their ability to maintain the stabilising fibrous cap [2]. Opposing effects can come from factors such as IL-10 that limits inflammation and SMC proliferation as well as encouraging interstitial collagen production. Furthermore, plaque macrophages and SMCs eventually undergo programmed cell death (apoptosis), in which the resulting cellular debris contributes to the formation of a necrotic core, a key indicator of plaque instability. A failure in efferocytosis, a clearance mechanism, also plays a role in necrotic core formation [14].

As the atherosclerotic plaque progresses, the growth initially expands out in a radial direction away from the vessel lumen (abluminal). This is to preserve the area of the lumen and limit obstruction to blood flow. This process is called ‘positive remodelling’ and typically results from the production of proteinases and matrix metalloproteinases (MMPs) by SMCs that degrade components of the vessel ECM and aid expansion. Positive remodelling of the vessel, however, has a limited capacity for retaining luminal area and eventually expanding plaques will encroach on the lumen and obstruct blood-flow [2].

Another way that the plaque can cause occlusion of the vessel is by rupture and subsequent acute thrombosis. This process is the most common pathway that results in an MI. The atherosclerotic plaques that are most prone to rupture are known as vulnerable plaque and typically exhibit a large necrotic core and thin fibrous cap. Stable plaque usually possess a thicker fibrous cap with a smaller necrotic core. Rupture is usually the result of enzymes (collagenases) degrading the fibrous cap, exposing the thrombogenic material in the core of the lesion, leading to a thrombotic event [4]. Under normal physiological conditions, the endothelium will protect against thrombosis by promoting thrombolysis. The heparan sulfate proteoglycans and thrombomodulin (thrombin co-factor) found on the surface of the endothelium along with prostacyclin and nitric oxide production are integral to providing anti-thrombotic and anti-coagulant properties. In addition, fibrinolysis is also promoted by the expression of urokinase, whilst tissue type plasminogen activator helps to prevent thrombi. In the context of atherosclerosis, the dysfunction of the endothelium is influenced by inflammatory activation in which the endothelial cells release plasminogen activator inhibitor 1 (PAI-1), inhibiting fibrinolysis and tissue factor, which is a pro-coagulant [2].

Atherosclerotic plaque erosion can also occur, and it is estimated that approximately 40% of patients with presentation of acute coronary syndrome (ACS) have plaque erosion within the culprit lesion. Over time the nature of atherosclerosis has shifted to more fibrous plaques that are less lipid-rich and inflamed, in part attributed to the increased use of statins. In line with this, patients with plaque erosion present with lower levels of LDL-cholesterol and C-reactive protein (CRP) [15]. Autopsy studies examining the characteristics of plaque erosion have demonstrated that these plaques present with thrombosis and an intact fibrous cap, but with a luminal surface lacking endothelial cell coverage. In contrast to ruptured plaque, eroded plaques present with higher levels of ECM components compared to lipids with fewer inflammatory cells and a higher smooth muscle cell content. Plaque erosion also presents with a white thrombus rich in platelets. This is in contrast to ruptured plaques that usually have a fibrin rich red thrombus [15].

There are several mechanisms that could contribute to the formation of eroded plaques. The impact of shear stress, due to changes in the blood flow dynamics, on the endothelium induces basement membrane degradation with desquamation and death of the endothelial cell layer. In addition, the effect of inflammatory mediators like cytokines and oxLDL can stimulate the production of MMPs that degrade the collagen in the basement membrane. Furthermore, the upregulation of a smouldering inflammatory response through toll-like receptor 2 (TLR2) activation and formation of neutrophil extracellular traps (NETs), composed of nuclear DNA and proteins that trap platelets, are thought to contribute to plaque erosion [15, 16].

1.5 The role of macrophages in atherosclerosis

Macrophages are phagocytic leukocytes that have essential roles in the innate immune system as well as being involved in many other homeostatic and physiological processes [17]. The role of macrophages in atherosclerosis can be attributed to their role in clearing of cellular debris and modulating the inflammatory response at the site of atherosclerotic plaque. Macrophages are one of the key cell types involved in the progression and destabilisation of atherosclerosis [18].

1.5.1 Classification of macrophage subtypes

The traditional view is that the majority of plaque associated macrophages are derived from circulating monocytes that are recruited from the bloodstream. However there vascular resident macrophages are also involved [19]. Macrophages are highly adaptive cells, able to respond to the local microenvironment and molecular cues to modify their characteristics appropriately. Despite the existence of highly heterogenous macrophage populations, a broad classification of the polarisation of macrophages has involved dividing macrophages into two major sub-types, M1 and M2.

Pro-inflammatory M1 macrophages are differentiated in response to toll-like receptor (TLR) and interferon-γ (IFN-γ) signalling. This signalling can be induced by exposure to pro-inflammatory stimuli including lipopolysaccharide (LPS), lipoproteins and pathogen-associated molecular patterns (PAMPs). M1 macrophages secrete several different pro-inflammatory factors such as interleukin-1β (IL-1β) and tumour necrosis factor-α (TNF-α). In addition, M1 macrophages contribute to increased reactive oxygen species (ROS) secretion and nitric oxide (NO) production to initiate and sustain inflammation [20]. In contrast, M2 macrophages exhibit primarily anti-inflammatory properties and are differentiated in response to the Th2-type cytokines IL-13 and IL-4 resulting in the secretion of anti-inflammatory factors such as IL-10 and transforming growth factor-β (TGF-β) that favour inflammatory resolution [21]. In the context of the M1/M2 polarisation paradigm, the predominate macrophage subtype found in atherosclerotic plaque are the M1 subtype. In atherosclerotic plaque, M1 macrophages are found in unstable, rupture prone regions and M2 macrophages in the more stable regions and adventitia [22].

1.5.2 Macrophage foam cells and lipid metabolism

Macrophage foam cells are a defining feature of atherosclerosis, with accumulation of these cells contributing to the growth and instability of atherosclerotic plaque. Although other cell types, like SMCs, can ingest and accumulate lipid, macrophages are the primary source of foam cells in atherosclerosis. Macrophages provide homeostatic mechanisms by influx and efflux of lipids to modulate levels of cholesterol in the vasculature. However, these functions become disrupted in atherosclerosis, with excessive cholesterol influx and decreased cholesterol efflux leading to accumulation of esterified cholesterol. oxLDL is taken up by macrophages via the assistance of scavenger receptors like CD36, lectin-like oxLDL receptor-1 (LOX-1) and SR-A1. Primarily the uptake of lipoproteins is mediated by SR-A1 and CD36, with cholesterol entering the cytoplasm of the macrophage via SR-mediated phago- and pino-cytosis. Once within the cytoplasm, lipoproteins are degraded by the endosomal and lysosomal compartments with the free cholesterol esterified within the endoplasmic reticulum to be stored as intracellular lipids, which in excess leads to foam cell formation [23].

Macrophages also engage in cholesterol efflux to prevent excessive cholesterol accumulation within the cell. There is a balance of hydrolysis of the cholesterol esters to free cholesterol. Free cholesterol can be transferred to cholesterol transporters in the plasma membrane or via passive diffusion across the membrane. The transporters that are involved in cholesterol efflux (removal) from macrophages include ATP-binding cassette transporter A1 (ABCA1) and G1 (ABCG1) and scavenge receptor-B1 (SR-BI). ABCA1 facilitates the release of free cholesterol to be accepted by lipid-poor apolipoprotein A-I (apoA-I) which forms nascent HDL particles whereas ABCG1 only transfers cholesterol to lipid-containing HDL particles [23]. SR-BI is particularly important because it is a multifunctional receptor transporting cargo bidirectionally, facilitating influx and efflux of cholesterol. In early atherosclerosis, SR-BI acts in a similar way to SR-A1 to facilitate influx of cholesterol to reduce plasma cholesterol levels. SR-BI also enables efflux to HDL which is regulated by both the cholesterol and phospholipid content of the cell and HDL particle [24].

Initially these mechanisms for lipoprotein uptake are beneficial, with the removal of damaging oxLDL particles from the vessel wall. Unfortunately, the ability for macrophage foam cells to process lipoproteins and remove cholesterol efficiently diminishes over time, with uncontrolled uptake and impaired cholesterol efflux. Subsequent endoplasmic reticulum stress and high levels of ROS initiates a pro-apoptotic cascade. Macrophage foam cells also release a host of pro-inflammatory mediators including cytokines (e.g. IL-1α, IL-1β, IL-6 and TNF-α) and MMPs, further promoting additional immune cell infiltration with the continuous cycle leading to plaque expansion [25]. Another way that macrophages can modulate the progression of atherosclerosis is the loss of the ability to clear away apoptotic cells known as defective efferocytosis. This process can be a result of the increased expression of the CD47 receptor, that responds to "do not eat me" signals, in apoptotic cells which prevents their clearance [18, 26]. Overall, this leads to the accumulation of cellular debris and lipids that contribute to the formation of the necrotic core.

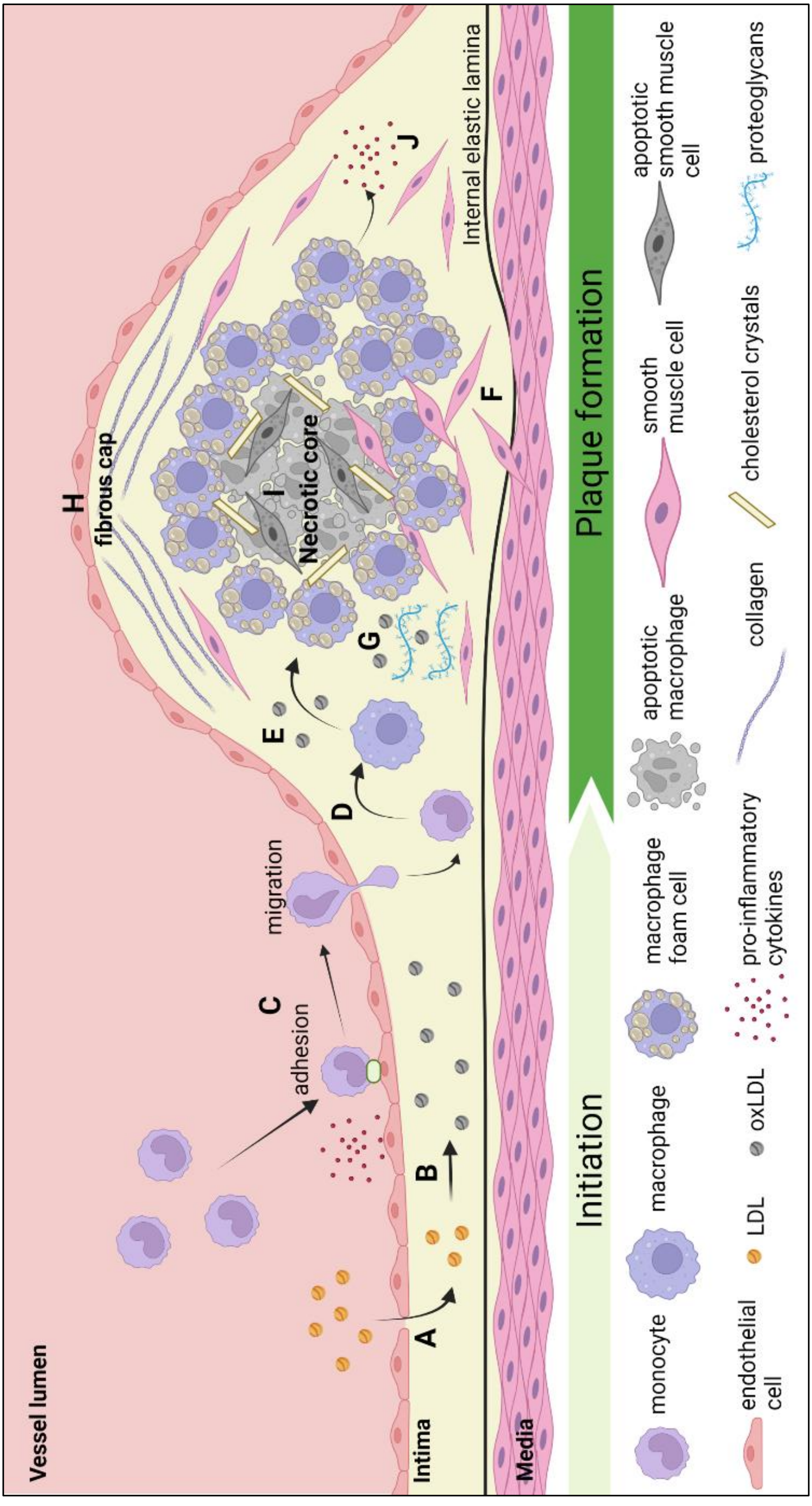
Vessel lumen
Intima
Media
A
B
C
adhesion
migration
D
E
F
G
H
fibrous cap
I
Necrotic core
J
Internal elastic lamina
Initiation
Plaque formation
monocyte
macrophage
macrophage foam cell
apoptotic macrophage
smooth muscle cell
apoptotic smooth muscle cell
endothelial cell
LDL
oxLDL
pro-inflammatory cytokines
collagen
cholesterol crystals
proteoglycans

Figure legend 1.2: The process of atherosclerotic plaque formation.

(**A**) Atherosclerosis is initiated when LDL infiltrates into the subintimal space where it is subsequently (**B**) modified by oxidation to become oxLDL. (**C**) Circulating monocytes from the bloodstream are attracted to the site of oxLDL deposition, attach to the endothelial surface by adhesion molecules and migrate across the endothelium. (**D**) Within the subintima, monocytes differentiate in macrophages. (**E**) These macrophages engulf the oxLDL to form foam cell macrophages. (**F**) Medial smooth muscle cells migrate into the intima where they release macromolecules like (**G**) proteoglycans that increase lipoprotein retention and (**H**) collagen which contributes to the formation of the fibrous cap overlying the plaque. (**I**) As the macrophages and smooth muscle cells undergo apoptosis the necrotic core is formed. (**J**) Macrophage foam cells also release pro-inflammatory cytokines that lead to further immune cell recruitment and infiltration, exacerbating atherosclerosis progression. LDL, low density lipoprotein; oxLDL, oxidised LDL. Figure created with BioRender.com

1.6 CAD Treatments

The primary interventional treatment approaches for CAD are revascularisation techniques that restore blood flow to the heart tissue. These include coronary artery bypass grafting (CABG) surgery and percutaneous coronary intervention (PCI). CABG surgery involves bypassing the narrowed (stenotic) segment of a coronary artery with either an arterial or venous graft. The choice of revascularisation technique is based on the individual, however typically those who are non-diabetic with multi-vessel disease have similar outcomes when comparing CABG and PCI [27]. For those individuals who are diabetic and have multi-vessel CAD, they tend to have poorer short-term outcomes with CABG than PCI [28].

1.6.1 Percutaneous Coronary Intervention (PCI)

For those who would benefit from PCI, this procedure is less invasive than CABG, typically only requiring the use of local anaesthetic and has a faster recovery time [27]. PCI includes the use of an intravascular catheter guiding an angioplasty balloon to either perform angioplasty, expanding the balloon to compress the target lesion, or to deploy a stent to provide mechanical support to the vessel to return blood flow. Originally balloon angioplasty was prone to causing restenosis and recoil of the vessel. The introduction of a stent, following angioplasty provides essential structural support to the vessel and prevents recoil (Fig 1.3). The types of stents that are used for PCI are bare metal stents (BMS) and drug eluting stents (DES) [7].

BMS are commonly made from 316L stainless steel. Whilst these stents provide excellent structural support to the vessel, there are inherent issues with the thrombogenic nature of their surface. To overcome this, dual anti-platelet therapy (DAPT) was introduced, a combination of aspirin with either clopidogrel or ticlopidine. DAPT is able to significantly reduce the risk of thrombosis in patients but is accompanied by an increased risk of bleeding complications when patients require surgery. BMS can also induce restenosis, an inflammatory response that is caused by the injury associated with stent implantation. Restenosis causes expansion of the vessel wall and thereby encroaches on the lumen, negating the original aim of stent deployment [7, 29].

Drug eluting stents were eventually developed to counteract restenosis by providing a constant supply of anti-proliferative drugs to the deployment site. The surface of DES are covered with a polymer-coating to enable controlled release of drugs. The types of antiproliferative drugs that DES use include mTOR inhibitors (e.g. sirolimus) and cytotoxic taxol derivatives (e.g. paclitaxel). Newer generation DES use lipophilic sirolimus analogues including everolimus and require lower drug concentrations which reduces drug toxicity [29].

Various device designs and coatings have also been developed that have improved the biocompatibility of DES. There are considerations when it comes to the radial strength of the stent with the type of metal used, architecture and strut thickness all important factors. Typically in newer generation stents, thinner more flexible struts are favoured and are made from cobalt–chromium or platinum–chromium [30].

There are also different types of polymer coatings and variations in the application of the stent coating. For example, durable polymer DES are made of fluoropolymers (highly fluorinated polymers) that reduce adhesion and activation of platelets, when compared to non-fluoropolymer coated stents. Bio-gradable polymer DES coatings have also been developed that slowly degrade following the release of the drug to eventually leave only the metallic stent in place. This is to combat the issues of delayed re-endothelisation and increased inflammation caused by the remaining polymer coating.

Abluminal coatings (present only on the surface facing the vessel wall) balance the drug release to minimise neointimal hyperplasia and also encourage re-endothelisation of the stent surface to promote healing. However, abluminal coated stents have also faced issues due to the thrombogenicity of the bare metal surface of the stent. This illustrates that there are several features in device design that can be modified to improve stent biocompatibility [29].

Some of the more recent work in improving stent design is the development of bioresorbable stents (BRS) [7]. The theory of using a BRS is the stent backbone, made of a material such as poly-lactic acid, would degrade after providing structural support to the vessel. This has many benefits that could potentially eliminate the risks of stent thrombosis and restenosis as well as restoring normal vasomotor tone of the stented region. However, despite the promise of BRS there are still concerns around widespread clinical implementation [31]. Trials of the ABSORB BRS (Abbott vascular) compared to everolimus eluting stents found that there was no significant improvement in vasomobility [32]. Furthermore, there are concerns about the increase in the prevalence of stent thrombosis with BRS, compared to DES [33, 34]. This illustrates some of the difficulties in translation of improved stent designs but also highlights the opportunities for further innovation.

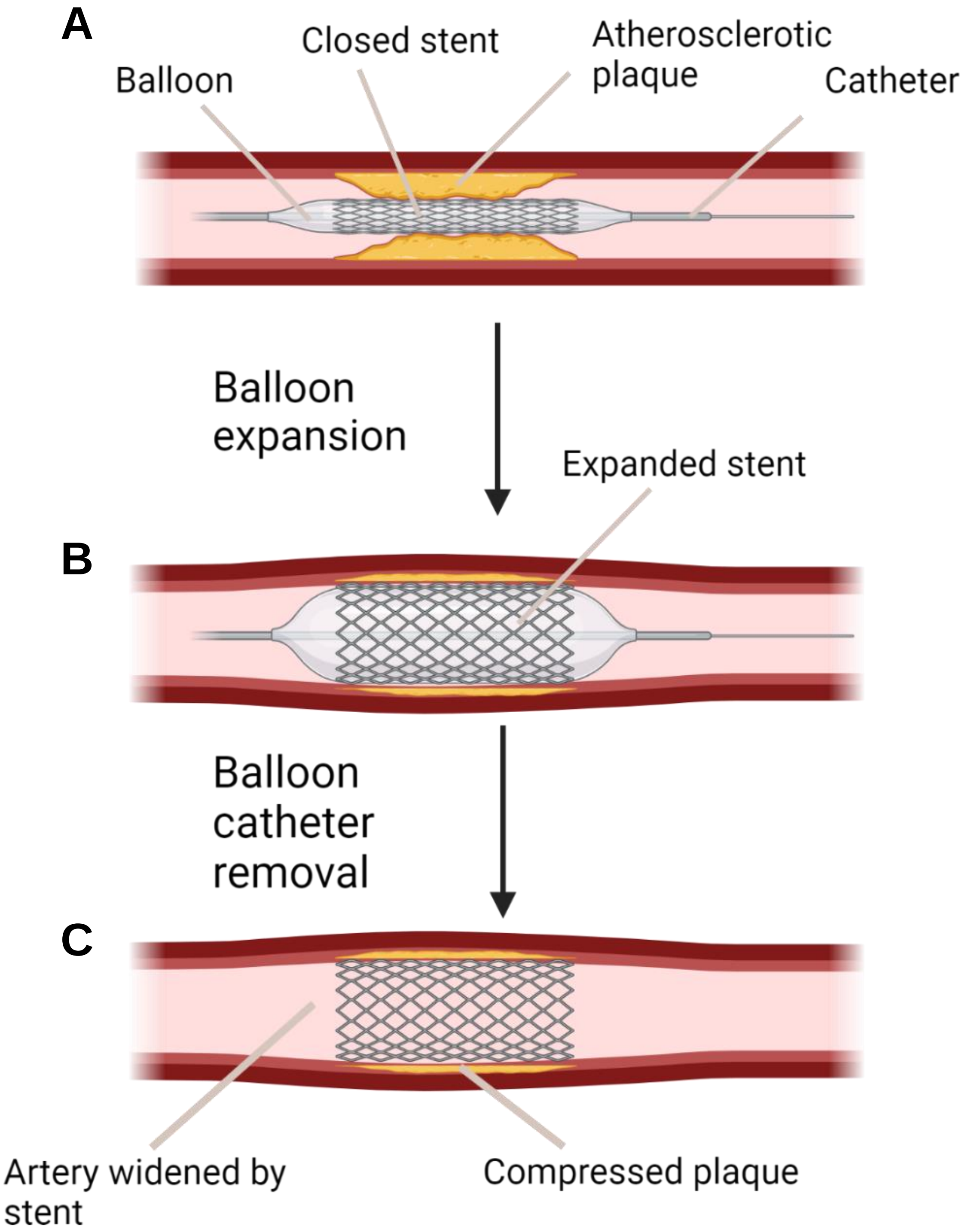
A
Balloon
Closed stent
Atherosclerotic plaque
Catheter
Balloon expansion
Expanded stent
B
Balloon catheter removal
C
Artery widened by stent
Compressed plaque

Figure legend 1.3: Schematic of the process of percutaneous coronary intervention to implant a stent at the atherosclerotic plaque site.

(**A**) Balloon catheter with stent crimped onto the balloon is inserted through to the site of the atherosclerotic plaque. (**B**) Inflation of the balloon catheter results in the expansion of the balloon and the stent. (**C**) This causes the restoration of blood flow and prevention of vessel recoil. Figure created with BioRender.com

1.7 PCI complications - mechanisms of restenosis

Despite the significant benefits of PCI, it is not without complications that include re-narrowing of the vessel via restenosis that can cause stent failure.

1.7.1 Neointimal hyperplasia (NIH)

Neointimal hyperplasia (NIH) is a process that contributes to in-stent restenosis. Damage to the vessel wall from balloon angioplasty and stent deployment causes medial SMCs to proliferate in an unregulated manner, leading to neointimal expansion. The secretion of extracellular matrix proteins and inflammatory mediators is also increased. When this occurs following stent implantation, the neointima growth covers the stent struts but then can expand into the lumen leading to restenosis of the vessel. When medial SMCs undergo apoptosis as a result of vascular injury from PCI, adventitial SMCs migrate and proliferate to replace these SMCs. The overall outcome of this response is a deleterious increase in neointimal area [30].

1.7.2 Stent thrombosis (ST)

Due to the location of the placement of stents within blood vessels, stents are susceptible to thrombotic complications post-deployment. No matter the type of stent, the surface of the stent is initially exposed directly to blood prior to being covered by neointimal growth. This means that all stents are thrombogenic by nature and therefore biocompatibility is an important consideration for constant improvement [29]. Although the introduction of DES has been successful in reducing the rates of in-stent restenosis by inhibiting neointimal hyperplasia, the first generation of DES were also associated with an increase in late (30–60 days) and very late stent thrombosis (> 1 year) [35, 36]. This is a cause for concern as stent thrombosis is one of the most catastrophic complications following PCI that can result in a large ST-segment elevation MI (STEMI) requiring emergency repeat PCI intervention or present as a sudden cardiac death [36]. Increasing the duration of DAPT to combat the risk of thrombosis can then introduce bleeding complications. Second-generation DES, have been demonstrated to improve outcomes for patients by reducing late thrombosis events and preserving anti-restenosis properties with a shorter duration of DAPT. [37]. Despite these recent evolutions in stent technology, there is still a need for new stent designs and strategies that reduce very late stent complications [36].

1.7.3 In-stent neoatherosclerosis

In-stent neoatherosclerosis is a form of atherosclerosis that develops following stent implantation at an accelerated rate compared to native atherosclerosis [38]. Neoatherosclerosis has been shown to be distinct from NIH in both the composition and time taken to develop. NIH is distinctively composed of smooth muscle cells in contrast to neoatherosclerosis, which is composed of infiltrated macrophage foam cells that over time create necrotic cores. Neoatherosclerosis primarily affects DES, especially first generation stents [39] and is associated with late vascular complications, including rupture and thrombosis, as detected by several histological and intravascular imaging studies [40, 41].

1.7.3.1 Morphological features of neoatherosclerosis

Histological analysis of stented neoatherosclerotic vessels has revealed the presence of lipid-rich macrophage foam cells in the neointima, necrotic cores and calcification [37, 42, 43]. Morphologically, in-stent neoatherosclerosis develops independently over the native atherosclerosis typically with no continuation of the underlying plaque. Early appearance of foam cell macrophages occurs frequently either in the peri-strut areas or near the luminal surface. The necrotic core of neoatherosclerotic lesions usually has acellular debris collections containing free cholesterol and depletion of the extracellular matrix (ECM). Sometimes the necrotic core may also present with haemorrhage and fibrin deposition. Further infiltration of foam cell macrophages into the neointimal area can result in fibrous cap thinning which can eventuate into in-stent plaque rupture [37, 42]. Another feature that is observed within neoatherosclerotic lesions is calcification, particularly in stents that have been implanted for long periods of time. This calcification is typically observed as either microcalcification and fragmented or sheet calcification. As seen in native atherosclerosis, the calcification could originate from foam cell or SMC apoptosis, for microcalcification, while the sheet or fragmented calcification may be attributed to collagen, ECM, and SMC calcification. Interestingly the calcification of fibrin seems to be a unique feature of DES, particularly in paclitaxel eluting stents [37].

1.7.3.2 Potential mechanisms of neoatherosclerosis

The exact mechanisms underlying the accelerated nature of neoatherosclerosis (Fig 1.4) remain unclear, including the reasons for differences between BMS and DES. It has been observed that in-stent neoatherosclerosis is more common in individuals that have evidence of native atherosclerosis, which points to a similar mechanism between both [44].

It is possible that underlying mechanisms of neoatherosclerosis in BMS may be different than that of DES. Although the rate of formation has been shown to be slower in BMS than DES, this is still significantly accelerated compared to native atherosclerosis. The transition from lipid pool to necrotic core is driven by the apoptosis of SMCs and foam cells which coincides with maturation of the neointima in the BMS. In the absence of anti-proliferative drugs, it is possible for the neointima to mature (causing restenosis) but with more endothelial cell coverage of the stent struts which may delay macrophage infiltration, and subsequent formation of lipid pools accompanied by cellular apoptosis. Mechanistically, the incomplete maturation of the endothelium presents as incomplete cell-to-cell junctions, reduced nitric oxide production and a decrease in anti-thrombotic molecule expression, which is seen more frequently in DES versus BMS [37]. For example the DES anti-proliferative drug, sirolimus - an mTOR inhibitor, has off-target effects on endothelial cells which impairs their barrier functionality [29]. These may be some of the reasons to explain why DES observe earlier incidence of neoatherosclerosis compared to BMS [43].

Delayed vascular healing

There is evidence that delayed vascular healing is induced by the implantation of DES and may cause the accelerated development of neoatherosclerosis. A similar prevalence of neoatherosclerosis still occurs with the newer generation of DES that are observed to have insufficient endothelial maturation when compared to BMS. The anti-proliferative drugs in DES are unlikely to be the only cause of in-stent neoatherosclerosis as BMS also develop neoatherosclerosis at an accelerated pace, when compared to native atherosclerosis. This points to other mechanisms being involved in the promotion of neoatherosclerosis [37].

Hemodynamics

Changes in vessel hemodynamics caused by stent implantation may be an important factor that induces neoatherosclerosis. The deployment of stents can disturb the local blood flow and cause spaciotemporal alterations in shear stress. These disturbances are known to increase the expression of adhesion molecules, including VCAM-1 and ICAM-1 in endothelial cells, in the peri-strut areas. Similar to native atherosclerosis, this increase in adhesion molecule expression allows for monocytes to adhere and then migrate into the sub-endothelial space, eventually transforming into foam cell macrophages. When thrombus formation occurs early after stent deployment, it is the direct result of vascular injury that has triggered the deposition of fibrin and platelets as part of the healing process. The initial thrombus is likely to resolve itself, however, turbulent flow from non-streamlined stent struts can lead to the continued pro-thrombotic fibrin deposition within the peri-strut areas [37].

Inflammation

Chronic inflammation is also likely to be a contributing factor in the development of in-stent neoatherosclerosis. For example, the polymer coating found on DES may promote chronic inflammation with infiltration of inflammatory cells including macrophages and lymphocytes. Histological analysis has found that the restenotic areas in DES contain a larger amount of proteoglycan deposition compared to BMS, which may be a contributing factor to neoatherosclerosis in DES as it is correlated with increased retention of lipoproteins [37, 45].

In addition, the continuous apoptosis of SMCs and macrophages at the stented site drive the formation of a necrotic core. In contrast to the progression of native atherosclerosis, which exhibits thickening of the intima with a lipid pool, in-stent neoatherosclerosis typically has a necrotic core that is primarily formed by macrophage apoptosis without a lipid pool [43].

Effects of the underlying lesion

Other considerations for the mechanisms of neoatherosclerosis include the nature of the underlying atherosclerotic lesion. The majority of neoatherosclerosis originates and persists in the stented vessel area. Extension of the neoatherosclerosis to the distal and proximal non-stented regions of the vessel is not seen frequently. In unstable lesions, during the implantation of DES, stent struts are commonly embedded into the necrotic core region that leads to a longer period of drug release. This is likely to result in delays to the recovery of the endothelium, thus accelerating neoatherosclerosis observed in stented unstable lesions [37, 43].

Detection of neoatherosclerosis

There are discrepancies in several studies that have observed neoatherosclerosis given the limitations of detection techniques. For example, studies that have observed higher incidences of neoatherosclerosis after stent implantation are those that rely on identification through histological analysis rather than intravascular imaging such as optical coherence tomography (OCT) imaging. This is due to the fact that the resolution of the OCT modality is not high enough to decipher some of the morphological features found in neoatherosclerosis, including foam cell macrophages [29, 37].

1.7.3.3 Preclinical models of neoatherosclerosis post-stent implantation

Because the incidence of neoatherosclerosis contributes to stent failure and stent thrombosis after stent implantation, there is a need for a small animal model that replicates this process to gain mechanistic insights and for testing of potential diagnostic and therapeutic agents. To expand on the investigations of neointimal hyperplasia, attempts to develop a small animal model of in-stent neoatherosclerosis have been explored. Preclinical studies, to complement clinical observations, are integral to better understand the mechanisms underlying in-stent neoatherosclerosis.

Many preclinical studies of in-stent restenosis have been conducted in atherosclerotic rabbits, however, very few have specifically examined in-stent neoatherosclerosis. Nakazawa *et al.* [46] used an atherosclerotic rabbit stenting model to examine differences in response to different types of DES including a new-generation biodegradable versus a durable polymer DES. The model involved an initial balloon injury in the iliac artery of rabbits fed an atherogenic diet. The rationale behind this initial balloon injury was to accelerate atheroma that is more SMC rich and contains lipid laden macrophages seen in human lesions rather than just foam cell-containing plaque from the hypercholesterolemia alone. After 4 weeks post-injury, the animals were switched to a lower cholesterol diet for 4 weeks before stents were implanted in the iliac artery [46]. Stented arteries were harvested after 28 days and then analysed for vascular changes. This rabbit model was not specifically designed to study neoatherosclerosis, however, foamy macrophage infiltration was observed in the neointima, a characteristic of neoatherosclerosis. They concluded that the biodegradable polymer-based DES (Synergy DES) demonstrated the most rapid stent strut coverage and observed the least amount of neoatherosclerosis.

Nicol *et al.* [47] also implanted stents into the iliac arteries of rabbits to model early in-stent neoatherosclerosis. This again involved the initiation of hyperlipidaemia with an atherogenic diet for 5 weeks which was switched to a reduced cholesterol diet until week 13. Balloon injury was then followed by stent implantation (a BMS) with repeated denudation of the stented segment completed at 8 weeks. After 13 weeks, at the end of the study, the stents were imaged using OCT and stented vessels were examined by histopathology. This model induced neointimal foam cell formation but required the animals to be fed a hypercholesterolemic diet and the repeated denudation of the stented area. Furthermore, this model only developed early signs of neoatherosclerosis (neointimal foam cells) and was limited by diet-induced liver failure, preventing a longer course of observation. This does not model the later stages of in-stent neoatherosclerosis, in which complications such as restenosis and late thrombosis may arise.

Other attempts to investigate in-stent neoatherosclerosis have involved the use of a rabbit model in which a stent is implanted into the carotid artery. Zhang *et al.* [48] utilised this model, with rabbits fed an atherogenic diet 1 week after the deployment of a sirolimus-eluting (SES) stent into the right common carotid artery. This study imaged the stented carotid vessel using OCT 4 and 12 weeks post-stent deployment. This study examined whether methotrexate, an immunosuppressant, could suppress neoatherosclerosis through modulation of vascular responses. They found that methotrexate treatment reduced rates of lipid-rich intima formation that led to smaller neointimal areas. Lower levels of serum pro-inflammatory factors such as interleukins, adhesion molecules and p65-NFκB following methotrexate treatment were also reported, suggesting that augmenting anti-inflammatory pathways may influence the development of in-stent neoatherosclerosis.

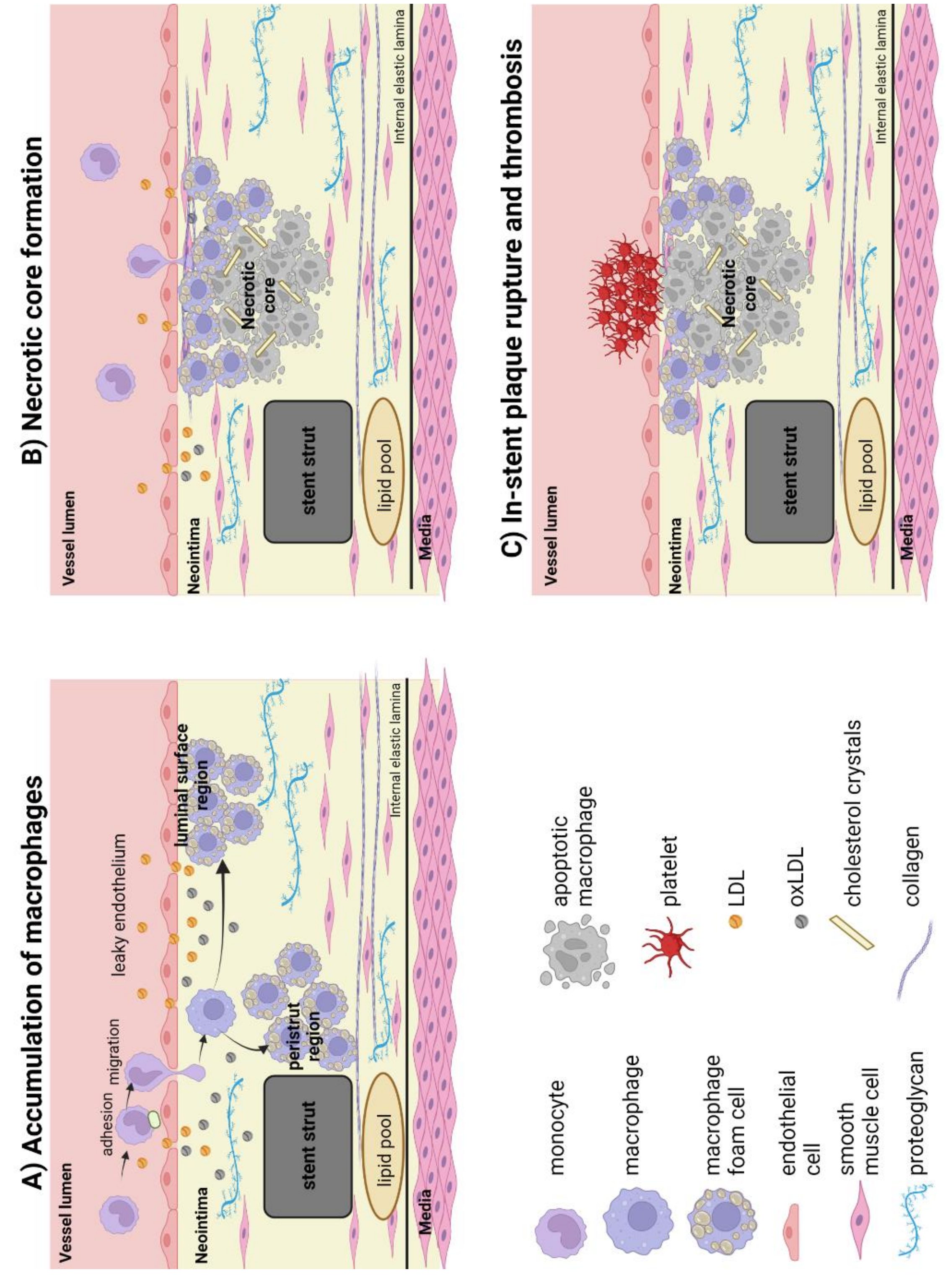
A) Accumulation of macrophages
Vessel lumen
adhesion
migration
leaky endothelium
Neointima
stent strut
lipid pool
peristrut region
luminal surface region
Internal elastic lamina
Media
B) Necrotic core formation
Vessel lumen
Neointima
stent strut
lipid pool
Necrotic core
Internal elastic lamina
Media
C) In-stent plaque rupture and thrombosis
Vessel lumen
Neointima
stent strut
lipid pool
Necrotic core
Internal elastic lamina
Media
monocyte
macrophage
macrophage foam cell
endothelial cell
smooth muscle cell
proteoglycan
apoptotic macrophage
platelet
LDL
oxLDL
cholesterol crystals
collagen

Figure legend 1.4: Potential mechanisms underlying in-stent neoatherosclerosis development

Mechanisms of in-stent neoatherosclerosis are thought to be similar to native atherosclerosis but are exacerbated by stent placement, especially drug-eluting stents. (**A**) Following vascular stent placement, the leaky endothelium is characterized by incomplete cell-to-cell junctions that could allow lipoproteins to enter the sub-endothelial space. Disturbance of the local blood flow may also cause inflammatory activation of the endothelium with resulting increases in both adhesion and migration of monocytes into the sub-endothelial space. These monocytes differentiate into macrophages and as they uptake lipoproteins convert to macrophage foam cells. These macrophage foam cells tend to accumulate in the peri-strut and subluminal regions. In addition, the increase in proteoglycan deposition in the neointima after stent placement can promote lipoprotein retention and exacerbate neoatherosclerosis. (**B**) Over time the continued accumulation of macrophage foam cells and subsequent apoptosis contributes to the formation of necrotic core. (**C**) As the necrotic core increases in size, the fibrous cap can be disrupted and lead to in-stent plaque rupture and thrombosis.

Figure created with BioRender.com Adapted from Otsuka *et al.* [37].

1.8 Imaging atherosclerosis

Current detection methods are sufficient to detect stenosis of vessels but are not adequate to characterise the molecular properties of the atherosclerotic plaque. The current gold-standard diagnostic method for atherosclerotic lesion detection involves the use of non-invasive angiography by X-ray, magnetic resonance (MR) or computed tomography (CT) modalities that detect the stenosis of the lumen [8, 49]. However, detection of stenosis is not able to provide compositional information which is important for determining whether a plaque is at risk of rupture. In addition, invasive imaging technologies such as intravascular ultrasound (IVUS) and OCT can be used to provide better resolution of the plaque composition as well as vessel wall thickness. IVUS can detect certain components of the plaque like the necrotic core with a certain amount of accuracy but cannot decipher the thin fibrous cap due to insufficient resolution. OCT can resolve and measure the fibrous cap thickness but does not have the sufficient tissue penetration to image all plaque features like the lipid pool [8, 49]. In addition to atherosclerosis, there is an inability to accurately identify the presence of in-stent neoatherosclerosis due to the difficulty in resolving the presence of foam cell macrophages, a key feature of neoatherosclerosis [29, 37].

Molecular imaging focuses on improving the resolution of current imaging approaches by incorporating information about the molecular and cellular characteristics of the target region [8]. For example, in atherosclerosis there is a need for characterising the cellular content of the plaque to better inform on the underlying pathology. Typically, this type of imaging uses nanoparticle tracers to monitor a particular aspect of atherosclerosis biology such as inflammatory activity.

Positron emission tomography (PET) is a nuclear imaging technique with high sensitivity that can be used to track distribution of radiotracers. Some of the advancements in nuclear imaging of atherosclerosis has included the use of 2-deoxy-2-[^{18}F]fluoro-D-glucose ([^{18}F]FDG) in identification of areas of inflammatory cells in atherosclerosis [50]. However there are limitations in the specificity of uptake of [^{18}F]FDG, with uptake by the metabolically active myocardium making the resolution of the plaque in coronary arteries difficult to discern [51]. In addition, PET is commonly utilised to image the distribution of radiolabelled nanoparticles typically combined with CT or MRI to provide anatomical reference [52, 53].

Another molecular imaging modality includes the use of near infrared fluorescence (NIRF) imaging which detects NIR fluorescent probes incorporated into nanoparticles. NIRF imaging has some advantages including the absence of radiation but also good sensitivity and spatial resolution. However NIRF is generally restricted to preclinical use in mice as the technique is limited by poor penetrance (<5cm) [8]. Typically this type of molecular imaging is used preclinically to demonstrate the accumulation of nanoparticles into areas of atherosclerotic plaque deposition [8, 54]. Fluorescence molecular tomography (FMT) is another type of fluorescence imaging that can generate a three-dimensional image of a fluorescent probe that can be used to monitor molecular changes. This has been used to track protease activity but also can also be used to track fluorescently labelled nanoparticles [54].

The composition of the plaque plays an important role in the clinical outcome, for example with vulnerable plaque that is prone to rupture. Therefore, improving the specific detection of plaques that are at risk of causing a clinical event would be a positive move towards preventing deaths from CVD.

1.9 Use of nanotechnology and nanoparticles in atherosclerosis

Nanotechnology is an area of research that involves the use of materials on the nanoscale. In medicine, nanotechnology can be applied to assist diagnosis and treatment of various diseases using specifically designed nanoparticles. Given the great flexibility in the design of nanoparticles, there are opportunities to incorporate both therapeutic and diagnostic aspects of conventional medicines to develop multifunctional theranostic nanoparticles. The obvious benefits of such an approach are the administration of a single agent to simultaneously treat and detect disease [55].

The incorporation of specific imaging agents into nanoparticles can improve the contrast of atherosclerosis on different imaging modalities. Imaging probes such as Iron (Fe) oxide, Manganese (Mn) oxide and Gadolinium (Gd) chelates can be used to improve contrast of MRI. CT contrast can be improved by gold and iodine labelled nanoparticles. For detection with PET imaging, radioisotopes such as ^{64}Copper (^{64}Cu) and ^{89}Zirconium (^{89}Zr) can be incorporated. In addition, some of the more experimental detection methods includes the use of fluorescence molecular tomography (FMT) with NIR fluorescent dyes and quantum dots [8].

For applications in CVD, specifically designing nanoparticles for atherosclerosis, there is an emphasis on targeting key characteristics of plaque and modulating the inflammatory environment. Macrophages, as discussed previously, are a key target for nanoparticles, having roles in both the progression and regression of atherosclerosis [55]. Furthermore, strategies to develop novel nanotechnology for applications in atherosclerosis have included therapeutic approaches that target macrophages and their role in atherosclerosis progression. Some recent examples include the design of nanoparticles to target defective efferocytosis in macrophages. An approach by Flores *et* *al.* [56] utilized single-wall carbon nanotubes (SWNTs) to target plaque macrophages and promote efferocytosis. SWNTs are preferentially taken up by the Ly-6CHi subset of activated monocytes that are known to subsequently differentiate into plaque macrophages. As efferocytosis is dysfunctional in atherosclerosis, the authors designed a SWNT-based nanoparticle that included an inhibitor of Src homology 2 domain-containing phosphatase-1 (SHP-1) which is downstream of the receptor CD47. CD47 is a receptor that binds to “don’t eat me” ligands and is upregulated in atherosclerotic plaque, including unstable plaque. These nanoparticles therefore inhibit the CD47 signalling cascade in inflammatory monocytes/macrophages and restore efferocytosis in atherosclerotic plaques. This study found that SWNT nanoparticles accumulate in plaques, improve the phagocytic ability of macrophages and reduce plaque burden in *Apoe-/-* mice.

Tao *et al.* [57] also investigated a nanoparticle-based strategy that incorporated an siRNA targeting Ca^{2+}/calmodulin-dependent kinase γ (CAMKIIγ). CAMKIIγ is a calcium-activated kinase that has previously been shown to be activated in advanced plaque and promote the development of unstable necrotic atherosclerotic plaques with a thin fibrous cap [57]. This mechanism is driven by the suppression of MerTK, a key receptor involved in efferocytosis. The design of the nanoparticles included a PLGA core loaded with CAMKIIγ siRNA and cationic lipid complexes. These particles also utilised a S2P peptide to target the particles to the stabilin receptor on macrophages. These nanoparticles could lower CAMKIIγ and increase MerTK expression in the macrophages of atherosclerotic plaques. Increased efferocytosis, reduced necrotic core area and an increase in fibrous cap thickness were also observed. This indicates that CAMKIIγ silencing nanoparticles can directly modify macrophage activity and increase the stability of atherosclerotic plaque by increasing efferocytosis.

In addition, approaches to nanoparticle development in atherosclerosis have included the use of high-density lipoprotein (HDL) and HDL-mimetic nanoparticles to improve the uptake of contrast agents and therapies. Given that endogenous HDL interacts with plaque macrophages, HDL provides an optimal structure for designing nanoparticles that accumulate at the site of atherosclerosis [58].

1.10 High Density Lipoprotein

High density lipoproteins (HDL) are endogenous particles composed of an inner hydrophobic core of cholesterol esters and triglycerides with an outer amphipathic layer of phospholipid and various apolipoproteins (apo A-I, A-II, A-IV, C, E, J and D). HDL precursors are discoidal-shaped particles synthesised in the liver or small intestine and typically consist of phospholipid and apolipoprotein A-I (apoA-I). The lecithin:cholesterol acetyltransferase (LCAT) reaction delivers cholesterol, mainly cholesterol esters, to discoidal HDL resulting in spherical HDL particles [58, 59].

HDL levels have been inversely linked with CAD risk, with the Framingham study conducted in the 1970's finding a correlation between lower levels of HDL and CAD [60]. Classically, HDL participates in the process of reverse cholesterol transport (RCT), whereby cholesterol is removed from peripheral tissues, including from macrophages in atherosclerotic plaques, via binding of cholesterol transporters ABCA1, ABCG1 and SR-BI. Cholesterol-carrying HDL then travel to the liver where they deliver cholesterol into the liver cells via SR-BI, a site where it can be safely processed and then excreted from the body [61]. This process of HDL-mediated reverse cholesterol transport is thought to contribute to the cardioprotective role of HDL. Preclinical studies have also shown that HDL inhibits adhesion molecule expression in endothelial cells [62], is anti-inflammatory (via suppression of adhesion molecules and cytokines/chemokine) [63], decreases macrophage content [64], inhibits macrophage apoptosis [65], is anti-oxidative (prevents oxidation of LDL) [66] and anti-thrombotic [67]. Despite the anti-atherosclerotic effects of HDL there have been significant problems in the translation of HDL-raising therapies into patients [68-71]. This raises the question of how to modify HDL in a way that optimises its beneficial effects so that it is effective in appropriate pathophysiological contexts.

1.11 HDL-like nanoparticles for atherosclerosis

HDL-like/ mimetic nanoparticles have some intrinsic advantages over other types of nanoparticles, with the ability to localise to the site of atherosclerotic plaque. This is achieved by exploiting the endogenous function of HDL in mediating reverse cholesterol transport from the plaque site which typically means additional targeting ligands are not required [58, 72]. In addition, HDL-like nanoparticles are inherently anti-atherosclerotic which means that the additional inclusion of drugs can be used to improve on these properties [58].

1.11.1 Examples of theranostic HDL-like nanoparticle therapies targeted to macrophages in atherosclerosis

Inhibition of inflammation has been proven to be a viable strategy to reduce recurrent cardiovascular events [73]. The CANTOS trial tested Canakinumab, a monoclonal antibody against the pro-inflammatory cytokine IL-1β. Canakinumab significantly reduced high-sensitivity C-reactive protein levels from baseline and lowered the incidence of recurrent cardiovascular events, when compared to placebo [73]. One drawback to systemic IL-1β inhibition was the finding of a higher rate of death from unrelated infections [73]. This highlights that improved targeting of inflammation of atherosclerotic plaque with nanoparticles [74, 75], through plaque-specific uptake of anti-inflammatory drugs which is mediated by macrophages, could be a highly effective strategy to reduce off-target effects of immunosuppressing therapies applied systemically [50, 54, 76, 77].

Statins are widely-used oral cholesterol-lowering medications that inhibit the rate-limiting enzyme of the cholesterol synthesis pathway 3-hydroxy-3-methylglutaryl coenzyme A reductase (HMGR) to reduce cholesterol production. Statins also exhibit anti-inflammatory properties at high doses. This anti-inflammatory effect can be enhanced further when using a high dose specifically targeted to the plaque site, thereby avoiding the off-target effects that may occur when delivering a high dose systemically [54]. One example of the success of this approach are reconstituted high-density lipoprotein (rHDL)-based nanoparticles loaded with simvastatin (S-HDL). S-HDL improved the bioavailability of the statin cargo as the nanoparticles were found to preferentially accumulate in plaque macrophages [78]. S-HDL reduced inflammation in macrophages *in vitro* and plaque inflammation *in vivo* using the atherosclerosis-prone apolipoprotein (*Apo)e*$^{-/-}$ mouse model. The authors in this study postulated that the anti-inflammatory effect of S-HDL was a direct result of the specificity of the statin delivery to macrophages. In parallel, S-HDL particles were shown to reduce the proliferation of plaque macrophages [79], which suppresses plaque expansion. Movement of the S-HDL particles was tracked using a combination of fluorescence and magnetic resonance imaging (MRI). Importantly, it was shown that S-HDL particles could successfully reduce inflammation in larger preclinical animal models of atherosclerosis such as the rabbit and pig [76], indicating the high potential for clinical translation.

During atherosclerosis progression, circulating monocytes are recruited to the vessel wall, which contributes to the accumulation of macrophages in the plaque. An interesting approach by Lameijer *et al.* [80] capitalised on this pathway by utilising an rHDL-based nanoparticle with a small molecule inhibitor of TRAF6 (TRAFi). Inhibition of TRAF6 blocks the activation of plaque resident monocytes and macrophages through suppression of CD40-TRAF6 interactions, causing an anti-atherogenic effect [81]. TRAF6i-rHDL nanoparticles were able to specifically accumulate in monocytes not lymphocytes and could be detected using both a fluorescent dye and positron emission tomography (PET) imaging of ^{89}Zr labelled particles in both *Apoe*$^{-/-}$ mice and non-human primates. They found that these particles were able to reduce plaque inflammation in *Apoe*$^{-/-}$ mice by impairing the migratory capacity of circulating monocytes [82].

As well as being an endogenous liposomal nanoparticle, HDL is a mediator of cholesterol efflux. The capacity of HDL to promote cholesterol efflux can be retained even when the internal core components are modified [83]. HDL-like magnetic nanostructures (HDL-MNS) consisting of an iron oxide (Fe_3O_4) core have been shown to promote cholesterol efflux in a comparable manner to native HDL, in parallel to improving MRI contrast in cultured macrophages [84].

1.12 Porphyrin-lipid nanoparticles

Some of the advances in nanoparticle design have been achieved by modifying the initial building blocks to be multifunctional. The Zheng laboratory (University of Toronto) have pioneered the synthesis of porphyrin-lipid nanoparticles [85]. These nanoparticles are unique as they are organic lipid-based nanoparticles that incorporate a range of functionalities that will be discussed in the following section.

1.12.1 Porphyrin chemistry

Porphyrins are a class of heterocyclic organic molecules which are integral to the survival of mammalian and plant life. For example, porphyrins and their derivatives are involved in biological processes such as oxygen transportation (heme in haemoglobin) and photosynthesis (chlorophyll in chloroplasts). Porphyrins are known for having unique photophysical properties, with an aromatic macrocyclic structure. The common optical signature for porphyrin compounds is the strong absorption of visible light at ~400nm (the Soret band) and absorption at four less intense bands between ~450-650nm [85, 86].

1.12.2 Photodynamic therapy from porphyrin compounds

Following absorption of light, during the conversion from different energy states down to the ground state, porphyrins undergo non-radiative vibrational relaxation, fluorescence emission or transition to a triplet state. Longer time spent in the triplet state allows porphyrin to either go through radiative decay by phosphorescence or generate ROS with the surrounding environment. This subsequent generation of highly reactive singlet oxygen in the presence of light is the basis for photodynamic therapy (PDT), which can cause damage to cellular components like DNA, protein, mitochondria and the cell membrane to induce the apoptosis of target cells [86].

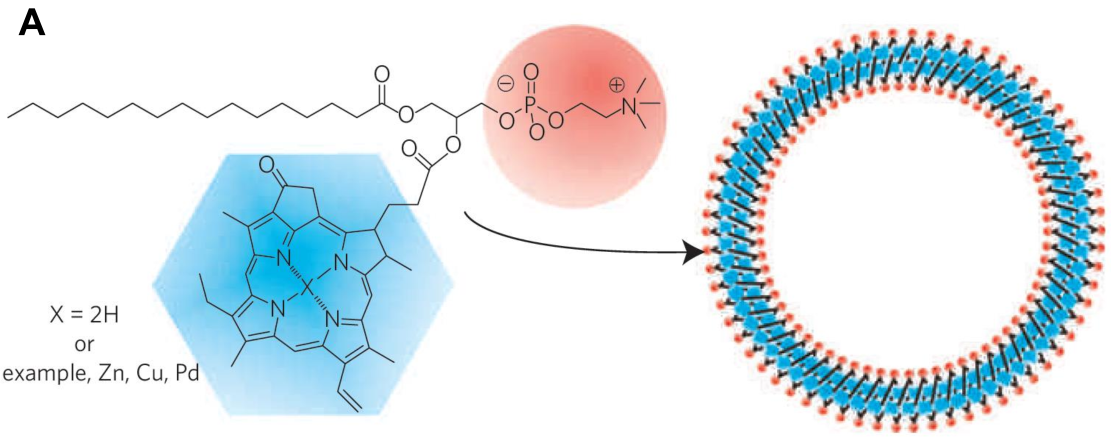
A
X = 2H
or
for example, Zn, Cu, Pd

Pyropheophorbide-phospholipid conjugate (porphyrin-lipid)

Porphysome

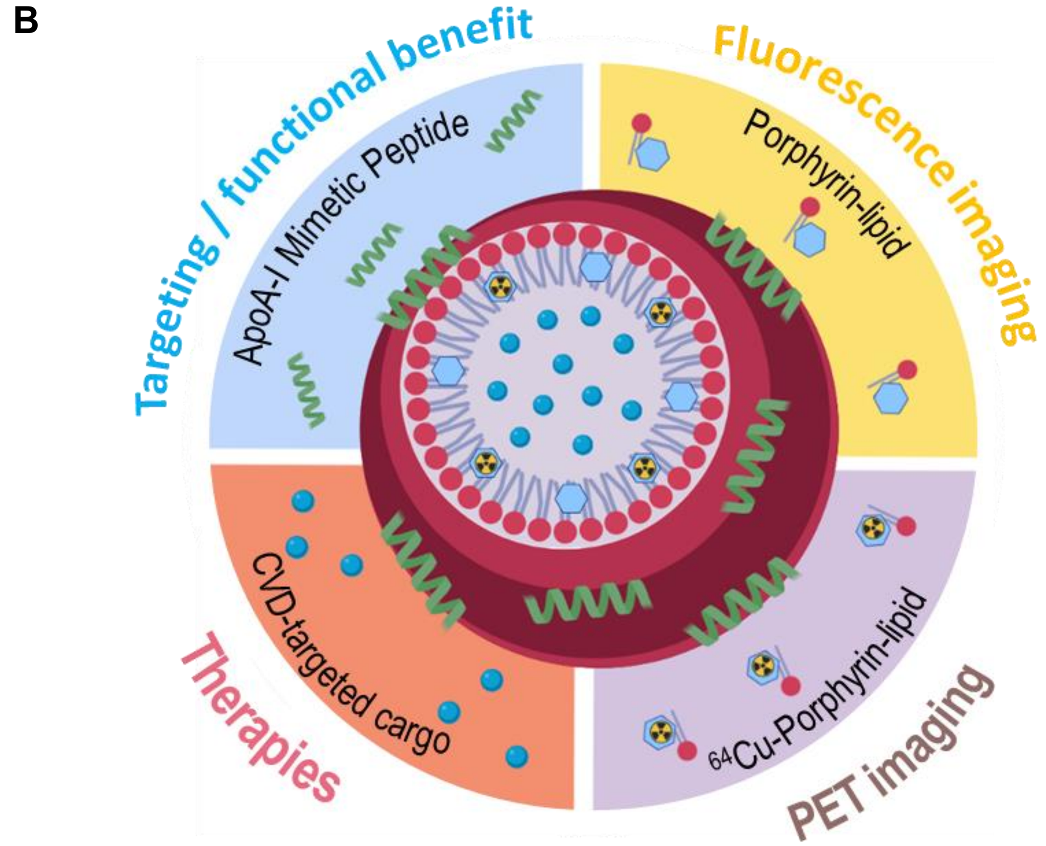
B
Targeting / functional benefit
ApoA-I Mimetic Peptide
Fluorescence imaging
Porphyrin-lipid
Therapies
CVD-targeted cargo
PET imaging
64Cu-Porphyrin-lipid

apoA-I linked porphysome/
Porphylipoprotein (PLP)

Figure legend 1.5: Chemical and structural diagrams of porphyrin-lipid based nanoparticles.

(**A**) Pyropheophorbide-phospholipid (porphyrin-lipid) conjugates form the liposomal nanoparticles porphysomes. Image modified from Lovell *et al*. [80] (**B**) Porphyrin-lipid combined with apoA-I mimetic peptide forms apoA-I-linked porphysome/ Porphylipoproteins (PLP) that can be detected via fluorescence and PET imaging, can be loaded with targeted therapies.

1.12.3 Fluorescence/ metal chelation properties of porphyrin compounds

The accumulation of porphyrin can also be exploited for the red/NIR fluorescence emission to be used with fluorescence imaging. Furthermore, porphyrins can chelate transition metals such as zinc (Zn), manganese (Mn), iron (Fe) or copper (Cu). This enables extension of the fluorescence imaging modality to be complemented with positron emission tomography (PET) using radiolabelled metals (e.g.^{64}Cu) or magnetic resonance imaging (MRI, with Mn) [86-88].

Despite porphyrin monomers possessing ideal photophysical properties they have some limitations when it comes to applications in biological systems. Monomeric porphyrins are highly hydrophobic, which can lead to aggregation in aqueous environments, causing a reduction in bioavailability and preventing accumulation at target sites. In addition, the chelation of certain metals quenches the fluorescence properties of porphyrins and decreases the capacity to generate singlet oxygen. This means that multimodal imaging capabilities cannot be simultaneously or effectively enacted by porphyrins in their monomeric form [86].

1.12.4 Porphysomes

The properties of porphyrin compounds can be improved by organisation into supramolecular structures that augment the structure to be more favourable for biological uptake. In the case of organic nanoparticles that incorporate porphyrin, the pyropheophorbide (chlorophyll-derived porphyrin derived analogue) is conjugated via an acylation reaction to lysophosphatidylcholine (phospholipid) to form porphyrin-lipid. By doing this the hydrophobic porphyrin chromophore is placed at the location of an alkyl side chain which retains the amphipathic structural properties of the phospholipid. Initially it was found that these porphyrin-lipid monomers formed into porphyrin lipid liposomes or "porphysomes" (Fig 1.5A). The inclusion of polyethylene glycol (PEG) into the structure can be used to improve the pharmacokinetic profile *in vivo.* These porphyrin-lipid conjugates self-assemble while in aqueous solution and are then extruded to form porphysomes, with a bilayer of porphyrin-lipid in the spherical vesicle with a diameter of 100nm [85]. These particles were found to be well tolerated *in vivo* with a low toxicity profile, with no detrimental effects reported following 1000mg/kg intravenous injection [85].

1.12.5 HDL-like apoA-I linked porphyrin-lipid nanoparticles

Cui *et al.* [89] has synthesised an HDL-like porphyrin-lipid nanoparticle that incorporates a mimetic peptide of apoA-I (Fig 1.5B). The addition of the mimetic peptide (R4F) was to take advantage of cytosolic delivery through the SR-BI pathway that apoA-I acts [90]. The lipoprotein-like, apoA-I-linked porphyrin-lipid nanoparticles, identified as porphylipoprotein (PLP), are composed of a porphyrin-lipid monolayer enveloping a hydrophobic drug-loadable core which is linked to the apoA-I mimetic R4F (Ac-FAEKFKEAVKDYFAKFWD). The apoA-I mimetic constrains the size of the particles (~20nm) making them ideal for uptake into tissues. Furthermore, addition of the apoA-I mimetic to the porphysome significantly improves the uptake of the particle into cells as shown *in vitro, in vivo* and *ex vivo* [89]. Therefore, by taking advantage of the endogenous lipoprotein transport of apoA-I, these porphysome particles are stable in blood circulation (half-life of 9.9 hrs) and can be taken up effectively by target cells, as shown by uptake of these particles into tumours in animal models [89, 91].

Other advantages of porphyrin-lipid nanoparticles with inclusion of the apoA-I mimetic, is that PEGylation is not required [89]. PEG is commonly used in the manufacture of nanoparticles as a "stealth coating" to improve blood circulation lifetimes. PEGylation is thought to reduce the level of opsonisation, which is the process by which larger particles and nanoparticles adsorb plasma proteins (opsonins) to label the particles as foreign substances. This leads to processing and removal by the mononuclear phagocyte system which means PEG can help to extend the circulation times of nanoparticles. However, PEG can have unwanted side-effects when it comes to carrier nanoparticles and delivery of cargo whereby PEG can compromise intracellular uptake by interfering with nanoparticle-cell interactions and endosomal escape of nanoparticles [89, 92-94]. Endosomal escape is a process whereby the nanoparticle escapes endosomal entrapment and subsequent degradation in acidic compartments of the cell. In addition there are concerns about the immunogenic nature of PEGylation, with repeated administration of PEGylated liposomal nanoparticles leading to a reduction in blood circulation times [94].

Some of the benefits of converting individual porphyrin molecules into larger supramolecular complexes are the inclusion of multiple porphyrin molecules into a single structure. This provides multiple sites to add in a metal chelator for radiolabelling for nuclear medicine applications. For example, porphysome nanoparticles have a high radiolabelling capacity, shown with ^{64}Cu for PET imaging, which could be achieved with a simple robust methodology. The chelation of the ^{64}Cu within porphyrin is stable in serum for at least 24 h and stable chemically for 30 h. This demonstrated that the intact radiolabelled porphysomes could be detected by PET *in vivo* [87, 95].

Another feature of porphysome structures is that the high-density packing of the bilayer of porphyrin-lipid (~80000 porphyrin units/particle) in the supramolecular structure, causes quenching of fluorescence emission from the porphyrin. This is a property that is useful for activatable fluorescence upon porphysome accumulation in tumours or other cellular targets [85, 86]. Cui *et al.* [89] also showed that HDL-like porphyrin-lipid nanoparticles undergo intracellular trafficking and rapid nanostructure dissociation on accumulation within a tumour which unquenches the fluorescence properties of porphyrin. This allows for more specific NIR fluorescence imaging and photodynamic therapy of target regions [85].

1.12.6 Theranostic applications of porphyrin-lipid based nanoparticles in preclinical models

Several studies have examined porphysome nanoparticles and lipoprotein-like porphyrin-lipid nanoparticles for their utility as theranostic nanoparticles. To date, they have been primarily used for pre-clinical cancer tumour detection applications. The advantage of using these types of nanoparticles is the multimodal properties which can be utilised to meet the needs for both diagnostic and therapy as an "one-for-all" approach. This approach is desirable as the porphyrin-lipid building block intrinsically incorporates the detection, via fluorescence and PET modalities, within the backbone of the nanoparticle [96].

Porphysomes

The primary application of porphysomes for cancer is to better delineate the cancerous tumour tissue from the surrounding healthy tissue. Porphysomes have been utilised in several cancer models, primarily for their ability to localise to the tumour of interest. Initially porphysomes were tested for their ability to associate with tumour tissue and for use with photothermal therapy. In a murine KB xenograft model (grafted tumours), porphysome NIR fluorescence was detected in the tumour region with low background fluorescence. Typically, photothermal therapy uses inorganic nanoparticles such as gold nanorods but porphysomes had a comparable photothermal efficiency and could be used *in vivo* to ablate cancer cells [85]. Furthermore, the ^{64}Cu-labelled porphysomes [87] were validated for PET/CT and fluorescence detection of tumour tissue delineation in preclinical models of prostate and bony metastatic cancer [88], head and neck cancer [91] and metastatic endometrial cancer [97]. The multimodal PET/CT and fluorescence imaging of prostate cancer tumours with porphysomes is shown in Fig 1.6.

Lipoprotein-like porphyrin-lipid nanoparticles

The addition of further targeting of porphysome nanoparticles has been improved by modifying the particles to resemble the structure of lipoproteins to improve uptake in specific cancer models. Lipoprotein-like porphyrin-lipid nanoparticles synthesised with either apoA-I mimetic peptide R4F (porphylipoprotein, PLP) [89, 98] or apolipoprotein E3 (apoE3) [99] were assessed in several different cancer models. The lipoprotein-mimicking porphyrin-lipid nanoparticles that Cui *et al.* [89] first described were observed to have activatable NIR fluorescence and PDT within tumours in preclinical cancer models. This also showed that the PLP nanoparticles had a rapid uptake and activation of fluorescence compared to the original porphysome. These PLP and ^{64}Cu-labelled PLP nanoparticles were utilised in several specific cancer models including ovarian, glioblastoma multiforme [89] and head and neck cancers [98]. Overall, these studies demonstrated that the PLP nanoparticles localised to the tumour region, were detected with fluorescence and PET/CT imaging with potential use for PDT and image-guided resection of tumour tissue (Fig 1.7).

The uptake of porphyrin-lipid apoE3 lipid nanoparticles (pyE-LNs) was examined in a pre-clinical model of glioblastoma. The rationale for incorporating apoE3 into nanoparticles was to utilise the capacity for high active transport via the low density lipoprotein receptor (LDLR), which is highly expressed on glioblastoma, attributed to an elevated cholesterol metabolism to support tumour growth. In addition, apoE3 can cross the blood brain barrier and facilitates the transcytosis of nanoparticles, allowing for transport into the brain. pyE-LNs were selectively taken up by tumour tissue, with biodistribution in a 4:1 ratio of tumour: healthy tissue specificity and this was able to be detected as a strong fluorescence signal at the tumour site. This study shows that derivative porphyrin-lipid nanoparticles can be taken up selectively with the potential to be used as a theranostic to deliver drug cargo and a contrast agent to improve glioblastoma treatment [99].

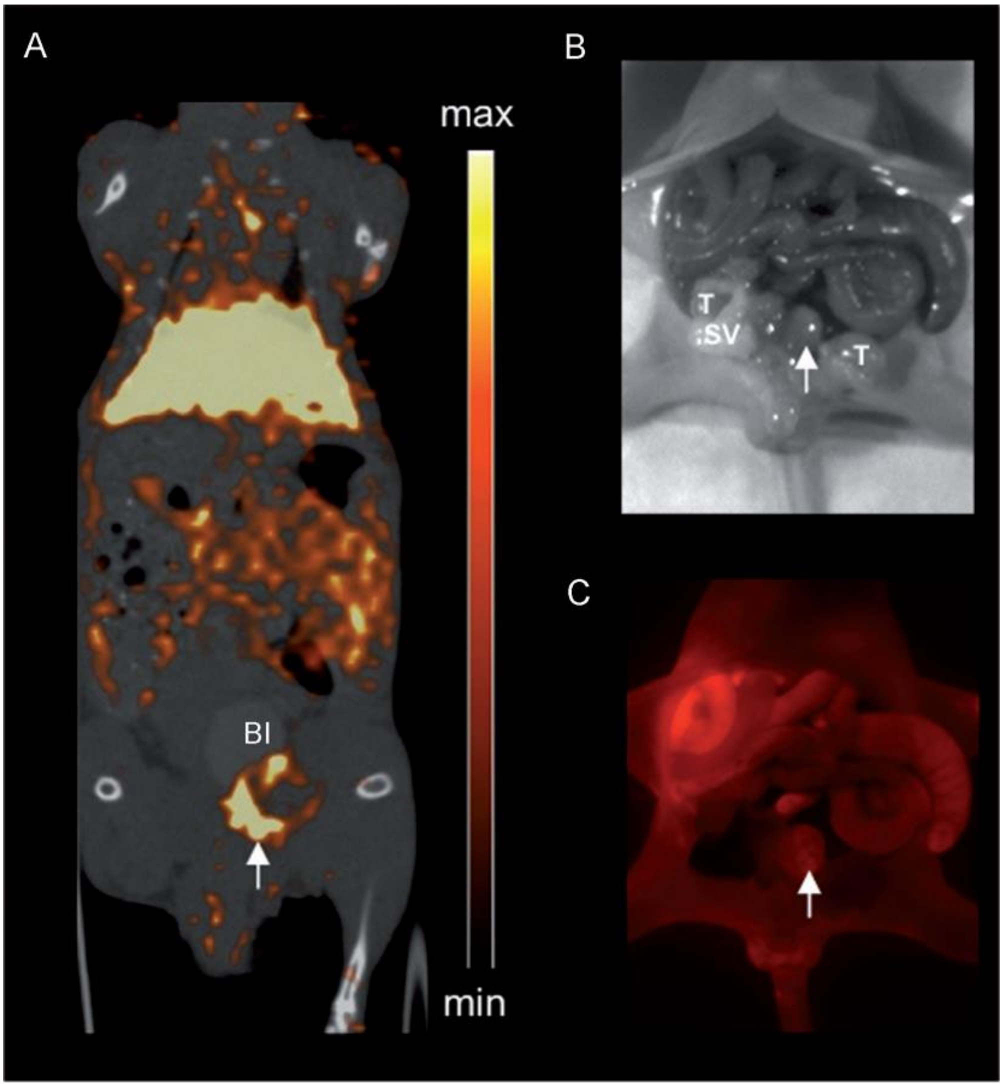

Figure legend 1.6: Multimodal imaging of ^{64}Cu-labelled porphysomes in prostate cancer model

(**A**) Representative MicroPET/CT images of coronal single slices through orthotopic PC3 tumour (n=4) at 24 h after intravenous injection of 500 mCi ^{64}Cu-porphysomes. PET image integration time 40 min. (**B**) White light image of orthotopic PC3 prostate tumour model. (**C**) Fluorescent image of orthotopic PC3 prostate tumour model. White arrows indicate prostate tumour, Bl indicates the bladder; SV indicates the seminal vesicles, and T indicates the testes.

Figure and legend from Liu *et al.* [87]

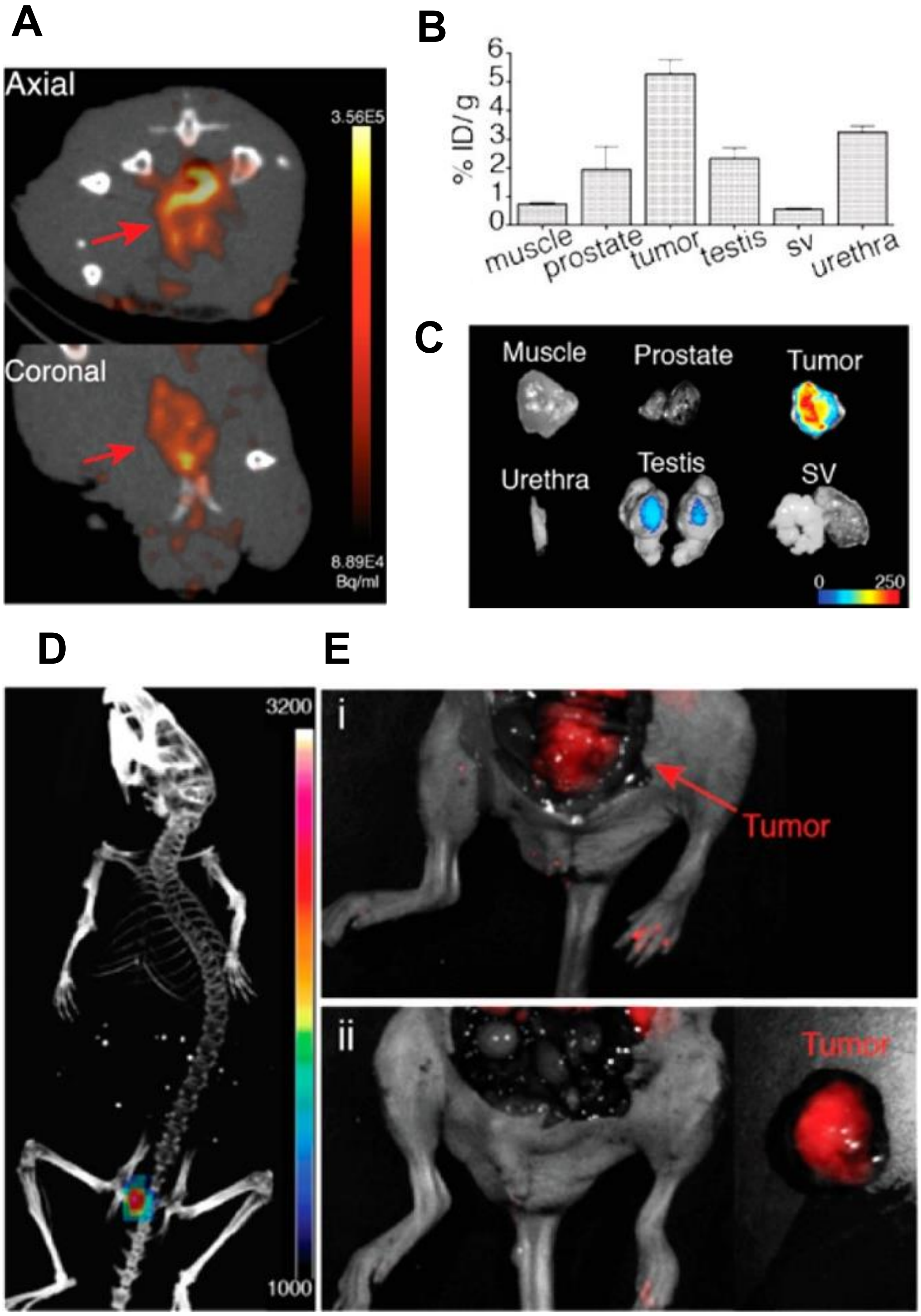
A
Axial
3.56E5
Coronal
8.89E4
Bq/ml
B
% ID/g
6
5
4
3
2
1
0
muscle
prostate
tumor
testis
sv
urethra
C
Muscle
Prostate
Tumor
Urethra
Testis
SV
0
250
D
3200
1000
E
i
Tumor
ii
Tumor

Figure legend 1.7: Tumour-specific uptake and multimodal imaging of apoA-I-linked porphylipoprotein (PLP) in an orthotopic prostate cancer model

(**A**) Representative axial and coronal views of PET/CT imaging of PC-3 orthotopic prostate cancer mice after 24 h intravenous injection of ^{64}Cu-PLP (red arrow: tumour). (**B**) Distribution of ^{64}Cu-PLP in tumour and surrounding tissues calculated as percentage of the injected dose per gram (% ID/g), sv stands for seminal vesicle (n = 4, $P < 0.05$). (**C**) *Ex vivo* fluorescence imaging of resected tumour and surrounding tissues. (**D**) Representative coregistration of CT and fluorescence molecular tomography (FMT) in the region of interest after 24 h intravenous injection of PLP, clearly revealing the tumour margin. (**E**) Intraoperative fluorescence imaging enabling the guidance of PC-3 orthotopic tumour resection: (i) before and (ii) after resection.

Figure and legend from Cui *et al.* [89]

1.12.7 ApoA-I mimetic peptide R4F

The R4F peptide used in the porphylipoprotein (PLP) nanoparticles [89, 98] is an apoA-I mimetic peptide. Typically, apoA-I mimetic peptides do not have sequence homology with the native apoA-I protein but are just structural mimetics initially designed to efflux cholesterol from target cells [100]. R4F is composed of 18 amino acid residues that form an amphipathic α-helix structure with 4 phenylalanine residues within the hydrophobic face ($\text{Ac-}\underline{\text{F}}\text{AEK}\underline{\text{F}}\text{KEAVKDY}\underline{\text{F}}\text{AK}\underline{\text{F}}\text{WD-NH}_2$).

The 4F peptide ($\text{Ac-DWFKAFYDKVAEKFKEAF-NH}_2$) as an apoA-I mimetic has previously been investigated for use in cardiovascular research, primarily for the treatment of atherosclerosis. Previously, the 4F peptide composed of D-amino acids was found to be stable orally. This allowed oral administration in mice. This was not the case for 4F peptide composed of L-amino acids. In *Ldlr*$^{-/-}$ mice on a western diet, oral administration of the D-amino acid was found to reduce atherosclerotic lesion size independently of changes in plasma or HDL-cholesterol [101].

The R4F peptide is made up of amino acids that are in the reverse order of the 4F peptide, hence the name reverse-4F (R4F). The R4F peptide, made with D-amino acids, reduced atherosclerotic lesion and macrophage content when administered orally to *Apoe*$^{-/-}$ mice. The underlying mechanism for these changes was proposed to be inhibition of endothelial inflammation and the improvement of HDL functionality [102].

In addition to the effects that apoA-I peptide mimetics have on atherosclerosis, there are also benefits for the synthesis of nanoparticles with mimetic peptides. There are several nanoparticles that use rHDL [54, 79, 103] but potentially there can be inter-batch variability due to the isolation of the apoA-I component from human plasma [104].

Therefore, apoA-I mimetic peptides may be a more feasible approach for synthesis of HDL-like nanoparticles.

1.12.8 Targeting of SR-BI by HDL-like nanoparticles

The primary reason for the use of the R4F apoA-I mimetic in HDL-like nanoparticles is its known targeting abilities towards the SR-BI scavenger receptor. This has previously been utilised for cancer cells that are known to upregulate SR-BI [89, 98, 105]. Previous work has shown that HDL-like nanoparticles with the R4F-peptide are able to deliver nanoparticle payloads directly into the cellular cytoplasm via a lipid-raft/ caveolae-like pathway [90]. The endogenous function of the SR-BI receptor is the high affinity binding with HDL (or R4F) to mediate both the efflux and cellular uptake of cholesterol ester from the core of the lipoprotein. It is thought that the uptake of the cytosolic lipid core is achieved by the formation of a non-aqueous channel that can evade lysosomal degradation [90, 106]. However, SR-BI in malignant cells also mediates the selective uptake of cholesterol in response to increased cholesterol metabolism, leading to the observed increase in SR-BI expression in patient tumours and cancer cell lines [105].

1.13 Translating theranostic nanoparticles: cancer to atherosclerosis

Cancer and atherosclerosis share a number of common mechanisms such as oxidative stress, inflammation, angiogenesis and defective efferocytosis [107-109]. In both disease conditions, many of these mechanisms are associated with the functions of macrophages. A number of inorganic and carbon-based nanoparticles that target different types of macrophages (M1 and M2) have been reported to exhibit anti-cancer effects [110]. The pro-inflammatory, M1-like macrophage targeting nanoparticles can be used to treat the negative effects of immune evasion in cancer, whereas M2 macrophages that secrete anti-inflammatory cytokines are also prospective delivery vehicles for nanoparticle-based cancer therapy [110]. Similar mechanisms controlled by M1, M2 and other types of macrophages operate in the development, progression, and regression of atherosclerotic plaque [22, 111]. A number of cancer-based therapies targeting different macrophage phenotypes can therefore have the potential to be translated to applications for atherosclerosis.

1.14 Applications of porphyrin-lipid based nanoparticles in cardiovascular disease

Although the apoA-I linked porphyrin-lipid nanoparticles have been successfully tested pre-clinically in cancer models [89, 91], as yet these particles have not been tested specifically in a model of atherosclerosis. It is predicted that apoA-I linked porphyrin-lipid nanoparticles have the potential for use in the detection and treatment of atherosclerosis, primarily due to the inclusion of the apoA-I mimetic. The development of atherosclerotic lesions involves the infiltration of monocytes within the plaque, differentiating into macrophages, resulting in an inflammatory milieu and continuing plaque enlargement. An important factor in the composition of atherosclerotic plaques is the activity of monocytes and macrophages. Macrophages can phagocytose foreign bodies, making them an ideal target to take up nanoparticles from the circulation [8]. SR-BI is highly expressed on atherosclerotic plaque macrophages where it mediates both the influx and efflux of cholesterol [24, 112]. The SR-BI targeting capabilities of R4F-linked porphyrin-lipid suggest they will also be able to target plaque macrophages, promote cholesterol efflux and exhibit anti-inflammatory effects. In another related porphysome [113] design, functionalisation was achieved with folate to enable targeting to the folate receptor, present on activated macrophages. Folate-porphysomes successfully tracked to activated macrophage infiltrates in the murine myocardial ischemia/reperfusion model, measured using both non-invasive fluorescent and PET imaging modalities [113].

Another feature of porphyrin-lipid nanoparticles is that the central core can be loaded with therapeutic cargo or other imaging agents, further adding to their theranostic capabilities [89]. Overall, the multiple properties and imaging capabilities of porphyrin-lipid nanoparticles suggest that they have potential as a theranostic for atherosclerosis [113].

1.15 Hypothesis and aims

CVD still remains the leading cause of mortality and morbidity despite the effectiveness of current treatments in reducing cardiac events. Interventional procedures such as PCI with DES are highly effective revascularisation techniques however there are concerns around the development of in-stent neoatherosclerosis as a cause of very late stent complications. In addition, current diagnostic imaging techniques are unable to identify individuals who will have an ischemic event with a high level of accuracy. This highlights the need for novel therapies and diagnostic techniques that can exploit the inflammatory microenvironment, in particular the activity and presence of macrophages, found within the atherosclerotic plaque. As discussed, nanotechnology is one avenue that provides the opportunity to deliver theranostic agents that combine both therapeutic and diagnostic properties, providing simultaneous treatment and diagnosis of atherosclerotic CVD. Exploring these types of technologies for atherosclerosis is a challenging but worthwhile endeavour in order to develop highly novel improvements on current CVD management strategies.

Therefore this thesis investigates the hypothesis that apoA-I-linked porphyrin-lipid nanoparticles have theranostic applications in atherosclerotic CVD. This is to address knowledge gaps in: (1) the therapeutic and diagnostic interactions of porphyrin-lipid nanoparticles in plaque macrophages and (2) the suitability of porphyrin-lipid nanoparticles for use as a theranostic in atherosclerosis. Overall this thesis addresses the following aims:

1) To characterise the athero-protective and diagnostic functions of porphyrin-lipid nanoparticles in macrophages *in vitro.*
2) To investigate the therapeutic and diagnostic properties of porphyrin-lipid nanoparticles in atherosclerosis *in vivo* using murine models of a) stable atherosclerosis, b) unstable atherosclerosis, and c) in-stent neoatherosclerosis.

CHAPTER 2
General Methods

2.1 Porphysome nanoparticles

2.1.1 Porphysome nanoparticle synthesis

The apoA-I-linked porphysome nanoparticles used in these studies were synthesised, characterised, and kindly sent to us by Maneesha Rajora and Gang Zheng (University of Toronto, Canada). These particles consist of an outer layer of the phospholipid 1,2-Dimyristoyl-sn-glycero-3-phosphocholine (DMPC), porphyrin-lipid and R4F. R4F is an apoA-I alpha helical mimetic peptide (Ac-FAEKFKEAVKDYFAKFWD). The porphyrin lipid is formed by conjugation of pyropheophorbide-a (porphyrin) and single chain phospholipid 1-palmitoyl-2-hydroxy-sn-glycero-3-phosphocholine (16:0 Lyso PC) as previously described [85, 89].

2.1.2 Porphysome composition

For the *in vitro* studies, discoidal and spherical porphysomes containing 0.3% porphyrin-lipid of the total moles of lipid (0.3 mol %) were used in experiments assessing their anti-inflammatory properties (at 10 µg/mL) and cholesterol efflux capacity (at 10, 25 µg/mL). Discoidal porphysomes consist of DMPC complexed with the porphyrin lipid and spherical porphysomes also contain cholesteryl oleate (CO). For the *in vivo* studies, discoidal porphysomes were used, which consist of a higher concentration of the R4F-peptide component but contain only the DMPC phospholipid and no porphyrin-lipid (0 mol %). For imaging studies, the highest porphyrin-lipid content consisted of the 30 mol % porphysomes which contain 30% porphyrin-lipid of the total moles of lipid. The composition of each nanoparticle is summarised in Table 2.1, 2.2, 2.3 and Fig 2.1.

Table 2.1 0.3% Porphyrin-lipid nanoparticle composition (0.3 mol % porphyrin-lipid/total lipid)

Conformation	**Porphyrin-lipid composition**		**R4F composition**	
	µM	mg/mL	mM	mg/mL
Discoidal	24.3	0.0246	1.34	3.098
CO-loaded (Spherical)	26.4	0.0267	1.40	3.23

Table 2.2 30% Porphyrin-lipid nanoparticle composition (30 mol % porphyrin-lipid/total lipid)

Conformation	**Porphyrin-lipid composition** (mM)	**R4F composition** (mg/mL)
Discoidal	2.29	2.58 ± 0.1
CO-loaded (Spherical)	2.21	2.44 ± 0.1

Table 2.3 Discoidal R4F HDL mimetic nanoparticle composition (0 mol % porphyrin-lipid/total lipid)

Conformation	**Batch**	**R4F composition (mg/mL)**	**Ave R4F composition (mg/mL)**
Discoidal HDL mimetic	1	4.72 ± 0.08	5.186 mg/mL
	2	5.32 ± 0.09	
	3	5.518	

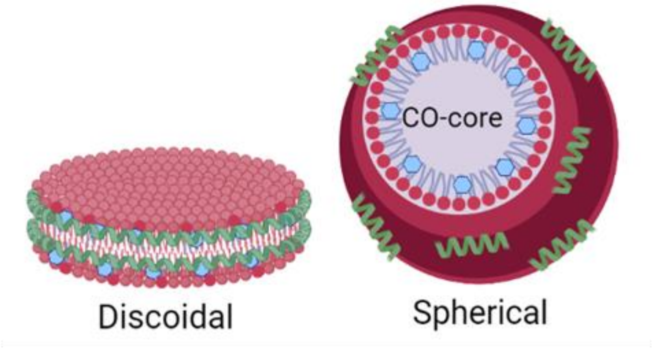

	POR-NPs (0.3 mol %)	**POR-NPs (30 mol %)**	**HDL-mimetic NPs (0 mol %)**
Porphyrin-lipid	0.3%	30%	0%
DMPC	99.7%	70%	100%
R4F apoA-I mimetic	3.1-3.2 mg/mL	2.4-2.6 mg/mL	4.7-5.5 mg/mL

Figure legend 2.1: Summary of porphyrin-lipid/ HDL mimetic nanoparticles.

Nanoparticles were either discoidal or spherical in structure with different composition of porphyrin-lipid, DMPC phospholipid (% of total moles of lipid per particle) and R4F mimetic peptide outlined for each nanoparticle formulation. 1,2-Dimyristoyl-sn-glycero-3-phosphocholine, DMPC.

2.1.3 ^{64}Cu-labelling of porphysome nanoparticles

^{64}Cu-Cl$_2$ production and nanoparticle labelling were conducted by the molecular imaging and therapy research unit (MITRU, SAHMRI, Adelaide, South Australia). 30 mol % porphyrin-lipid porphysome nanoparticles were labelled as previously described [87, 89]. Porphysomes were diluted 1:1 (vol/vol) with 0.1M NH_4OAc buffer (pH 5.5), mixed with ^{64}Cu-Cl$_2$ and incubated for 1 h at 37^{o}C. Radiochemical purity was verified by thin layer chromatography and activity measured using a dose calibrator prior to intravenous injection.

2.2 Preparation of discoidal reconstituted HDL

2.2.1 Reconstitution of apoA-I

Human apoA-I protein was reconstituted into reconstitution buffer (10 mM Tris, 3.0 M guanidine hydrochloride, 0.01% w/v EDTA-Na$_2$, pH 8.2) then dialysed against 5 x 1 L TBS (10 mM Tris-HCl, 150 mM NaCl, 0.006% w/v NaN_3 and 0.005% w/v EDTA-Na$_2$, pH 7.4).

2.2.2 Complexing apoA-I with PLPC

To prepare discoidal reconstituted HDL (rHDL), lipid-free apoA-I was complexed with 1-palmitoyl-2-linoleoyl-phosphatidylcholine (PLPC). In brief, PLPC was dried into a thin layer on the bottom of glass tubes with nitrogen gas. PLPC was then lyophilised overnight to ensure complete drying. Sodium cholate (30 mg/mL) was added to the tubes and vortexed until optically clear. 2 mg of apoA-I was added to each tube and incubated on ice for 2 h. Tubes were pooled and dialysed against 5 x 1 L TBS over 5 days, followed by dialysis against 3 x 1 L PBS for 3 days. The protein concentration of the apoA-I was determined using the BCA assay (Thermofisher Scientific).

2.3 Animal methods

2.3.1 Animal care

All experiments and procedures were approved by the South Australian Health and Medical Research Institute Animal Ethics Committee (AEC application SAM422.19) and conformed to the Australian code for the care and use of animals for scientific purposes (National Health and Medical Research Council, NHMRC). Male Apolipoprotein-E deficient (*Apoe*$^{-/-}$) mice on a C57Bl/6J background were fed *ad libitum* a high cholesterol diet (HCD) containing 21% Fat and 0.15% Cholesterol (SF-00219, Semi-Pure Rodent Diet, Specialty Feeds, WA, Australia) or standard rodent chow for various periods of time depending on the experimental model. Mice were housed in a facility with a 12 h light/dark cycle and had free access to sterilised water. All injected substances were administered with a 27G needle.

For all surgical procedures, mice were anaesthetised under isoflurane. Saline and buprenorphine (0.1 mg/kg) were also administered subcutaneously during the procedure. Mice were monitored following surgery, given pain relief with buprenorphine (0.1 mg/kg) as required and weighed regularly.

For all live-animal imaging procedures, mice were maintained under isoflurane anaesthesia and scans did not exceed 30 min.

2.3.2 Positron Emission Tomography (PET)

18.5-24 MBq of ^{64}Cu labelled porphysomes were injected intravenously via the tail vein of experimental *Apoe*$^{-/-}$ mice. Mice were then imaged 6 h and 24 h post-injection using the Albira PET (Bruker, MA, USA) for a 5 min scan. For porphysome biodistribution studies, mice were imaged at 1, 3, 6, 24 and 48 h post-injection.

PET images were generated and quantified using PMOD v3.509 software (PMOD technologies LLC, Zurich, Switzerland). Volume of interest regions were defined using the VOI tool to define areas of high signal intensity in the carotid, heart and liver regions.

2.3.3 Magnetic Resonance Imaging (MRI)

Animals were imaged in an axial orientation with an ICON 1T MRI (Bruker) for anatomical imaging to complement the PET imaging. These were taken in the axial plane and only in the thoracic region.

2.3.4 Micro-Computed Tomography (microCT)

Animals were imaged in the Skyscan 1176 microCT (Bruker, MA, USA) in the neck/thoracic region for anatomical imaging to visualise the carotid and heart.

2.3.5 IVIS fluorescence imaging of *ex vivo* tissues/ organs

Tissues were harvested 24 h following intraperitoneal injection of PBS or 30 mol % porphysome nanoparticles and prior to histological analysis were imaged on an In Vivo Imaging System (IVIS) Spectrum (PerkinElmer, MA, USA) at excitation and emission wavelengths 670 nm and 720 nm respectively. Focus was manually adjusted to object height prior to acquiring images. Epi-fluorescence images were acquired with auto-exposure, F/stop = 2 and smallest binning settings with a field of view of between 6.6 cm and 23 cm. Images were analysed for ROI fluorescence with Aura imaging software (Spectral Instruments Imaging, AZ, USA).

2.3.6 Blood processing

At the conclusion of the experimental periods, blood was collected from the mice via terminal cardiac puncture into EDTA lined blood tubes (Interpath Services, Australia) and centrifuged at 3000 rpm for 10 min at 4°C. Plasma was carefully aliquoted and stored at -80°C.

2.3.7 Plasma lipid analysis

Triglycerides, total cholesterol, LDL-cholesterol and HDL-cholesterol were measured enzymatically in plasma using a commercially available kit (Wako diagnostics). For triglycerides, 2 µL of plasma was assayed according to manufacturer's instructions with colour change to blue measured at 600 nm absorbance. The same protocol was followed for total cholesterol, but plasma was first diluted 1:1 with distilled water. To determine the HDL-cholesterol concentration, 20 µL of plasma was mixed with 20 µL of precipitation reagent from HDL-C kit (Wako diagnostics) which were incubated for 10 min at room temperature before centrifugation at 3000 rpm for 15 min. 10 µL of the supernatant was assayed with the total cholesterol kit to determine HDL-C concentration. LDL-C concentration was calculated by subtracting HDL-C concentrations from total cholesterol concentrations.

2.4 Histology

2.4.1 OCT Embedding of fresh frozen tissues

Animals were euthanised via cardiac puncture, blood collected and then perfusion flushed with saline (10 mL). Lungs, liver, spleen and kidneys were dissected out and embedded in optimal cutting temperature (OCT) compound (TissueTek). The heart was removed, and a transverse cut was made through the entire heart carefully positioned perpendicular to the base of the two atria and ~1 mm below. The upper half of the heart was embedded in OCT.

For the tandem stenosis model [114], the sutured carotid was divided into the three segments (Segment I, II and III) of the model and embedded upright in OCT.

OCT embedded tissues were stored at -80°C until sectioned. All sections were thawed at room temperature for approximately 30 min prior to staining.

2.4.2 Hematoxylin and eosin (H&E) staining

Fresh frozen OCT-embedded sections were fixed with 2% PFA or 10% neutral buffered formalin then stained using a standard H&E staining protocol. Slides were washed for 5 min under running reverse osmosis (RO) water and for all subsequent washing steps. Sections were stained in Mayer's hematoxylin for 6 min and washed for 1 min. Sections were dipped twice in 0.3% acid ethanol (70% v/v ethanol, 0.3% v/v HCl acid) then incubated in Scott’s tap water (0.35% w/v Sodium Bicarbonate, 2% w/v Magnesium Sulphate) for 1 min. Sections were washed for 2 min and then stained in eosin (0.1% w/v eosin Y, 2% w/v $CaCl_2$) for 3 min. Sections were rinsed by dipping in water twice and then dehydrated through an ethanol gradient (70%, 95% and 100%) then into xylene. Sections were briefly dried and mounted in Dibutylphthalate Polystyrene Xylene (DPX, Sigma-Aldrich Inc., MO, USA).

2.4.3 Oil red O staining

Fresh frozen OCT-embedded sections were fixed in 10% neutral buffered formalin for 4 min and were then washed in PBS for 4 min. Sections were washed with 60% v/v isopropanol then stained in oil red O working solution (0.6% w/v oil red O, 60% v/v isopropanol) for 1 h at room temperature. Sections were differentiated in 60% v/v isopropanol and subsequently washed in distilled water for 2 min. Sections were stained in Mayer's hematoxylin for 2 min, washed under tap water for 3 min and then distilled water for 3 min. Excess water was removed and sections mounted with Aquatex (Merck-Millipore). Images of stained sections were acquired on the day of staining.

2.4.4 Masson’s Trichrome staining

Masson’s trichrome staining was conducted using a kit following the manufacturer’s instructions with some modifications (Abcam) with all rinsing steps in RO water. Fresh frozen OCT-embedded sections were fixed in 4% PFA for 10 min and were then rinsed in water before incubation in Bouin’s fluid overnight at room temperature. Sections were then washed under tap water until clear. Slides were stained in Weigert’s hematoxylin for 5 min, rinsed under water for 2 min, incubated in Biebrich scarlet for 15 min and rinsed. Sections were differentiated with Phosphomolybdic/Phosphotungstic Acid for 10 min before staining with Aniline Blue for 10 min. Sections were then rinsed and incubated in 1% Acetic acid solution for 4 min. Sections were finally dehydrated quickly through an ethanol and xylene gradient prior to being mounted with Dibutylphthalate Polystyrene Xylene (DPX, Sigma-Aldrich Inc., MO, USA).

2.4.5 Alpha-smooth muscle actin immunohistochemistry

PBST was used for all staining steps with 0.05% tween added. Fresh frozen OCT-embedded sections were fixed in 2% PFA for 10 min. Sections were blocked with 10% goat serum (Sigma-Aldrich Inc., MO, USA) for 4 h. Sections were incubated with 1:100 of α-SMA conjugated to alkaline phosphatase (AP) primary antibody (mouse monoclonal, clone 1A4, A5691, Sigma-Aldrich Inc., MO, USA) overnight at 4^{o}C. Following manufacturer’s instructions, the Vector Red substrate kit (Vector Laboratories, Burlingame, CA, USA) was used to develop staining. Sections were then counterstained in Mayer’s hematoxylin, dehydrated and mounted in DPX.

2.4.6 CD68 immunofluorescence staining

Sections were fixed with 2% PFA for 10 min and then washed with 0.1 M glycine solution to quench unreacted aldehydes. Sections were then blocked with 5% goat serum for 1 h. The primary antibody was used at a dilution of 1:250/1:500 anti-CD68 (rat monoclonal, Clone FA-11, IgG2a, MCA1957GA, Biorad) or 1:1250 Rat IgG2a κ Isotype Control (#559073, BD Biosciences), incubated on sections overnight at 4^{o}C. Then sections were incubated with 1:2000 Donkey anti-Rat IgG (H+L) Alexa Fluor 488 secondary antibody (A-21208, Invitrogen) for 1 h at 37^{o}C. Sections were mounted with VECTASHIELD® Antifade Mounting Medium with DAPI (Vector Laboratories).

2.4.7 Microscopy of tissue sections

Stained sections were imaged under the Axiolab microscope attached to a camera (Zeiss) or imaged via a Nanozoomer digital slide scanner (Hamamatsu). Fluorescence in aortic sinus sections was detected using the 20x objective on an Axio Scan.Z1 slide scanner microscope (Zeiss) with CD68 and porphyrin-lipid detected on the AF488 (ex: 493 nm, em: 517 nm) and Cy5 (ex: 631 nm, em: 647 nm) fluorescence channels respectively. Fluorescence in segment I in the carotid artery of the tandem stenosis model was detected using the 10x objective on a NiE fluorescence microscope (Nikon) with CD68 and porphyrin-lipid detected on the FITC and Cy5 fluorescence channels respectively.

2.5 Image analysis

Image analysis of tissue sections was conducted using Image Pro-Premier 9.2 (Media Cybernetics) software.

2.6 Statistical Analysis

GraphPad Prism 9 (San Diego, California, USA) statistical software was used for collation and statistical analysis of all data and to prepare graphs. Data are expressed as mean ± standard deviation (SD). Data was analysed using an unpaired two-tailed student's t-test when comparing two groups or one-way analysis of variance (one-way ANOVA) with Tukey's multiple comparisons for more than two groups.

CHAPTER 3

Anti-atherosclerotic effects of apoA-I-linked porphysome nanoparticles *in vitro*

3.1 Introduction

Atherosclerosis is driven by an inflammatory milieu in the vasculature with accumulation of inflammatory cells in the vascular wall. A hallmark of atherosclerosis progression is the recruitment of monocytes from the circulation to the site of atherosclerotic plaque followed by differentiation into macrophages. These plaque macrophages are known to engulf modified lipoproteins to form foam cells that accumulate, driving plaque instability and growth. Macrophages also release pro-inflammatory mediators, chemokines and cytokines, further driving the recruitment of inflammatory cells to the lesion site [3, 115].

Due to their importance in atherosclerotic plaque development and their predominance in lesions, macrophages present as a target for therapeutic treatments and for detection of disease. Their excellent phagocytic properties also facilitate the passive uptake of therapies, including nanoparticle-based interventions [8, 116].

High density lipoproteins (HDL) are known to be anti-atherosclerotic with previous studies examining a range of different properties including those that inhibit inflammation and promote cholesterol efflux. For example, HDL can lower the expression of pro-inflammatory chemokines in both endothelial and smooth muscle cells [63, 117]. In macrophages, there are both anti- and pro- inflammatory effects of HDL, but overall, in atherosclerotic plaque macrophages, these effects are anti-inflammatory [118-120]. Several studies have been conducted using HDL-like nanoparticles for these anti-atherogenic properties, as well as use as carriers for drug release to target atherosclerosis [54]. In addition, there have been numerous studies examining the use of HDL-like nanoparticles labelled with either radioactive or fluorescent dyes for the detection of atherosclerosis [8].

One particularly unique organic nanoparticle, the ‘porphysome’, has also demonstrated excellent potential as anti-atherosclerotic theranostic agent. ApoA-I-linked porphysomes consist of a single outer layer of phospholipid in combination with a highly fluorescent porphyrin-lipid conjugate with excellent fluorescent imaging capabilities [89]. The porphyrin-lipid can be chelated with radioisotopes such as ^{64}Cu, allowing non-invasive positron emission tomography (PET) imaging. Also in the outer layer is the apoA-I mimetic peptide, ‘R4F’. This peptide provides porphysomes with HDL-like properties by enabling specific interactions with the HDL receptor, SR-BI, which is highly expressed on macrophages. Taken together, porphysomes display multimodal imaging capabilities, macrophage-targeting and therapeutic properties [90]. This suggests that porphysome nanoparticles have excellent utility as theranostic agents for the simultaneous identification and suppression of atherosclerosis.

ApoA-I-porphysome nanoparticles have previously been shown to be internalised by cancer cell lines *in vitro* [89] but this has not yet been examined in macrophages. The effects of porphysomes on atherosclerosis-related macrophage functions are also currently unknown. Accordingly, this Chapter has investigated the ability of porphysome nanoparticles to be internalised by cultured macrophages *in vitro*, their effects on cholesterol efflux and inflammation, and examined the associated mechanisms of action.

3.2 Methods

3.2.1 Immortalised bone marrow derived macrophages cell culture

Immortalised murine bone marrow derived macrophages (iBMDMs) were kindly provided by Dr Ashley Mansell (Hudson Institute of Medical Research, Victoria, Australia). iBMDMs were originally isolated from C57BL/6 mouse bone marrow, then differentiated into macrophages prior to being immortalised using the Cre-J2 retroviral infection method as previously published [121, 122].

iBMDMs were maintained in low glucose DMEM (D5523, Sigma) supplemented with 10% FBS (Sigma) in a 37°C, 5% CO_2 incubator and cells were passaged every 2-3 days once confluency was reached. Cells were passaged by washing twice with 1 x Dulbecco's PBS (D-PBS, D1408, Sigma) and lifting with Gibco™ Trypsin-EDTA (0.5%, Thermofisher Scientific) before transferring to a new culture vessel (T75 flask).

3.2.2 Inflammatory stimulation of iBMDMs

iBMDMs were seeded into 6 or 12 well plates at a density of 1.5-2 x 10^5 cells/well 24 h prior to treatments. Between each treatment cells were washed once with PBS. For real time (RT)-qPCR analysis and whole protein analysis, iBMDMs were incubated with PBS (vehicle control), HDL (600 µg/mL), discoidal or spherical CO-loaded porphysomes (0.3 mol % porphyrin-lipid, 10 µg/mL) for 17-18 h and were subsequently stimulated with either 10 ng/mL LPS (E. coli 0111:B4, L4391, Sigma) or 10 ng/mL recombinant murine IFN-γ (315-05, Peprotech) for 16-17 h.

For the p65-NFκB nuclear protein analysis, iBMDMs were incubated with PBS (vehicle control), methyl-cyclodextrin (4% v/v), discoidal or CO-loaded R4F HDL mimetic nanoparticles (no porphyrin-lipid, 10 µg/mL), discoidal or CO-loaded porphysomes (0.3 mol % porphyrin-lipid, 10 µg/mL) for 17-18 h. iBMDMs were then stimulated with 100 ng/mL of LPS.

3.2.3 Real time-qPCR

Treated iBMDMs were washed once with PBS and total RNA was then extracted from lysates with TRI-reagent (Sigma-Aldrich) following manufacturer's instructions. RNA was quantified spectrophotometrically using a NanoDrop Spectrophotometer (Thermo Scientific). The absorbance of RNA samples was measured at 260 nm and 280 nm with the purity of the samples assessed using the absorbance ratio (A260/A280 ~2.0 for RNA). The RNA concentration for each sample was normalised within individual experiments to between 615-750 ng/µL. Between 1400-1845 ng of total RNA (within individual experiments) was reverse transcribed to cDNA using iScript Reverse Transcriptase Supermix (Biorad) according to manufacturer's instructions. Primers for *Rplp0*, *p65-Nfκb*, *Ccl2*, *Ccl5*, *Il-1β*, *Il-18*, *Asc*, *Nlrp3*, *Caspase-1* and *Il-6* (Table 3.1) were used to measure gene changes [PCR program: 95^{o}C for 30 min, (95^{o}C for 15 min, 60^{o}C for 30 min, 72^{o}C for 30min) x 40, 95^{o}C for 10 min] using CFX connect (Biorad). To ensure consistent efficiency between primers, 1000 ng of cDNA from iBMDMs was serially diluted 1:10 into 1000 ng, 100 ng, 10 ng, 1 ng, 0.1 ng samples. Dilutions were run on CFX connect thermocycler and qPCR efficiency determined (Table 3.1). Changes in gene expression were calculated using the $^{\Delta\Delta}$Ct method referenced to the housekeeper gene *Rplp0*.

3.2.4 Cell media sample preparation

Media from treated iBMDMs was collected and stored at -80^{o}C. Supernatants were thawed, centrifuged at 13,500 rpm and aliquoted for subsequent ELISA assays.

3.2.5 Nuclear protein extraction

The nuclear protein of iBMDMs was extracted using the NE-PER nuclear and cytoplasmic extraction reagents (Thermo Scientific) according to manufacturer’s instructions. Cells were trypsinised, washed with PBS and transferred to Eppendorf tubes. Cells were resuspended in cytoplasmic extraction reagent I (CER I), vortexed and incubated on ice for 10 min. CER II was then added to tubes, vortexed and incubated on ice for 1 min. Tubes were centrifuged at maximum speed (~13,500 -14,000 rpm) for 5 min. Supernatant (cytoplasmic extract) was transferred to a new tube and stored at -80^{o}C. The remaining pellet was suspended in nuclear extraction reagent (NER), vortexed and incubated on ice for 40 min, vortexing the tubes in 10 min intervals. Tubes were then centrifuged for 10 min at maximum speed. Supernatant (nuclear extract) was transferred to clean tubes and stored at -80^{o}C.

3.2.6 Whole cell protein extraction

Cells were washed once with PBS and 100 μL of radioimmunoprecipitation (RIPA) buffer was added to each well of a 6-well plate. Cells were scraped and transferred to Eppendorf tubes then sonicated for 3 secs at 20% amplitude. Tubes were then centrifuged at 4400 x *g* for 4 min at 4^{o}C. The supernatant containing protein from whole cells was transferred to clean tubes and stored at -80^{o}C.

3.2.7 Western Blotting

Nuclear protein (15 μg) and Precision Plus Protein Standards (Biorad) were run on 4-12% Bis-Tris Bolt gels using electrophoresis (Thermo Fisher Scientific) at 120V until proteins were sufficiently separated based on size. The gels were transferred to nitrocellulose membranes (Thermo Fisher Scientific) using the 7-minute P0 transfer setting on the iBlot 2 Dry Blotting System (Invitrogen).

To develop Western blot membranes, membranes were first blocked with 10% w/v skim-milk TBST (TBS + 0.1% v/v Tween-20) for 1 h at room temperature. Membranes were then washed for 3 x 5 min with TBST and incubated with a rabbit recombinant anti-NF-κB p65 subunit antibody [E379] (ab32536, Abcam) primary antibody diluted 1:1000 in 2% w/v skim-milk TBST overnight at 4^{o}C. After a further 3 x 5 min washes, membranes were incubated with a goat anti-rabbit HRP conjugated secondary antibody diluted 1:2000 in 2% w/v skim-milk TBST for 2-3 h and then imaged using 1:1 ratio of ECL substrates (Biorad). Chemiluminescence was imaged using a Chemidoc system (Biorad). Membranes were then stripped using a stripping buffer (Biorad) for 15 min, washed and blocked as performed previously. The membranes were then re-probed with a rabbit antibody against the nuclear protein loading control TATA-binding protein (TBP, ab63766, Abcam) at a dilution of 1:1000 in 2% w/v skim-milk TBST overnight at 4^{o}C.

3.2.8 ELISAs

3.2.8.1 IL-1β ELISA

To measure IL-1β protein levels in treated iBMDM cell culture supernatants, a mouse IL-1β/IL-1F2 Quantikine® ELISA kit (MLB00C, R&D systems) was used according to manufacturer's instructions with some modifications. Purified *E. coli*-expressed recombinant mouse IL-1β was used to create a standard curve from concentrations of 0-800 pg/mL. The assay diluent (50 µL) followed by standards (50 µL) and media samples (100 µL) were added to the ELISA plate wells pre-coated with a monoclonal antibody that specifically binds mouse IL-1β. Both the standards and samples were incubated on the plate overnight at 4^{o}C. Unbound substances were washed away and an enzyme-linked polyclonal antibody specific for murine IL-1β was added and incubated at room temperature for 2 h. Any non-specifically bound enzyme-linked antibody was washed away and substrate for the enzyme was added and incubated for 30 min at room temperature protected from light. The reaction of the enzyme resulted in production of a blue product which changed to yellow upon addition of stop solution (100 µL). The intensity of the resulting colour change was measured using absorbance at 450 nm with wavelength correction at 560 nm with concentration of IL-1β protein in each sample calculated from the standard curve.

3.2.8.2 CCL5 ELISA

To measure the protein levels of CCL5, treated iBMDM media was diluted 1:75 in calibrator diluent RD5-16 and assayed with a Mouse/Rat CCL5/RANTES Quantikine® ELISA kit (MMR00, R&D Systems) according to manufacturer’s instructions, similar to that described for IL-1β. Media samples (50 µL) were added to the ELISA plate wells. The intensity of the resulting colour change was measured using absorbance at 450 nm with wavelength correction at 560 nm with concentration of CCL5 protein in each sample calculated from the standard curve and multiplied by the dilution factor.

3.2.8.3 CCL2 ELISA

To measure the protein levels of CCL2, treated iBMDM media was diluted 1:500 in PBS and assayed with a Mouse CCL2/JE/MCP-1 Quantikine® ELISA kit (MJE00B, R&D Systems) according to manufacturer’s instructions, similar to that described for IL-1β. Diluted media samples (50 µL) and standards (50 µL) were added to the assay diluent (50 µL) in the ELISA plate wells and incubated for 2 h at room temperature. The intensity of the resulting colour change was measured using absorbance at 450 nm with wavelength correction at 560 nm with concentration of CCL2 protein in each sample calculated from the standard curve and multiplied by the dilution factor.

3.2.8.4 Caspase-1 ELISA

Treated iBMDM whole cell lysates were tested for changes in caspase-1 by ELISA (NBP2-75014, Novus Biologicals) according to manufacturer's instructions. Cell lysates (10 µL) prepared in RIPA buffer were added to the ELISA wells. The concentration of Caspase-1 protein was calculated from the standard curve.

3.2.9 Cholesterol efflux assay

To measure cholesterol efflux, iBMDMs were seeded at a density of 1.5-2 x 10^5 cells/well into 24 well plates the day prior to starting the assay in DMEM supplemented with 10% FBS. iBMDMs were then incubated with 500 µL of 2 µCi/mL (0.074 MBq/mL) [1,2-3H(N)]-labelled cholesterol (Perkin-Elmer) in DMEM supplemented with 1% FBS for 24 h at 37^{o}C. iBMDM were then washed twice with 500 µL of warmed 1% BSA in PBS. Cells were incubated with 500 µL of 0.2% BSA in DMEM for 18 h for equilibration of labelled cholesterol in the cells and media. Cells were incubated with 300 µL of acceptor either PBS (blank, background efflux), rHDL (25 µg/mL, positive control), and discoidal or spherical porphysome nanoparticles (10 or 25 µg/mL) in 0.2% BSA in DMEM for 4 h at 37^{o}C. Supernatant was removed and cells washed twice with PBS and lysed with 500 µL of 0.2 M NaOH/0.15 M NaCl solution. Supernatants and lysates were transferred to scintillation vials and scintillation counts per minute (CPM) were measured using liquid scintillation analyser (Tricarb-2810TR, Perkin Elmer). Cholesterol efflux was calculated using the formula:

$$\%Cholesterol\ Efflux = \frac{Supernatant\ CPM}{Supernatant\ CPM + Lysate\ CPM} \times 100\%$$

3.2.10 Flow cytometry of iBMDMs

To measure porphysome uptake by iBMDMs using flow cytometry, cells were seeded at 1.5 x 10^5 cells/ well in 6 well plates 24 h prior to treatment. Cells were incubated with either PBS vehicle or 10 µM of discoidal apoA-I porphysome nanoparticles (30 mol % porphyrin-lipid) for 24 hours. Cells were washed with PBS and lifted with trypsin-EDTA then subsequently washed twice with 500 µL of media (centrifuged 500 x *g*) and fixed with 110 µL of FACs fix buffer (Becton Dickinson). Cells were analysed on a BD LSR Fortessa (Becton Dickinson) with the red laser (excitation λ: 640 nm; emission λ: 670/30 nm) to detect the presence of porphyrin-lipid.

3.2.11 Fluorescence/ Confocal microscopy of cultured cells

To visualise porphysome uptake in iBMDMs, 30,000 cells treated with porphysomes (10 µM, 24 h) were spun onto microscope slides (Superfrost plus) using a cytospin centrifuge (Thermo-scientific). Cells were dried on the slides overnight at 4°C and subsequently fixed using 4% PFA in PBS for 15 min. Cells were washed in PBS and coverslip mounted with VECTASHIELD® antifade mounting medium with DAPI (Vector Laboratories). Porphyrin-lipid signal from the nanoparticles was detected with a TCS SP8X/MP multiphoton confocal microscope (Leica, excitation λ: 653 nm; emission λ: 670 nm beyond) at 63x magnification.

Table 3.1: RT-qPCR conditions and primer sequences used to measure gene changes in treated murine iBMDMs.

Murine RT-qPCR Primers	**Forward (5'-3')**	**Reverse (5'-3')**	**Primer Vol. (µL)**	**Primer Conc. (pmol)**	**Annealing Temp. (^{o}C)**	**Efficiency (%)**	**R^2**
Rplp0	CAA CGG CAG CAT TTA TAA CCC	CCC ATT GAT GGA GTG TGG	0.6	6	60	97.3	0.99
p65-Nfκb	AGT ATC CAT AGC TTC CAG AAC C	ACT GCA TTC AAG TCA TAG TCC	0.6	6	60	99.6	0.99
Ccl2	GCT GGA GCA TCC ACG TGT T	ATC TTG CTG GTG AAT GAG TAG CA	0.6	6	60	93.4	0.99
Ccl5	GCA AGT GCT CCA ATC TTG CA	CTT CTC TGG GTT GGC ACA CA	0.6	6	60	97.9	0.99
Il-1β	ACC TGT CCT GTG TAA TGA AAG ACG	TGG GTA TTG CTT GGG ATC C	0.6	6	60	106.9	0.99
Il-18	GAC TCT TGC GTC AAC TTC AAG G	CAG GCT GTC TTT TGT CAA CGA	0.6	6	60	93.3	0.99
Asc	CTT GTC AGG GGA TGA ACT CAA AA	GCC ATA CGA CTC CAG ATA GTA GC	0.6	6	60	78.7	0.99
Nlrp3	ATC AAC AGG CGA GAC CTC TG	GTC CTC CTG GCA TAC CAT AGA	0.6	6	60	80.2	0.99
Caspase-1	CTT GGA GAC ATC CTG TCA GGG	AGT CAC AAG ACC AGG CAT ATT CT	0.6	6	60	85.5	0.99
Il-6	GGT GAC AAC CAC GGC CTT CCC	AAG CCT CCG ACT TGT GAA GTG GT	0.6	6	60	91.5	0.98

Efficiency and R^2 values were determined by titrating the cDNA concentration from iBMDMs for each primer pair.

3.3 Results

3.3.1 Porphysome nanoparticles are internalised by macrophages *in vitro*

We first determined whether porphysome nanoparticles can be internalised within macrophages, our main cellular target, *in vitro*. Initially discoidal 30 mol % apoA-I porphysomes were utilised, these were synthesised to contain 30% porphyrin-lipid as a proportion of the total moles of lipid. Porphysomes were visibly internalised by cultured iBMDMs when comparing the PBS and porphysome treated cells, with the red porphyrin fluorescence signal detected in the cytoplasm of macrophages incubated with porphysomes which was absent in the PBS control cells (Fig 3.1A). Porphyrin uptake could also be detected using flow cytometry (670/30 channel, Fig 3.1B). Macrophages incubated with discoidal porphysomes (10 µM porphyrin lipid) demonstrated a significant increase in the median fluorescence intensity (Fig 3.1C).

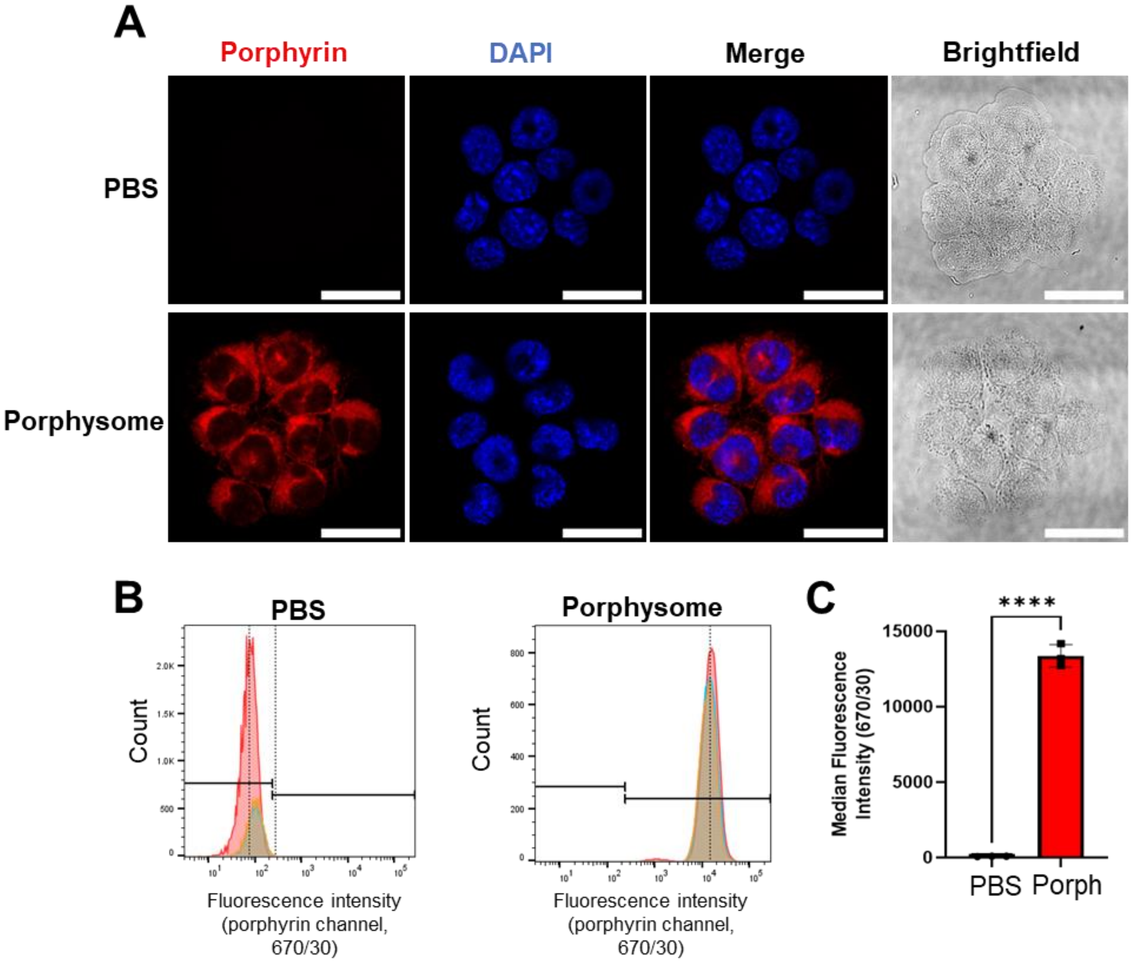
A
Porphyrin
DAPI
Merge
Brightfield
PBS
Porphysome
B
PBS
Count
Fluorescence intensity (porphyrin channel, 670/30)
Porphysome
Count
Fluorescence intensity (porphyrin channel, 670/30)
C
****
15000
10000
5000
0
Median Fluorescence Intensity (670/30)
PBS
Porph

Figure legend 3.1: Fluorescence detection of porphysome nanoparticles in macrophages *in vitro*

iBMDMs were incubated with either PBS or discoidal porphysome nanoparticles at 10 µM of porphyrin-lipid for 24 h prior to analysis with microscopy or flow cytometry. **A**) Representative confocal microscopy images of iBMDMs treated with PBS or discoidal 30 mol % porphysomes with porphyrin-lipid detected at 653 nm excitation. **B**) Flow cytometry of porphyrin-lipid iBMDMs treated with either PBS or discoidal 30 mol % porphysomes detected using red laser (640 nm) and fluorescence measured with the 670/30 channel. **C**) Median fluorescence intensity (MFI) was quantified from flow cytometric analysis of the porphyrin-lipid fluorescence. Data expressed as Mean ± SD (n=3). ****P<0.0001 vs PBS control by unpaired two-tailed t-test. Scale bar = 25 µm.

3.3.2 Porphysomes promote cholesterol efflux from macrophages *in vitro*

As porphysome nanoparticles are structurally designed to mimic native HDL particles we decided to test their cholesterol efflux capacity, which is a known functional characteristic of native HDL. These assays tested discoidal and spherical porphysomes that contain 0.3% porphyrin-lipid as a proportion of the total moles of lipid (0.3 mol %). The spherical porphysomes contain an inner core of cholesteryl oleate (CO) which is not present in the discoidal particles. A cholesterol efflux assay was used to compare the efflux capacity of both discoidal and spherical porphysome nanoparticles to reconstituted HDL (rHDL). As expected, incubation with rHDL led to a significant increase in cholesterol efflux as compared to the PBS control (Fig 3.2, +232%, $P<0.05$). Likewise, compared to the PBS control, incubation with 10 μg/mL of the discoidal and spherical porphysomes also led to an increase in cholesterol efflux (Fig 3.2, Disc: +225%, $P<0.05$; Sphere: +214%, $P=0.0914$).

In addition, incubation with 25 μg/mL of porphysomes led to a significant increase in cholesterol efflux compared to the PBS control (Fig 3.2, Disc: +399%; Sphere: +513%, $P<0.001$). Interestingly compared to the rHDL at the same concentration of 25 μg/mL, incubation with the porphysome nanoparticles led to an increase in cholesterol efflux (Fig 3.2, Disc: +50%, $P=0.1620$; Sphere: +85%, $P<0.05$).

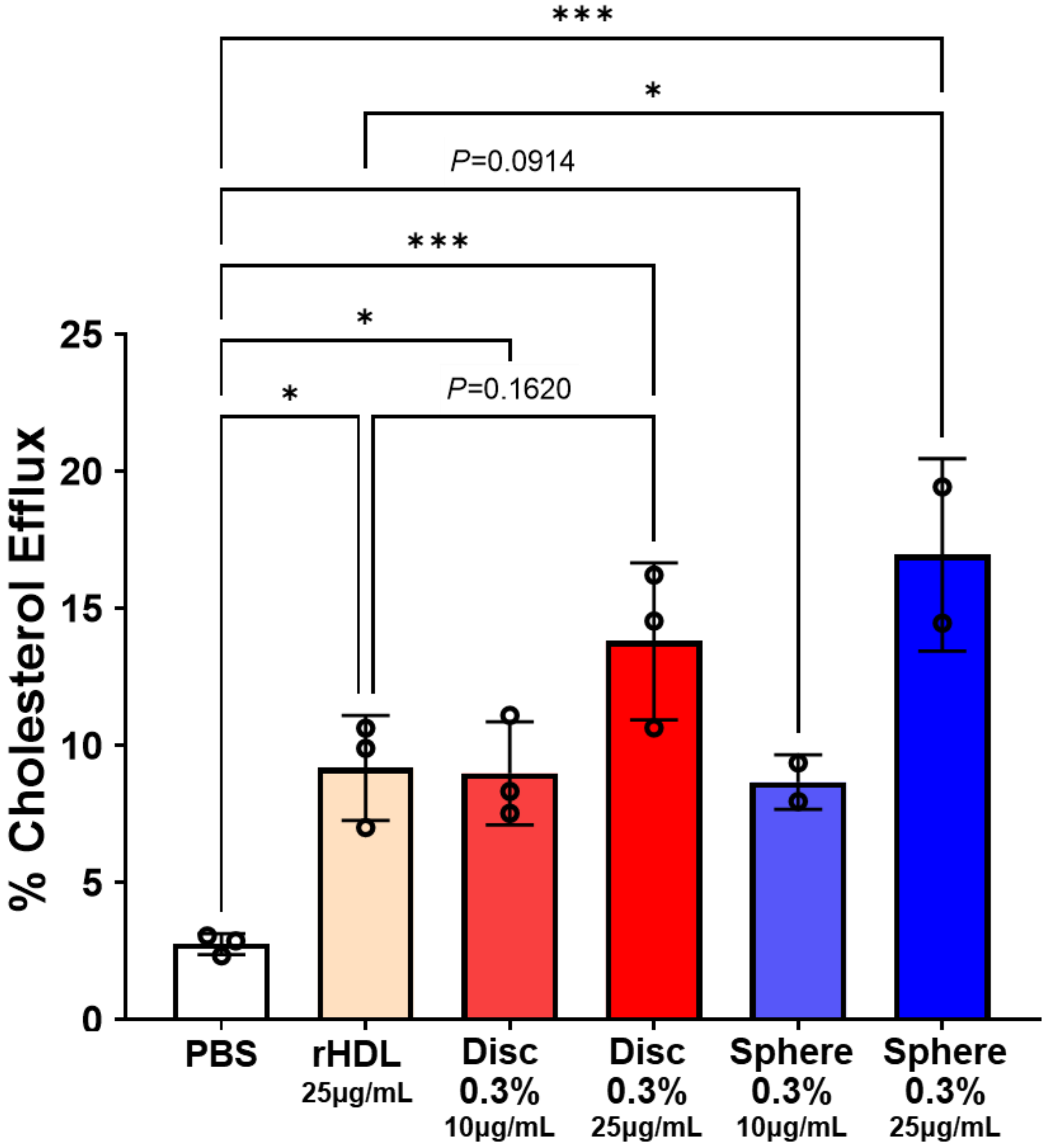
***
*
P=0.0914
***
*
*
P=0.1620
% Cholesterol Efflux
0
5
10
15
20
25
PBS
rHDL
25μg/mL
Disc
0.3%
10μg/mL
Disc
0.3%
25μg/mL
Sphere
0.3%
10μg/mL
Sphere
0.3%
25μg/mL

Figure legend 3.2: Porphysome nanoparticles efflux cholesterol from macrophages

iBMDMs were loaded with ^{3}H-cholesterol and % cholesterol efflux calculated for incubation with reconstituted HDL (rHDL), discoidal (Disc) and spherical (Sphere) porphysomes containing 0.3 mol % porphyrin-lipid (0.3%). Concentrations are based on the protein component of the acceptor, (apoA-I in rHDL; R4F peptide in porphysomes). Data from two independent experiments (n=2-3). Data expressed as Mean ± SD. *$P<0.05$, ***$P<0.001$ by one-way ANOVA with Tukey's multiple comparisons.

3.3.3 Porphysome nanoparticles inhibit the expression of pro-inflammatory cytokines *Il-1β* and *Il-18*

We next determined the anti-inflammatory effects of porphysomes on iBMDMs. We first investigated changes in the mRNA levels of *Il-1β* and *Il-18,* two important inflammatory cytokines involved in the development of atherosclerosis.

Incubation of iBMDMs with IFN-γ significantly increased *Il-1β* mRNA levels from baseline control levels (4.5-fold, *P*<0.01, Fig 3.3A). However, when iBMDMs were preincubated with both discoidal and spherical porphysomes, it suppressed the induction of *Il-1β* mRNA expression such that there were significantly lower levels of *Il-1β* mRNA following preincubation with discoidal (-93%, *P*<0.01) and spherical (-91%, *P*<0.01) porphysomes, when compared to the IFN-γ stimulated control (Fig 3.3A). Stimulation with LPS also significantly increased *Il-1β* mRNA levels in iBMDMs (1019-fold, *P*<0.0001), when compared to the non-stimulated PBS control (Fig 3.3B). Preincubation with discoidal and spherical porphysomes significantly reduced this LPS-induced stimulation of *Il-1β* mRNA levels (Disc: -88%, *P*<0.0001; Sphere: -85%, *P*<0.001), compared to LPS only controls (Fig 3.3B).

Given that there were changes in *Il-1β* gene expression, we also measured IL-1β protein in the iBMDM culture media by ELISA to determine changes in the amount of secreted IL-1β protein. As expected, LPS treatment significantly increased the concentration of IL-1β in the cell culture media compared to the PBS control (Fig 3.3C, 24-fold, *P*<0.0001). Pre-incubation of porphysomes led to a significant decrease in the extracellular IL-1β protein concentration with LPS stimulation (Fig 3.3C, Disc: -69%, *P*<0.001; Sphere: -61%, *P*<0.01). This is in agreement with the observed decrease in *Il-1β* mRNA expression following porphysome pre-incubation (Fig 3.3B).

Furthermore, the measurement of changes in *Il-18* mRNA levels revealed that stimulation with IFN-γ significantly increased *Il-18* mRNA expression (2-fold, P<0.0001), when compared to the PBS baseline control (Fig 3.3D). iBMDMs preincubated with discoidal and spherical porphysomes displayed significantly lower *Il-18* mRNA levels than IFN-γ only control iBMDMs (Disc: -54%; Sphere: -43%, P<0.0001). Unexpectedly, incubation of iBMDMs with LPS caused a significant decrease in *Il-18* mRNA levels (Fig 3.3E, -54%, P<0.001). However, treatment with both discoidal and spherical porphysomes caused an additional decrease in *Il-18* mRNA levels (Disc: -48%, P<0.05; Sphere: -42%, P=0.1018).

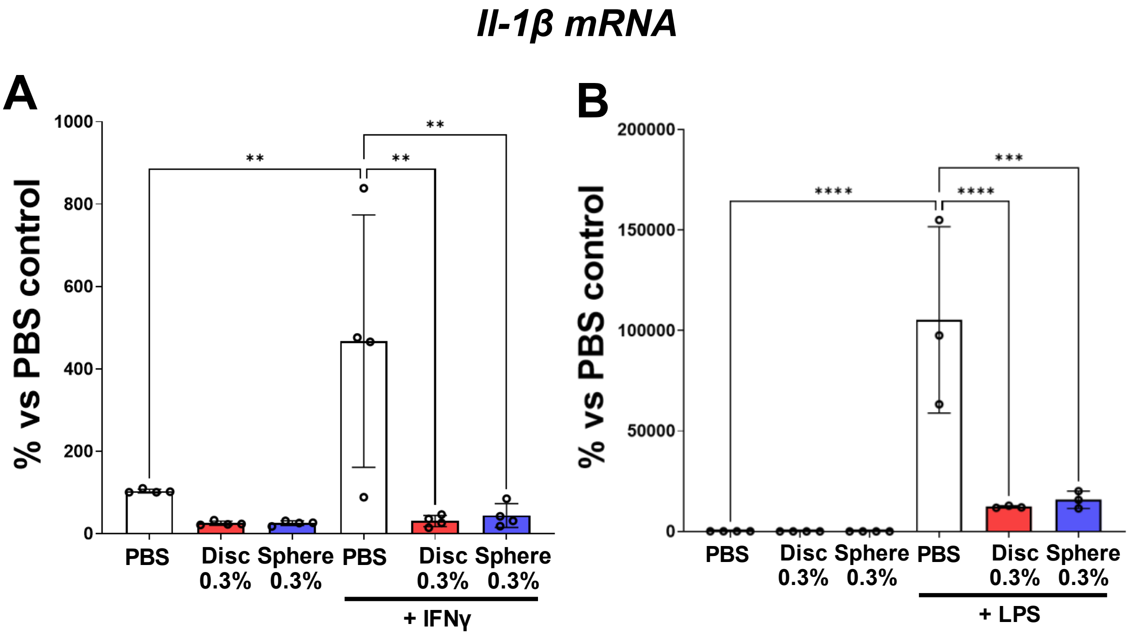
Il-1β mRNA
A
% vs PBS control
1000
800
600
400
200
0
**
**
**
PBS
Disc 0.3%
Sphere 0.3%
PBS
Disc 0.3%
Sphere 0.3%
+ IFNγ
B
% vs PBS control
200000
150000
100000
50000
0
****
****
***
PBS
Disc 0.3%
Sphere 0.3%
PBS
Disc 0.3%
Sphere 0.3%
+ LPS

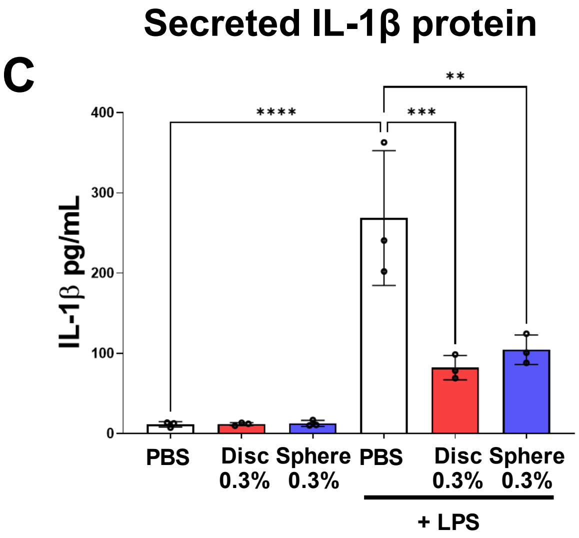
Secreted IL-1β protein
C
IL-1β pg/mL
400
300
200
100
0
****
***
**
PBS
Disc 0.3%
Sphere 0.3%
PBS
Disc 0.3%
Sphere 0.3%
+ LPS

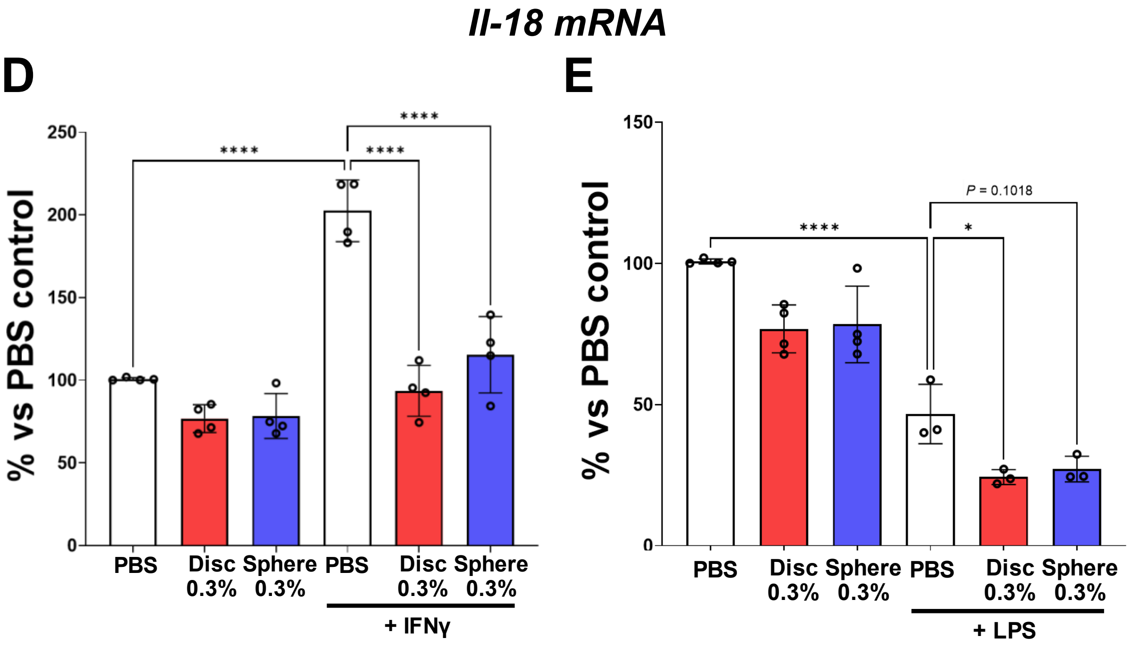
Il-18 mRNA
D
% vs PBS control
250
200
150
100
50
0
****
****
****
PBS
Disc 0.3%
Sphere 0.3%
PBS
Disc 0.3%
Sphere 0.3%
+ IFNγ
E
% vs PBS control
150
100
50
0
P = 0.1018
****
*
PBS
Disc 0.3%
Sphere 0.3%
PBS
Disc 0.3%
Sphere 0.3%
+ LPS

Figure legend 3.3: Discoidal and spherical porphysomes inhibit expression of cytokines *Il-1β* and *Il-18* in macrophages in response to inflammatory stimulation

iBMDMs were pre-treated with discoidal (Disc, 10 μg/mL) or spherical (Sphere, 10 μg/mL) porphysomes containing 0.3 mol % porphyrin-lipid (0.3%) then stimulated with IFN-γ (10 ng/mL) or LPS (10 ng/mL) for 18 h. RT-qPCR was used to measure changes in mRNA levels of *Il-1β* (**A-B**) and *Il-18* (**D-E**). To measure extracellular IL-1β protein, cell culture media from treated cells were collected and analysed by mouse IL-1β ELISA (**C**). qPCR data are from 3-4 independent experiments with n=3 replicates, and protein data are from 1-3 independent experiments with n=3 replicates. Data expressed as Mean ±SD. *$P<0.05$, **$P<0.01$, ***$P<0.001$, ****$P<0.0001$ by one-way ANOVA with Tukey’s multiple comparisons.

3.3.4 Porphysome nanoparticles inhibit the expression of pro-inflammatory chemokine CCL5

To further investigate the effect of porphysomes on inflammation we also examined expression of *Ccl5* (*Rantes*) a key pro-inflammatory chemokine involved in monocyte recruitment and the progression of atherosclerosis.

We observed that *Ccl5* expression was significantly increased following stimulation of iBMDMs with either IFN-γ (Fig 3.4A, 89-fold, $P< 0.0001$) or LPS (Fig 3.4B, 225-fold, $P<0.001$) as compared to the unstimulated PBS control. However, when pre-incubated with porphysomes, expression of *Ccl5* was reduced significantly (Disc: -66%, $P<0.01$; Sphere: -49%, $P<0.05$) as compared to the IFN-γ stimulated PBS control (Fig 3.4A). Similarly, pre-incubation with porphysomes led to a significant reduction in LPS-stimulated *Ccl5* expression (Fig 3.4B, Disc: -75%; Sphere: -70%, $P<0.05$).

Given that *Ccl5* mRNA expression was reduced by porphysome nanoparticles, we measured CCL5 protein in the media by ELISA. We observed an increase in extracellular CCL5 protein concentration following treatment with both IFN-γ (Fig 3.4C, 6.5-fold, $P<0.0001$) and LPS (Fig 3.4D, 49-fold, $P<0.001$) compared to the PBS control. Furthermore, pre-incubation of porphysomes was able to significantly lower the concentration of secreted CCL5 protein following stimulation with IFN-γ (Fig 3.4C, Disc: -53%; Sphere: -51%, $P<0.001$) and LPS (Fig 3.4D, Disc: -82%; Sphere: -81%, $P<0.01$) as compared to the PBS control. These changes mirror those seen in the *Ccl5* mRNA (Fig 3.4 A&B).

Ccl5 mRNA

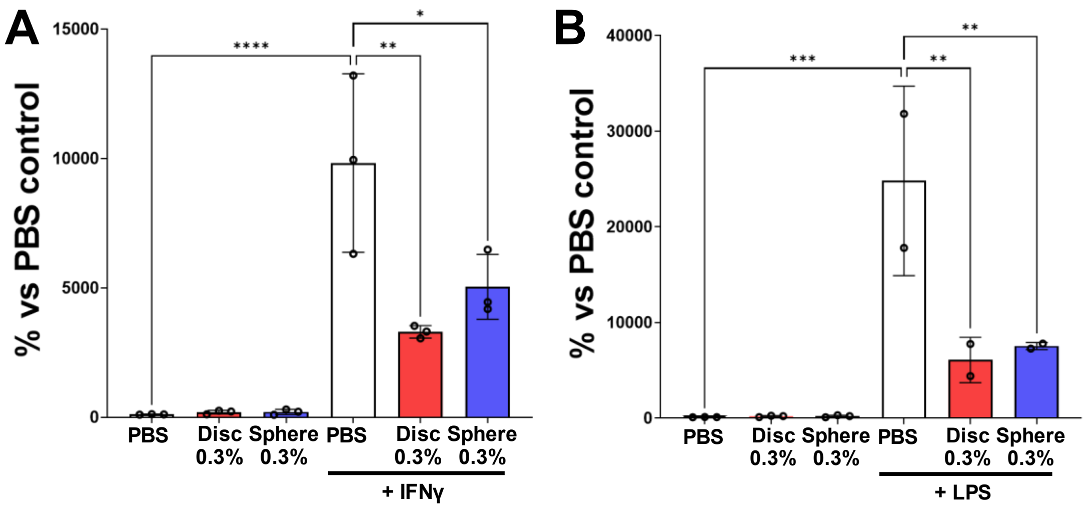

Secreted CCL5 protein

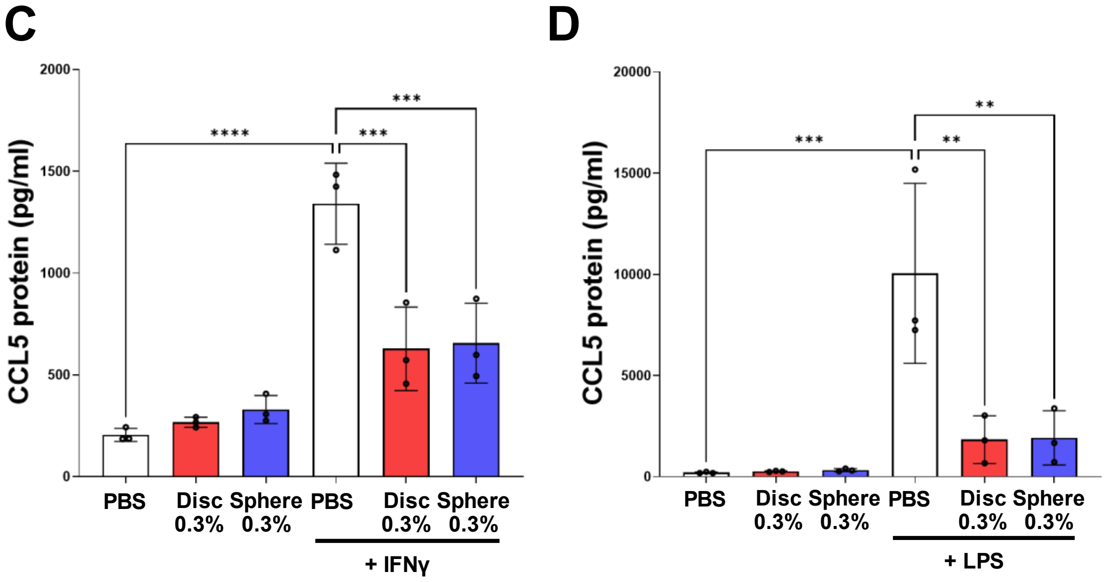

Figure legend 3.4: Porphysomes inhibit the expression of CCL5 in macrophages following inflammatory stimulation

iBMDMs were pre-treated with discoidal (Disc, 10 µg/mL) or spherical (Sphere, 10 µg/mL) porphysomes containing 0.3 mol % porphyrin-lipid (0.3%) then stimulated with IFN-γ (10 ng/mL) or LPS (10 ng/mL) for 18 h. RT-qPCR was used to measure changes in mRNA levels of *Ccl5* (**A-B**)**.** To measure extracellular CCL5 protein, cell culture media from treated cells were collected and analysed by mouse CCL5 ELISA (**C-D**). qPCR data are from 2-3 independent experiments with n=3 replicates, and protein data are from 3 independent experiments with n=3 replicates. Data expressed as Mean ±SD. **P*<0.05, ***P*<0.01, ****P*<0.001, *****P*<0.0001 by one-way ANOVA with Tukey's multiple comparisons.

3.3.5 The effect of porphysome nanoparticles on expression of pro-inflammatory chemokine CCL2 in macrophages

We also measured expression of another pro-inflammatory chemokine implicated in atherogenesis, CCL2 (MCP-1). Likewise, stimulation of iBMDMs with IFN-γ resulted in a significant increase in the expression of *Ccl2* (Fig 3.5A, 4-fold, $P< 0.0001$). LPS stimulation also significantly elevated *Ccl2* mRNA levels (Fig 3.5B, 28-fold, $P< 0.001$). However, despite these changes with inflammatory stimulus, porphysome pre-incubation did not significantly affect expression of *Ccl2* (Fig 3.5A&B).

Furthermore, stimulation with IFN-γ did not significantly alter levels of secreted CCL2 protein (Fig 3.5C) when compared to the unstimulated PBS control. Despite this, the discoidal porphysome pre-treatment significantly increased the secretion of CCL2 protein into the media compared to the IFN-γ stimulated PBS control (Fig 3.5C, +115%, $P<0.05$). In contrast, LPS treatment alone was able to significantly increase the levels of secreted CCL2 protein (Fig 3.5D, +447%, $P< 0.0001$). Interestingly, following LPS stimulation, the spherical porphysomes significantly raised the levels of secreted CCL2 protein compared to the PBS control (Fig 3.5D, +49%, $P< 0.01$).

Ccl2 mRNA

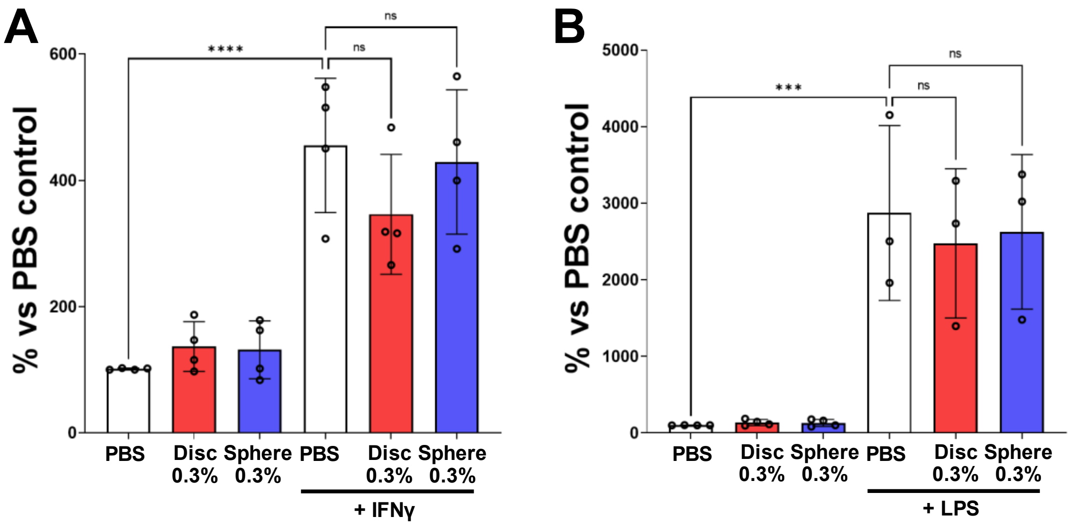

Secreted CCL2 protein

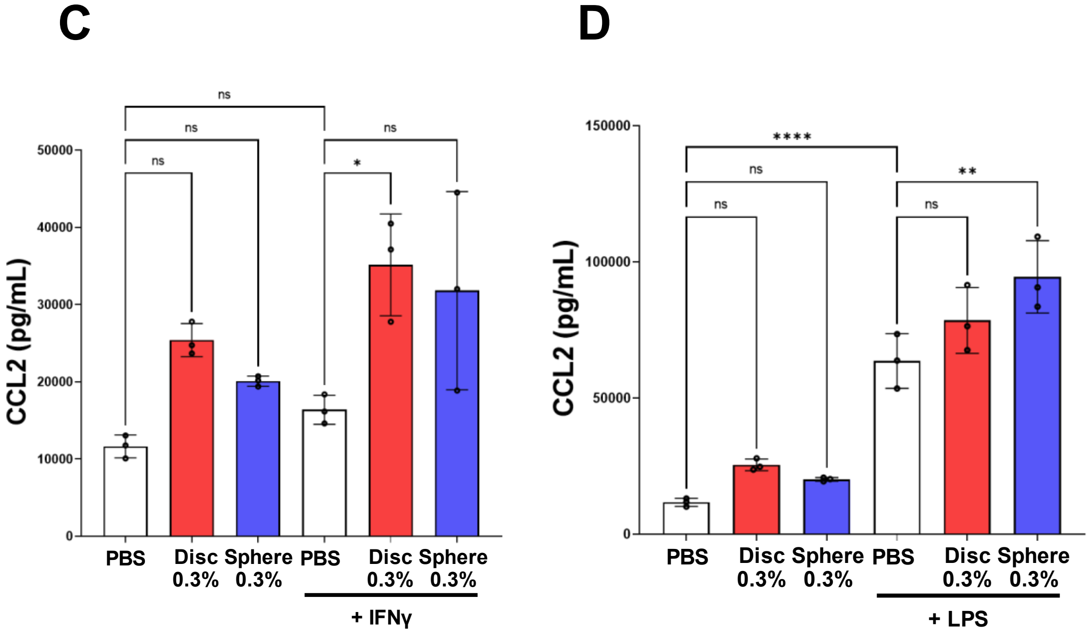

Figure legend 3.5: The effect of porphysome nanoparticles on expression of CCL2 in macrophages following inflammatory stimulation

iBMDMs were pre-treated with discoidal (Disc, 10 μg/mL) or spherical (Sphere, 10 μg/mL) porphysomes containing 0.3 mol % porphyrin-lipid (0.3%) then stimulated with IFN-γ (10 ng/mL) or LPS (10 ng/mL) for 18 h. RT-qPCR was used to measure changes in mRNA levels of *Ccl2* (**A-B**). To measure extracellular CCL2 protein, cell culture media from treated cells were collected and analysed by mouse CCL2 ELISA (**C-D**). qPCR data are from 3-4 independent experiments with n=3 replicates, and protein data are from 1-3 independent experiments with n=3 replicates. Data expressed as Mean ±SD. not-significant (ns) $P>0.05$, *$P<0.05$, **$P<0.01$, ***$P<0.001$, ****$P<0.0001$ by one-way ANOVA with Tukey’s multiple comparisons.

3.3.6 Porphysome nanoparticles did not affect pro-inflammatory cytokine *Il-6* expression in macrophages

Interestingly, the stimulation of iBMDMs with IFN-γ and LPS did not significantly increase *Il-6* expression (Fig 3.6). In addition, there was no significant change in *Il-6* expression following porphysome pre-incubation with IFN-γ or LPS stimulation (Fig 3.6).

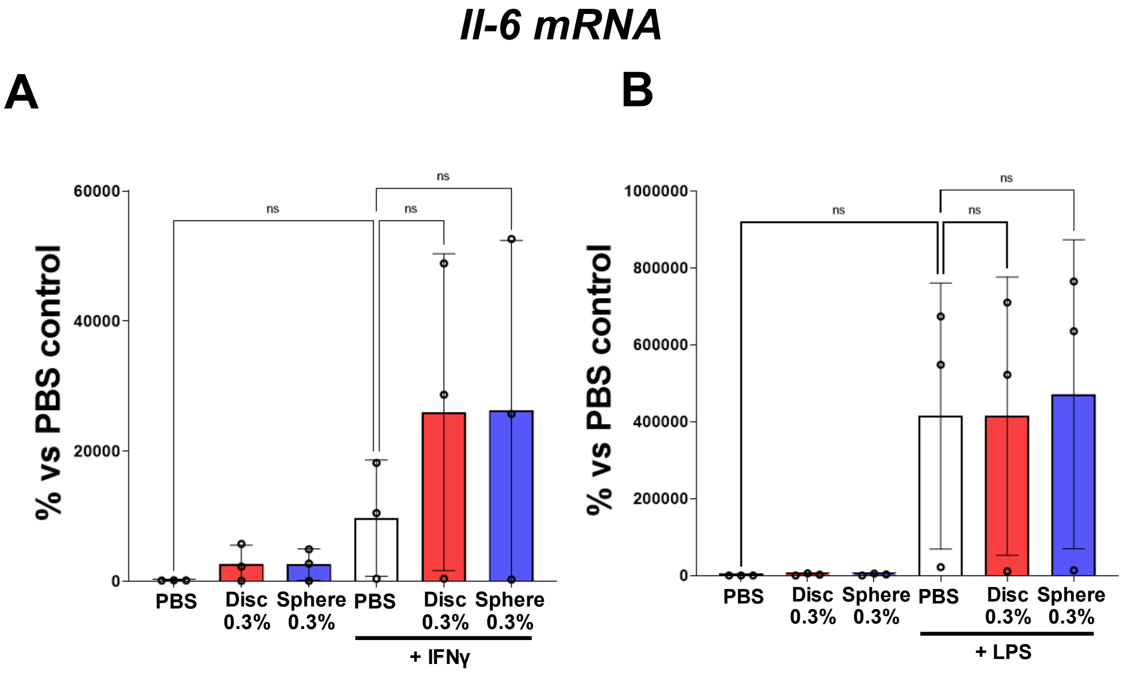
Il-6 mRNA
A
% vs PBS control
60000
40000
20000
0
ns
ns
ns
PBS
Disc 0.3%
Sphere 0.3%
PBS
Disc 0.3%
Sphere 0.3%
+ IFNγ
B
% vs PBS control
1000000
800000
600000
400000
200000
0
ns
ns
ns
PBS
Disc 0.3%
Sphere 0.3%
PBS
Disc 0.3%
Sphere 0.3%
+ LPS

Figure legend 3.6: Porphysome nanoparticles have no effect on the expression of *Il-6* mRNA in macrophages following inflammatory stimulation

iBMDMs were pre-treated with discoidal (Disc, 10 μg/mL) or spherical (Sphere, 10 μg/mL) porphysomes containing 0.3 mol % porphyrin-lipid (0.3%) then stimulated with 10 ng/mL of IFN-γ (**A**) or LPS (**B**), with *Il-6* expression measured by RT-qPCR. Data is from 3 independent experiments with n=3 replicates. Data expressed as Mean ±SD. not-significant (ns) P>0.05 by one-way ANOVA with Tukey's multiple comparisons.

3.3.7 Effect of porphysomes on levels of p65-NFκB mRNA and nuclear protein in macrophages

Given that there were gene expression changes observed in the *Il-1β* and *Il-18* which are secreted from macrophages as part of NLRP3 inflammasome activation, we decided to measure expression of the transcription factor *p65-Nfkb*. Despite stimulation with IFN-γ and LPS, there was no significant increase in the expression of *p65-Nfkb* (Fig 3.7A-B). Furthermore, we found that there was no significant change in *p65-Nfkb* expression following pre-incubation with porphysome nanoparticles (Fig 3.7A-B) as compared to the IFN-γ or LPS stimulated PBS control.

When NFκB is activated, the p65 subunit translocates to the nucleus to regulate the expression of pro-inflammatory genes, e.g. *Il1b* and *Il18*. Therefore, we determined whether there were any changes in the amount of p65-NFκB protein in the nuclear fraction of macrophages, which is a measure of the nuclear translocation of the p65 subunit. In agreement with the mRNA expression data, the LPS stimulation also did not lead to a significant increase in p65-NFκB protein in the nucleus. There was, however, a significant reduction in nuclear p65-NFκB protein following incubation with discoidal 0 mol % porphyrin-lipid particles (Fig 3.7C, Disc: -70%, P<0.05), when compared to PBS control in unstimulated iBMDMs. There was also a non-significant decrease in nuclear p65 protein in response to incubation with discoidal 0.3 mol% porphyrin-lipid particles (Fig 3.7C, Disc: -35%; P<0.01), when compared to the PBS control in LPS stimulated iBMDMs. This suggests that the discoidal nanoparticles may inhibit the nuclear translocation of p65-NFκB.

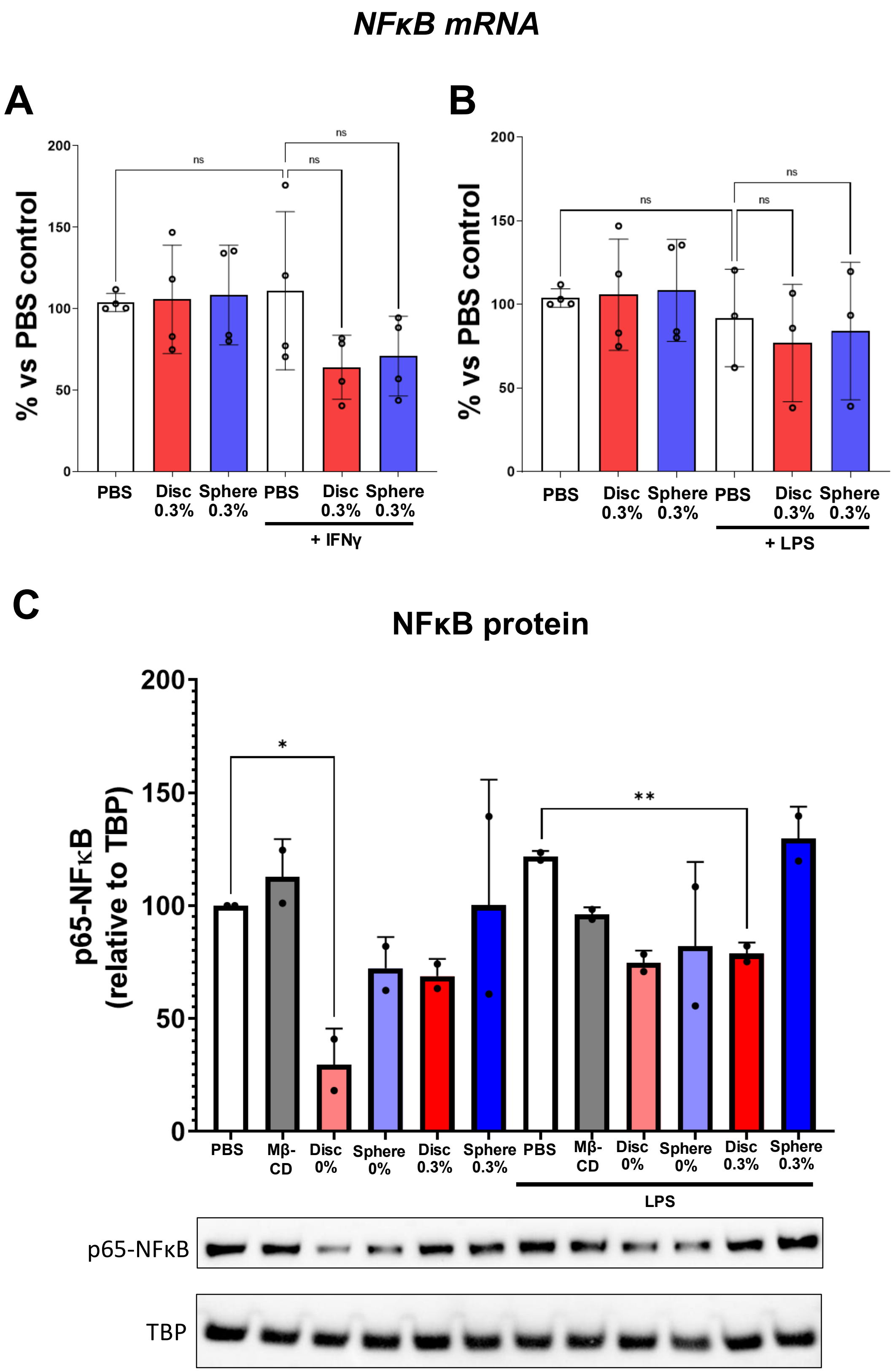
NFκB mRNA
A
% vs PBS control
200
150
100
50
0
ns
ns
ns
PBS
Disc 0.3%
Sphere 0.3%
PBS
Disc 0.3%
Sphere 0.3%
+ IFNγ
B
% vs PBS control
200
150
100
50
0
ns
ns
ns
PBS
Disc 0.3%
Sphere 0.3%
PBS
Disc 0.3%
Sphere 0.3%
+ LPS
C
NFκB protein
p65-NFκB (relative to TBP)
200
150
100
50
0
*
**
PBS
Mβ-CD
Disc 0%
Sphere 0%
Disc 0.3%
Sphere 0.3%
PBS
Mβ-CD
Disc 0%
Sphere 0%
Disc 0.3%
Sphere 0.3%
LPS
p65-NFκB
TBP

Figure legend 3.7: Porphysomes suppress p65-NFκB mRNA and nuclear protein in macrophages

iBMDMs were pre-treated with discoidal (Disc, 10 µg/mL) or spherical (Sphere, 10 µg/mL) porphysomes containing 0.3 mol % porphyrin-lipid (0.3%) then stimulated with IFN-γ (10 ng/mL) or LPS (10 ng/mL) for 18 h. RT-qPCR was used to measure changes in mRNA levels of *p65-NfκB* (**A-B**). Western blotting of nuclear extracts from cultured iBMDM cells pre-treated with PBS, 4% v/v methyl-β-cyclodextrin (MβCD), Disc (10 µg/mL), Sphere (10 µg/mL) porphysomes containing 0 mol % (0%) or 0.3 mol % porphyrin-lipid (0.3%) for 18 h. Cells were then stimulated with LPS at 100 ng/mL for 15 min. Nuclear p65-NFκB and TBP detected by specific binding of antibodies at ~65 kDa and ~37 kDa respectively (**C**). RT-qPCR data are from 3-4 independent experiments with n=3 replicates. Data expressed as Mean ±SD. not-significant (ns) $P>0.05$ by one-way ANOVA with Tukey's multiple comparisons. Nuclear protein data are from two independent experiments with n=2-3 replicates total. Intensity of bands were quantified and normalised to TBP (TATA-binding protein). Data expressed as Mean ±SD. not-significant (ns) $^*P<0.05$, $^{**}P<0.01$ by unpaired t-two tailed t-test.

3.3.8 Porphysome nanoparticles suppress some components of the NLRP3 inflammasome in macrophages

Il-1β and *Il-18* are key cytokines involved in the NLRP3 inflammasome pathway. This led us to further investigate whether there were changes in the expression of the components of the NLRP3 inflammasome including Apoptosis-Associated Speck-Like Protein Containing A CARD (ASC) and NOD-, LRR and pyrin domain- containing protein 3 (NLRP3).

Stimulation with IFN-γ increased the expression of *Asc* as compared to the unstimulated PBS control (Fig 3.8A, +70%, *P*=0.0541). Pre-incubation with the discoidal porphysomes led to a non-significant reduction in the expression of *Asc* in response to IFN-γ stimulation (Fig 3.8A, -36%, *P*=0.1011). In contrast to IFN-γ, stimulation of iBMDMs with LPS led to a significant decrease in expression of *Asc* as compared to the PBS control (Fig 3.8B, -39%, *P*<0.001). Furthermore, pre-incubation of porphysomes had no significant effect on the expression of *Asc* as compared to LPS stimulated control (Fig 3.8B).

IFN-γ or LPS stimulation of iBMDMs did not induce any significant change in the expression of *Nlrp3* (Fig 3.8C&D) as compared to the PBS control. Pre-incubation with porphysomes lowered *Nlrp3* expression (Fig 3.8C, Disc: -69%, *P*<0.05; Sphere: -62%, *P*=0.0533) as compared to the IFN-γ stimulated control. However, this reduction in *Nlrp3* expression with porphysome pre-incubation was not seen following LPS stimulation (Fig 3.8D).

Asc mRNA

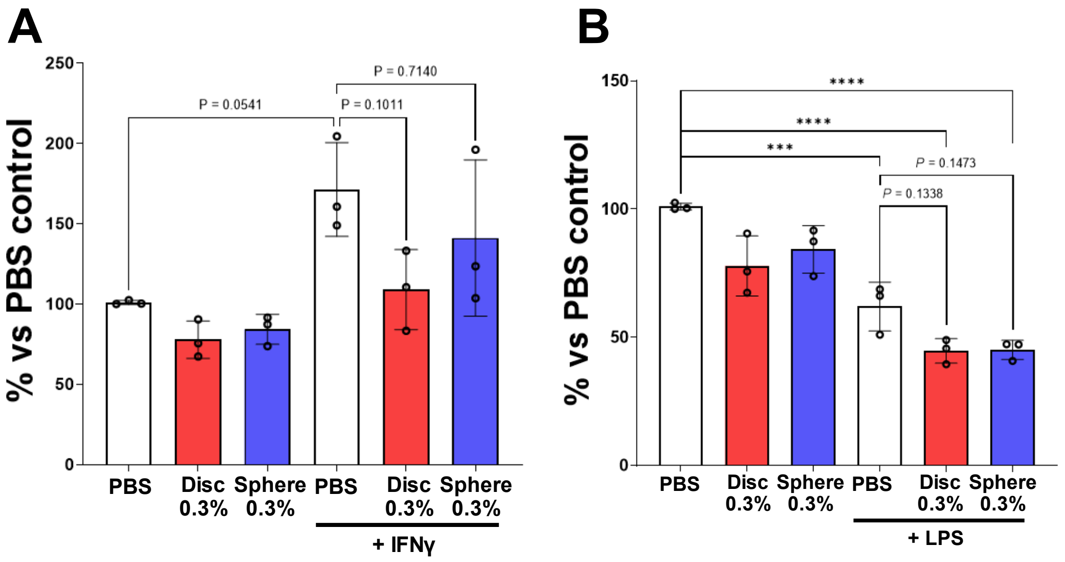

Nlrp3 mRNA

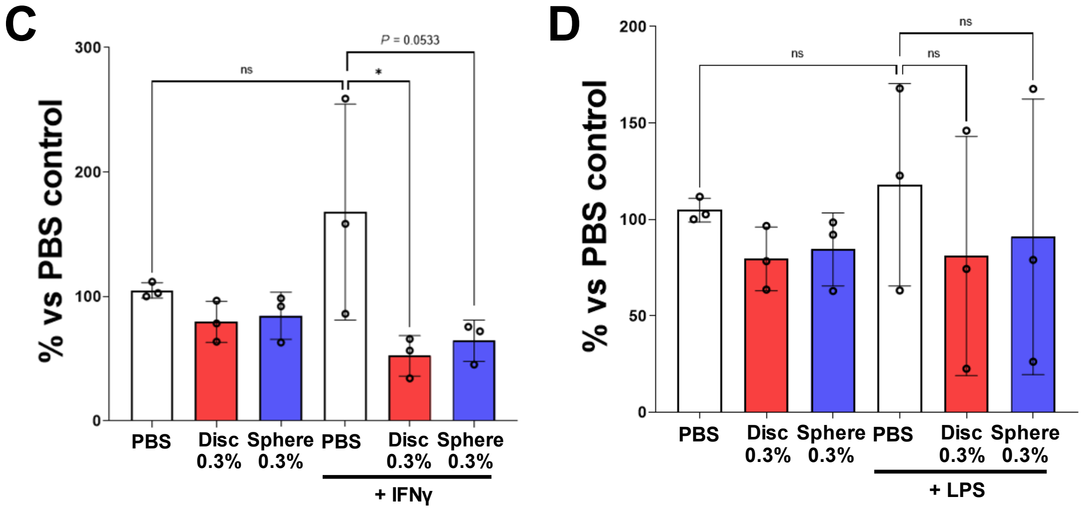

Figure legend 3.8: Porphysome nanoparticles decrease *Asc* and *Nlrp3* expression in macrophages following inflammatory stimulation

iBMDMs were pre-treated with discoidal (Disc, 10 µg/mL) or spherical (Sphere, 10 µg/mL) porphysomes containing 0.3 mol % porphyrin-lipid (0.3%) then stimulated with IFN-γ (10 ng/mL) or LPS (10 ng/mL) for 18 h. RT-qPCR was used to measure changes in mRNA levels of *Asc* (**A-B**) and *Nlrp3* (**C-D**). Data are from 3 independent experiments with n=3 replicates. Data expressed as Mean ±SD. not-significant (ns) $P>0.05$, ***$P<0.001$, ****$P<0.0001$ by one-way ANOVA with Tukey's multiple comparisons.

3.3.9 Porphysome nanoparticles have no effect on Caspase-1 expression in macrophages

Caspase-1 mRNA expression significantly increased following IFN-γ stimulation as compared to the PBS control (Fig 3.9A, 3-fold, *P*<0.001). However, the porphysome nanoparticles had no significant effect on *Caspase-1* expression following IFN-γ stimulation (Fig 3.9A). In addition, LPS treatment did not affect the expression of *Caspase-1* compared to the PBS control (Fig 3.9B). Interestingly as compared to the LPS stimulation control, the spherical porphysomes led to a non-significant increase in *Caspase-1* expression (Fig 3.9B, +54%, *P*=0.0897).

To further investigate the possible effect that porphysomes have on the NLRP3 inflammasome, Caspase-1 protein levels were measured in cell lysates. Given that Caspase-1 enzymatic activity functions to cleave pro-IL-1β and pro-IL-18 into their active secreted forms, an ELISA was used to determine whether there were any changes in intracellular Caspase-1 protein levels. Interestingly LPS stimulation led to a significant decrease in Caspase-1 protein levels as compared to the unstimulated PBS control (Fig 3.9C, -34%, *P*<0.01). However, with porphysome pre-treatment no change in Caspase-1 protein concentration was observed (Fig 3.9C).

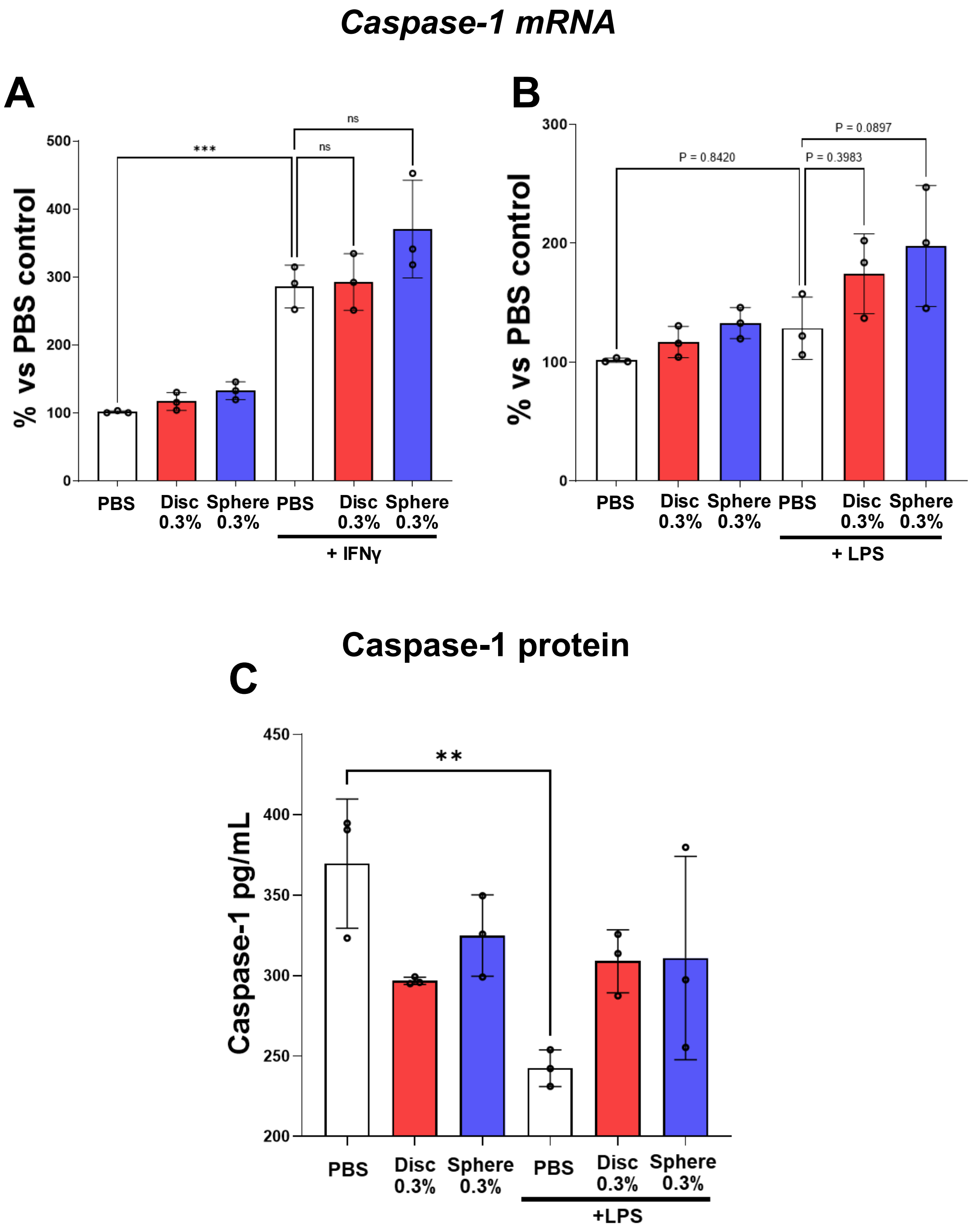
Caspase-1 mRNA
A
% vs PBS control
500
400
300
200
100
0
***
ns
ns
PBS
Disc 0.3%
Sphere 0.3%
PBS
Disc 0.3%
Sphere 0.3%
+ IFNγ
B
% vs PBS control
300
200
100
0
P = 0.8420
P = 0.3983
P = 0.0897
PBS
Disc 0.3%
Sphere 0.3%
PBS
Disc 0.3%
Sphere 0.3%
+ LPS
Caspase-1 protein
C
Caspase-1 pg/mL
450
400
350
300
250
200
**
PBS
Disc 0.3%
Sphere 0.3%
PBS
Disc 0.3%
Sphere 0.3%
+LPS

Figure legend 3.9: Effect of porphysome nanoparticles on Caspase-1 expression in macrophages following inflammatory stimulation

iBMDMs were pre-treated with discoidal (Disc, 10 μg/mL) or spherical (Sphere, 10 μg/mL) porphysomes containing 0.3 mol % porphyrin-lipid (0.3%) then stimulated with IFN-γ (10 ng/mL) or LPS (10 ng/mL) for 18 h. RT-qPCR was used to measure changes in mRNA levels of *Caspase-1* (**A**-**B**). Caspase-1 protein was measured by ELISA in whole cell protein extracts from iBMDMs pre-incubated with discoidal (Disc) or spherical (Sphere) porphysomes for 18 h nanoparticles then stimulated with LPS (10 ng/mL) (**C**). qPCR data are from 3 independent experiments with n=3 replicates, and protein data are from one independent experiment with n=3 replicates. Data expressed as Mean ±SD. not-significant (ns) $P>0.05$, **$P<0.01$, ***$P<0.001$ by one-way ANOVA with Tukey’s multiple comparisons.

3.3.10 Porphysome nanoparticles suppress inflammation in macrophages independently of passive cholesterol efflux

Methyl-β-cyclodextrin (MβCD) 4% vol/vol initiates passive cholesterol depletion, enabling investigation of whether porphysomes modulate inflammation through a cholesterol depletion mechanism. Firstly, the cholesterol efflux capacity of MβCD treated cells was compared to that of the porphysome treatment. As expected, the MβCD caused a high level of cholesterol efflux with 48% of the cholesterol removed (Fig 3.10A, 8-fold, vs PBS control, *P*<0.0001). Although porphysome treatment induced cholesterol efflux, this was to a much lesser extent than the MβCD (Fig 3.10A). Also, there were no observed differences in cholesterol efflux capacity between the 0 mol % and 0.3 mol % porphyrin-lipid containing nanoparticles (Fig 3.10A).

To compare the effects of MβCD and porphysomes on inflammation, following pre-treatment of iBMDMs with either MβCD or porphysome nanoparticles then stimulating with LPS, *Ccl5* and *Il-1β* mRNA was measured by RT-qPCR. As observed previously, LPS significantly increased *Il-1β* mRNA expression compared to the PBS control (Fig 3.10B, 278-fold, *P*<0.0001). Following LPS stimulation, *Il-1β* expression did not significantly change between the PBS and MβCD treatments (Fig 3.10B). However, we observed a significant reduction in *Il-1β* expression following porphysome incubation as found previously compared to the LPS stimulation control (Fig 3.10B, Disc: -84%; Sphere: -81%, *P*<0.0001). This indicates that the reduction in *Il-1β* by porphysomes occurs independently of cholesterol efflux.

Compared to the PBS control, LPS stimulation also significantly increased expression of *Ccl5* (Fig 3.10C, +34780%, *P*<0.0001). Firstly, as shown previously the porphysome nanoparticles were able to significantly decrease *Ccl5* compared to the stimulated PBS control (Fig 3.10C, Disc: -93%; Sphere: -90%, *P*<0.0001). Although *Ccl5* mRNA also significantly decreased following MβCD treatment (Fig 3.10C, -38%, p<0.0001), porphysome pre-incubation led to a greater reduction in expression (Fig 3.10B, Disc: -89%; Sphere: -84%, *P*<0.0001) when compared to MβCD treatment. These findings suggest that the reduction in *Ccl5* by porphysome may in part be a result of cholesterol efflux, but other mechanisms are also operating.

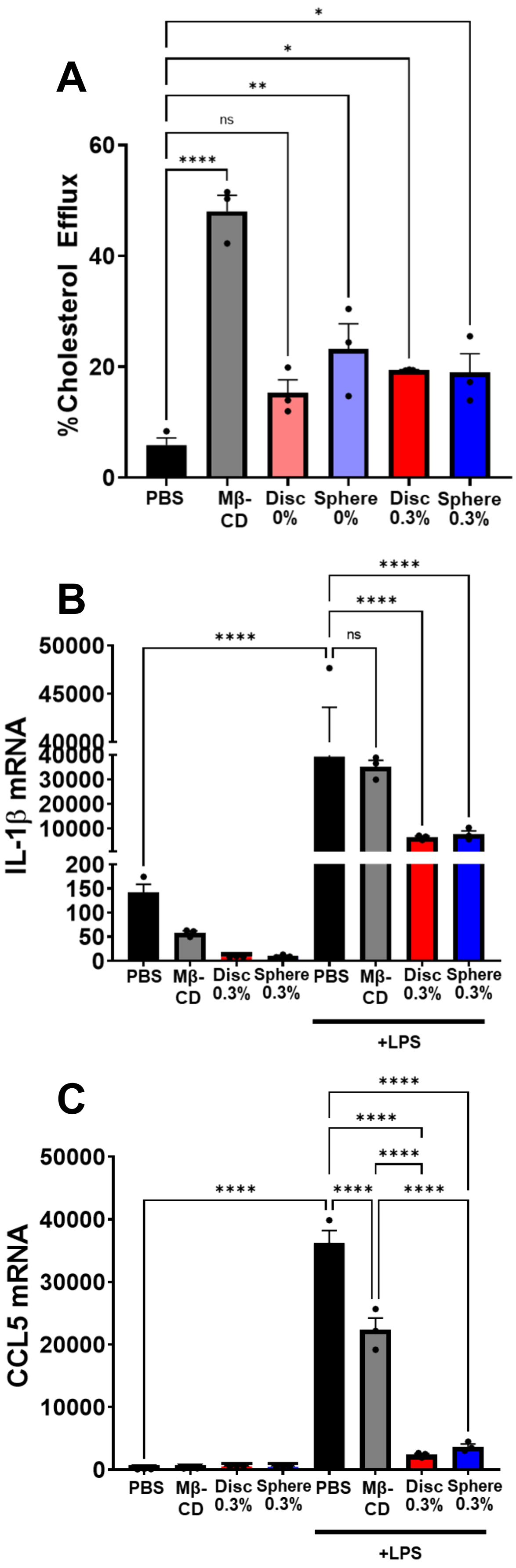
A
% Cholesterol Efflux
60
40
20
0
****
ns
**
*
*
PBS
Mβ-CD
Disc 0%
Sphere 0%
Disc 0.3%
Sphere 0.3%
B
IL-1β mRNA
50000
45000
40000
40000
30000
20000
10000
200
150
100
50
0
****
ns
****
****
PBS
Mβ-CD
Disc 0.3%
Sphere 0.3%
PBS
Mβ-CD
Disc 0.3%
Sphere 0.3%
+LPS
C
CCL5 mRNA
50000
40000
30000
20000
10000
0
****
****
****
****
****
****
PBS
Mβ-CD
Disc 0.3%
Sphere 0.3%
PBS
Mβ-CD
Disc 0.3%
Sphere 0.3%
+LPS

Figure legend 3.10: The anti-inflammatory properties of porphysomes occur independently of cholesterol efflux

(**A**) Cholesterol efflux was measured in iBMDMs following treatment with PBS, methyl-β-cyclodextrin (4% v/v, MβCD), discoidal (Disc) or spherical (Sphere) porphysomes (25μg/mL) containing 0 mol % (0%) or 0.3 mol % porphyrin-lipid (0.3%). iBMDMs were pre-incubated with PBS, 4% v/v methyl—cyclodextrin (MβCD), discoidal or CO-loaded 0.3 mol % (0.3%) porphysomes at 10 μg/mL. Then stimulated with LPS (10 ng/mL) and mRNA levels measured for *Il-1β* (**B**) and *Ccl5* (**C**). Data is from one independent experiment with n=3 replicates. Data expressed as Mean ±SD. not-significant (ns) $P>0.05$, *$P<0.05$, **$P<0.01$, ****$P<0.0001$ by one-way ANOVA with Tukey’s multiple comparisons.

3.4 Discussion

Atherosclerosis is a process that is exacerbated by macrophage accumulation and lipid uptake. The studies of this Chapter were focussed on determining the nature of interactions between porphysomes and macrophages *in vitro*. We report the following important findings, that porphysomes: 1) efflux cholesterol from macrophages 2) show potent anti-inflammatory properties and 3) are taken up by macrophages and can be detected fluorescently. Our results have implications for further investigation of the efficacy of apoA-I porphysome nanoparticles for targeting macrophages for theranostic functionality in atherosclerosis.

Macrophages are the primary cell target for porphysome NPs in atherosclerosis, we first determined the capacity for porphysome NPs to be taken up by cultured macrophages. Similar HDL-mimetic NPs containing the apoA-I mimetic R4F peptide have previously been shown to specifically interact with cells via the SR-BI receptor to deliver cargo to the cytoplasm [90]. Given that SR-BI is expressed and functionally utilised by macrophages to facilitate both efflux and influx of cholesterol [24] we measured the uptake of the porphysome NPs within cultured macrophages. We observed uptake of porphysome NPs by immortalised bone marrow derived macrophages (iBMDMs) which could be detected with fluorescent imaging of the whole cells with confocal microscopy and fluorescence quantified with flow cytometry. This observed uptake is consistent with other HDL-like NPs [83, 123] with conjugated fluorophores for detection via fluorescence imaging. In similar experiments, folate-conjugated porphysome NPs were also found to be taken up by cultured macrophages (RAW 264.7 cells), however these were targeting the folate receptor on macrophages for localisation following myocardial infarction [113]. To our knowledge this is the first time that an HDL-mimetic NP synthesised with fluorescent porphyrin-lipid conjugate has been shown to be internalised by macrophages and detected using the fluorescent properties of the porphyrin-lipid. This establishes that macrophages *in vitro* can take up porphysome NPs with the ability to be detected using conventional fluorescence imaging. This is an important step in validating the ability of porphysome NPs to be internalised by macrophages *in vitro*.

Porphysomes were able to efflux cholesterol from macrophages and, when compared to rHDL, were highly efficient efflux acceptors. Given that HDL is known to be involved in the reverse cholesterol transport (RCT) pathway, with this ability to efflux cholesterol from plaque associated with reduced CAD events [59, 60]. However, HDL-raising therapies have demonstrated a lack of benefit in reducing cardiac events in clinical trials [124, 125], highlighting the need for developing HDL alternatives that can retain anti-atherosclerotic functionality. Increased cholesterol efflux from macrophages prevents foam cell formation and accumulation in atherosclerotic plaque. Excessive foam cell deposition is a hallmark feature of atherosclerosis progression, therefore any agent that can reduce cholesterol accumulation could be immensely valuable in regard to preventing plaque development. Cholesterol efflux to HDL particles is mediated via transporters ABCA1, ABCG1 and SR-BI in macrophages [23]. Although not specifically tested, we would predict that the porphysome NPs would act via SR-BI to induce cholesterol efflux, as the R4F peptide of HDL-mimetic NPs is specifically designed to interact with SR-BI [90, 126]. SR-BI is a unique receptor in that it mediates the passage of cholesterol both in and out of cells. Previous studies using HDL-mimetic NPs synthesised with the R4F peptide were in some cases intended to exploit the cholesterol influx properties of SR-BI that facilitates the uptake of the NP inner cargo by target cells. Knockout lines of SR-BI were used to establish the specificity of the interaction with SR-BI, but this was primarily focused on examining the cargo uptake within cells [90, 126].

Therefore, it is entirely possible that the porphysome NP particles used in this study interact with SR-BI, to facilitate both particle uptake and cholesterol efflux.

It was found that when reconstituted HDL (rHDL) was directly compared to the porphysome NPs at the same concentration of 25 μg/mL, the porphysome NPs had a significantly (~50%) higher cholesterol efflux capacity. An explanation for this may be due to the concentration of the porphysomes being based on the protein concentration of the R4F peptide rather than that of endogenous apoA-I as found in the rHDL. The apoA-I mimetic R4F peptide in the porphysome NPs is a short amphipathic alpha helical peptide, which consists of 18 amino acids (aa), whereas the full-length endogenous apoA-I in the rHDL particles is approximately 243 aa [100] and each apoA-I protein contains 10 alpha helices [127]. Initially apoA-I mimetic peptides were developed to functionally mimic the cholesterol efflux properties of endogenous HDL [100]. Therefore, at the same protein concentration, the porphysome NPs may function more efficiently to efflux cholesterol in comparison to the rHDL particles, as appears to be the case in our study. Furthermore, other HDL-like nanoparticles have been shown to have preserved function of cholesterol efflux including nanoparticles containing apoA-1 [83, 84] and R4F [123]. This demonstrates that porphysome NPs retain the capacity to effectively efflux cholesterol macrophages *in vitro*, which is a known anti-atherosclerotic function of endogenous HDL particles.

We hypothesised that because porphysome NPs interact with SR-BI [90], they may also have effects on cell signalling pathways directly influenced by SR-BI interaction similar to those exhibited by HDL [24]. For example, HDL has been shown to mediate some of the demonstrated anti-inflammatory effects in macrophages via interaction with SR-BI by reducing NFκB activation [128]. Accordingly we assessed whether porphysome NPs also exert anti-inflammatory properties on macrophages.

In order to study the effect of porphysomes on inflammation, we used an *in vitro* model comprising the use of immortalised bone marrow derived macrophages (iBMDMs) stimulated with either IFN-γ or LPS. During atherogenesis, the release of pro-inflammatory mediators from cells such as macrophages [129] leads to the continued recruitment of immune cells and exacerbates the growth of atherosclerotic plaque [2]. This *in vitro* model of inflammatory activation of macrophages was used to assess the impact of porphysome NPs on the expression of several pro-inflammatory genes.

IL-1β and IL-18 are pro-inflammatory cytokines released from cells as part of the NLRP3 inflammasome response. Typically, the NLRP3 inflammasome requires stimulation with a priming step, such as LPS binding toll like receptors (TLRs), and then an activation step, with cholesterol crystals or ATP. The purpose of the priming step with LPS is to increase the transcriptional expression of *Il-1β, Il-18,* and *Nlrp3* ready for the activation step to assemble the NLRP3 complex and activate caspase-1 to cleave pro-IL-Iβ and pro-IL-18 [130]. In this study *Il-1β* mRNA expression was increased in the presence of IFN-γ and LPS alone which is consistent with previous studies. However, *Il-18* mRNA expression only significantly increased with IFN-γ stimulation whereas LPS stimulation reduced *Il-18* expression. This could be explained by the type of cultured macrophages used (iBMDMs) or there also could be negative feedback on the transcriptional regulation of *Il-18*. We could not measure IL-18 protein as the concentration in cell culture media and lysates was below the detection capabilities of the ELISA, even in stimulated conditions.

Interestingly there was an increase in the level of secreted IL-1β protein following LPS stimulation which did not require a second activation step. There is previous evidence that the NLRP3 inflammasome can be activated by a single step with only TLR-4 stimulation required to initiate IL-1β release, this was only seen in human and porcine monocytes but not murine monocytes [130, 131]. Therefore, it is possible that an alternative activation of the NLRP3 inflammasome is occurring in iBMDMs. Other cytokines and chemokines (e.g. *Il-6, Ccl5, Ccl2*) also increased following inflammatory stimulation, it is therefore possible that other inflammatory pathways are also activated in the iBMDMs used in these studies.

Despite the inconsistencies in the response of some of the components of the inflammasome to stimulation, pre-treatment with either discoidal and spherical 0.3% porphyrin-lipid porphysomes significantly inhibited expression of *Il-1β* and *IL-18* mRNA. Consistent with this, porphysome NPs significantly inhibited secretion of IL-1β protein. Although these changes were only observed in cultured macrophages *in vitro,* this is significant given that IL-1β and IL-18 have been shown to have a key role in atherogenesis [132, 133]. This is particularly true of IL-1β, with the CANTOS trial showing that inhibition by Canakinumab (an IL-1β monoclonal antibody) significantly reduced recurrent cardiovascular events [6, 73]. This demonstrates that reducing inflammation therapeutically has the potential to improve upon current treatments for atherosclerotic cardiovascular disease.

ASC and NLRP3 are integral components of the inflammasome which are involved in facilitating signalling during activation of the NLRP3 inflammasome. Firstly, NLRP3 acts as the sensor which oligomerises and recruits the adaptor ASC. The assembled ASC then recruits Caspase-1 which cleaves pro-IL-18 and pro-IL-1β into their active form [130]. We therefore measured *Asc, Nlrp3* and *Caspase-1* mRNA expression. In a similar way to *Il-18,* not all genes were elevated following IFN-γ and LPS stimulation. This may be due to something specific about the expression profile of iBMDMs. Despite this, in response to porphysome treatment we saw a significant reduction in *Asc* and *Nlrp3* (with IFN-γ stimulation). Interestingly *Caspase-1* mRNA only significantly increased under LPS stimulation and treatment with spherical porphysome NPs. Furthermore, intracellular Caspase-1 protein levels decreased following LPS stimulation which would not be expected if the inflammasome was activated. Given that secreted IL-1β increased following LPS stimulation and this requires cleavage of pro- IL-1β by Caspase-1, lower Caspase-1 protein levels are not consistent with these results. However, protein levels of Caspase-1 may not entirely reflect the activity of Caspase-1. During inflammasome activation, Caspase-1 is cleaved and subsequently activated [130]. The active cleaved Caspase-1 can be separated from pro-Caspase-1 using western blotting to determine the degree of Caspase-1 activation [134]. However, the ELISA that was used to determine Caspase-1 protein concentration in this study only detects pro-Caspase-1. Therefore, future studies could assess the level of Caspase-1 activation. The dual reduction in mRNA and secreted protein levels of IL-1β by porphysome NPs also suggests transcriptional regulation by porphysome NPs, not Caspase-1 cleavage of pro-IL-1β. This may also explain why the activation step with ATP was not required to stimulate IL-1β secretion. Overall, these studies suggest that porphysome NPs suppress NLRP3 inflammasome activation, however this requires further investigation.

We also examined the effect of porphysome NPs on the expression of chemokines CCL5 and CCL2 [135]. In atherosclerosis, the release of chemokines from the plaque microenvironment attracts the recruitment of leukocytes to the activated endothelium or migration through to the subendothelial space [4]. Both CCL5 and CCL2 are implicated in atherogenesis [135]. Porphysome NPs significantly decreased CCL5 mRNA and protein, demonstrating a potent anti-inflammatory effect in macrophages. However, although porphysome NPs had no effect on *Ccl2* mRNA levels, secreted CCL2 protein unexpectedly increased following incubation with spherical NPs after LPS stimulation.

This result presents a striking contrast to our findings with CCL5 and suggests that porphysome NPs can discriminate with regard to which chemokine they suppress/upregulate. This is similar to what has been previously observed with HDL, with both pro- and anti-inflammatory effects observed in macrophages [118, 120, 136]. Furthermore, porphysome NPs had no effect on *Il-6* mRNA expression similar to the *Ccl2* results. This indicates that porphysome NPs do not seem to affect the transcriptional regulation of all pro-inflammatory mediators in macrophages. In the context of other HDL-like nanoparticles, Duivendoorn *et al.* [54] also tested the anti-inflammatory effects of statin-loaded HDL particles (S-HDL) in macrophages. They found that the free statin and S-HDL particles both reduced levels of CCL2 and TNFα, indicating that the particles had anti-inflammatory effects in cultured murine macrophages (J774A.1). However, the anti-inflammatory effects of these S-HDL particles were attributed to inhibition of the mevalonate pathway by the loaded statin.

Our findings that show a striking reduction in *Il-1β, IL-18* and *Ccl5* mRNA levels suggests porphysomes are influencing their transcriptional regulation. These genes are regulated by the transcription factor NFκB [137]. When NFκB becomes activated the p65 subunit translocates from the cytoplasm to the nucleus [137, 138]. Normally this can be initiated by stimulation with LPS [130], however incubation of iBMDMs with LPS did not elicit a significant change in p65-NFκB mRNA or protein expression. Despite time-course experiments (data not shown) to optimise the concentration and timing to measure p65-NFκB protein, there was no observed increase in nuclear p65-NFκB following LPS stimulation. We found a significant reduction, however, in p65-NFκB following incubation with discoidal porphyrin-lipid free NPs with no LPS stimulation. Furthermore, when comparing the effects of PBS and porphysome discoidal NPs following LPS stimulation, there was a non-significant trend for a reduction in p65-NFκB with porphysome discoidal NPs. This is consistent with the reductions in *Il-1β, IL-18* and *Ccl5*, and provides a possible mechanism of action for these anti-inflammatory effects.

There is evidence that cholesterol efflux is linked to anti-inflammatory effects exerted by HDL in macrophages. Modulation of cholesterol content is known to have many pleiotropic effects on cellular function, which may explain some of the observed anti-inflammatory and anti-atherogenic effects of HDL [136]. Given that the HDL-mimetic porphysome NPs used in these studies have demonstrated anti-inflammatory effects in macrophages, we sought to resolve whether these changes in inflammatory gene expression might be attributed to the observed cholesterol efflux capacity of these NPs or another pathway. To determine this, we compared porphysome NPs to MβCD induced cholesterol depletion. In the cholesterol efflux assay, MβCD induced cholesterol efflux as shown by approximately half of the cholesterol being removed from the macrophages which is consistent with previous studies [139]. In comparison, the porphyrin-lipid NPs had a much lower level of cholesterol efflux capacity, which suggests that porphysome NPs are not inducing passive cholesterol efflux. In addition, there were no differences in cholesterol efflux between NPs that contained porphyrin-lipid (0.3 mol %) and those that contained no porphyrin-lipid. This indicates that the porphyrin-lipid is not essential for mediating cholesterol efflux and is most likely due to the HDL-like structure of the NPs (R4F peptide complexed with phospholipid). When the anti-inflammatory effect of MβCD was compared to porphysome NPs, porphysome NPs demonstrated a larger reduction on the LPS-stimulated expression of *IL-1β* and *Ccl5* when compared to MβCD treatment. This suggests that the observed anti-inflammatory changes in macrophages are not entirely explained by the porphysome NP-induced cholesterol efflux. HDL has previously been shown to have both anti- and pro-inflammatory effects on macrophages [120, 136], but this is thought to be dependent on the cholesterol content status of the cell, with pro-inflammatory effects of HDL only seen under excessive cholesterol depletion [118]. HDL has reported cholesterol efflux dependent and independent mechanisms of exerting anti-inflammatory effects. Cholesterol efflux dependent mechanisms includes a reduction in TLR4 signalling by HDL accepting cholesterol via ABCA1 and ABCG1 that results in the decreased surface expression of TLR4. There are also cholesterol-independent mechanisms which may be attributed to an increase in activating transcription factor 3 (ATF3) leading to inhibition of pro-inflammatory cytokine expression downstream of NFκB, although the full mechanism has not been elucidated [59]. Overall, these results suggest that porphysome NPs may have both cholesterol efflux dependent and independent anti-inflammatory effects.

In future experiments, examining the way that porphysome NPs interact with macrophages in terms of mediating both cholesterol efflux and inflammation would provide further information on mechanisms of action. For example, HDL is known to mediate efflux in macrophages via ABCA1, ABCG1 and SR-BI [59, 140] but this has not been established for porphysome NPs. Initially this could be achieved by knockdown of these transporters to determine whether observed cholesterol efflux or anti-inflammatory effects are dependent on the presence of these receptors.

Native HDL is found in several different conformations including nascent discoidal particles consisting of apoA-I and phospholipid that become spherical as they accumulate free cholesterol from the peripheral tissues as well as other lipoproteins [59, 141]. In the studies described here, a combination of both discoidal and cholesteryl oleate (CO)-loaded spherical particles were used to compare any functional differences based on the structural features of the NPs. Interestingly the structure of the discoidal compared to the spherical porphysome nanoparticles caused little difference in its effects on inflammation or cholesterol efflux capacity. This suggests that the shape of the nanoparticles does not significantly affect functionality, at least in the context of these processes. However discoidal and spherical particles were not directly compared in uptake experiments with macrophages, so it is possible that there are differences in cellular uptake due to the shape of the particles [142]. In previous studies of a different type of porphyrin-lipid NPs, there was a higher uptake of the spherical vs discoidal glioblastoma-targeted porphyrin-lipid apoE3 lipid nanoparticles (pyE-LNs) in U87 glioblastoma cells. However these nanoparticles were targeting the LDL receptor so this would have to be further investigated with the apoA-I-linked porphysomes and interactions with SR-BI [99]. However, it would be expected that the spherical NPs would be taken up more readily by macrophages as this is seen with previously studied NPs [143]. To measure differences in uptake, it would be ideal to employ time course experiments to determine the kinetics of uptake of discoidal compared to spherical porphysomes.

It is hypothesised that the active component in the particles is the apoA-I mimetic peptide R4F via interactions with the SR-BI receptor on macrophages to initiate the effects seen *in vitro*. Therefore, in the following chapters investigating the therapeutic effects on atherosclerosis *in vivo*, the discoidal particles without porphyrin-lipid were further tested (discoidal R4F HDL mimetic, see Table 2.3). Furthermore, given the optimal fluorescence detection properties, the 30 mol % porphysome NPs were subsequently used for *in vivo* imaging.

This study has demonstrated *in vitro* that porphysome nanoparticles: 1) can be internalised and detected in macrophages using the fluorescent porphyrin-lipid, 2) demonstrate anti-inflammatory properties exerted by reducing the expression of pro-inflammatory cytokines and chemokines implicated in atherogenesis and 3) retain cholesterol efflux capacity. Together these suggest that porphysome NPs *in vitro* possess potent anti-atherogenic properties. However, there are still mechanistic questions about how these porphysome NPs mediate these processes which requires further investigation beyond this thesis, although the suppression of p65 and inflammasome activation appear to play a part. Overall, this chapter has established the basis for the next three chapters which will further explore the theranostic properties of porphysome nanoparticles in murine atherosclerosis models *in vivo.*

CHAPTER 4

Theranostic properties of apoA-I-linked porphysome nanoparticles in stable atherosclerosis

4.1 Introduction

There are several limitations to the identification of atherosclerosis, with current non-invasive and invasive approaches unable to determine the molecular characteristics of the lesion. In addition, there is a need for novel ways to therapeutically manage atherosclerosis. Previously, HDL-like nanoparticles have been investigated for their ability to detect atherosclerosis *in vivo*, with studies finding successful localisation to sites of atherosclerotic plaque [144, 145]. In addition, others have also investigated the use of HDL as a therapeutic nanoparticle carrier to inhibit atherosclerosis by targeting inflammation and proliferation [54, 79].

Nanoparticles, like other pharmaceutical agents, are further assessed to determine that the properties established *in vitro* are maintained *in vivo* and the overall distribution of the particles within a biological system. Porphyrin-lipid based nanoparticles or ‘porphysomes’ have been previously investigated in animal models of cancer. ApoA-I mimetic peptide-linked porphyrin-lipid nanoparticles were found to be distributed in a way similar to other HDL-like nanoparticles, with the highest uptake in the liver [89].

A key step in assessing the ability of nanoparticles for diagnostic and therapeutic properties in atherosclerosis is to assess activity in an animal model of stable atherosclerosis. There are several available genetic knockout mice that can be used to assess changes in stable plaque deposition. For example, Apolipoprotein E deficient (*Apoe*$^{-/-}$) mice rapidly develop atherosclerosis when fed a high cholesterol diet [146, 147]. This development of atherosclerosis is primarily the result of the ApoE deficiency causing higher than normal cholesterol levels due to the impaired clearance of circulating chylomicron and VLDL particles [148]. Plaque deposition in the vasculature can be assessed for both volume and compositional changes to determine the efficacy of a therapeutic intervention to inhibit atherosclerosis. Porphysome nanoparticles have demonstrated theranostic potential. We therefore sought to examine both the uptake and therapeutic effects of porphysome nanoparticles *in vivo* in a murine model of stable atherosclerosis.

As demonstrated in Chapter 3, porphysome nanoparticles displayed anti-inflammatory effects on macrophages and excellent cholesterol efflux capabilities *in vitro*. In this Chapter, we aimed to investigate whether these effects translate to changes in atherosclerotic lesion size and composition *in vivo* using the *Apoe*$^{-/-}$ murine model of stable plaque. Furthermore, the ability of porphysomes to be taken up by plaque macrophages *in vivo* was investigated and whether porphysomes localise to atherosclerotic lesions. Using the PET and fluorescence imaging capabilities of porphysomes, we also sought to determine whether *in vivo* imaging techniques could be applied successfully to detect plaque in a model of stable atherosclerosis.

4.2 Methods

4.2.1 *In vivo* stable atherosclerosis model protocols

For the *in vivo* studies, a dose of 40 mg/kg based on the R4F peptide concentration was administered either 3 times per week or on alternate days. The 40mg/kg concentration is based on the previous use of apoA-I protein in previous murine atherosclerosis studies in *Apoe*$^{-/-}$ mice [149]. The 40 mg/kg dosage was calculated by the average of the initial weight of the cohort of animals prior to commencing injections (injection volume between 200-250 µL/ animal). For the imaging studies, 5 mg/kg of the discoidal 30 mol % porphysome nanoparticles, based on the porphyrin-lipid content, was administered as per average animal weight. All mice were humanely killed (sacrificed) by cardiac puncture and perfusion flushed with saline through the left ventricle prior to tissue collection. The methods for each cohort of mice are summarised below:

4.2.1.1 *Apoe*$^{-/-}$ mice for PET/MRI, IVIS fluorescence imaging and flow cytometry

5-6-week-old *Apoe*$^{-/-}$ mice were fed *ad libitum* a high-cholesterol diet (HCD) or standard chow diet for a total of 12 weeks. After 4 weeks, intraperitoneal administration of PBS or discoidal R4F-HDL mimetic porphysome nanoparticles commenced for 8 weeks (40 mg/kg of R4F peptide, 3 times/ week, n=7-8/group). For the PET/MRI imaging protocol, mice were intravenously injected via the tail vein with ~18.5-20 MBq of ^{64}Cu-porphysomes (30 mol %) at week 7 and 11 of the study and imaged 6 h after injection. 24 h prior to sacrifice, mice were administered via intraperitoneal injection with either PBS or 5 mg/kg of discoidal 30 mol % porphysome nanoparticles and flow cytometric analysis conducted on the aorta. A separate cohort of animals that underwent this treatment protocol were subjected to IVIS fluorescence imaging *ex vivo* of the aortic arch, descending aorta, liver, spleen, kidney and lungs.

4.2.1.2 *Apoe*$^{-/-}$ mice for histological analysis of the aortic sinus

11-12-week-old *Apoe*$^{-/-}$ mice were fed *ad libitum* a HCD for a total of 13 weeks. After 6 weeks, intraperitoneal administration of discoidal R4F-HDL mimetic NPs commenced for 7 weeks (40 mg/kg of R4F peptide, alternate days, n=13-14/group). 24 h prior to sacrifice, mice were administered via intravenous or intraperitoneal injection with either PBS or 5 mg/kg of discoidal 30 mol % porphysome nanoparticles, with plaque in the aortic sinus from these mice subjected to histological analysis.

4.2.1.3 *Apoe*$^{-/-}$ mice for biodistribution with γ-counting and PET imaging

5-6-week-old *Apoe*$^{-/-}$ mice were fed *ad libitum* a HCD or standard chow diet for a total of 32 weeks. Mice were administered ~18.5 MBq of ^{64}Cu-porphysomes (30 mol %) and mice imaged at 1, 3, 6, 24 and 48 h post-injection with PET. Mice were then humanely killed 48 h post-injection and processed for γ-counting biodistribution.

4.2.2 ^{64}Cu-porphysome gamma (γ-) counting in organs/tissues

For the assessment of ^{64}Cu-porphysome biodistribution, tubes containing the organs: heart, aorta, liver, lungs spleen, kidney, gut, fat, thymus and blood were all pre-weighed. All tissues/blood in tubes were weighed and the weight of the empty tube subtracted from the overall weight of the tissues/blood in the tube. Gamma counts were measured from the tissues, blood and the original infused ^{64}Cu-porphysome sample (total injected dose) with an automatic gamma counter (Hidex) and % injected dose (%ID)/g was calculated as below:

$$\%ID/g = \frac{\dfrac{^{64}Cu\ gamma\ counts\ (sample)}{^{64}Cu\ gamma\ counts\ (total\ injected\ dose)}\ \mathrm{X}\ 100\%}{Tissue\ weight\ (g)}$$

4.2.3 Sectioning of the aortic sinus

Embedded hearts were trimmed until the first leaflet emerged and then sections were collected from this point. At least sixty 7 µm sections of the OCT-embedded aortic sinus were collected continuously on a cryostat (Leica CM3050S) and mounted onto microscope slides (Superfrost Plus) then stored at -20°C or -80°C until analysis.

4.2.4 Image analysis of the aortic sinus

Image analysis of tissue sections was performed using Image Pro-Premier 9.2 (Media Cybernetics) software. Three sections of aortic sinus were analysed/mouse that spanned the sinus region and only sections that contained three leaflets were analysed. Total lesion area was calculated per section and then averaged across the three analysed sections. For histological and immunochemical analyses, the area of staining from a single mid-point section was calculated as a percentage of the selected total sinus lesion area (% of plaque area).

4.2.5 Flow cytometry of the descending aorta

Perivascular fat was carefully removed from the descending aorta and excised from the mice. Harvested aortas were cut into pieces and placed into Iscove’s Modified Dulbecco’s Media (IMDM, Sigma). To digest the aortas into a single-cell preparation they were transferred into Hank’s Balanced Salt Solution (HBSS, Sigma) containing Liberase (Roche), vortexed and incubated for 45 min at 37°C. The aortic digest was passed through a cell strainer (40 µm) and stained with AF-700 viability dye. Digests were stained for 45 min at 4°C with fluorochrome-conjugated antibodies against F4/80, CD11b, CD86, CD206, CD31, α-SMA and TREM2 made up to a 1:10 dilution in Brilliant Stain Buffer (BD Biosciences). Samples were subsequently washed with IMDM + 10% FBS and fixed with Cytofix fixation buffer (BD Biosciences). In addition, fluorescence minus one (FMO) background control samples were prepared using livers from PBS and porphysome treated mice. The liver was processed in the same way as the aorta, but the FMO samples were stained with each antibody except one to set the flow cytometry gates for each antibody. The antibodies and reagents for flow cytometry experiments are summarised in Table 4.1.

All samples were run on a BD LSRFortessa™ X-20 Analyser and data analysed with FlowJo™ v10.8.1 software. Cell samples were gated to exclude debris (using forward and side scatter area), include single (using forward side scatter height and area) and viable cells (AF-700 viability dye negative cells). The FMO samples were to set the gates for the expression of different cell markers detected with antibodies with the porphyrin-lipid gated using the PBS mouse liver. Porphyrin-lipid$^+$ cells were detected on the AF647 channel (excitation with red laser at 640 nm and emission filter 670/30 nm). Macrophages were identified as CD11b$^+$ F4/80$^+$ cells. M1 macrophages as CD11b$^+$ F4/80$^+$ CD86$^+$ CD206$^-$ cells. M2 macrophages as CD11b$^+$ F4/80$^+$ CD86$^-$ CD206$^+$ cells. Monocytes as CD11b$^+$ F4/80$^-$ cells. Endothelial cells (ECs) as CD11b$^-$ F4/80$^-$ CD31$^+$ cells. Smooth muscle cells (SMCs) as CD11b$^-$ F4/80$^-$ α-SMA$^+$ cells. Gating strategy for aortic cell types is illustrated in Fig 4.1.

Table 4.1: Flow cytometry antibodies and reagents

Antibody/ Reagent	**Catalog #, Manufacturer**
Brilliant Violet 785™ anti-mouse F4/80	123141, Biolegend, CA, USA
APC-Cy™7 Rat Anti-CD11b	557657, BD Biosciences, NJ, USA
BV421 Rat Anti-Mouse CD86	564198, BD Biosciences, NJ, USA
PE/Cyanine7 anti-mouse CD206 (MMR)	141720, Biolegend, CA, USA
PerCp-Cy™5.5 Rat Anti-mouse CD31	562861, BD Biosciences, NJ, USA
Anti-Actin, α-Smooth Muscle – FITC, Mouse monoclonal	F3777, Sigma-Aldrich Inc., MO, USA
Human/Mouse TREM2 PE-conjugated Antibody	FAB17291P, Biotechne, MN, USA
Hanks' Balanced Salt solution (Phenol red free)	H9394-500ML, Sigma-Aldrich Inc., MO, USA
Iscove's modified dulbecco's medium (IMDM)	I3390-500ML, Sigma-Aldrich Inc., MO, USA
40µm Easystrainer green	542040, Greiner Bio-One, Interpath Services, Victoria, Australia
Liberase™ Research Grade	5401127001, Sigma-Aldrich Inc., MO, USA
Brilliant Stain Buffer	566349, BD Biosciences, NJ, USA
Compensation Beads (Rat/Hamster)	552843, BD Biosciences, NJ, USA
Cytofix Fixation Buffer 100mL	554655, BD Biosciences, NJ, USA
Fixable Viability Stain 700	564997, BD Biosciences, NJ, USA

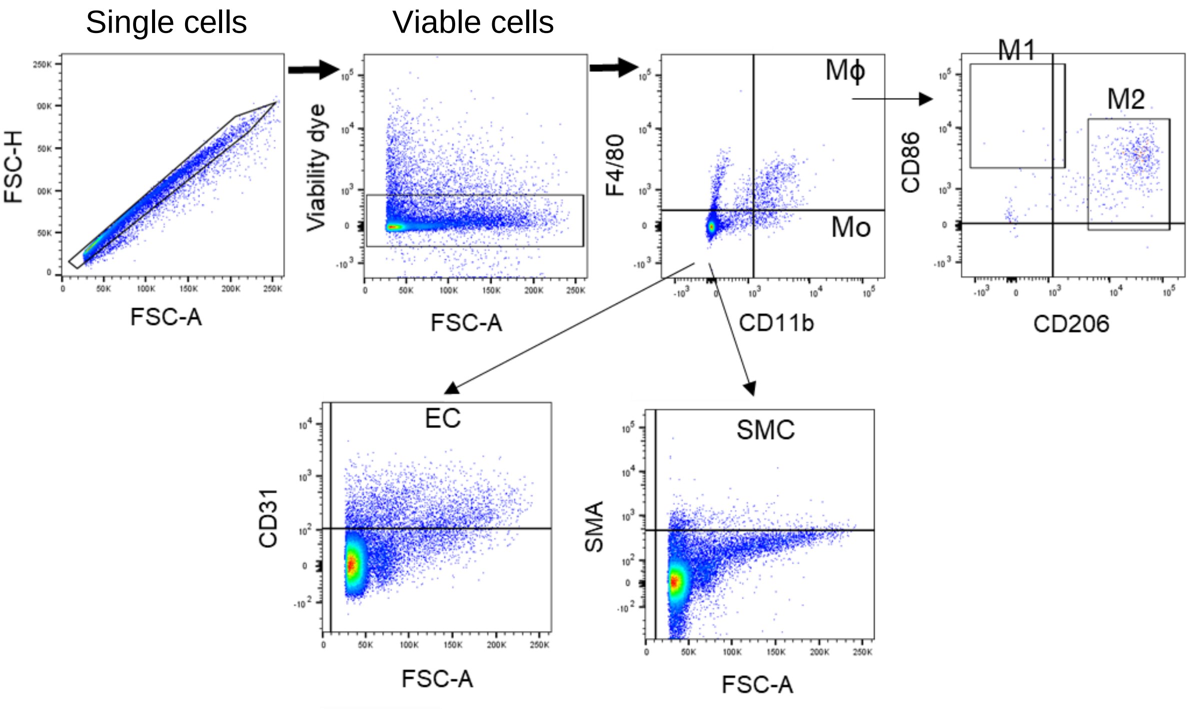

Figure legend 4.1: Gating strategy for flow cytometry analysis of aortic cell types.

Macrophages, M1/M2-like macrophages, endothelial and smooth muscle cells were gated from viable cells. Forward scatter height, FSC-H. Forward scatter area, FSC-A. Macrophage, MΦ. Endothelial cell, EC. Smooth muscle cell, SMC

4.3 Results

4.3.1 Porphysome nanoparticles localise to the aortic arch region in HCD fed *Apoe*$^{-/-}$ mice, detected by IVIS fluorescence imaging

Initially an aliquot of 30 mol % porphysome nanoparticles was placed in a 96-well plate for comparison to PBS and for verification of the fluorescence properties detected by the IVIS. This demonstrated that porphysomes could be detected and had a higher mean radiance than PBS (Fig 4.2A). In addition, when an equal volume of triton x-100 detergent was added to the porphysomes to disrupt the particle structure, there was an observed increase in fluorescence signal (Fig 4.2A), confirming the unquenching of the porphyrin-lipid fluorescence observed previously [89].

We then compared the fluorescence imaging capabilities of porphysomes and their localisation in HCD-fed and chow-fed *Apoe*$^{-/-}$ mice. HCD fed *Apoe*$^{-/-}$ mice develop atherosclerosis at an accelerated rate, compared to chow fed *Apoe*$^{-/-}$ mice [148]. We therefore considered the chow-fed *Apoe*$^{-/-}$ mice to be “non-atherosclerotic”, relative to the HCD fed *Apoe*$^{-/-}$ mice. Initially, we determined whether porphysome nanoparticles could be detected *in vivo* using a fluorescence *in vivo* imaging system (IVIS, PerkinElmer). Visualising the opened chest cavity of mice *ex vivo, Apoe*$^{-/-}$ mice fed HCD for 12 weeks then injected with porphysomes had a noticeable increase in fluorescence signal in the plaque-containing arch region, which did not occur in the chow-fed mouse (Fig 4.2B). Excised aortic arch and descending aorta from these mice were also compared to mice injected with PBS (Fig 4.2C). IVIS imaging showed a larger fluorescence signal in mice injected with porphysomes, compared to PBS (Fig 4.2B&C), and HCD-fed mice also had a stronger fluorescence signal in the arch region than chow-fed porphysome-injected mice (Fig 4.2D, +55%, $P<0.05$). However, quantification of the fluorescence from the descending aorta indicated no significant change between the chow and HCD fed mice (Fig 4.2E).

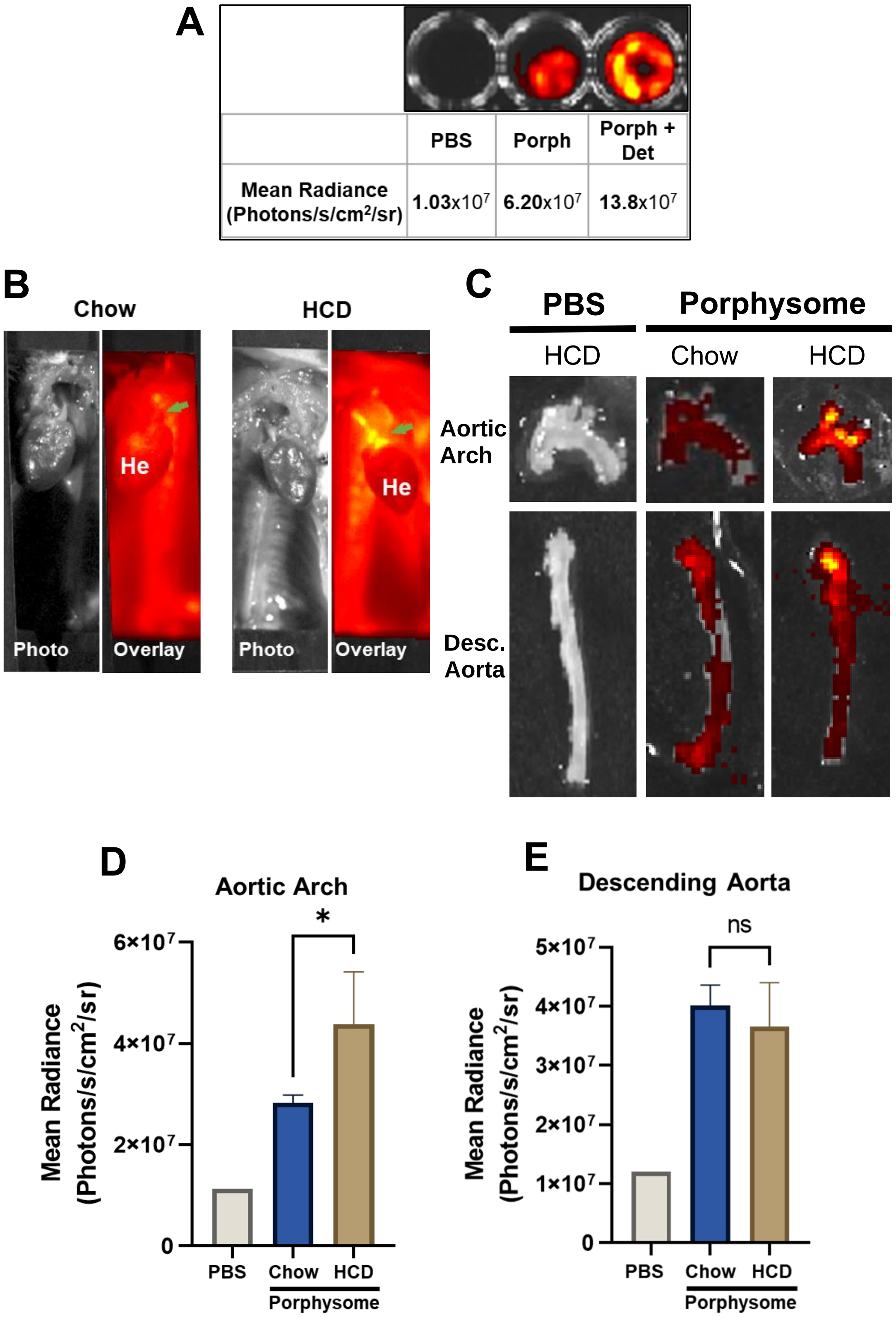

	PBS	Porph	Porph + Det
Mean Radiance (Photons/s/cm^2/sr)	1.03x10^7	6.20x10^7	13.8x10^7

Figure legend 4.2: Porphysome nanoparticles can be detected using fluorescence imaging *ex vivo* in *Apoe*$^{-/-}$ mice and localise to the aortic arch.

(**A**) 10 µL of PBS, 30 mol % porphysomes alone (Porph) and with addition of 10 µL of 1% triton x-100 detergent (Porph + Det) were measured in a black 96 well plate to confirm fluorescence detection in IVIS prior to injection. Fluorescence of porphysomes detected by IVIS with an excitation and emission wavelength of 675 nm and 720 nm respectively. *Apoe*$^{-/-}$ mice were fed for 12 wks on chow or HCD and 24 h prior to sacrifice PBS or 30 mol % discoidal porphysomes were administered via intraperitoneal injection. Representative images of IVIS fluorescence images of the *in-situ* heart and aorta within the chest cavity of mice fed a chow or HCD (**B**), and the excised aortic arch and descending aorta of PBS or porphysome chow or HCD fed mice (**C**). Quantification of the fluorescence signal from images of excised aortic arch (**D**) and descending aorta (**E**) expressed as mean radiance (Photons/s/cm^2/sr). Fluorescence imaging experiment conducted on n=1-4 mice/group (PBS, n=1; POR Chow, n=1; POR HCD, n=4). Chow and HCD aortas were captured side-by-side in one image frame with the IVIS camera. Data expressed as Mean ± SD. not-significant (ns) $P > 0.05$, $*P < 0.05$ vs chow control by unpaired two-tailed t-test. In vivo imaging system, IVIS; s, second; sr, steradian. POR, porphysome.

4.3.2 Porphysome nanoparticle detection *ex vivo* in the organs of *Apoe*$^{-/-}$ mice

Fluorescence was measured *ex vivo* in the liver, kidney, spleen and lung in mice injected with porphysomes. When compared to PBS-injected control mice fed HCD, the porphysome injected mice had a visibly higher fluorescence signal (Fig 4.3A). Interestingly, in the liver a much higher fluorescence signal was observed in the liver of porphysome-injected mice fed HCD compared to chow-fed. This was confirmed by quantification of the fluorescent signal in which fluorescence in the liver of porphysome-treated HCD fed mice was higher compared to both the chow mice and PBS infused HCD fed mice (Fig 4.3B, HCD vs Chow: 2-fold, $P<0.0001$; HCD vs PBS HCD, 67-fold, $P<0.0001$). In HCD fed mice there was significantly higher fluorescence (radiance) in the liver, when compared to the other organs (Fig 4.3B, $P<0.0001$). Also, in the other organs there was no difference in fluorescence signal between porphysome-injected chow-fed and HCD-fed mice.

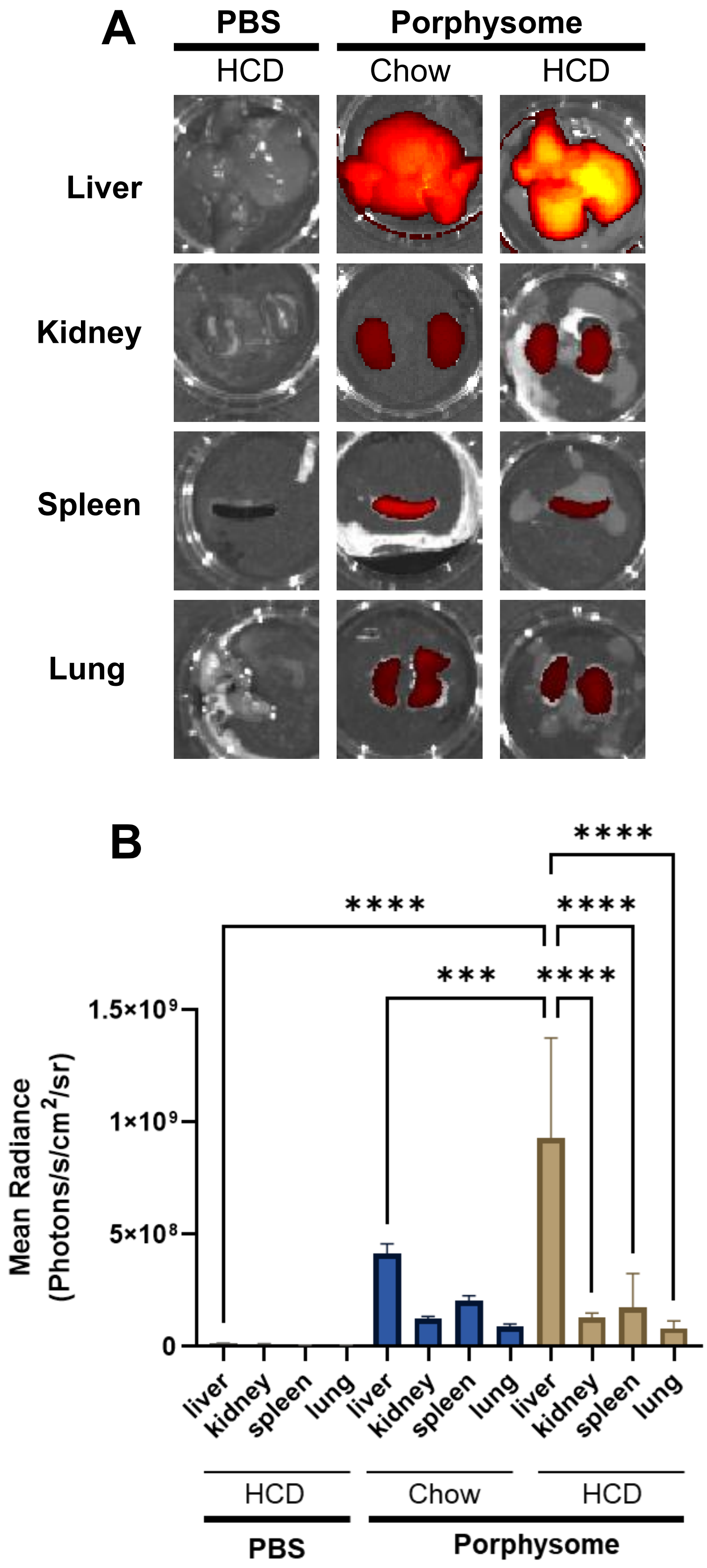
A
PBS
Porphysome
HCD
Chow
HCD
Liver
Kidney
Spleen
Lung
B
****
****
****
***
****
Mean Radiance
(Photons/s/cm²/sr)
1.5×10⁹
1×10⁹
5×10⁸
0
liver
kidney
spleen
lung
liver
kidney
spleen
lung
liver
kidney
spleen
lung
HCD
Chow
HCD
PBS
Porphysome

Figure legend 4.3: Biodistribution of porphysome nanoparticles in organs of chow and HCD fed mice detected ex vivo using fluorescence.

(**A**) Representative images of excised liver, kidney, spleen and lung from *Apoe*$^{-/-}$ mice fed either a chow or HCD collected 24 h following intraperitoneal injection of PBS or discoidal 30 mol % porphysomes. (**B**) Fluorescence quantified from IVIS images of excised organs expressed as mean radiance (Photons/s/cm^2/sr). Fluorescence imaging experiment conducted on n=1-4 mice/group (PBS, n=1; POR Chow, n=1; POR HCD, n=4). Fluorescence images of PBS, porphysome chow and HCD organs all captured side-by-side in one image frame with the IVIS camera. Data expressed as Mean ± SD. ***P<0.001, ****P<0.0001 by one-way ANOVA with Tukey's multiple comparisons. *In vivo* imaging system, IVIS; s, second; sr, steradian. POR, porphysome.

4.3.3 Determination of the biodistribution of 30 mol % porphysomes using ^{64}Cu-radiolabelling

To determine the biodistribution of 30 mol % ^{64}Cu-radiolabelled porphysomes, they were injected into a cohort of *Apoe*$^{-/-}$ mice fed a chow diet or HCD for 32 weeks. Gamma counts (γ-counts) of ^{64}Cu in the labelled porphysomes were measured after 48 h (Fig 4.4A&C). This revealed that for both the chow and HCD fed mice the highest uptake was by the liver followed by spleen, other abdominal organs and the lung. There were also detectable counts in the heart and aorta of these mice (Fig 4.4A and C). PET imaging captured after 6 hours to visualise the distribution of ^{64}Cu-radiolabelled porphysomes in abdominal organs, with a high amount of activity seen in the liver of both chow and HCD fed mice (Fig 4.4B&D).

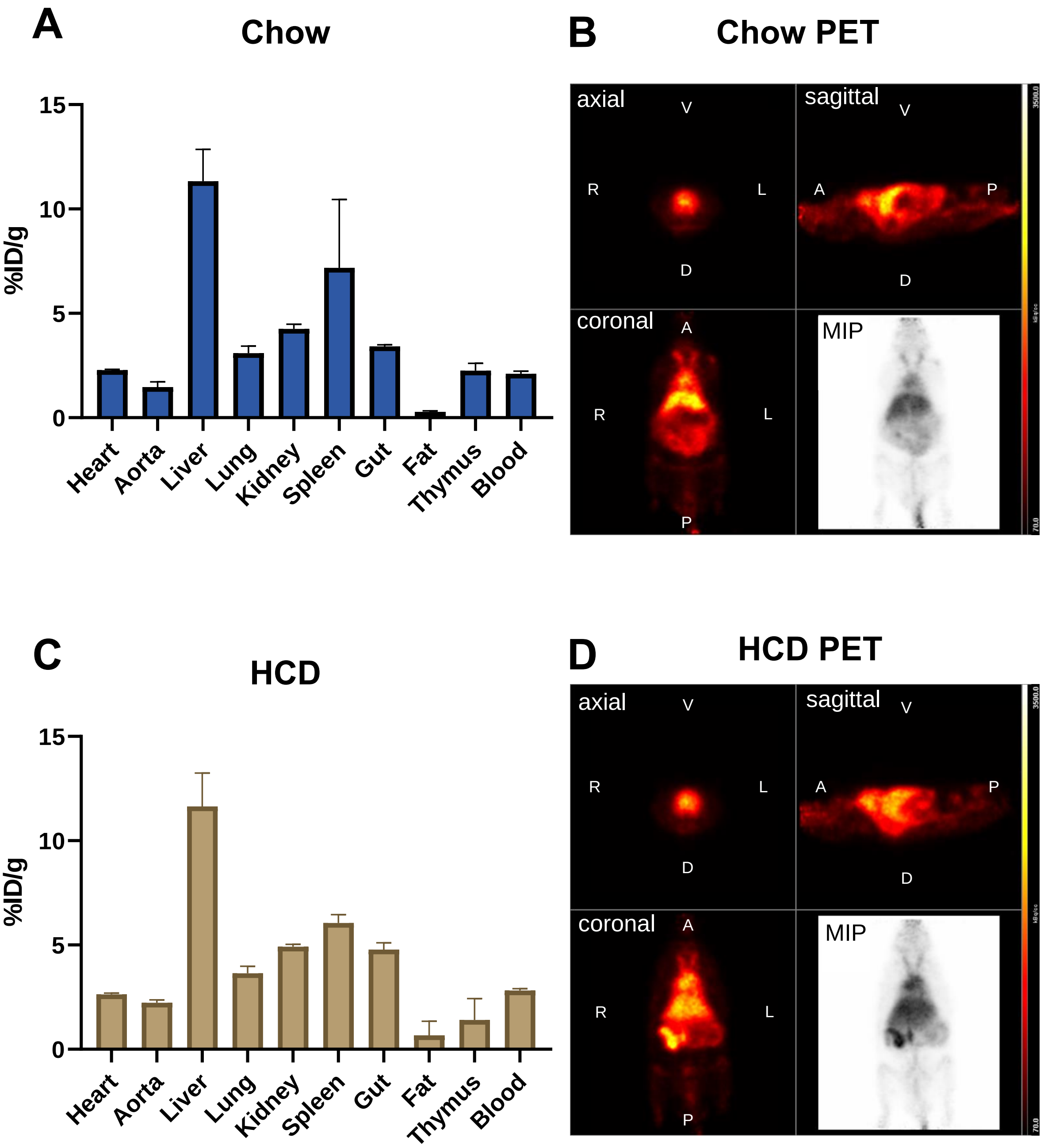
A
Chow
%ID/g
15
10
5
0
Heart
Aorta
Liver
Lung
Kidney
Spleen
Gut
Fat
Thymus
Blood
B
Chow PET
axial
V
R
L
D
sagittal
V
A
P
D
coronal
A
R
L
P
MIP
3500.0
70.0
C
HCD
%ID/g
15
10
5
0
Heart
Aorta
Liver
Lung
Kidney
Spleen
Gut
Fat
Thymus
Blood
D
HCD PET
axial
V
R
L
D
sagittal
V
A
P
D
coronal
A
R
L
P
MIP
3500.0
70.0

Figure legend 4.4: Overall biodistribution of ^{64}Cu-radiolabelled porphysomes in chow or HCD fed *Apoe*$^{-/-}$ mice using γ-counting

γ-counts were taken 48 h post injection of ^{64}Cu-labelled discoidal porphysomes (30 mol % porphyrin-lipid) and expressed as % injected dose per gram (% ID/g) for organs from *Apoe*$^{-/-}$ mice fed either a chow diet (**A**) or HCD (**C**) for 32 weeks. Representative images of PET of mice fed chow (**B**) or HCD (**D**) at 6 h post-injection of ^{64}Cu-porphysomes in axial, sagittal and coronal. Data expressed as Mean ± SD (n=2/group). V, Ventral; D, Dorsal; R, Right; L, Left; A, Anterior; P, Posterior. MIP, Maximal image projection.

4.3.4 The biodistribution of 30 mol % ^{64}Cu-radiolabelled porphysome NPs in *Apoe*$^{-/-}$ mice fed a HCD for 32 weeks indicates increase in uptake in heart but not liver

The γ-counts of the 30 mol % ^{64}Cu-radiolabelled porphysomes in organs/ tissues measured in Fig 4.3 were directly compared between chow and HCD fed *Apoe*$^{-/-}$ mice (Fig 4.5). These comparisons revealed that there was a significantly higher uptake of ^{64}Cu-porphysomes in the heart of HCD-fed mice, compared to chow-fed mice (Fig 4.5A, +15%, $P<0.05$). There was also a non-significant trend indicating higher uptake in the aorta of mice fed the HCD compared to chow (Fig 4.5B, +51%, $P=0.0623$). In addition, there was a significantly higher uptake of ^{64}Cu-porphysomes in both the blood (Fig 4.5C, +34%, $P<0.05$) and gut (Fig 4.5D, +39%, $P<0.05$) in HCD fed mice compared to the chow fed controls. The HCD fed mice also had a non-significant trend towards an increase in uptake in the kidney (Fig 4.5E, +34%, $P=0.0647$). However, in the remaining tissues (spleen, lung, liver, fat, and thymus) there were no observed changes in uptake between the chow and HCD-fed mice (Fig 4.5F-J). Interestingly there was no significant change in liver uptake in the chow and HCD fed mice in this cohort (Fig 4.5H).

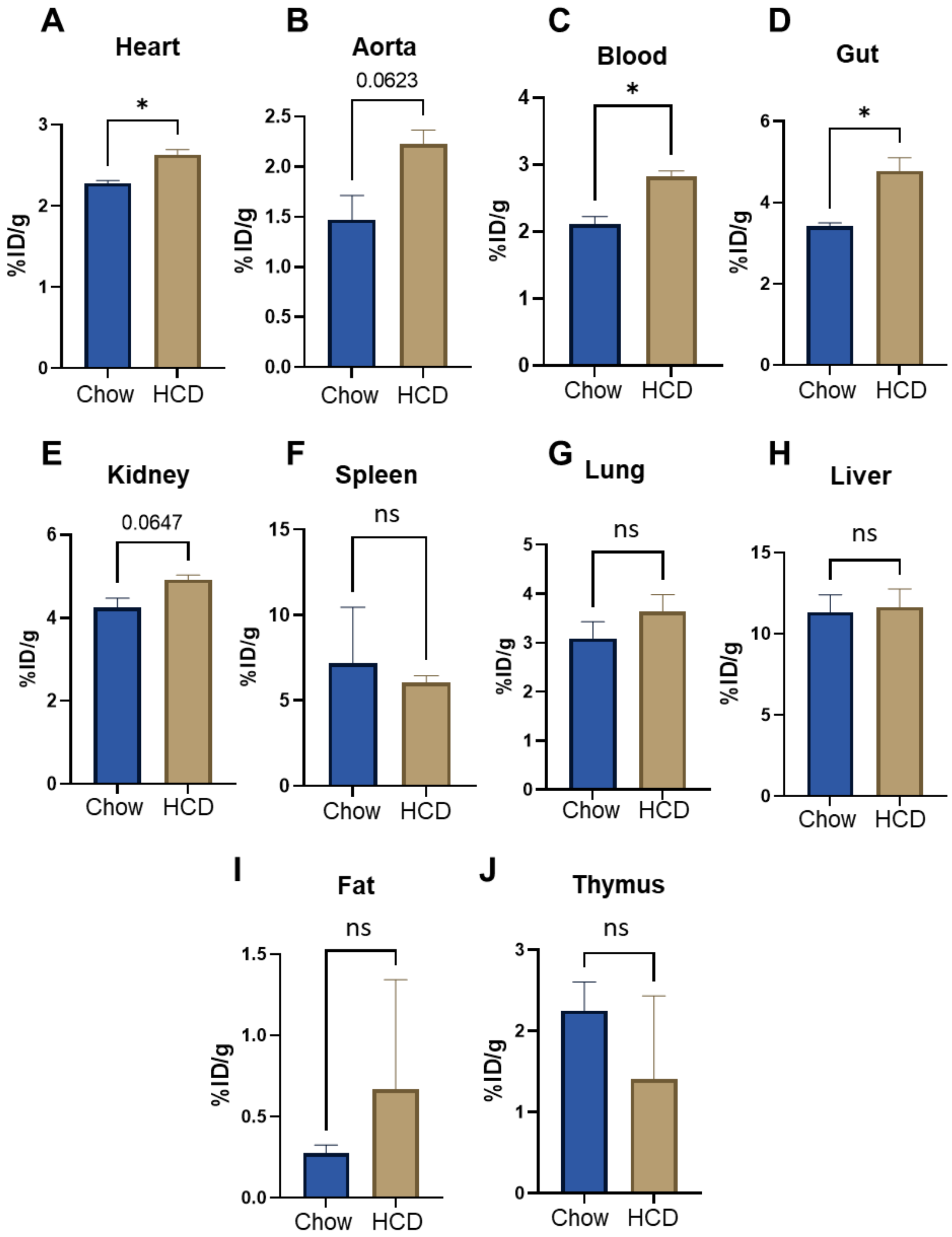
A
Heart
*
%ID/g
0
1
2
3
Chow
HCD
B
Aorta
0.0623
%ID/g
0.0
0.5
1.0
1.5
2.0
2.5
Chow
HCD
C
Blood
*
%ID/g
0
1
2
3
4
Chow
HCD
D
Gut
*
%ID/g
0
2
4
6
Chow
HCD
E
Kidney
0.0647
%ID/g
0
2
4
6
Chow
HCD
F
Spleen
ns
%ID/g
0
5
10
15
Chow
HCD
G
Lung
ns
%ID/g
0
1
2
3
4
5
Chow
HCD
H
Liver
ns
%ID/g
0
5
10
15
Chow
HCD
I
Fat
ns
%ID/g
0.0
0.5
1.0
1.5
Chow
HCD
J
Thymus
ns
%ID/g
0
1
2
3
Chow
HCD

Figure legend 4.5: ^{64}Cu-radiolabelled porphysomes in *Apoe*$^{-/-}$ mice fed either chow diet or HCD

Data from **Fig 4.3** represented with pairwise comparisons of γ-counting from *Apoe*$^{-/-}$ mice fed chow diet or HCD for 32 weeks in heart (**A**), aorta (including the aortic arch and descending aorta) (**B**), blood (**C**), gut (**D**), kidney (**E**), spleen (**F**), lung (**G**), liver (**H**), fat (**I**) and thymus (**J**) expressed as % injected dose per gram (% ID/g). Data expressed as Mean ± SD (n=2/group). not-significant (ns) $P>0.05$, *$P<0.05$ vs chow control by unpaired two-tailed t-test.

4.3.5 PET/MRI imaging reveals some increase in signal in the heart region of mice fed a HCD compared to chow fed mice for 11 weeks

Apoe$^{-/-}$ mice fed a chow or HCD for 11 weeks were subjected to PET imaging which was manually co-registered with MRI to add anatomical information of the thoracic region. Visual inspection of PET/MRI images showed that there was a higher activity in the heart region of mice fed a HCD compared to the chow fed mouse (Fig 4.6A). Semi-quantitative PET analysis of the heart volume of interest (VOI) to determine the ^{64}Cu-porphysome uptake revealed that there was a slight increase in the activity (averaged injected dose per mL, ID/mL) in this region in mice in HCD fed mice compared to the chow fed mice (Fig 4.6B; Chow, 1.33×10^{-2} ID/mL, n=1; HCD, 1.74×10^{-2} ID/mL, n=8). Furthermore, there was a slight increase in the activity in the liver region of HCD fed mice (Fig 4.6C; Chow, 1.63×10^{-2} ID/mL, n=1; HCD, 1.864×10^{-2} ID/mL, n=8).

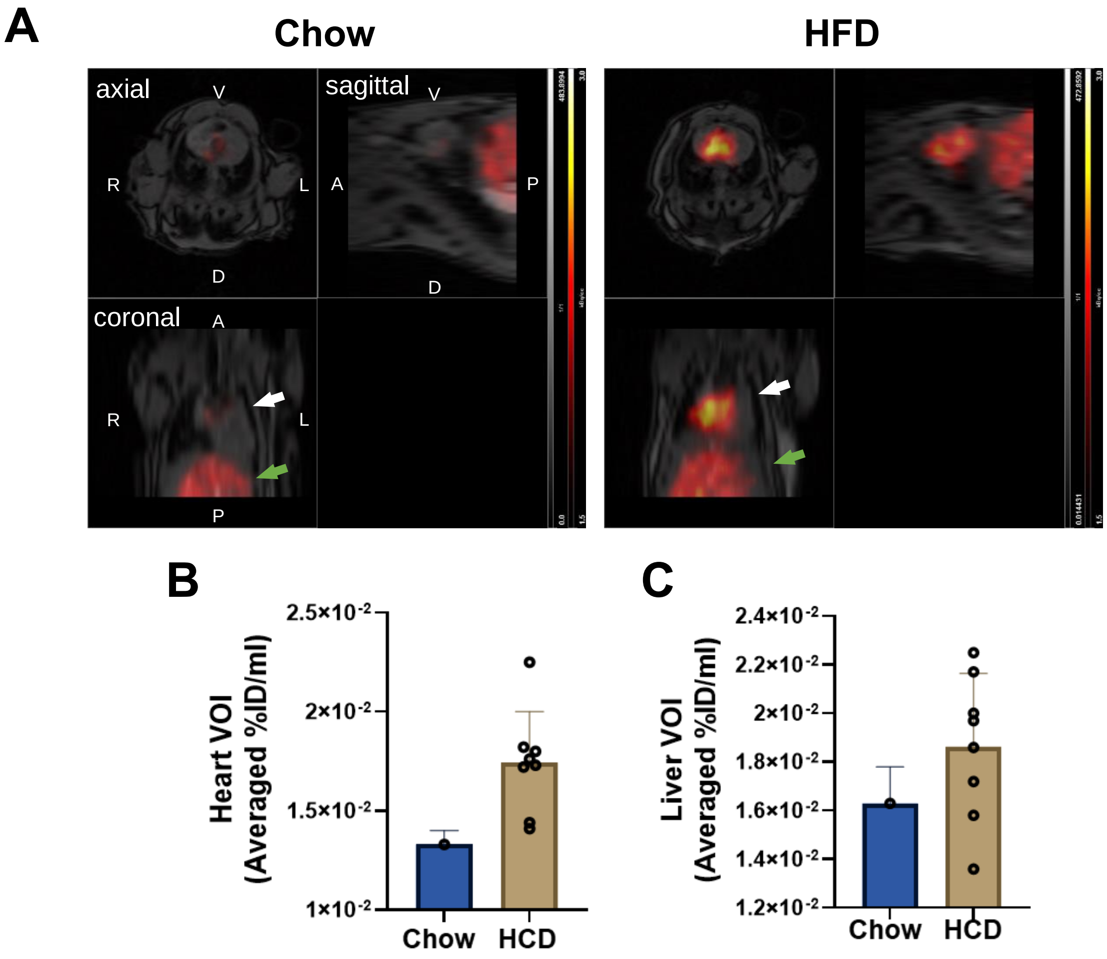
A
Chow
HFD
axial
V
R
L
D
sagittal
V
A
P
D
coronal
A
R
L
P
B
Heart VOI
(Averaged %ID/ml)
2.5×10⁻²
2×10⁻²
1.5×10⁻²
1×10⁻²
Chow
HCD
C
Liver VOI
(Averaged %ID/ml)
2.4×10⁻²
2.2×10⁻²
2×10⁻²
1.8×10⁻²
1.6×10⁻²
1.4×10⁻²
1.2×10⁻²
Chow
HCD

Figure legend 4.6: PET/MRI imaging of ^{64}Cu-porphysomes in *Apoe$^{-/-}$* mice fed chow or HCD

(**A**) Merged PET/MRI images in the axial, sagittal and coronal planes 6 h after intravenous administration of ^{64}Cu-porphysomes in *Apoe*$^{-/-}$ mice fed chow and HCD for 11 weeks. White arrows show signal in the heart region and green arrows show signal in part of the liver region. Volume of interest (VOI) measurements of heart region (**B**) and liver region in chow (n=1) and HCD (n=8) fed mice at week 11 (**C**). Data expressed as Mean ± SD. V, Ventral; D, Dorsal; R, Right; L, Left; A, Anterior; P, Posterior. VOI, volume of interest. ID, Injected Dose.

4.3.6 Porphysomes reduce body weight but have no effect on plasma lipids in HCD fed *Apoe*$^{-/-}$

To study the theranostic effects of porphysomes, *Apoe*$^{-/-}$ mice were treated with both therapeutic R4F nanoparticles (no porphyrin-lipid) three times per week and at two timepoints 4 weeks apart (at week 7 and week 11 of HCD) were injected with 30 mol % ^{64}Cu-porphysomes to image with PET (timeline summarised in Fig 4.7). Prior to sacrifice, mice were injected with an additional dose of the 30 mol % porphysomes. Tissues were examined for flow cytometry and histological analyses for both fluorescence detection (diagnostic properties) and changes in stable atherosclerosis (therapeutic properties). Weight changes were also monitored throughout the course of this study following commencement of treatment. At the beginning, in the first week of treatment, there were no significant differences in the weight of the mice (Fig 4.8A). However, after 4 weeks of treatment (and 8 weeks of HCD), the R4F nanoparticle-treated mice weighed less than the PBS control mice for each week of the remainder of the study (Fig 4.8A, $P<0.01$). Plasma lipid levels were also measured in these mice but there were no significant changes observed in triglycerides, total cholesterol, LDL cholesterol or HDL cholesterol (Fig 4.8B).

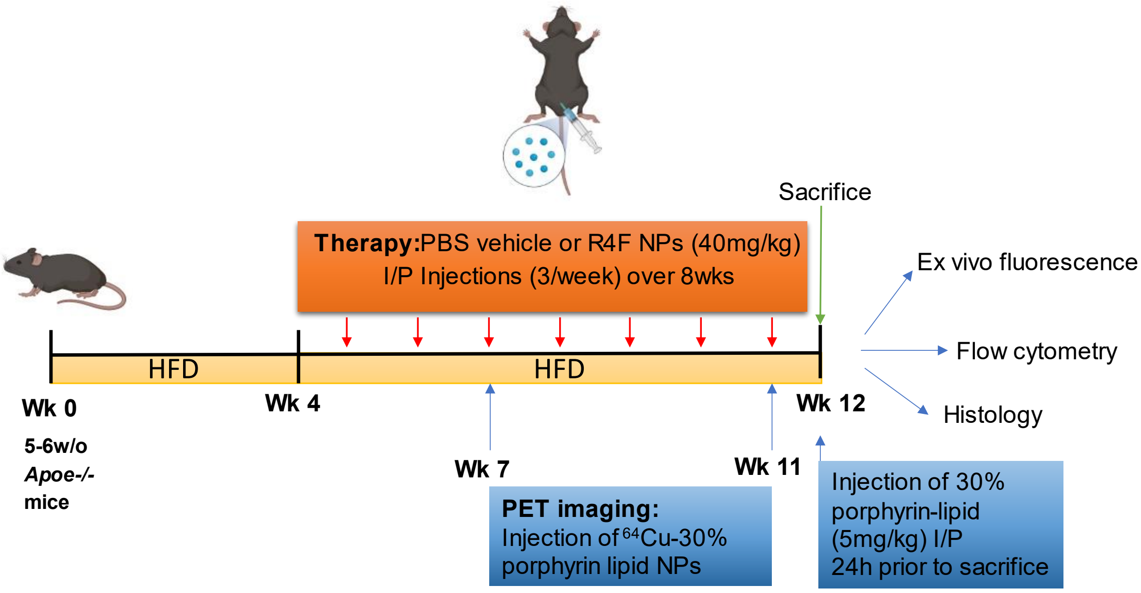
Sacrifice
Therapy:PBS vehicle or R4F NPs (40mg/kg)
I/P Injections (3/week) over 8wks
Ex vivo fluorescence
Flow cytometry
Histology
HFD
HFD
Wk 0
Wk 4
Wk 12
5-6w/o
Apoe-/-
mice
Wk 7
Wk 11
PET imaging:
Injection of ^{64}Cu-30% porphyrin lipid NPs
Injection of 30% porphyrin-lipid (5mg/kg) I/P 24h prior to sacrifice

Figure legend 4.7: Schematic of the treatment and imaging regime for *Apoe*$^{-/-}$ mice to study the theranostic properties of apoA-I linked porphysomes in stable atherosclerosis

Apoe$^{-/-}$ mice were fed a high cholesterol diet to induce stable atherosclerosis formation and administered R4F mimetic-HDL nanoparticles (R4F-NPs) three times per week for 8 weeks via intraperitoneal injection. At week 7 and week 11 of HCD feeding period, mice were injected with ^{64}Cu-porphysomes and 24 h prior to sacrifice 30 mol % porphysomes.

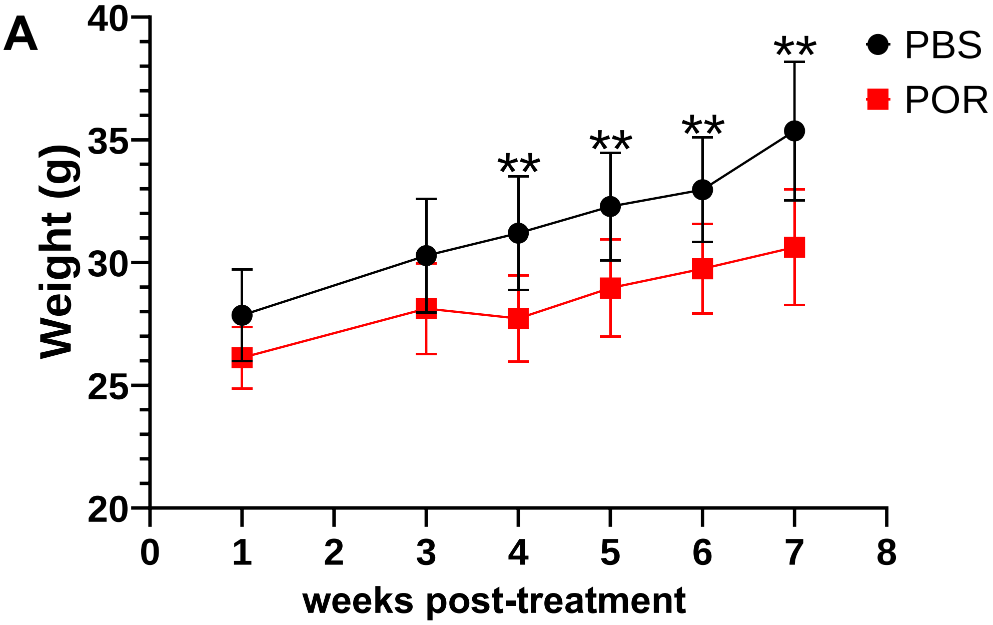

B

Plasma levels	PBS	POR	*P*-value
Triglycerides (mmol/L)	3.82±1.094	3.508±0.9268	0.5601
Cholesterol (mmol/L)	14.07±1.173	15.43±1.512	0.0772
LDL Cholesterol (mmol/L)	13.57±1.252	14.83±1.548	0.1094
HDL Cholesterol (mmol/L)	0.4956±0.2016	0.5904±0.1334	0.2959

Figure legend 4.8: Weight and plasma lipid measures from *Apoe*$^{-/-}$ mice fed a HCD administered PBS or porphysome nanoparticles

(**A**) Weight changes from week 1 to week 7 of treatment period. (**B**) Plasma lipid analysis at sacrifice of triglycerides, total cholesterol, LDL cholesterol and HDL cholesterol. Data expressed as mean ± SD (n=7-8). ***P*<0.01 vs PBS control by unpaired two-tailed t-test. POR, porphysome.

4.3.7 Fluorescent porphyrin-lipid detection in aortic cells of *Apoe*$^{-/-}$ mice by flow cytometry

Flow cytometry was conducted on aortic digests from HCD-fed *Apoe*$^{-/-}$ mice to determine whether the porphysome porphyrin-lipid fluorescence could be detected in individual aortic cells. This involved digesting the entire descending aorta and staining with antibodies for different cell markers (Fig 4.9A). To gate the cells, viable single cells were selected with the porphyrin-lipid^{+} cells (on the AF647 channel) and the cell type markers used to determine the proportion of uptake in different aortic cell types (Fig 4.9B). Firstly, there were no changes in the proportion of viable cells between the PBS and porphysome treated mice (Fig 4.9C). When the total proportion of porphyrin lipid positive cells of the total viable cells was measured for each group the porphyrin-lipid could only be detected in the porphysome treated mice and there were no porphyrin-lipid positive cells in the aortas of the PBS control mice (Fig 4.9D). Of the porphysome-treated mice, when comparing the different cell markers found on the porphyrin-lipid positive cells, the highest proportion were detected in the macrophage population (~53%) compared to the monocyte (~19%), endothelial cell (~27%) and smooth muscle cell (~18%) populations (Fig 4.9E). Furthermore, of the porphyrin-lipid positive cells, the predominant macrophage subtype population was M2 as compared to M1 (Fig 4.9E, ~0.15% vs ~51%, $P<0.001$).

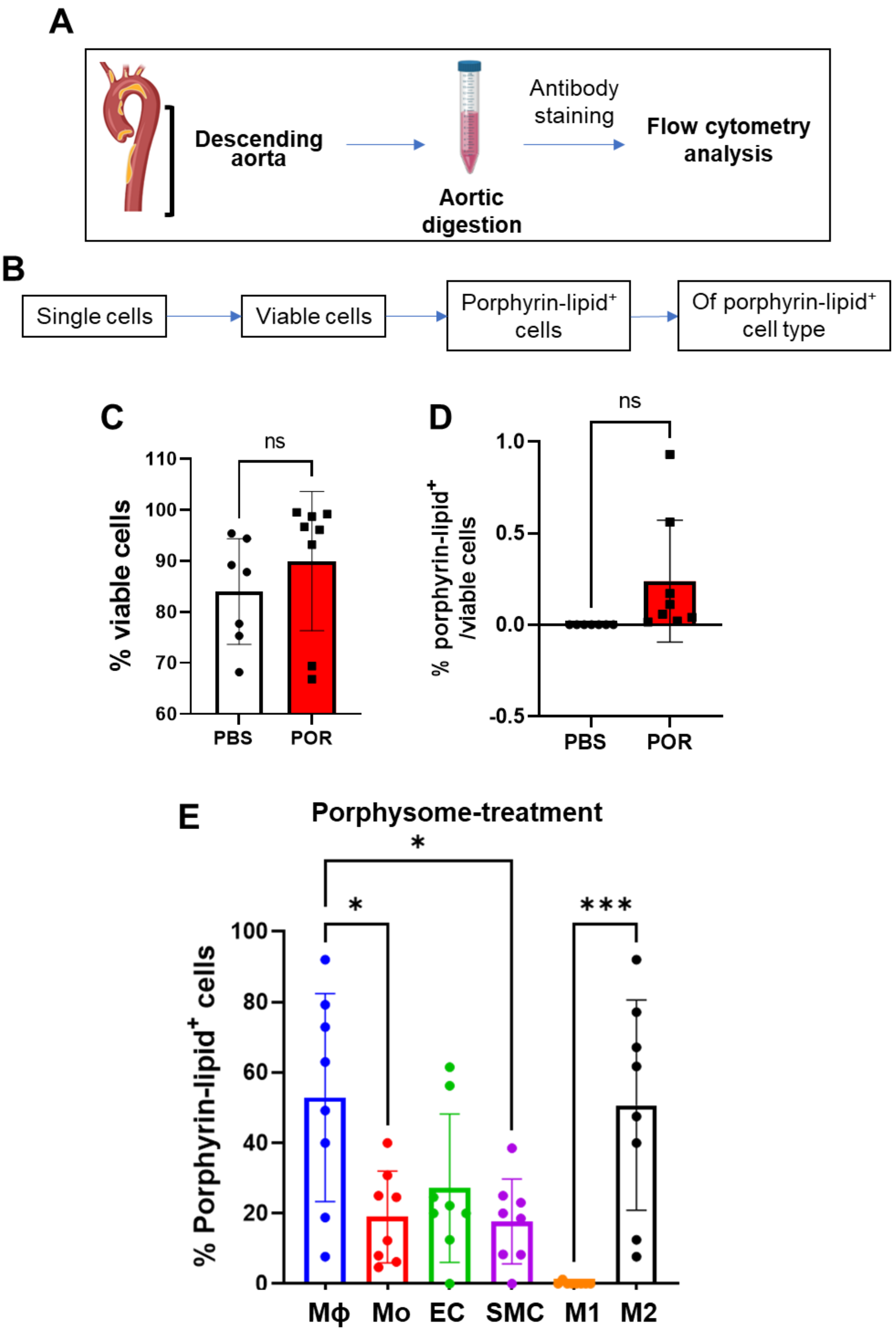
A
Descending aorta
Aortic digestion
Antibody staining
Flow cytometry analysis
B
Single cells
Viable cells
Porphyrin-lipid$^+$ cells
Of porphyrin-lipid$^+$ cell type
C
% viable cells
110
100
90
80
70
60
ns
PBS
POR
D
% porphyrin-lipid$^+$ /viable cells
1.0
0.5
0.0
-0.5
ns
PBS
POR
E
Porphysome-treatment
% Porphyrin-lipid$^+$ cells
100
80
60
40
20
0
*
*
***
Mϕ
Mo
EC
SMC
M1
M2

Figure legend 4.9: Flow cytometry can be used to detect the porphyrin-lipid from porphysomes in aortic cells from porphysome treated HCD fed *Apoe*$^{-/-}$ mice

(**A**) The workflow showing summarizing the method used to isolate aortic cells from the descending aorta. (**B**) The gating strategy to measure proportion of porphyrin-lipid^{+} cells and the aortic cell type. (**C**) Proportion of viable cells from PBS and porphysome treated mice. (**D**) Proportion of porphyrin-lipid positive cells of viable cells. (**E**) Proportion of porphyrin lipid^{+} cell type of the total porphyrin-lipid^{+} cells. Mϕ, macrophages; Mo, Monocytes; EC, endothelial cells; SMC, smooth muscle cells; M1/M2 macrophages. Data expressed as mean ± SD (n=7-8). **C**-**D**: not-significant (ns) *P*>0.05 vs PBS control by unpaired two-tailed t-test. **E**: **P*<0.05, ****P*<0.001, *****P*<0.0001 by one-way ANOVA with Tukey’s multiple comparisons. POR, porphysome.

4.3.8 Aortic cells from HCD fed *Apoe*$^{-/-}$ mice uptake porphysomes with a higher proportion of porphyrin-lipid cells in aortic macrophages

A second approach to flow cytometric analysis was used to determine the proportion of porphyrin-lipid positive cells after gating for the different aortic cell type markers (Fig 4.10A). For each cell type, the aortas from porphysome-treated mice were compared to the PBS control mice and the proportion of porphyrin lipid positive cells measured. For all cell types there were no porphyrin-lipid positive cells (detected on the AF647 channel) in the PBS treated mice which indicates that the detection method is specific for porphyrin-lipid fluorescence (Fig 4.10B-G). There was a significantly higher proportion of porphyrin-lipid positive cells in the porphysome treated mice, compared to the PBS control mice for aortic macrophages (Fig 4.10B, $P<0.0001$) and monocytes (Fig 4.10C, $P<0.01$). Furthermore, there was also a significantly higher proportion of porphyrin-lipid positive aortic endothelial cells (Fig 4.10D, $P<0.01$) and smooth muscle cells (Fig 4.10E, $P<0.05$) in porphysome-NP treated mice compared to PBS control mice. We also examined if there were any differences in the proportion of porphyrin-lipid positive cells in aortic M1 and M2 macrophage subtypes. Although there was no change in aortic M1 macrophages (Fig 4.10F), there was a significantly higher proportion of porphyrin-lipid positive M2 macrophages in the porphysome treated mice (Fig 4.10G, $P<0.01$). When the different cell type populations were compared from porphysome treated mice, the highest proportion of porphyrin-lipid positive cells were found in the macrophage population (~9%) as compared to the monocyte (~1.8%), endothelial (~0.09%) and smooth muscle (~2%) cell populations (Fig 4.10H, $P<0.0001$). Overall, this indicates that porphysome NPs are primarily taken up by aortic macrophages *in vivo* compared to other vascular cell types.

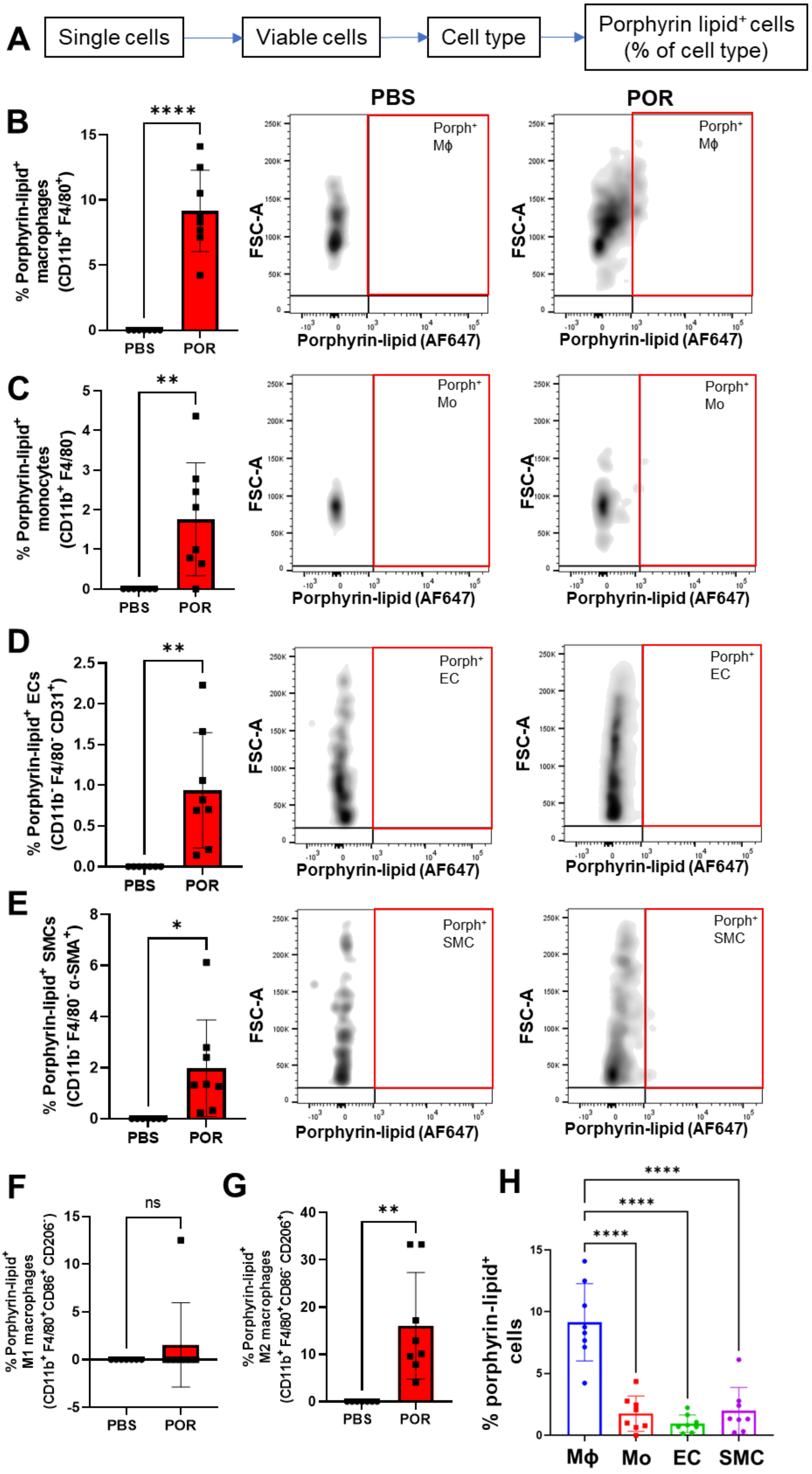
A
Single cells
Viable cells
Cell type
Porphyrin lipid+ cells (% of cell type)
B
% Porphyrin-lipid+ macrophages (CD11b+ F4/80+)
****
PBS
POR
PBS
POR
Porph+ Mϕ
FSC-A
Porphyrin-lipid (AF647)
C
% Porphyrin-lipid+ monocytes (CD11b+ F4/80-)
**
Porph+ Mo
D
% Porphyrin-lipid+ ECs (CD11b- F4/80- CD31+)
**
Porph+ EC
E
% Porphyrin-lipid+ SMCs (CD11b- F4/80- α-SMA+)
*
Porph+ SMC
F
% Porphyrin-lipid+ M1 macrophages (CD11b+ F4/80+CD86+ CD206-)
ns
G
% Porphyrin-lipid+ M2 macrophages (CD11b+ F4/80+CD86- CD206+)
**
H
% porphyrin-lipid+ cells
****
****
****
Mϕ
Mo
EC
SMC

Figure legend 4.10: Flow cytometric analysis of the descending aorta of HCD fed *Apoe*$^{-/-}$ mice reveals higher proportion of uptake of porphyrin-lipid in macrophages compared to other aortic cell types

(**A**) Strategy to gate the cell type prior to identifying proportion of porphyrin-lipid cells for each aortic cell type. Graphs and representative flow density plots of proportion of porphyrin-lipid^{+} cells for macrophages (**B**), monocytes (**C**), endothelial cells (**D**), smooth muscle cells (**E**), M1 macrophages (**F**) and M2 macrophages (**G**). Summary of proportion of porphyrin-lipid^{+} cells in porphysome treated mice (**H**). Data expressed as mean ± SD (PBS, n=7; POR, n=8). **B-G**: not-significant (ns) $P>0.05$, *$P<0.05$, **$P<0.01$, ****$P<0.0001$ vs PBS control by unpaired two-tailed t-test. **H**: ****$P<0.0001$ vs Mϕ by one-way ANOVA with Tukey’s multiple comparisons. Mϕ, macrophages; Mo, Monocytes; EC, endothelial cells; SMC, smooth muscle cells. POR, porphysome.

4.3.9 Porphysome detection in CD68$^+$ macrophage regions of plaque in the aortic sinus of *Apoe*$^{-/-}$ mice administered porphysomes

To confirm porphysome uptake was localised to areas of plaque, we conducted histological analysis on the aortic sinus of mice fed a HCD using fluorescence microscopy. This involved immunohistochemical staining of CD68$^+$ macrophages within the plaque region. The majority of the CD68$^+$ macrophages were found localised towards the luminal region of the plaques in both PBS and porphysome-treated mice (Fig 4.11). However, porphyrin-lipid could only be clearly detected in porphysome-treated mice within the plaque of the aortic sinus, particularly in the shoulder and luminal-facing regions of the plaque (Fig 4.11). Furthermore, the porphyrin-lipid fluorescence was primarily co-localised to regions of CD68$^+$ macrophages in the plaque, indicating that porphysomes accumulate in macrophage-rich regions.

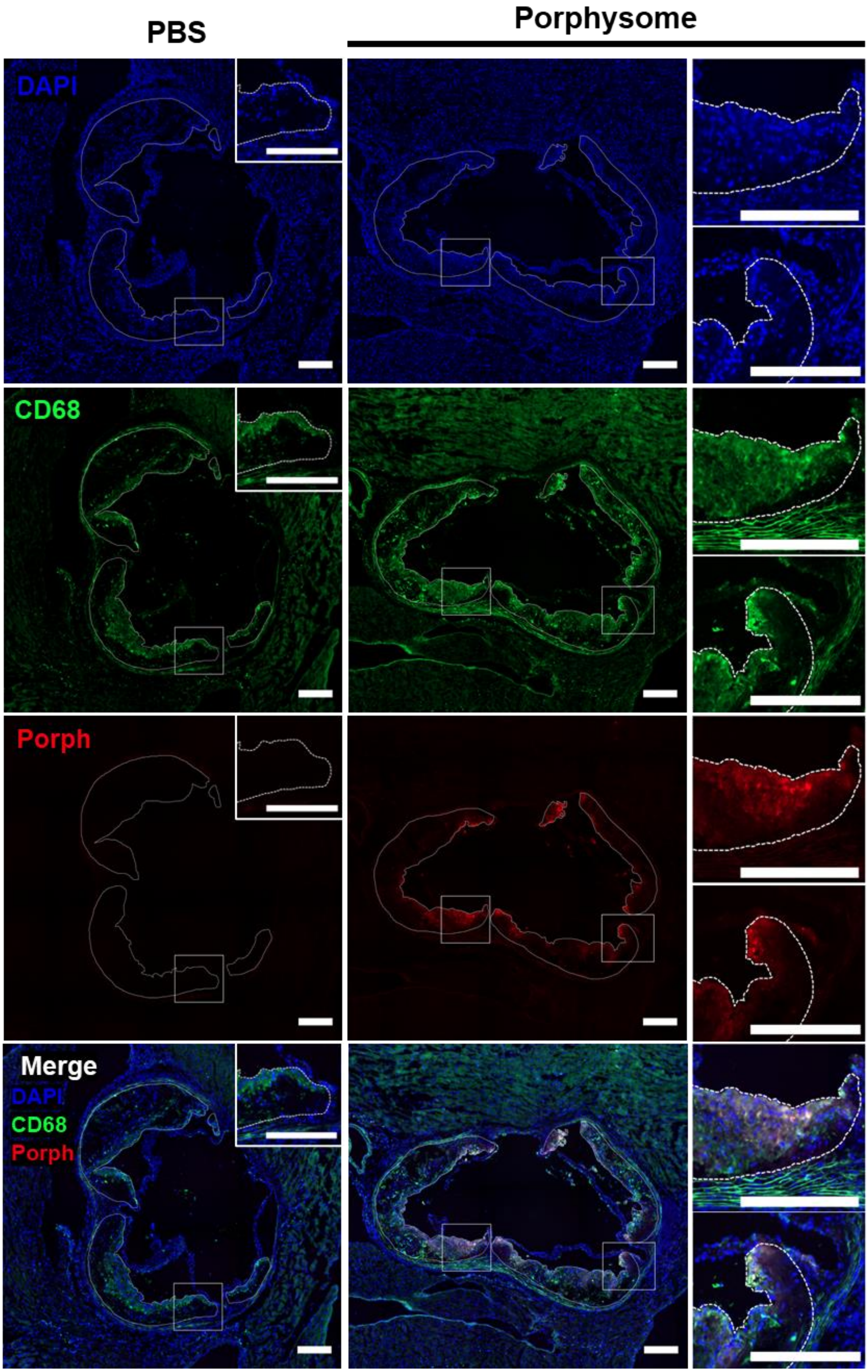
PBS
Porphysome
DAPI
CD68
Porph
Merge
DAPI
CD68
Porph

Figure legend 4.11: Representative fluorescence images of plaque in the aortic sinus of HCD fed *Apoe*$^{-/-}$ mice shows detection of porphyrin-lipid in CD68^{+} macrophage regions in mice administered porphysomes

Apoe$^{-/-}$ mice were fed a HCD for 13 weeks with alternate day intraperitoneal injections of PBS or Discoidal HDL-mimetic particles and 24 h prior to sacrifice were injected intravenously with 30 mol % porphysomes or PBS. Aortic sinus sections were stained for **CD68** (green) and **DAPI** to detect the cell nuclei (blue). Porphyrin-lipid (**Porph**) was detected within sections using Cy5-filter (red). Dashed white lines indicate plaque area. Scale bar = 200 µm.

4.3.10 ^{64}Cu-Porphysomes can be longitudinally imaged in the heart region of *Apoe*$^{-/-}$ mice

We also sought to determine whether ^{64}Cu-labelled porphysomes could be used to track uptake to areas of plaque deposition and whether this could be imaged over two timepoints. PET/MRI imaging of *Apoe*$^{-/-}$ fed a HCD demonstrated that there was a visible increase in activity in the heart region of these mice at the latter timepoint at week 11 compared to the earlier timepoint of week 7 (Fig 4.12A). In addition, when this was manually quantified from the PET data, there was a slight but significant increase in activity in the heart VOI of these mice from week 7 to week 11 (Fig 4.12B; Wk 7, $1.42\text{x}10^{-2}$ ID/mL, n=6; Wk 11, $1.741\text{x}10^{-2}$ ID/mL, n=8; $P<0.05$). However, there was no significant change in activity the liver VOI analysed (Fig 4.12C; Wk 7, $1.567\text{x}10^{-2}$ ID/mL, n=6; Wk 11, $1.864\text{x}10^{-2}$ ID/mL, n=8).

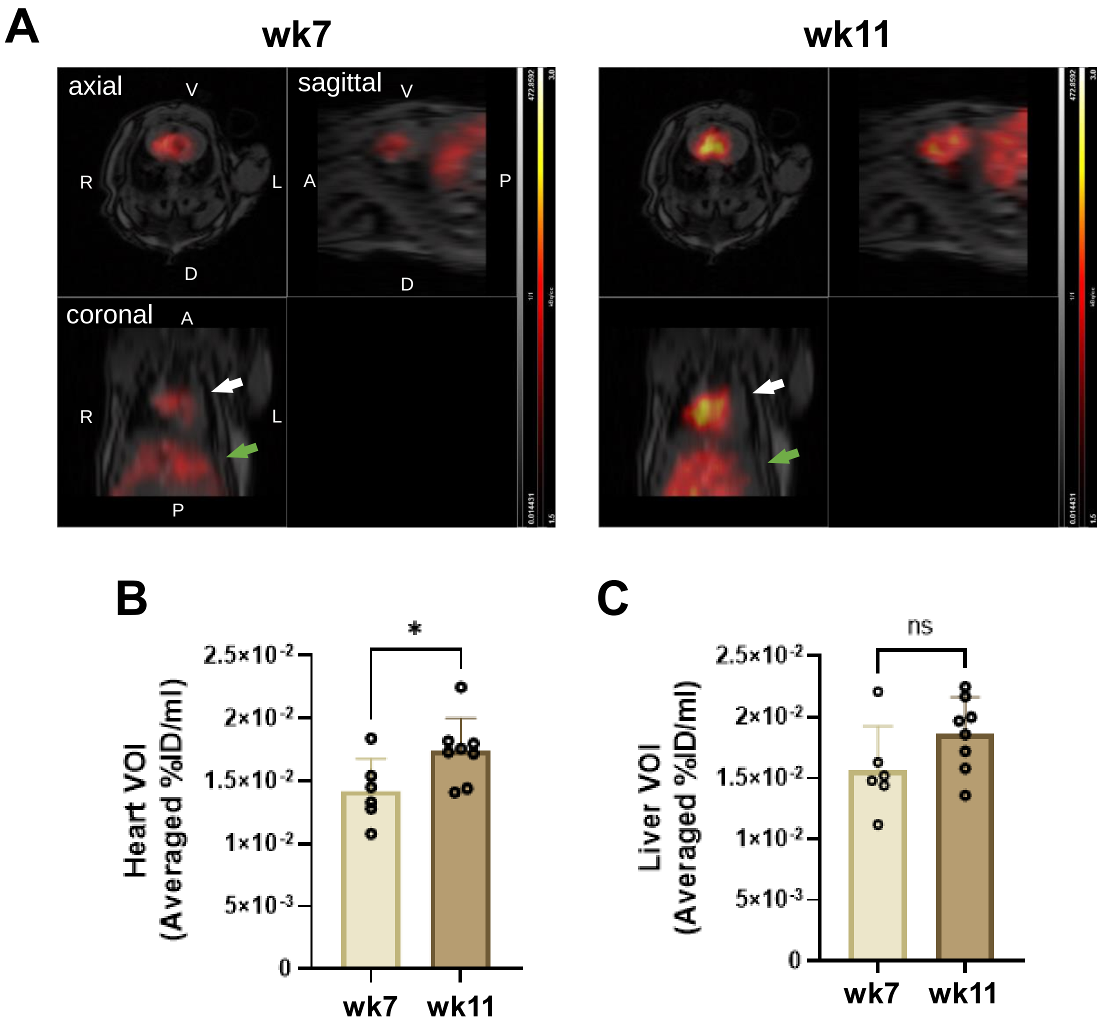
A
wk7
wk11
axial
V
R
L
D
sagittal
V
A
P
D
coronal
A
R
L
P
472.8592
0.014431
B
*
Heart VOI
(Averaged %ID/ml)
2.5×10-2
2×10-2
1.5×10-2
1×10-2
5×10-3
0
wk7
wk11
C
ns
Liver VOI
(Averaged %ID/ml)
2.5×10-2
2×10-2
1.5×10-2
1×10-2
5×10-3
0
wk7
wk11

Figure legend 4.12: Longitudinal PET/MRI imaging of ^{64}Cu-porphysomes in HCD fed *Apoe*$^{-/-}$ mice at week 7 and week 11

(**A**) Merged PET/MRI images in the axial, sagittal and coronal planes in HCD fed *Apoe*$^{-/-}$ mice and at week 7 and week 11, 6 h after intravenous administration of ^{64}Cu-porphysomes. White arrows show signal in the heart region and green arrows show signal in part of the liver region. VOI measurements of heart region (**B**) and liver region (**C**) in HCD fed mice at week 7 (n=6) and week 11 (n=8). V, Ventral; D, Dorsal; R, Right; L, Left; A, Anterior; P, Posterior. ID, Injected Dose. MRI image from week 11 timepoint. Data expressed as mean ± SD. not-significant (ns) $P>0.05$, $^*P<0.05$ vs wk7 by unpaired two-tailed t-test.

4.3.11 Porphysome treatment did not affect aortic sinus plaque size, collagen, lipid, α-SMA$^+$ smooth muscle cells or CD68$^+$ macrophage content in HCD fed *Apoe*$^{-/-}$ mice

The aortic sinus plaques were further analysed to determine changes in lesion size and composition. Aortic sinus sections from *Apoe*$^{-/-}$ mice administered either PBS or R4F-nanoparticles/ porphysome nanoparticles (POR) were stained for H&E, Masson's trichrome, oil-red O. Immunohistochemistry was also used to detect smooth muscle cells (α-SMA) and macrophages (CD68) (Fig 4.13A). Negative and IgG controls were used to confirm specific immunohistochemistry detection of α-SMA and CD68 respectively (Fig 4.13A). Subsequent quantification of lesion size (Fig 4.13B), plaque collagen (Fig 4.13C) and plaque lipid content (ORO$^+$ area, Fig 4.13D) found no significant changes between the PBS and porphysome-treated mice. Within the plaque area there were also no changes in CD68$^+$ macrophage (Fig 4.13E) or α-SMA$^+$ smooth muscle cell content (Fig 4.13F).

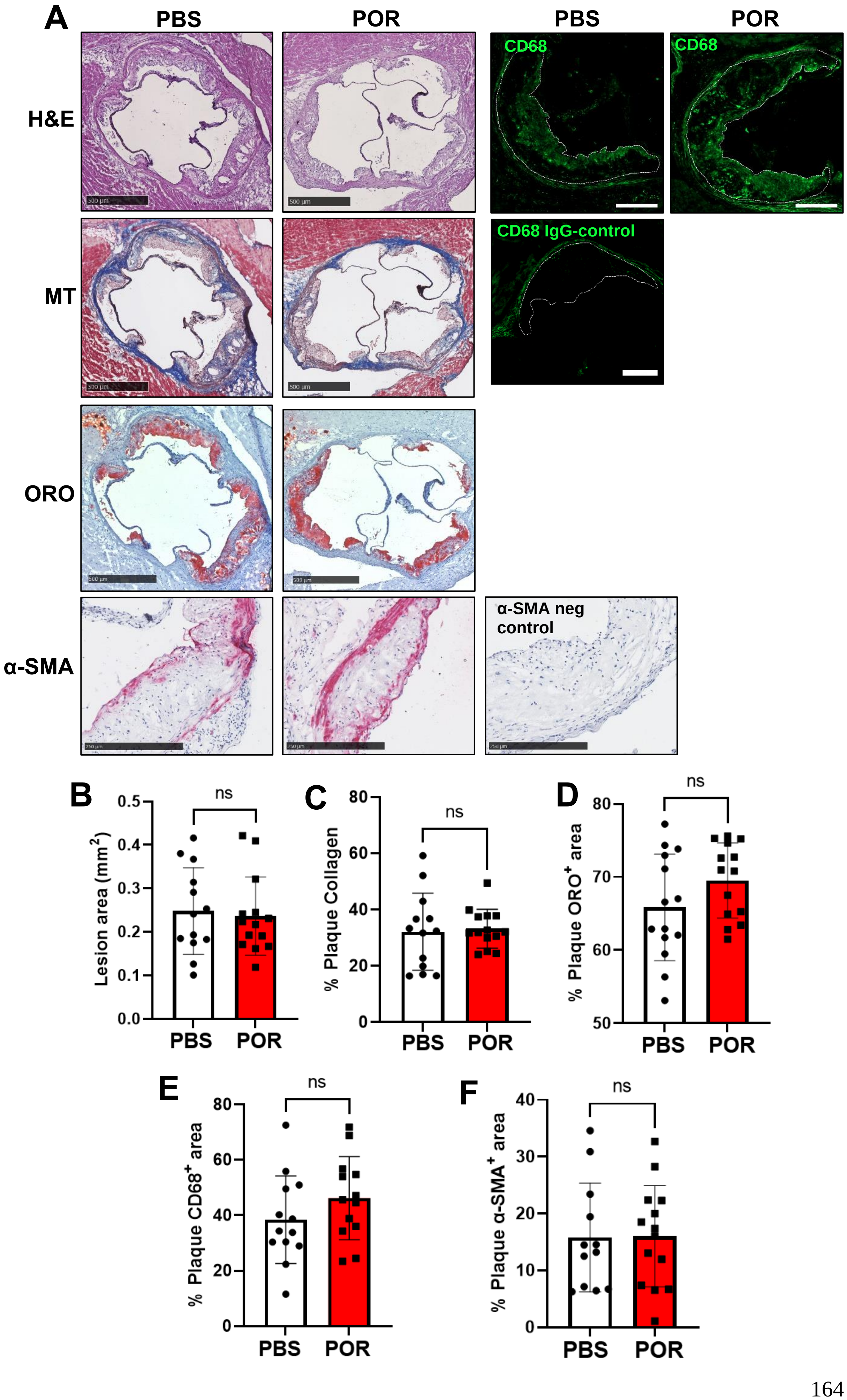
A
PBS
POR
PBS
POR
H&E
CD68
CD68
500 µm
500 µm
MT
CD68 IgG-control
500 µm
500 µm
ORO
500 µm
500 µm
α-SMA
α-SMA neg control
250 µm
250 µm
250 µm
B
Lesion area (mm²)
0.0
0.1
0.2
0.3
0.4
0.5
ns
PBS
POR
C
% Plaque Collagen
0
20
40
60
80
ns
PBS
POR
D
% Plaque ORO⁺ area
50
60
70
80
ns
PBS
POR
E
% Plaque CD68⁺ area
0
20
40
60
80
ns
PBS
POR
F
% Plaque α-SMA⁺ area
0
10
20
30
40
ns
PBS
POR

Figure legend 4.13: Histological analysis of stable atherosclerotic lesions in the aortic sinus of *Apoe*$^{-/-}$ mice fed a HCD for 13 weeks

(**A**) Representative images of aortic sinus stained with Hematoxylin and Eosin (H&E) for plaque morphology, Masson's Trichrome (MT) for collagen, oil red O (ORO) for lipid content and immunohistochemistry to detect smooth muscle alpha-actin (α-SMA) and CD68 with respective negative (neg) and IgG controls. (**B**) Lesion area quantified from H&E-stained sinus. (**C**) % plaque collagen quantified from MT staining. (**D**) % ORO positive plaque area (ORO^{+}) quantified. (**E**) Quantification of % CD68^{+} area of the total plaque area. (**F**) % α-SMA positive plaque area (α-SMA^{+}) quantified. Data expressed as mean ± SD (n=12-14/group). not-significant (ns) $P>0.05$ vs PBS control by unpaired two-tailed t-test. Dashed white lines indicate plaque area. Scale bar: H&E, MT and ORO = 500 µm, α-SMA = 250 µm and CD68 = 200 µm. POR, Porphysome.

4.3.12 Changes in aortic cell types observed in *Apoe*$^{-/-}$ mice treated with porphysome NPs compared to PBS control mice

Changes in different aortic cell types were also measured by flow cytometry between both the PBS and porphysome treated mice (Fig 4.14A). This was achieved by comparing the proportion of aortic cell types (macrophages, monocytes, M1/M2 macrophages, endothelial and smooth muscle cells) in each group as well as TREM2^{+} macrophages and monocytes. TREM2 has been found to be expressed in foamy macrophages and only in plaque, not healthy aorta [150]. There was a non-significant trend observed for a reduction in the proportion of aortic macrophages (CD11b^{+} F4/80^{+}) with porphysome treatment (Fig 4.14B, -49%, P=0.1080), compared to PBS. In comparing changes in the macrophage subtypes, it appeared that the majority of this reduction occurred in the M2 macrophage population (Fig 4.14C, -60%, P=0.0787) and not the M1 macrophage population in which there were no obvious changes between groups (Fig 4.14D). Furthermore, aortic monocytes (CD11b^{+} F4/80^{-}) were measured but there were no observed changes in porphysome treated mice (Fig 4.14E). There were no significant changes to the proportion of endothelial or smooth muscle cells between the two treatment groups (Fig 4.14 F&G). TREM2^{+} macrophages and monocytes were also measured, which showed a non-significant trend in reduction of aortic TREM2^{+} macrophages in the porphysome treated mice (Fig 4.14H, -50%, P=0.1320). However, there was no significant reduction in the proportion of aortic TREM2^{+} monocytes in the porphysome treated mice as compared to PBS control mice (Fig 4.14I)

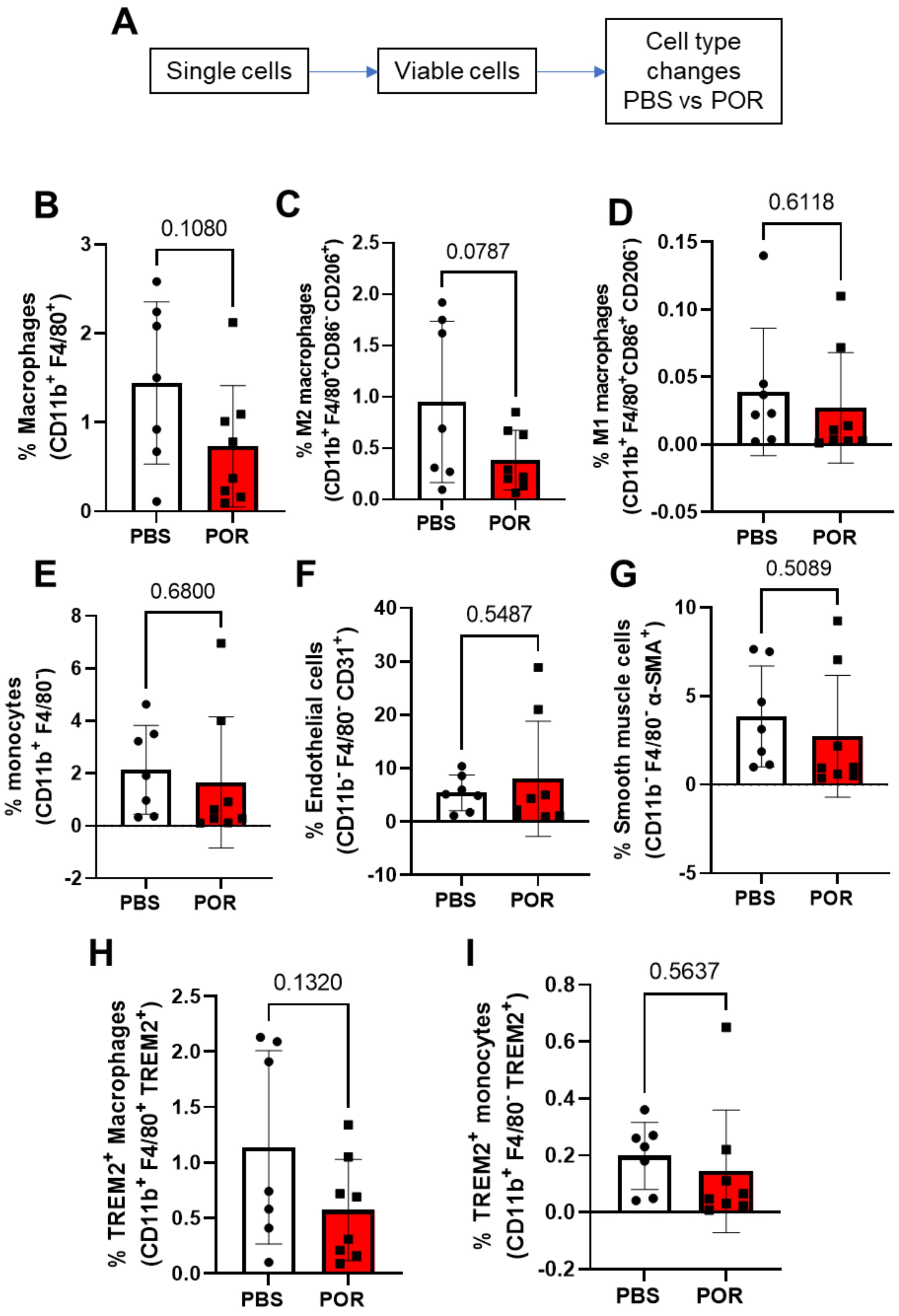
A
Single cells
Viable cells
Cell type changes PBS vs POR
B
% Macrophages (CD11b+ F4/80+)
0.1080
PBS
POR
C
% M2 macrophages (CD11b+F4/80+CD86- CD206+)
0.0787
PBS
POR
D
% M1 macrophages (CD11b+F4/80+CD86+CD206-)
0.6118
PBS
POR
E
% monocytes (CD11b+ F4/80-)
0.6800
PBS
POR
F
% Endothelial cells (CD11b- F4/80- CD31+)
0.5487
PBS
POR
G
% Smooth muscle cells (CD11b- F4/80- α-SMA+)
0.5089
PBS
POR
H
% TREM2+ Macrophages (CD11b+ F4/80+ TREM2+)
0.1320
PBS
POR
I
% TREM2+ monocytes (CD11b+ F4/80- TREM2+)
0.5637
PBS
POR

Figure legend 4.14: Flow cytometry to determine changes in proportion of aortic cell types in PBS and porphysome treated HCD fed *Apoe*$^{-/-}$ mice

(**A**) Gating strategy of different aortic cell types to compare PBS and porphysome (POR) treatment groups. Changes between PBS and POR treated mice in flow cytometric markers for: macrophages (**B**), M2 macrophages (**C**), M1 macrophages (**D**), monocytes (**E**), endothelial cells (**F**), smooth muscle cells (**G**), TREM2^{+} macrophages and (**H**) TREM2^{+} monocytes (**I**). Data expressed as mean ± SD (n=7-8/group). not-significant (ns) P>0.05 vs PBS control by unpaired two-tailed t-test.

4.4 Discussion

In this chapter, we established the diagnostic and therapeutic properties of porphysome nanoparticles in a stable atherosclerosis model *in vivo* investigating their therapeutic and diagnostic properties. The overall findings from this work have demonstrated robustly detectable accumulation of porphysomes in areas of plaque deposition using both fluorescence/ PET imaging modalities. This accumulation was shown to be most likely a result of plaque macrophage uptake. There were, however, no significant changes in atherosclerotic plaque size or composition in these mice following infusions of the therapeutic porphyrin-lipid free particles.

The benefits of using porphysomes for imaging is that the integrated porphyrin-lipid removes the need for additional fluorophores to be conjugated to the particles [85, 89, 151]. The NIR fluorescence properties of porphysomes therefore can be detected *in vivo*. We detected a higher porphyrin-lipid fluorescence signal in the aortic arch of atherosclerotic HCD *Apoe*$^{-/-}$ mice *ex vivo*, compared to the chow-fed control which indicates specific uptake in a region of atherosclerotic plaque deposition. In contrast, there were no differences in the descending aorta. This likely reflects the lower level of plaque deposition in this region following 12 weeks on HCD, when compared to the aortic arch [152]. In agreement with the observed fluorescence found in the aortic arch, we also observed porphyrin-lipid fluorescence in the plaque of the aortic sinus. The aortic sinus is one of the earliest sites to develop plaque in HCD fed *Apoe*$^{-/-}$ mice [152, 153] and interestingly the porphyrin-lipid fluorescence was only detected specifically in the plaque and was not in the surrounding myocardial tissue. Furthermore, PET imaging indicated that there was a higher ^{64}Cu-porphysome presence in the heart region in atherosclerotic HCD *Apoe*$^{-/-}$ mice compared to the chow-fed control after 11 weeks. In agreement with the imaging data, the γ-counting of the heart and aorta indicated an increased uptake in mice fed HCD for 32 weeks with advanced, established plaque, compared to the chow-fed mice. Overall, this suggests specific uptake of porphysomes within stable atherosclerotic plaque *in vivo*.

It was revealed with *ex vivo* γ-counting and fluorescence imaging, that the 30 mol %-porphysomes primarily localised to the liver in both chow and HCD fed mice. This is consistent with a distribution profile of HDL-mimetic nanoparticles, and apoA-I porphysomes in an ovarian cancer model, where uptake was also highest in the liver [89]. This suggests that the porphysomes in this model of atherosclerosis are processed via hepatic clearance mechanisms and similar to HDL, may also avoid rapid clearance via the mononuclear phagocyte system [58, 89]. Moreover, it was expected that there would be a considerable uptake of the nanoparticles within the liver of the mice as SR-BI, thought to be the primary receptor target of the R4F peptide [90], is also expressed on hepatocytes where it participates in reverse cholesterol transport (RCT) to remove cholesterol from the circulation [24, 112]. The *ex vivo* fluorescence measure of the porphysomes after 12 weeks of diet indicated that there was an increase in the uptake in the liver in the atherosclerotic HCD fed mice compared to the chow-fed control. HCD causes pleiotropic effects in *Apoe*$^{-/-}$ mice. It can increase lipid deposition, inflammation and fibrosis in the liver [154], which may explain the increased uptake of porphysomes in the HCD-fed mice. In contrast, in the 32-week diet cohort measured by γ-counting there was no observed differences in liver uptake in the HCD and chow-fed mice. This is likely due to the longer HCD feeding period for this cohort. In addition, the *ex vivo* fluorescence of the tissues was only measured on a single chow-fed mouse, therefore may require further investigation of HCD on nanoparticle distribution in *Apoe*$^{-/-}$ mice.

We also investigated the uptake of porphysomes in aortic cells using flow cytometry. As the porphyrin-lipid found in porphysomes is fluorescent in the near infrared (NIR) range, we could detect the particles by the presence of the porphyrin fluorescent signal of the cells. Previously ApoE3 porphyrin-lipid conjugated particles have been detected *in vitro* with flow cytometry [99] but we decided to measure uptake *in vivo* in the cells of the aorta harvested from *Apoe*$^{-/-}$ mice, which has been used with other nanoparticles targeting atherosclerosis [52, 56, 103]. Of the aortic cell populations examined, it was found that the macrophage population had the highest proportion of porphyrin-lipid positive cells as compared to monocytes, endothelial and smooth muscle cells. This is consistent with the histological observations that the porphyrin-lipid fluorescence was detected in the CD68^{+} macrophage-rich region in the plaque of the aortic sinus, indicating that these particles are taken up by plaque macrophages. Uptake in M1 and M2 macrophages was also examined using flow cytometry, which demonstrated that porphysome NPs were preferentially taken up by M2 macrophages. M2 macrophages are thought to be the predominately anti-inflammatory macrophage type and have been shown to be more phagocytic [155]. Therefore, the preferential uptake in the M2 over M1 macrophages *in vivo* could be attributed to the increased phagocytosis of porphysomes by M2-like macrophages. SR-BI is thought to interact with the R4F peptide in these particles, however there are also passive uptake mechanisms that can be mediated by macrophage phagocytosis and other non-specific uptake mechanisms. In addition, the enhanced permeability effect that is associated with a leaky endothelium and plaque neovascularisation in atherosclerotic plaque can also increase uptake of nanoparticles [156, 157]. We can be confident that the fluorescence observed in the flow cytometric analysis is that of the porphyrin-lipid as there was an absence of porphyrin-lipid positive cells found in the PBS control mice. Overall, this demonstrates that porphysomes are taken up preferentially by aortic macrophages and can subsequently be detected in atherosclerotic plaque. This points to the ability of porphysomes to be used as a molecular imaging tool to localise to and detect the presence of atherosclerotic plaque macrophages.

To facilitate non-invasive imaging *in vivo,* ^{64}Cu-radiolabelled porphysomes were used to assess whether we could longitudinally track the particles *in vivo.* The ^{64}Cu is chelated within the porphyrin moiety which enables simple one-step labelling of the porphysomes and detection with PET imaging [87]. PET is an imaging modality that allows for the high sensitivity detection of radionuclides to a high level of penetrance within tissue but is limited by poor spatial resolution and does not provide information on the anatomical regions within the animal [158]. Therefore, for these studies, we decided to complement the PET imaging with MRI of the thoracic region. Although this provided some anatomical reference, these images had to be manually co-registered. We found that using PET imaging there was a small but significant increase in activity in the heart region after 11 weeks of HCD as compared to 7 weeks. This suggests that porphysomes can detect an increase in plaque deposition in this region over time. However, it remains to be confirmed that changes in the plaque size and composition over this 4-week period correlate with the PET imaging data.

When aortic cell changes between the PBS and the porphysome treated mice were measured with flow cytometry, there was a trend towards a reduction in the proportion of M2-like macrophages. Whether this is due to the higher uptake of porphysomes in the M2-like macrophages or could be attributed to a general reduction in the proportion of macrophages is unclear. There was also a non-significant trend of lower levels of aortic TREM2^{+} macrophages in the porphysome-treated mice which may be indicative of fewer foam cells in the aorta [150, 159]. Overall, these results suggest some potential anti-atherosclerotic effects of porphysomes *in vivo.*

Atherosclerotic plaque in the aortic sinus of *Apoe*$^{-/-}$ mice typically develop complexity over time with foam cell deposition and eventually fibrous cap formation [148, 152]. We decided to examine the histology of this region to determine any relevant changes in stable atherosclerosis in this model. However, despite our *in vitro* findings indicating anti-atherosclerotic functional effects and some promising changes in aortic cell composition measured with flow cytometry, this did not translate to any significant changes in atherosclerotic plaque volume. Neither did we detect changes in plaque composition with porphysome treatment. As compared to previous studies using apoA-I, the main protein component of HDL, a concentration of 40mg/kg inhibited atherosclerosis but only in early-stage plaque (2 weeks HCD prior to 6 weeks of treatment) in *Apoe*$^{-/-}$ mice. This was attributed to improvements in the functionality of HDL with improved cholesterol efflux and anti-inflammatory/ anti-apoptotic properties boosted by apoA-I [149]. As the apoA-I porphyrin-lipid particles have cholesterol efflux capacity and anti-inflammatory effects demonstrated *in vitro,* it was assumed that the particles may influence atherosclerosis *in vivo.* Although apoA-I and porphysomes are not equivalent, it is possible that with a shorter HCD feeding period (earlier stage plaque), porphysome treatment may be more effective by reducing inflammation and improving cholesterol efflux at the earliest stages of atherosclerotic plaque initiation where modulating these processes exert the most beneficial effects. Furthermore, we based our dosage of the therapeutic porphysomes of 40mg/kg on these studies. However, the concentration was calculated on the apoA-I mimetic R4F peptide that is not the exact equivalent to apoA-I. Therefore, further investigation of the therapeutic effects of these particles *in vivo* is required.

ApoA-I has been associated with reduced weight gain in mice [160] which may explain the reduced weight gain over time in porphysome treated mice. However, the weight changes could also be attributed to effects of stress and anaesthetic from imaging procedures that were conducted only on the porphysome/ R4F-HDL mimetic treated mice but not the PBS-control mice. In addition, it was found that there were no significant changes in any of the plasma lipid measures in these mice which seems to indicate that porphysomes do not interfere with lipid metabolism in *Apoe*$^{-/-}$ mice.

Despite the promising results from these studies, there were some limitations in the design and implementation of these experiments that could be improved. The primary aim of these experiments was to show that porphysomes could act in a theranostic capacity. Some caveats of this approach are that using imaging procedures on only the treatment group could have introduced confounding variables on the results of the therapeutic side of the study. Moreover, the reason that two formulations of the nanoparticles were required is that to incorporate a higher concentration of R4F into the therapeutic nanoparticles required a lower concentration of porphyrin-lipid during synthesis. Given that the R4F-HDL mimetics were only used for therapeutic purposes, the decision was made that porphyrin-lipid would not be included in these particles. Ideally the nanoparticles used for imaging and therapy would be identical in composition, but this was not possible within the scope of this thesis. Looking forward, there are possibilities to improve the therapeutic capacity of the porphysomes by loading the inner core with statins [54] or other anti-atherosclerotic drugs, which is a possible future direction for this work.

In future, an alternative way to conduct these studies could be to separate the cohorts of mice to observe the diagnostic properties apart from the therapeutic effects. For example, using the ^{64}Cu-30 mol %-porphysomes for each imaging timepoint (e.g. wk 7 and wk 11) the mice could have been imaged using PET and subsequently sacrificed for γ-counting of ^{64}Cu-porphysomes to verify the biodistribution in non-atherosclerotic and atherosclerotic mice. The distinction of non-atherosclerotic and atherosclerotic could also be expanded to compare HCD fed wildtype *Apoe*$^{+/+}$ mice to *Apoe*$^{-/-}$ mice as wildtype mice develop negligible atherosclerosis, which has been adopted in other atherosclerosis PET imaging studies [52, 161]. Further histology could be used to determine uptake of porphysomes and extent of atherosclerotic plaque deposition in the aorta. This would provide information on any changes in the distribution profile and further verify that the uptake of porphysomes is specific for atherosclerotic regions in mice. Furthermore, this could determine if there is a correlated increase in uptake over time with plaque size. A similar study examined folate-conjugated porphysomes for longitudinal imaging following myocardial infarction [113].

This chapter has explored and established the properties of porphysomes as a potential theranostic agent in a murine model of stable atherosclerosis. Given that there is a need to also investigate theranostic agents that target and identify unstable atherosclerosis, the next chapter further explores the theranostic properties of porphysomes in the tandem stenosis murine model of plaque instability.

CHAPTER 5

Theranostic properties of apoA-I-linked-porphysome nanoparticles in a model of atherosclerotic plaque instability

5.1 Introduction

Atherosclerosis is a complex process that results in the deposition of highly inflammatory, lipid-rich plaque in the vasculature. There are several possible outcomes from atherosclerosis development with either continued growth until complete vessel occlusion, plaque rupture or erosion leading to a thrombotic event. The most common cause of acute thrombosis that leads to a MI originates from plaque rupture [2]. Features of plaque at the highest risk of rupture are classified as unstable or vulnerable plaque, with a thin fibrous cap and a large lipid-rich necrotic core. In this process of plaque rupture, the fibrous cap structure can be compromised by inflammatory-driven inhibition of interstitial collagen synthesis by smooth muscle cells and increased enzymatic degradation of this collagen. Upon rupture of the fibrous cap, thrombogenic material within the core is released into the lumen leading to thrombosis and subsequent MI [2, 13, 14]. However, despite what is known about these clinical outcomes there is a need to further investigate both treatments and diagnostic tools that may be able to improve plaque stability as well as identify plaques that are at the highest risk of rupture.

The previous chapter has described the use of the *Apoe*$^{-/-}$ HCD fed murine model of stable atherosclerosis. However, there are many complexities of the human atherosclerotic plaque that the stable atherosclerotic model does not develop easily, which includes the development of unstable plaques that are prone to rupture with intraplaque haemorrhage, intravascular thrombus and thin, ruptured fibrous caps [14]. The tandem stenosis murine model of plaque instability has been previously described and can model some of the features of unstable plaque that the stable murine model of atherosclerosis cannot. This model utilises lower shear and high tensile stress in the carotid of mice with two tandem stenoses to induce an unstable plaque development [114, 162]. The advantage of this model is the ability to examine whether experimental interventions can improve or prevent features that are characteristic of unstable plaques [114]. The significance of utilising this type of disease model in mice for this study is the ability to determine whether porphysomes are able to localise to vulnerable unstable plaques in order to assist identification of atherosclerotic plaque *in vivo*.

The ultimate goal of any type of nanoparticle used for non-invasive imaging of atherosclerosis is to better characterise the molecular composition of plaque to distinguish between features of stable plaque and vulnerable unstable plaques that are at risk of rupture [8]. Although this work does not explore the ability of porphysome nanoparticles to distinguish between stable and unstable plaque, this study investigates the capacity of porphysomes to localise to areas of unstable plaque *in vivo* using the tandem stenosis model of plaque instability using fluorescence and positron emission tomography (PET) imaging. In addition, we also investigate whether porphysomes are able to improve plaque stability and reduce plaque burden in this model.

5.2 Methods

5.2.1 Carotid artery tandem stenosis procedure in *Apoe*$^{-/-}$ mice

11–12-week-old mice were fed a HCD for 6 weeks followed by tandem stenosis carotid artery ligation surgery. Briefly, to expose the right common carotid artery a midline incision was made with the salivary gland placed on saline-soaked gauze. The tandem stenoses were made with an outer diameter of 150 μm using a suture needle probe (ETHILON 2809G Nylon suture 9-0, Ethicon, NJ, USA) with the distal stenosis 1 mm from the carotid bifurcation and the proximal stenosis 3 mm from the distal stenosis. The stenoses were held in place by white 6-0 TI-CRON braided polyester sutures (Covidien CD3113K, Medtronic, Dublin, Ireland), tied around the needle probe which was subsequently removed. The skin was closed using 6-0 silk sutures (639G Black braided, Ethicon, NJ, USA) and the median time of the procedure was approximately 30-45 min. Mice were maintained on HCD for seven weeks following tandem stenosis until sacrifice via cardiac puncture.

5.2.2 Nanoparticle administration in *Apoe*$^{-/-}$ mice post-tandem stenosis surgery

Immediately following tandem stenosis surgery and then every alternate day thereafter (approximately every 48 h), mice were administered 250 µL of PBS vehicle or discoidal R4F-HDL mimetic nanoparticles (40mg/kg) via intraperitoneal injection over seven weeks until sacrifice. Mice were injected intravenously with approx. 18.5MBq of ^{64}Cu-labelled 30 mol %-porphyrin-lipid discoidal porphysome nanoparticles 6 h prior to imaging with PET.

5.2.3 Sectioning and histological analysis of tandem stenosis carotid Segment I

The carotid artery segment of the tandem stenosis model that develops unstable plaque, TS Segment I, was serially sectioned at 6 µm [114]. Segment I was sectioned from the proximal suture for a length of approximately 2.3 mm at ~96 µm intervals. Four sections 96 µm apart in the mid-point region of the segment I (approx. 768-1152 µm from the proximal suture) were assessed for compositional changes with various immunohistochemistry and staining procedures (α-SMA, TER-119, CD68, Masson's trichrome and Oil red O). Plaque area and necrotic area (acellular area, white unstained areas) were measured in H&E-stained sections in three separate regions spanning the length of the vessel at 0-384 µm, 768-1152 µm and 1920-2304 µm from the proximal suture.

5.2.4 TER-119 immunohistochemistry

PBST was used for all staining steps containing 0.1% tween. All steps were performed at room temperature unless otherwise stated. Fresh frozen OCT-embedded sections were fixed in ice-cold acetone at -20°C for 20 min. Sections were then washed twice in PBST for 5 min. Sections were incubated in 3% v/v H_2O_2 in PBS for 20 min. Sections were blocked with 10% normal horse serum (Cat# S-2000-20, Vector Laboratories, CA, USA) in PBS for 30 min and excess solution removed. Using avidin/biotin blocking kit (Cat# SP2001, Vector Laboratories, CA, USA), sections were blocked in avidin and biotin for 15 min each, with a PBST rinse after each incubation. Sections were incubated overnight at 4°C with TER-119 biotinylated rat anti-mouse monoclonal antibody (Cat# 13-5921 eBioscience, Thermofisher, MA, USA) diluted 1:400 in 10% normal horse serum for a final concentration of 1.3 µg/mL. TER-119 was detected using the Vectastain Elite ABC HRP kit (Cat# PK-6100, Vector Laboratories, CA, USA) by incubation for 30 min and then incubated in DAB substrate for 3 min. Sections were counterstained in Mayer's hematoxylin, dehydrated and mounted in DPX.

5.3 Results

5.3.1 Porphysomes are detected by PET imaging *in vivo* and IVIS fluorescence imaging *ex vivo* in unstable plaque

To determine whether porphysome nanoparticles localised to areas of unstable plaque we infused ^{64}Cu-labelled porphysomes then performed PET imaging in mice that had undergone tandem stenosis surgery (Fig 5.1A). A ^{64}Cu-porphysome signal was detected in the left and right carotid regions using PET imaging (Fig 5.1B). The tandem stenoses are induced in the right common carotid artery. We next compared the left and right carotid regions for differences in ^{64}Cu-porphysome signal intensity. This revealed a slight, but non-significant, increase in the activity in the right carotid with tandem stenosis-induced unstable plaque deposition (Fig 5.1C, Left, 6.533x10^{-3} %ID/mL; Right, 6.9x10^{-3} %ID/mL; P=0.0733).

To further investigate the uptake of porphysome nanoparticles in the tandem stenosis unstable plaque model, IVIS fluorescence imaging was conducted *ex vivo* on the vascular tree of the mice. This revealed that there was porphyrin-lipid fluorescence detected only in the porphysome treated mice and not the PBS infused control (Fig 5.1D). The fluorescence signal was quantified from the different regions in the vascular tree including aortic arch, descending aorta, and tandem stenosis segments I and II, with a clear increase in fluorescence signal detected in porphysome treated mice compared to the PBS group (Fig 5.4E). Although no statistical testing was conducted on this data due to the small sample size (PBS, n=1; POR, n=2) there was a higher level of fluorescence detected in the arch as compared to other regions, with no clear increase in the fluorescence signal in either TS segment I or II. In addition, the descending aorta had lower levels of fluorescence detected as compared to the aortic arch (Fig 5.4E).

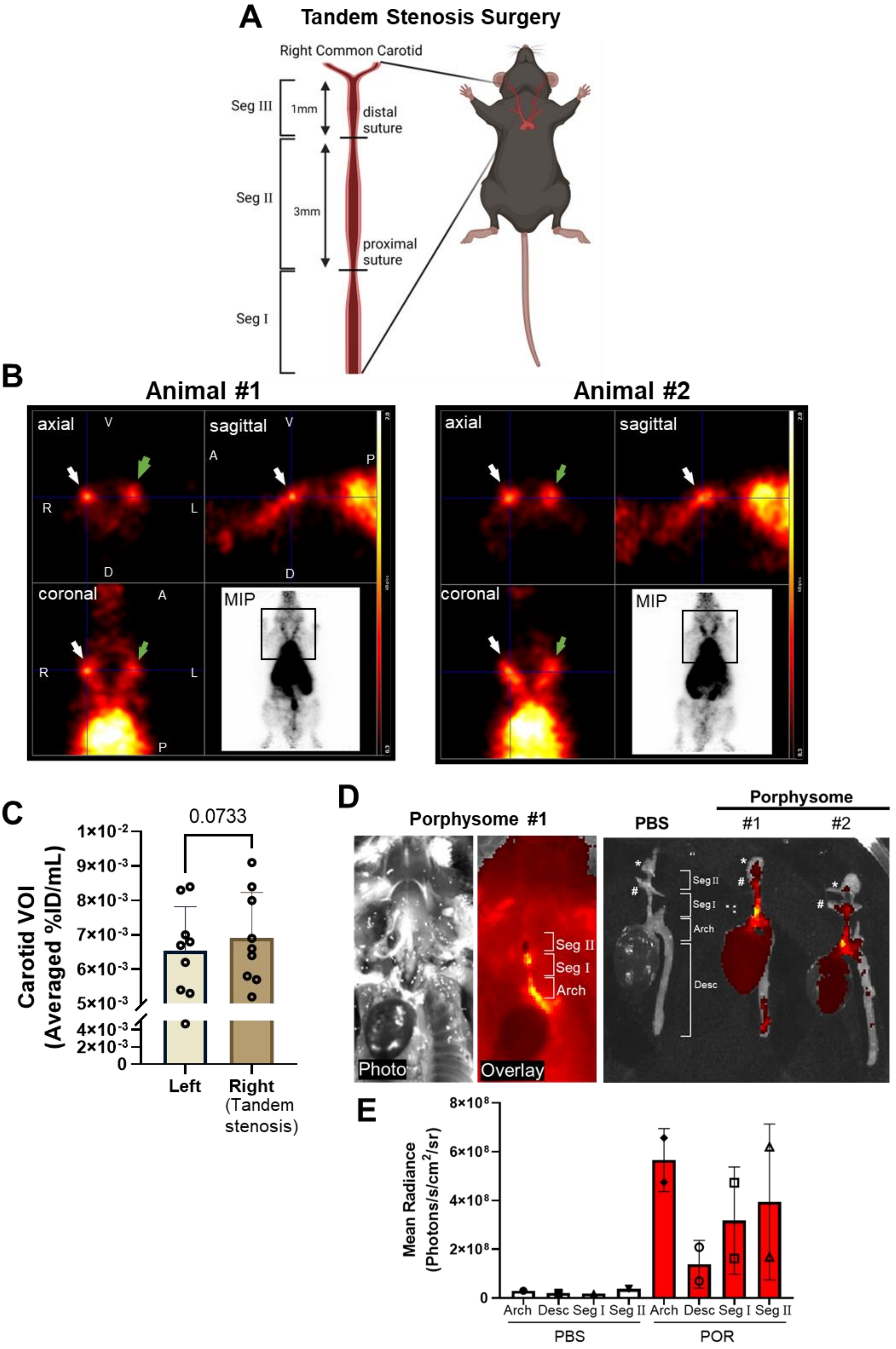
A
Tandem Stenosis Surgery
Right Common Carotid
Seg III
1mm
distal suture
Seg II
3mm
proximal suture
Seg I
B
Animal #1
axial
V
R
L
D
sagittal
A
P
coronal
MIP
Animal #2
C
0.0733
1×10⁻²
9×10⁻³
8×10⁻³
7×10⁻³
6×10⁻³
5×10⁻³
4×10⁻³
2×10⁻³
0
Carotid VOI (Averaged %ID/mL)
Left
Right (Tandem stenosis)
D
Porphysome #1
Photo
Overlay
Seg II
Seg I
Arch
PBS
Porphysome
#1
#2
Desc
E
8×10⁸
6×10⁸
4×10⁸
2×10⁸
Mean Radiance (Photons/s/cm²/sr)
Arch
Desc
Seg I
Seg II
PBS
POR

Figure legend 5.1: PET and IVIS fluorescence imaging of porphysomes in the *Apoe*$^{-/-}$ tandem stenosis murine model of plaque instability

Apoe$^{-/-}$ mice were fed a HCD for six weeks prior to tandem stenosis surgery and remained on this diet for seven weeks following surgery. (**A**) Schematic of the tandem stenosis surgical procedure which involved the introduction of tandem stenoses with the placement of two sutures around the right common carotid (with TS segments I-III shown). (**B**) Representative PET images of two animals in the axial, sagittal and coronal planes at 6 weeks post-surgery (week 12) of the left and right carotid in *Apoe*$^{-/-}$ mice with a tandem stenosis in the right common carotid artery, 6 h post-intravenous injection of ^{64}Cu-porphysome NPs. White and green arrows indicate the right and left common carotid artery respectively. (**C**) Quantification of the PET activity in the left and right carotid volume of interest (VOI) in *Apoe*$^{-/-}$ TS mice 6 h post-injection of porphysome nanoparticles. Data expressed as mean ± SD (n=9). not-significant (ns) $P>0.05$ vs left carotid by unpaired two-tailed t-test. (**D**) *Apoe*$^{-/-}$ mice were injected with porphysomes 24 h prior to sacrifice and IVIS fluorescence imaged both *in situ* and in the vascular tree of *Apoe*$^{-/-}$ mice with tandem stenoses in the right common carotid artery with distal (*) and proximal (#) sutures indicated, and TS Segments I&II (Seg I&II) shown. (**E**) Quantified fluorescence from vascular tree image in **D** comparing PBS and porphysome groups (PBS, n=1; POR, n=2). V, Ventral; D, Dorsal; R, Right; L, Left; A, Anterior; P, Posterior. VOI, volume of interest. ID, Injected Dose. MIP, Maximal Image Projection. Desc, descending aorta. Arch, aortic arch. POR, porphysomes. TS, Tandem Stenosis. IVIS, In Vivo Imaging System.

5.3.2 Porphysome fluorescence is detected in CD68$^+$ macrophage regions of unstable plaque in TS Segment I

To further investigate whether porphysome nanoparticles localise to and are detected within unstable plaque, we conducted fluorescence microscopy on TS carotid Segment I where unstable plaque accumulation occurs [114]. We found that porphyrin-lipid (porphysome) fluorescence could be detected specifically in plaque of TS carotid segment I and this was only detected in the porphysome treated mice, not PBS treated mice (Fig 5.2). In addition, porphysome fluorescence also co-localised with CD68$^+$ macrophages (Fig 5.2).

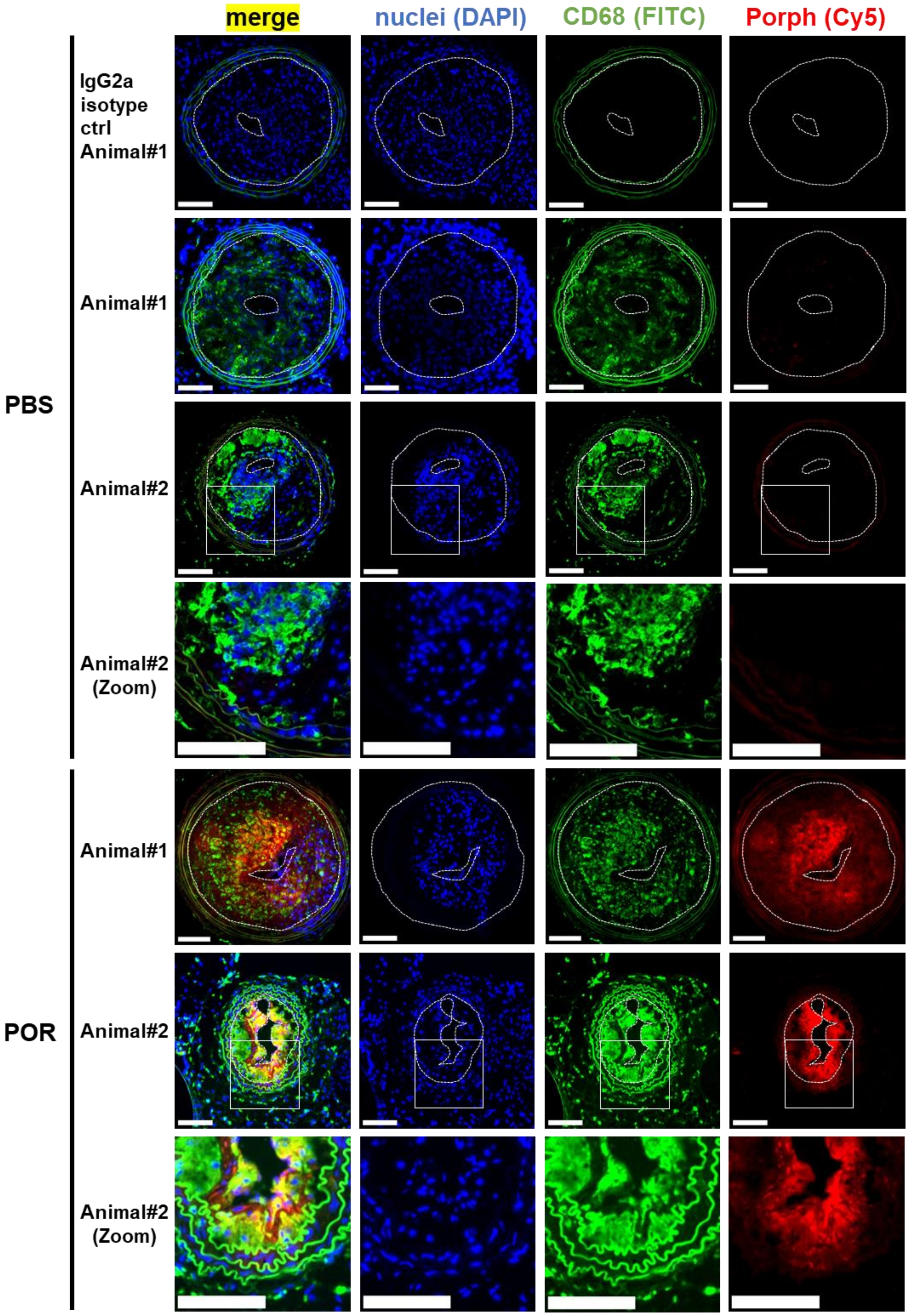
merge
nuclei (DAPI)
CD68 (FITC)
Porph (Cy5)
PBS
IgG2a isotype ctrl Animal#1
Animal#1
Animal#2
Animal#2 (Zoom)
POR
Animal#1
Animal#2
Animal#2 (Zoom)

Figure legend 5.2: Detection of porphyrin-lipid fluorescence and CD68$^+$ macrophages in unstable plaque of TS segment I

Apoe$^{-/-}$ mice that had undergone tandem stenosis surgery were injected intravenously 24 h prior to sacrifice with PBS or 30 mol% porphysomes. Segment I carotid sections were immunohistochemically stained for CD68 (green) with IgG2a isotype control shown. Sections stained with DAPI to detect the cell nuclei (blue). Porphyrin-lipid (Porph) was detected within sections using Cy5-filter (red). Two animals are shown for PBS and porphysome groups with two animals from each group (Animal#1 and #2) including zoomed in areas of interest. Sections collected 768-1152 μm from the proximal suture. Scale bar = 100 μm. Dashed white lines indicate plaque area. TS, Tandem Stenosis. POR, Porphysome.

5.3.3 Effect of porphysome nanoparticles on unstable atherosclerotic plaque area in the tandem stenosis model of plaque instability

To determine the overall changes in the plaque area, H&E-stained sections of TS Segment I were analysed for changes in plaque area at three different regions of the vessel, 0-384 μm, 768-1152 μm and 1920-2304 μm from the proximal suture, to give an indication of the average plaque area spanning each vessel (as illustrated in Fig 5.3A-B). At the mid-point of the vessels, 768-1152 μm from the proximal suture, we found a significant decrease in plaque area in the porphysome treated group, when compared to the PBS treated control group (Fig 5.3D, -52%, $P<0.05$). There were, however, no differences observed in the 0-384 μm (Fig 5.3C) or 1920-2304 μm (Fig 5.3E) regions.

When the three regions were averaged to provide a measure of the plaque area across the vessel, no significant changes were observed between the PBS and porphysome groups (Fig 5.3F). It was observed that there was some variation in the overall size of the carotid sections, even within the same vessel (Fig 5.3B). Given this variation in vessel size, the degree of vessel occlusion as the % plaque area of the vessel area was also calculated which revealed that there was no change the degree of occlusion of the vessel between the PBS and porphysome groups (Fig 5.3G).

The necrotic or acellular areas that contain extracellular lipid were defined as areas that were unstained with H&E (white area). Across the entire vessel there were no significant changes in the proportion of acellular area in the TS segment I plaque between treatment groups (Fig 5.3H).

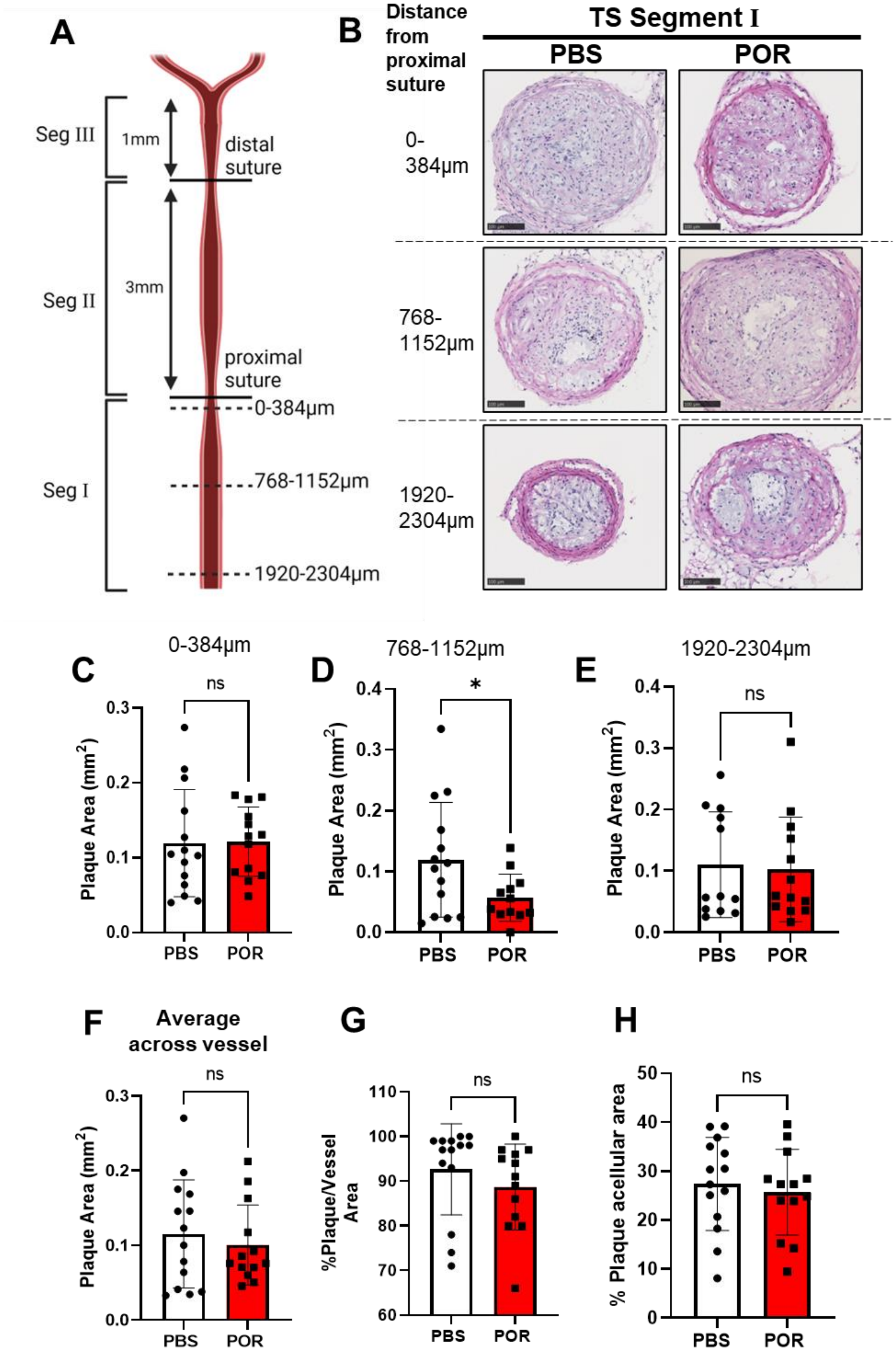
A
Seg III
1mm
distal suture
Seg II
3mm
proximal suture
0-384µm
Seg I
768-1152µm
1920-2304µm
B
Distance from proximal suture
TS Segment I
PBS
POR
0-384µm
768-1152µm
1920-2304µm
C
0-384µm
ns
Plaque Area (mm²)
0.0
0.1
0.2
0.3
PBS
POR
D
768-1152µm
*
Plaque Area (mm²)
0.0
0.1
0.2
0.3
0.4
PBS
POR
E
1920-2304µm
ns
Plaque Area (mm²)
0.0
0.1
0.2
0.3
0.4
PBS
POR
F
Average across vessel
ns
Plaque Area (mm²)
0.0
0.1
0.2
0.3
PBS
POR
G
ns
%Plaque/Vessel Area
60
70
80
90
100
110
PBS
POR
H
ns
% Plaque acellular area
0
10
20
30
40
50
PBS
POR

Figure legend 5.3: Unstable plaque area changes between PBS and porphysome groups in TS Segment I

(**A**) Diagram of the sectioned areas of Segment I in the right common carotid with three regions analysed for area measurements at approximately the beginning, middle and end of the segment corresponding to 0-384 µm, 768-1152 µm, and 1920-2304 µm from the proximal suture respectively. (**B**) Representative images of H&E-stained TS Segment I at the three sectioned areas. Plaque area in TS segment I measured for 0-384 µm (**C**), 768-1152 µm (**D**) and 1920-2304 µm (**E**). Average plaque area in TS Segment I from the three regions (**F**). % Plaque burden of the total vessel area (**G**). % acellular area (unstained area) of the total plaque area (**H**). Data expressed as mean ± SD (n=12-14/group). not-significant (ns) $P>0.05$, $^*P<0.05$ vs PBS control by unpaired two-tailed t-test. TS, Tandem Stenosis. POR, porphysome. Seg, Segment. Scale bar = 100 µm.

5.3.4 No change in the inner vessel area (vessel size) of TS Segment I carotid sections

Given the variation in the size of the segment I vessel, the inner vessel area (Fig 5.4A) was also compared between the PBS and porphysome groups. However there were no changes in the inner vessel area at 0-384 µm (Fig 5.4B), 768-1152 µm (Fig 5.4C), and 1920-2304 µm (Fig 5.4D) from the proximal suture between the porphysome and PBS groups. Overall, this shows there were no changes in vessel size between groups but rather indicates some of variation that was observed in vessel size in Segment I in this model (Fig 5.4A-E).

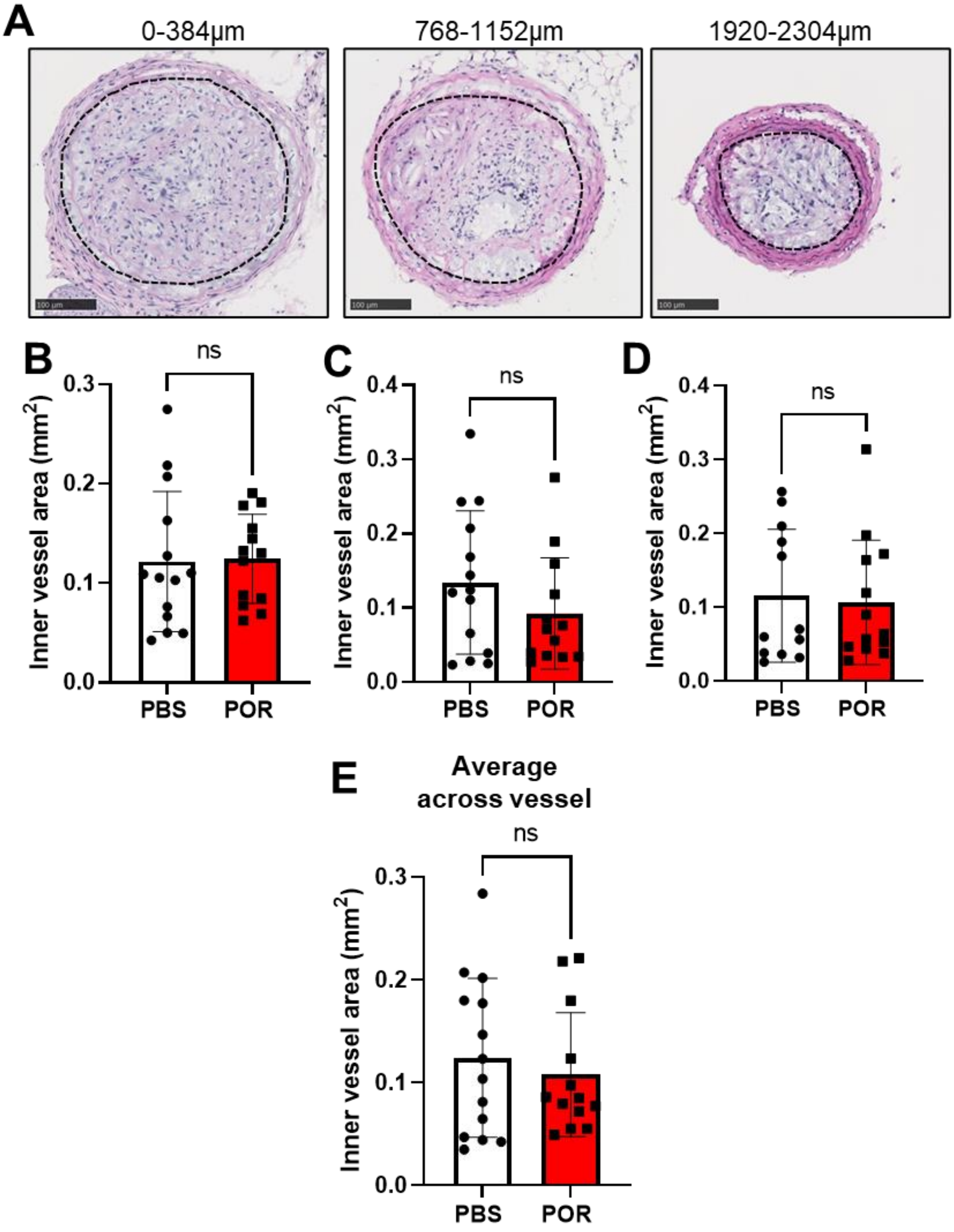
A
0-384µm
768-1152µm
1920-2304µm
100 µm
100 µm
100 µm
B
ns
Inner vessel area (mm^2)
0.3
0.2
0.1
0.0
PBS
POR
C
ns
Inner vessel area (mm^2)
0.4
0.3
0.2
0.1
0.0
PBS
POR
D
ns
Inner vessel area (mm^2)
0.4
0.3
0.2
0.1
0.0
PBS
POR
E
Average across vessel
ns
Inner vessel area (mm^2)
0.3
0.2
0.1
0.0
PBS
POR

Figure legend 5.4: Inner vessel area measurements of TS segment I following treatment with PBS or porphysomes

(**A**) Representative images of TS segment I, showing the inner vessel area measurement of the inner perimeter of the carotid of PBS group at the three vessel regions. Inner vessel area quantified sections at 0-384 μm (**B**), 768-1152 μm (**C**) and 1920-2304 μm (**D**) from the proximal suture of the tandem stenoses. Average of the inner vessel area across the three regions of the TS segment I (**E**). Data expressed as mean ± SD (n=12-14/group). Non-significant (ns) $P > 0.05$ vs PBS control by unpaired two-tailed t-test. TS, Tandem Stenosis. POR, porphysome. Scale bar = 100 μm.

5.3.5 Porphysomes decrease unstable plaque collagen content, with no change in lipid content in TS Segment I

Collagen content is a reflection of atherosclerotic plaque stability. Using Masson's trichrome staining we next determined changes in plaque collagen between PBS and porphysome groups in TS Segment I (Fig 5.5A). A significant decrease in collagen content was observed in the porphysome treatment group, when compared to the PBS control group (Fig 5.5B, -48%, $P<0.05$). To examine changes in plaque lipid content, TS Segment I sections were stained with Oil red O (ORO) to detect areas of lipid in the unstable plaque (Fig 5.5A). No changes plaque lipid content were detected between the PBS and porphysome groups (Fig 5.5C).

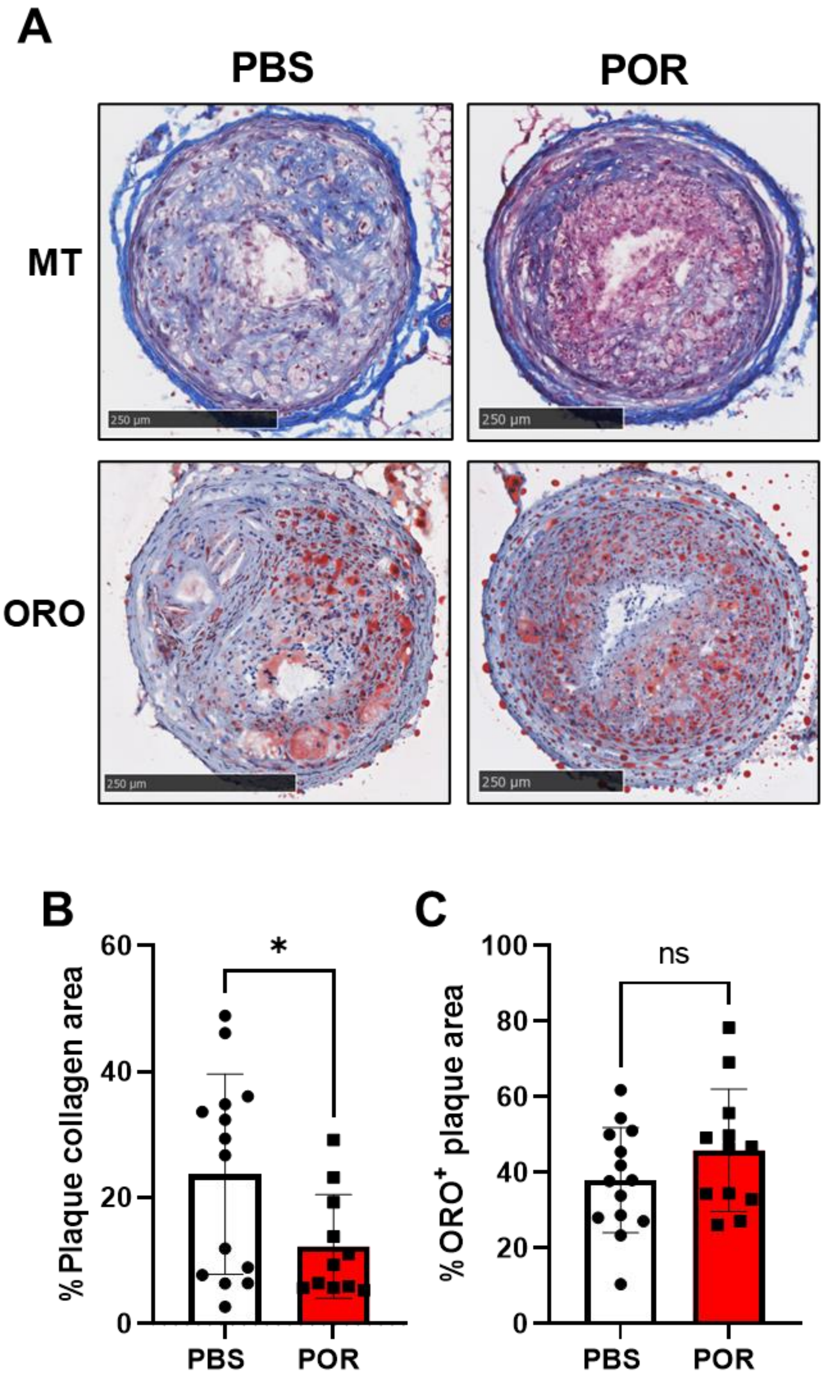
A
PBS
POR
MT
ORO
250 µm
250 µm
250 µm
250 µm
B
% Plaque collagen area
60
40
20
0
*
PBS
POR
C
% ORO⁺ plaque area
100
80
60
40
20
0
ns
PBS
POR

Figure legend 5.5: Decrease in collagen but not lipid content in TS segment I of *Apoe*$^{-/-}$ mice treated with porphysomes in the tandem stenosis model of plaque instability

(A) Representative image of TS Segment I sections stained with Masson's Trichrome (MT) and Oil Red O (ORO) to measure collagen and lipid content respectively. Percentage of plaque area calculated for collagen from MT staining (**B**) and lipid content from ORO^{+} staining **(C**). Sections collected 768-1152 μm from the proximal suture. Data expressed as mean ± SD (n=11-14/group). not-significant (ns) $P>0.05$, $*P<0.05$ vs PBS control by unpaired two-tailed t-test. TS, Tandem Stenosis. POR, porphysome. Scale bar = 250 μm.

5.3.6 Porphysome have no effect on plaque smooth muscle cell, erythrocyte or macrophage content in the tandem stenosis model of plaque instability

To further determine changes in plaque composition between the PBS and porphysome groups, immunohistochemical staining was performed on plaque in carotid TS Segment I to detect alpha-smooth muscle actin (α-SMA) positive smooth muscle cells, TER-119$^+$ erythrocytes as a measure of intraplaque haemorrhage and CD68$^+$ macrophages (Fig 5.6A). No changes observed in α-SMA$^+$ (Fig 5.6B), TER-119$^+$ (Fig 5.6C) or CD68$^+$ (Fig 5.6D) staining between the PBS and porphysome treatment groups.

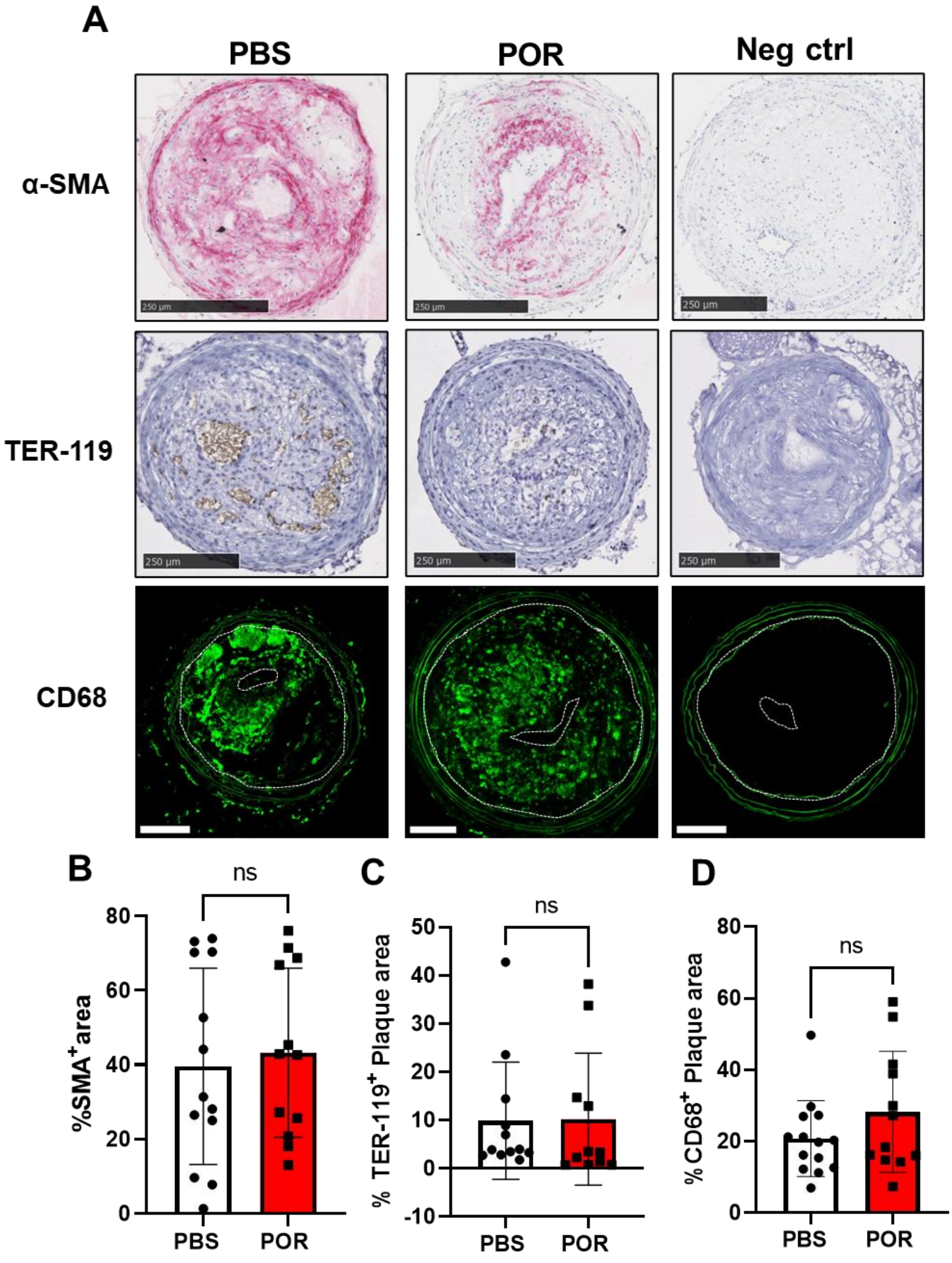
A
PBS
POR
Neg ctrl
α-SMA
TER-119
CD68
250 µm
B
ns
%SMA⁺area
0
20
40
60
80
PBS
POR
C
ns
% TER-119⁺ Plaque area
-10
0
10
20
30
40
50
PBS
POR
D
ns
% CD68⁺ Plaque area
0
20
40
60
80
PBS
POR

Figure legend 5.6: Porphysomes have no effect on SMC, erythrocyte, or macrophage content in TS Segment I

(**A**) Representative images of TS Segment I with alpha smooth muscle actin (α-SMA), TER-119, and CD68 detected with immunohistochemistry (IHC) staining showing negative controls for all antibodies. Percentage of plaque area calculated for α-SMA$^+$ (**B**), TER-119$^+$ (**C**) and CD68$^+$ (**D**) positive staining. Sections collected 768-1152 µm from the proximal suture. Data expressed as mean ± SD (n=11-14/group). not-significant (ns) $P>0.05$ vs PBS control by unpaired two-tailed t-test. TS, Tandem Stenosis. POR, porphysome. Dashed white lines indicate plaque area. Scale bar: α-SMA, TER-119 = 250 µm; CD68 =100 µm.

5.3.7 Reduced bodyweight and lower plasma triglycerides observed following treatment with porphysomes in the tandem stenosis model of unstable plaque

The bodyweight of animals were recorded prior to and in the seven weeks following the tandem stenosis surgical procedure (Fig 5.7A). As expected, there was an observed decrease in bodyweight following surgery in both the PBS and porphysome treatment groups. Over the course of the study all mice gained bodyweight however from week 5 and the remainder of the study the porphysome treatment group had a significantly lower bodyweight as compared to the PBS group (Fig 5.7A, $P<0.05$). Furthermore the plasma lipid levels in these mice were measured at the end of the study revealing significantly lower triglycerides levels in mice treated with porphysomes (Fig 5.7B, -31%, $P<0.01$). No changes were observed in total, LDL or HDL cholesterol between groups (Fig 5.7B).

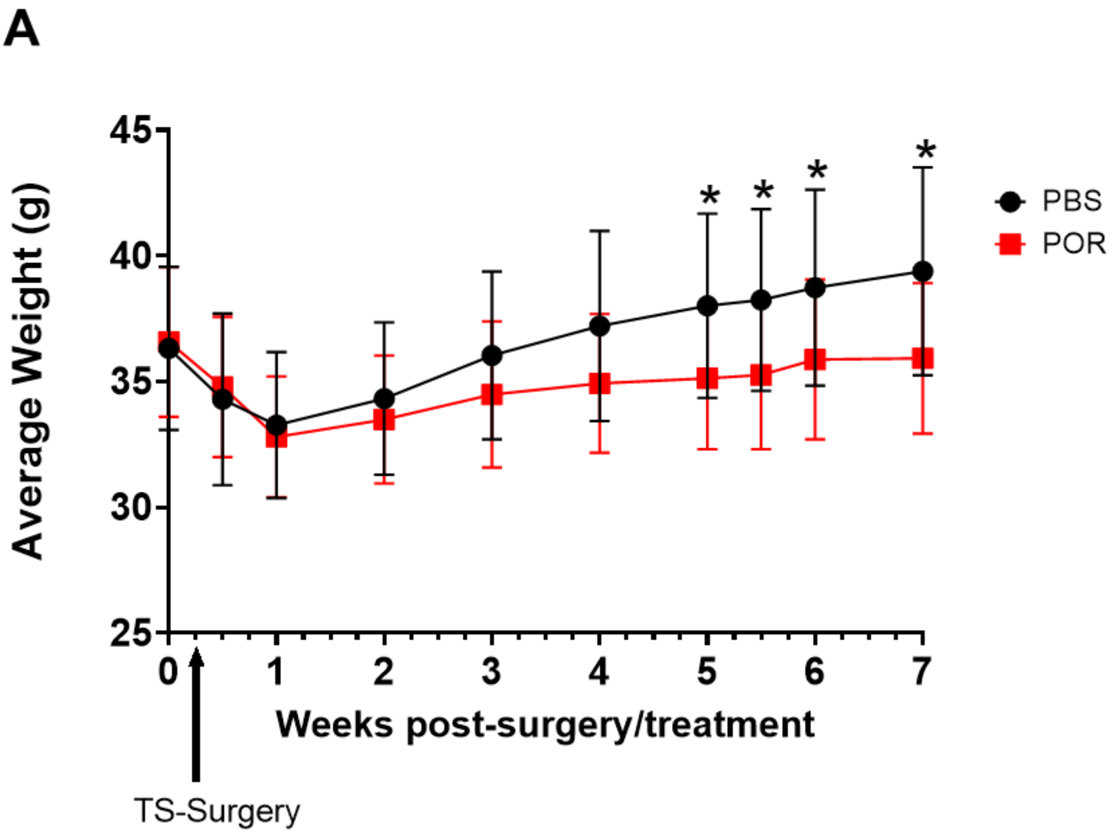

B

Plasma Levels	PBS	POR	*P*-value
Triglycerides (mmol/L)	3.606±1.011	2.506±0.7674**	0.0037
Cholesterol (mmol/L)	15.83±3.49	15.32±3.924	0.7284
LDL Cholesterol (mmol/L)	14.97±3.586	13.6±2.085	0.2456
HDL Cholesterol (mmol/L)	0.8617±0.3255	0.6213±0.3312	0.0743

Figure legend 5.7: Bodyweight and plasma lipid changes following tandem stenosis surgery in *Apoe*$^{-/-}$ mice administered PBS or porphysomes

(**A**) Changes in average bodyweight of animals immediately prior to and over the seven weeks following tandem stenosis surgery. (**B**) Changes in plasma lipids including triglycerides, total cholesterol, LDL and HDL cholesterol. Data expressed as mean ± SD (n=13-14/group). **P*<0.05, ***P*<0.01 vs PBS control by unpaired two-tailed t-test. POR, porphysome. TS, Tandem Stenosis.

5.4 Discussion

This study has further investigated the theranostic properties of porphysome nanoparticles *in vivo*, in the tandem stenosis model of atherosclerotic plaque instability. The primary findings from this study are: (1) ^{64}Cu-porphysomes can be detected by PET imaging in the unstable atherosclerotic plaque region of the carotid arteries *in vivo*, (2) porphysome fluorescence can also be detected within regions of unstable plaque using both IVIS imaging *ex vivo* and in TS segment I sections using fluorescence microscopy, and (3) porphysome treatment causes modest changes in plaques with a reduction in plaque area at the mid-point of TS Segment I and in collagen content. No other changes in plaque composition were detected. These findings have implications for the use of apoA-I-porphysomes as a theranostic nanoparticle targeted to unstable atherosclerotic plaque.

PET imaging detected ^{64}Cu-porphysomes in the carotid region of mice, with a non-significant trend for an increase in PET signal in the unstable plaque region in the right carotid artery, compared to the left carotid artery. There are some limitations to the use of PET imaging in this model which may explain these findings. Firstly, the size of murine plaque in the carotid artery is at or close to the limit of PET imaging resolution and the size of the unstable plaque is therefore difficult to resolve. The largest plaque deposits in mice are found in the aorta (average diameter ~1 mm), and are larger than those in the carotid of the TS model [51]. Porphysomes have previously been used for cancer detection in tumour models in which the number of target cells in these lesions are typically higher than that of murine atherosclerotic plaque [8, 51, 89]. This makes preclinical PET imaging of atherosclerotic plaque in mice at this site in the carotid artery inherently difficult. Other sites in the aorta may be more appropriate and a higher resolution would be necessary so PET could be used to quantitatively assess murine plaque.

With *ex vivo* fluorescent IVIS imaging we were able to detect porphysomes in the excised vascular tree, which included detection in TS segment I, the aortic arch and the descending aorta. This is consistent with the detection of porphysomes in the aortic arch using the IVIS in the stable plaque model (Chapter 4). Once again, the fluorescent porphysome signal was only observed in the animals injected with porphysomes and not in the PBS control animals, suggesting no influence from background fluorescence. We also observed that porphysomes localised to the areas of CD68$^+$ macrophages in plaques, similar to what was observed in stable atherosclerotic plaque in the aortic sinus (Chapter 4). Whilst we cannot conclude that porphysomes specifically accumulate in unstable plaque in TS segment I, we show that porphysomes do accumulate in atherosclerotic plaque *in vivo* in both unstable and stable plaque. The mechanism for this uptake by macrophages is likely to be via SR-BI that is highly expressed in plaque macrophages and interacts with the R4F peptide in the porphysome outer shell [89, 90]. Macrophages are the predominant cell type in both stable and unstable atherosclerotic plaques, so uptake would be expected in both.

To identify unstable plaque, other studies have explored the possibility of targeting factor XIIa which is implicated in thrombosis and inflammation in atherosclerosis. When Searle *et al.* [163] utilised an antibody targeting factor XIIa they found fluorescent detection of the factor XIIa antibody in both TS segment I and the aortic arch. A more specific way of detecting unstable plaque was demonstrated by near-infrared (NIR) autofluorescence of intraplaque haemorrhage within the unstable plaque in both human plaque and the tandem stenosis model. This NIR autofluorescence was found to be associated with heme degradation products of intraplaque haemorrhage [164].

Therefore depending on the strategy it may be possible to develop a porphysome nanoparticle that specifically targets unstable plaque, but this will require further development.

It was observed that in TS segment I there were variations in vessel size. Larger vessels consistently had a higher plaque burden, indicative of positive remodelling of the vessel [14, 114]. There were also large variations in plaque burden across the length of TS segment I. Some vessels had very little plaque while others were almost completely occluded, but this was observed in both the control and porphysome treatment groups. Despite these variations, we observed a significant decrease in plaque area at the mid-point of TS Segment I of mice receiving porphysomes. The mechanism for this could be related to the ability of the apoA-I-porphysomes to inhibit inflammation *in vitro* which may have led to a reduction in the recruitment and accumulation of immune cells like macrophages. Furthermore, enhanced cholesterol efflux, as demonstrated *in vitro,* could also inhibit macrophage foam cell accumulation by removal of cholesterol from macrophages. However, apoA-I-porphysomes did not influence changes in either the $CD68^+$ macrophage or ORO^+ lipid areas in the unstable plaque. Therefore it is difficult to determine from the histological data the exact mechanism behind the observed reduction in plaque volume, especially as this was only seen at one site of the unstable plaque in the carotid artery.

Furthermore, there was an observed decrease in the collagen content as measured by Masson’s trichrome staining in the unstable plaque in mice that were treated with porphysomes, compared to the PBS control mice. Collagen deposition is a stabilising factor in atherosclerotic plaque that forms a fibrous cap. Over time, this cap can start to degrade leading to rupture and thrombosis [14, 165]. Therefore, it seems that porphysomes have some destabilising effects on the unstable plaque in this tandem stenosis model.

There are other measures of plaque stability that were assessed including α-SMA staining of smooth muscle cells, which did not change in contrast to the plaque collagen. In addition, TER-119 which detects erythrocytes, is able to identify areas of intra-plaque haemorrhage which is a key feature of unstable vulnerable plaques [114, 166]. However, we observed no change in TER-119 staining which indicates that porphysomes do not have a significant impact on intraplaque haemorrhage in unstable plaque. Overall, the only plaque stability indicator that was altered by porphysomes was the collagen content.

Given that porphysomes were shown to have some anti-inflammatory effects in macrophage culture *in vitro* (Chapter 3), we also assessed whether there was any effect on macrophages in unstable plaque. CD68 staining revealed no change in macrophage content in the unstable plaque between the PBS and porphysome groups. Except for the changes in collagen content, there were no significant compositional changes observed in α-SMA$^+$ smooth muscle cells, ORO lipid content and CD68$^+$ macrophages in the unstable plaque. This is consistent with what was observed previously in the stable plaque in Chapter 4. Although we did find lower levels of macrophage expression of inflammatory genes such as *Il-1β in vitro* following porphysome treatment, this was not observed with *Ccl2* (MCP-1), and we even saw some increases in CCL2 expression (Chapter 3). CCL2 has been shown to negatively impact plaque stability by increasing expression of destabilising metalloproteinases (MMPs) as well as increasing migration and infiltration of monocytes and macrophages [167, 168]. Therefore it is possible that despite some anti-inflammatory effects shown *in vitro* this may not necessarily translate to improving plaque stability *in vivo.*

Interestingly we observed that plasma triglycerides were significantly lower in the porphysome treatment group as compared to the PBS control. Given that triglycerides are typically associated with chylomicrons and VLDL, this demonstrates that porphysomes are impacting lipid metabolism in these mice. Hypertriglyceridemia is a risk factor for CVD in humans, therefore a reduction in triglycerides might be beneficial. However triglycerides have not been shown to be directly atherogenic [169]. In addition these changes in plasma triglycerides were not seen in the stable atherosclerosis model in *Apoe*$^{-/-}$ mice (Chapter 4). It is possible in the surgically induced model of plaque instability, that the effect of porphysomes on plasma triglycerides is more pronounced. However there were no significant changes in any of the other plasma lipid parameters, indicating that this is specific for plasma triglycerides. In this cohort of mice with tandem stenosis there was a significant difference in bodyweight between the two cohorts from five weeks post-surgery until the end of the study, with a similar trend observed in the *Apoe*$^{-/-}$ stable atherosclerosis model (Chapter 4). Which once again may reflect the increased stress imposed on these mice with imaging procedures conducted on the porphysome group as compared to the PBS control group or possibly effects of the apoA-I mimetic [160].

The limitations of this study surround some of the experimental and technical protocols used. Due to technical issues with the IVIS fluorescence imager, there were only a few animals that were imaged resulting in a small sample size. This may require further investigation with a larger sample size and possibly dividing up each area of interest (e.g. Segment I/II, aortic arch, descending aorta) to determine the exact fluorescence distribution for each region of the vascular tree.

Previous studies of the tandem stenosis model of plaque instability have used picrosirius red to determine the collagen content of unstable plaque sections [114, 163, 170]. The advantage of using picrosirius for collagen staining is the ability to enhance the natural birefringence of collagen with polarised light, allowing specific collagen identification in tissue sections [171]. Masson's trichrome used in this study works by acidic components facilitating the staining of the collagenous connective tissue within the section with aniline blue. Therefore Masson's trichrome is still a suitable stain for detecting areas of collagenous connective tissue in the unstable plaque but is less specific for collagen than picrosirius red [171].

Although there were no significant changes in macrophage accumulation in the unstable plaque, given the anti-inflammatory properties exhibited *in vitro* on macrophages, it may be useful to further investigate specific effects of porphysomes on inflammation *in vivo.* In future, it may be useful to investigate changes in inflammatory cytokines in the plasma of these mice to determine if porphysome have an effect *in vivo* on systemic inflammation. It may also be suitable to assess the levels of cytokine expression in the vasculature, in particular the aortic arch or descending aorta to further investigate if porphysome are able to influence inflammation *in vivo.*

Overall this chapter has investigated the theranostic potential of porphysomes in the tandem stenosis model of plaque instability. Although we discovered that porphysomes did not significantly improve plaque stability, we were able to detect porphysome nanoparticle fluorescence in unstable plaque and reveal a reduction in plaque area in TS Segment I. Given that the last two chapters have investigated the theranostic properties of porphysomes in native atherosclerosis, the next chapter explores the development of a novel in-stent neoatherosclerosis murine model to further assess the properties of porphysomes *in vivo*.

CHAPTER 6

Development of a murine in-stent neoatherosclerosis model

6.1 Introduction

In-stent neoatherosclerosis is a phenomenon observed following percutaneous coronary intervention (PCI) where, as the name suggests, a unique form of atherosclerosis develops within the stented region [37]. This manifests histologically as an accumulation of lipid-rich foam cell macrophages in the neointimal area of stented regions typically with or without presence of a necrotic core and/or calcification [37, 42, 43]. Despite the development of newer generation drug eluting stents (DES), in-stent neoatherosclerosis has emerged as a contributor to the incidence of very late stent thrombosis and late restenosis, which are late vascular complications of PCI [37]. Furthermore in-stent neoatherosclerosis develops at an accelerated rate as compared to native atherosclerosis and has been consistently observed in DES earlier than bare metal stents (BMS) [39, 172]. The underlying mechanisms of this accelerated rate of formation are unknown but likely factors include the dysfunctional endothelium caused by stent deployment allowing increased infiltration of lipoproteins and foam cell macrophage accumulation [37, 42, 43]. Therefore, there is a need to better understand the molecular and cellular mechanisms of in-stent neoatherosclerosis to inform the development of technologies to further improve on current devices and therapies.

There is a very limited amount of previous work reporting the development of in-stent neoatherosclerosis in animal models. Thus far, studies have focused on examining mechanisms of in-stent restenosis such as neointimal hyperplasia [173]. Intense focus on reducing the rates of in-stent restenosis following PCI with BMS led to the development of DES that are widely used in clinical settings today [7, 29]. There are some groups that have investigated in-stent neoatherosclerosis in preclinical rabbit models. In these rabbits, following stent deployment and atherogenic diet feeding, there was evidence of foam cell macrophages present in the neointima which is a key feature of in-stent neoatherosclerosis [46, 47]. However, there is no murine model of in-stent neoatherosclerosis to date.

There are many technical challenges associated with a stenting model in mice given the small scale. However murine models generally have the benefit of higher throughput, lower cost and availability of genetically modified strains enabling in-depth mechanistic understanding of biological processes *in vivo* [173, 174]. Previously, Ali *et al.* [174] examined a novel approach to investigating in-stent restenosis caused by neointimal hyperplasia, which is the proliferation and migration of medial smooth muscle cells that leads to the expansion of the neointima of the stented region. This model involves deployment of a BMS into the aorta of a donor mouse which is surgically grafted onto the carotid of a recipient mouse. When fed a normal chow diet, *Apoe*$^{-/-}$ mice developed significantly more in-stent stenosis than the C57Bl/6 wildtype mice after 28 days. The elevated cholesterol and vascular inflammation present in *Apoe*$^{-/-}$ mice was hypothesised to influence the increased rate of stenosis observed. In the study by Ali *et al.* [174], the focus was solely on in-stent restenosis and did not examine in-stent neoatherosclerosis. Using the same surgical approach, we hypothesised that following stent deployment in the *Apoe*$^{-/-}$ mice if a HCD was then introduced [148, 175] it would trigger the formation of a plaque-like phenotype in the stented region mirroring that of in-stent neoatherosclerosis.

Accordingly, this Chapter has explored the development of a murine in-stent neoatherosclerosis model. The initial intent was to determine if porphysomes could detect and suppress neoatherosclerosis development. This first foray into model development, however, presented challenges and only a limited number of stents-maintained patency throughout the experiment. Therefore, this chapter describes the results of these experiments as we work towards the development of a novel murine in-stent neoatherosclerosis model.

6.2 Methods

6.2.1 Stented aorta-carotid interposition grafting procedure

For one week before and throughout the duration of the study, mice were supplied aspirin dissolved in their drinking water at 10 mg/kg/d (Aspro Clear, Bayer). The surgical procedure has been previously described by Ali *et al.* [174]. Briefly, the thoracic aorta of the donor mouse was isolated from the arch to the diaphragm and periaortic fat was dissected off. A small transverse arteriotomy was made marginally superior to the diaphragmatic outlet. For stent deployment, a 1.25 mm x 6 mm (nominal diameter x balloon length) Pantera-pro balloon angioplasty catheter (Biotronik, Berlin, Germany) with a stainless-steel stent (2.5 x 0.6 mm in dimension), crimped onto the balloon, was inserted retrograde up the thoracic aorta and deployed by inflation of the balloon to 12 atm of pressure for 30 sec. After inflation, the heart was flushed with heparinised PBS (10 iU/mL), the balloon catheter removed and aorta harvested by electrocautery, sealing the branching intercostal vessels. The harvested aortas did not exceed a total ischemic time of 3 h and were stored in PBS.

In the recipient mouse, a ventral midline incision was made in the neck, with the sternocleidomastoid muscle cauterised and salivary gland removed. The right common carotid artery was isolated from the thoracic inlet to the bifurcation, ligated, and divided between ties at the midpoint using 7-0 silk sutures (768G Black braided, Ethicon, NJ, USA). Polyimide cuffs with an outer diameter of 0.0215”/0.55 mm (Cole Parmer, IL, USA) were threaded over each end and anchored by haemostatic clamps. The artery was everted over cuffs using vessel dilator forceps (0.2 mm tips) and secured with 8-0 silk sutures (SMOS81 Blue, Bydand Medical, Australia). The donor aorta was then interposition-grafted by sleeving its ends over the carotid artery cuffs and securing using 8-0 silk sutures. Vessel patency was determined by removing clamps and restoring blood flow to the vessel. The skin was closed using 6-0 silk sutures (639G Black braided, Ethicon, NJ, USA) and the median time of the procedure was approximately 60-90 minutes.

6.2.2 In-stent neoatherosclerosis model and nanoparticle administration

Immediately following the stenting procedure, mice were fed 21% fat, 0.15% cholesterol Semi-Pure Rodent Diet (SF-00219, Specialty Feeds) for 6-8 weeks (42-56 days). Mice were injected on alternate days with either 40 mg/kg of discoidal R4F-HDL mimetic nanoparticles (POR) or PBS vehicle via the intraperitoneal cavity.

At six weeks post-surgery, a sample of animals were injected intravenously with approx. 18.5 MBq of ^{64}Cu-labelled 30 mol %-porphyrin-lipid discoidal porphysome nanoparticles (^{64}Cu-porphysomes) 6 h prior to imaging with PET. 24 h prior to sacrifice, animals were administered 5 mg/kg of the 30 mol %-porphyrin-lipid discoidal porphysome nanoparticles.

6.2.3 JB-4 resin embedding of stented aortas

Mice were humanely killed by cardiac puncture then perfusion flushed via the left ventricle with 10 mL of PBS. Stented aortas were excised and fixed overnight at 4^{o}C in 4% paraformaldehyde (PFA). The stented aortas were then set in 00 easy moulds (Proscitech) with approx. 2-3 drops of 4% agar to position the stent upright and then removed from moulds and stored in 70% ethanol at 4^{o}C prior to embedding in resin. For JB-4 glycol methacrylate resin embedding, the aortas were dehydrated through an ethanol gradient (90% for 2 h, 100% for 1-2 h) and subsequently a 50:50 ethanol: infiltration solution (50 mL solution A + 0.45 g of catalyst) for 1 h, then infiltration solution for 1 h followed by a final overnight infiltration solution at 4^{o}C. The aortas were then embedded in a solution consisting of 25 mL infiltration solution + 1.25 mL solution B in the 00 easy moulds. Resin was set under anaerobic conditions at 4^{o}C. Resin blocks were then dried for 1-2 h and stored at room temperature.

6.2.4 Sectioning, staining and immunohistochemistry of JB-4 resin embedded stented aortas

Transverse sections of the stented aortas were cut to 5 μm on a tungsten-carbide blade with an automatic microtome (Microm HM 355S microtome, Thermo Fisher Scientific). Sections were stained with Multiple stain (Polysciences, PA, USA) according to manufacturer's instructions and imaged with the brightfield 20x objective on an Axio Scan.Z1 slide scanner microscope (Zeiss) or Nanozoomer slide scanner (Hamamatsu Photonics).

Immunohistochemistry of α-SMA on the resin embedded sections was performed with antigen retrieval by microwave for 10 min at 95°C in Tris-EDTA buffer (10 mM Tris-base, 1 mM EDTA, 0.05% v/v Tween 20 at pH 9.0). After heat retrieval, sections were placed in ice cold H_2O to cool. Once cold, sections were placed in PBS for 10 min before blocking with 10% goat serum (Sigma-Aldrich Inc., MO, USA) in PBS for 1 h at room temperature. Sections were incubated with 1:400 of α-SMA conjugated to alkaline phosphatase primary antibody (mouse monoclonal, clone 1A4, A5691, Sigma-Aldrich Inc., MO, USA) overnight at 4^{o}C. Following manufacturer's instructions, the Vector Red substrate kit (Vector Laboratories, Burlingame, CA, USA) was used to develop the staining. Sections were then dehydrated and mounted in DPX.

6.2.5 Analysis of neointimal area and strut to lumen distance in stented aortas

Analysis was performed on the stented aortas that were patent at sacrifice (i.e. no in-stent thrombosis). Five sections/mouse spanning the length of the stented aorta were analysed. Neointimal area analysis involved measuring area inside the internal elastic lamina and subtracting the luminal area. A second measure was made, ‘strut to lumen distance’, which was measured between the luminal-facing edge of stent struts and the edge of the lumen.

6.2.6 Sectioning and staining of grafted aortas without stent deployment

Paraffin embedded grafted aortas were sectioned to 5 μm on a microtome (HM340E, Thermo Fisher) and stained with H&E as described in Chapter 2 but with prior hydration with xylene-ethanol gradient. Sections were imaged with Nanozoomer slide scanner (Hamamatsu Photonics).

6.3 Results

6.3.1 In-stent neoatherosclerosis model optimisation in *Apoe*$^{-/-}$ mice fed HCD for 6 weeks

To optimise the murine model of in-stent neoatherosclerosis, a previous model of in-stent restenosis [174] was performed as illustrated in Fig 6.1. This involved the grafting of an aorta that had a stent expanded by balloon expansion from a donor mouse into the carotid region of a second recipient mouse. Initially a single mouse underwent this procedure and was fed a HCD for 6 weeks. The stented aorta graft from this mouse was examined for morphological changes. The stented aorta excised from this mouse was patent following the procedure (Fig 6.2A&B). This stented aorta was examined histologically, which revealed morphological features reminiscent of atherosclerotic plaque with cholesterol crystal deposits and regions of foam-like cells (Fig 6.2C). Furthermore, α-SMA^{+} staining of this stented aorta revealed smooth muscle cells on the luminal surface of the neointima and in the vessel wall. This suggested the formation of a stabilising cap, similar to that which also occurs in atherosclerotic plaques (Fig 6.2D).

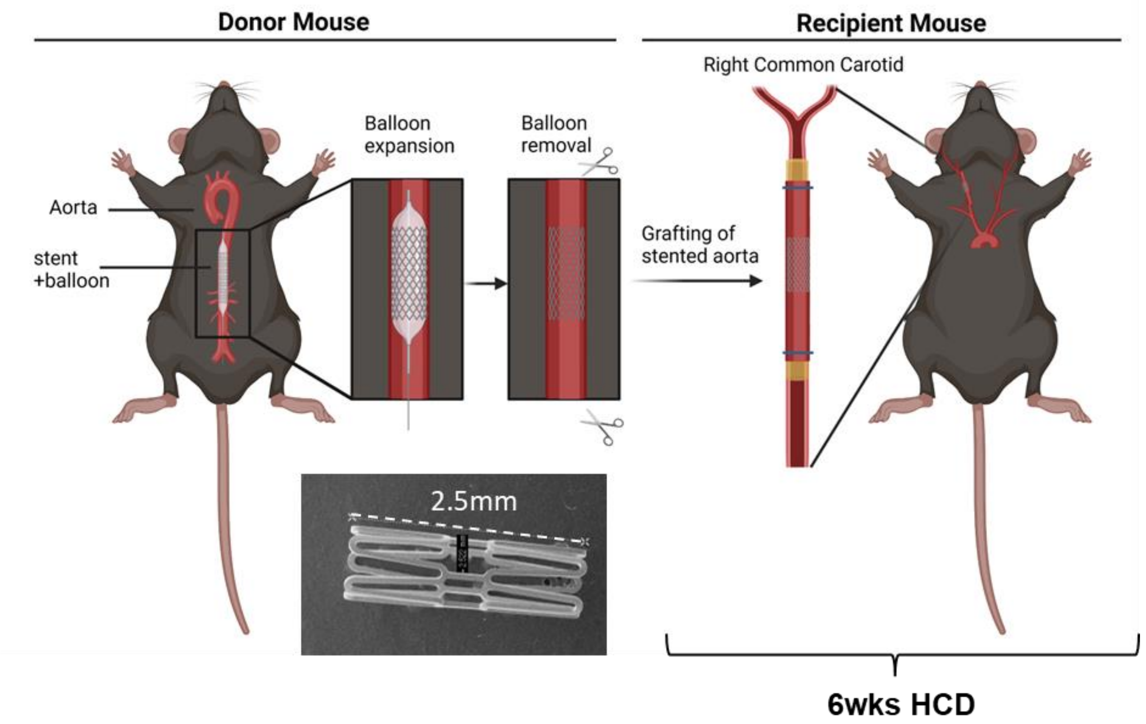
Donor Mouse
Recipient Mouse
Right Common Carotid
Balloon expansion
Balloon removal
Aorta
stent +balloon
Grafting of stented aorta
2.5mm
6wks HCD

Figure legend 6.1: Murine in-stent neoatherosclerosis model with stent deployment and carotid interposition grafting surgical procedure in *Apoe*$^{-/-}$ mice

In donor mice a 2.5 x 0.6 mm stainless steel stent was deployed by balloon catheter expansion within the thoracic aorta of donor mice. The stented region of the aorta was grafted into the right common carotid artery of recipient mice. Recipient mice were maintained on HCD for 6 weeks following surgical intervention.

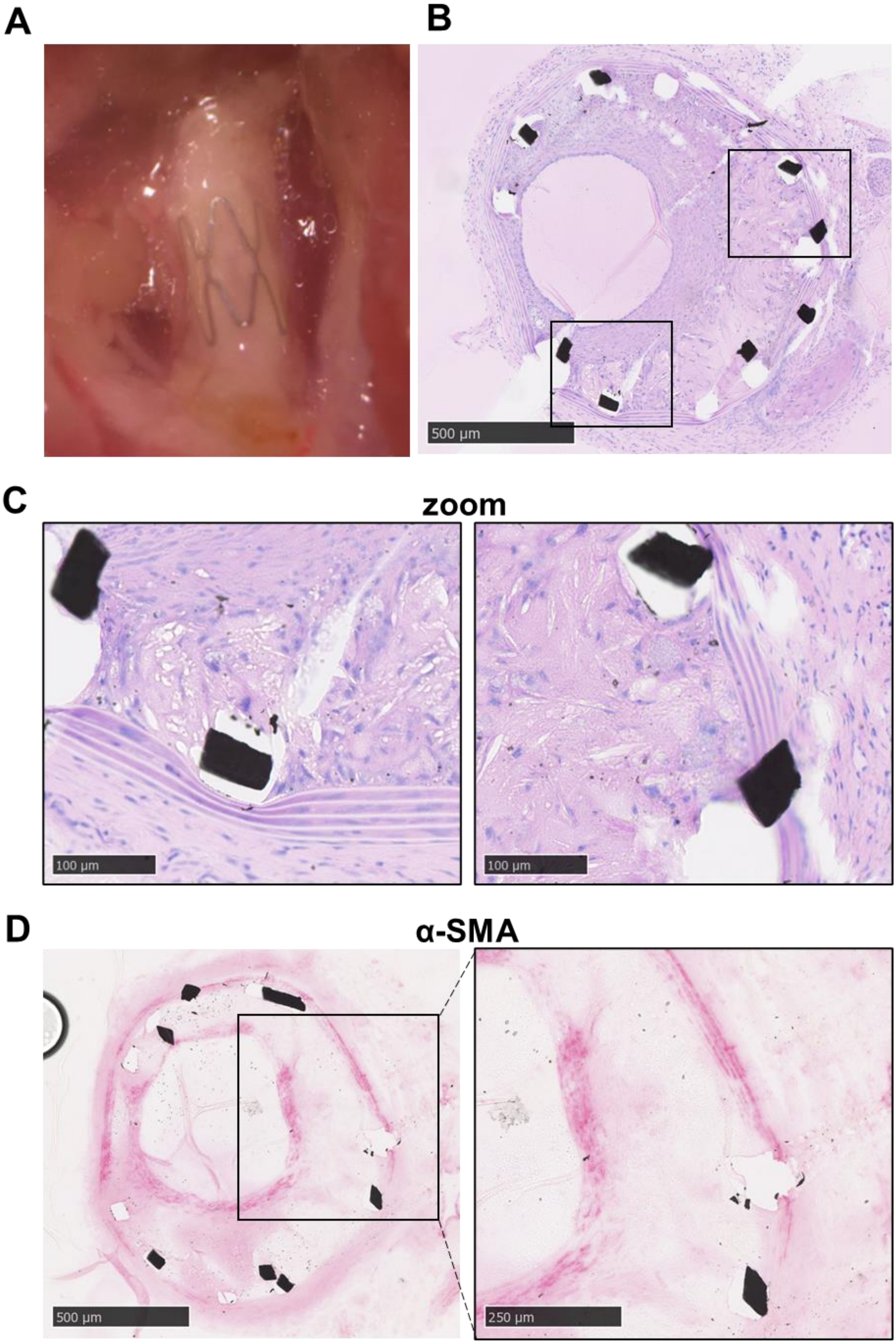
A
B
500 µm
C
zoom
100 µm
100 µm
D
α-SMA
500 µm
250 µm

Figure legend 6.2: Pilot testing of the murine neoatherosclerosis model in *Apoe*$^{-/-}$ mice reveals features of plaque development

Apoe$^{-/-}$ mouse was maintained on HCD six weeks following stenting surgery and sacrificed to examine morphology of stented aorta. (**A**) Image of stented aorta *in situ* immediately following sacrifice showing expanded stent in aorta. (**B**) Representative image of stented aorta and (**C**) zoomed images of the neointimal area near stent struts. (**D**) α-SMA staining of stented aorta. Scale bar: (B) 500 µm, (C) 100 µm and (D) 500/250 µm.

6.3.2 In-stent neoatherosclerosis model revealed a high rate of in-stent occlusion

Further experiments were conducted to measure the effect of porphysomes on in-stent neoatherosclerosis. However, upon visualisation of the stented aorta sections there was a high rate of occlusion observed, with 66% (4/6) of each of the PBS and porphysome group completely occluded. Only two aortas from both groups (33%, 2/6) were non-occluded and had maintained patency throughout the course the study. Images of these aortas are shown for each animal in Fig 6.3 showing both the occluded and patent vessels from both groups. Although most of the stented aortas were occluded only one animal was observed to have developed a thrombus within the stent following sacrifice (POR #4, Fig 6.3). In addition, in one stented aorta complete perforation of the elastic lamina was observed with the stent struts surrounding this structure (POR #1, Fig 6.3).

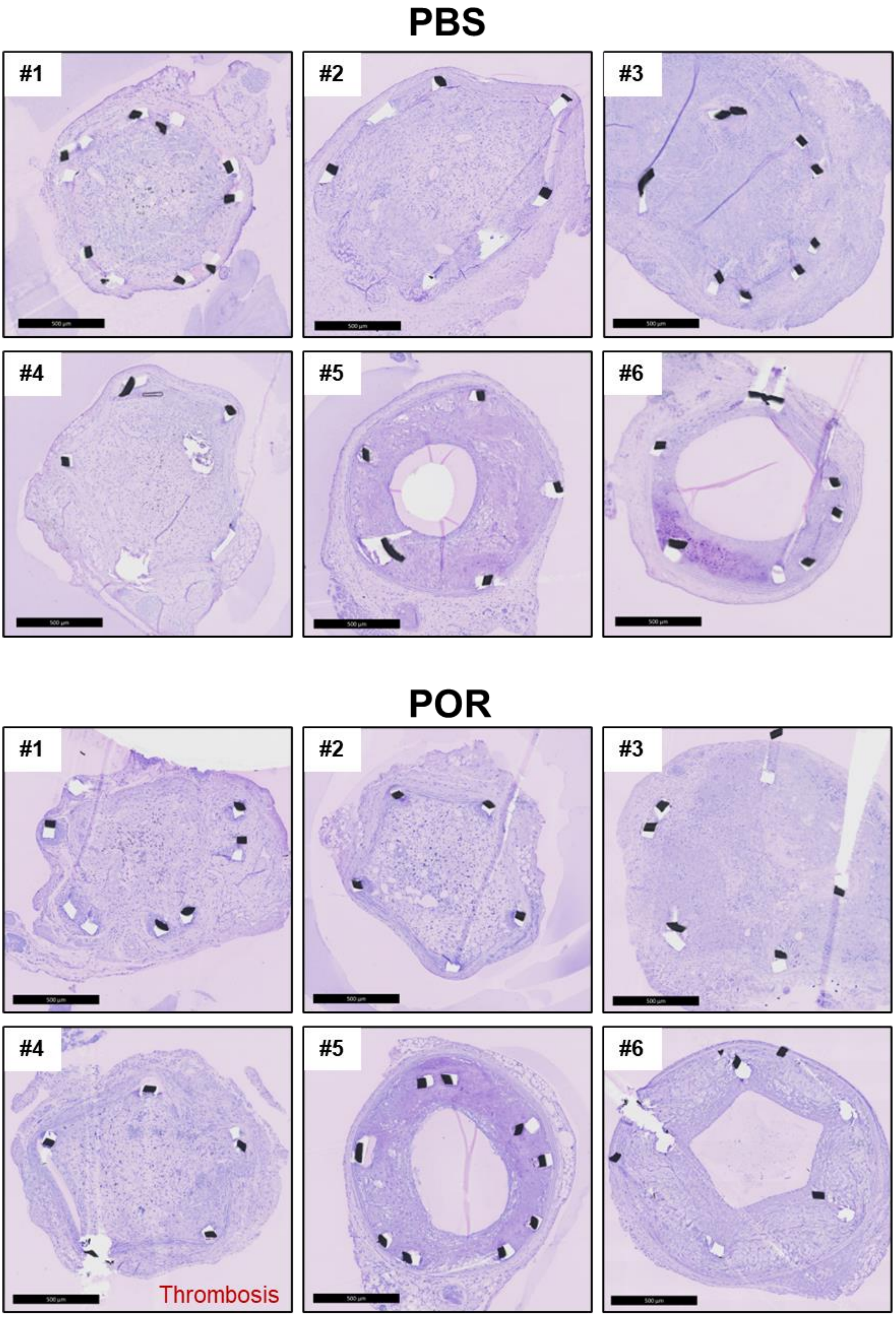
PBS
#1
#2
#3
#4
#5
#6
500 µm
POR
#1
#2
#3
#4
#5
#6
Thrombosis
500 µm

Figure legend 6.3: Representative images of stented aortas grafted into *Apoe*$^{-/-}$ mice fed a HCD for 6 weeks: Evidence of significant vessel occlusion

Apoe$^{-/-}$ recipient mice underwent interposition surgery to graft stented aortae from donor mice. In the next 6 weeks mice were fed a HCD and administered intraperitoneal injections of PBS or porphysomes on alternate days. Representative images of stented aorta sections from each animal in the PBS and porphysome groups (n=6/group) with each animal labelled #1-6 for each group. One animal (POR #4) had visible thrombosis within stent upon dissection. Scale bar = 500 μm. POR, porphysome.

6.3.3 Neoatherosclerotic area and stent strut to lumen distance measures from in-stent neoatherosclerosis model

The small number of stented aortas that maintained patency were measured for changes in the neoatherosclerotic size (Fig 6.4A). Firstly, we observed no significant changes between the neoatherosclerotic area of the PBS and porphysome treated mice (Fig 6.4B, n=2/ group). Furthermore, we also examined the distance between the stent struts and lumen, which also was not significantly different between the treatment groups (Fig 6.4C, n=2/ group). For all samples combined, the pooled measurements had an average neointimal area of 0.8096 mm^2 and a strut to lumen distance of 0.2056 mm (Fig 6.4D, n=4).

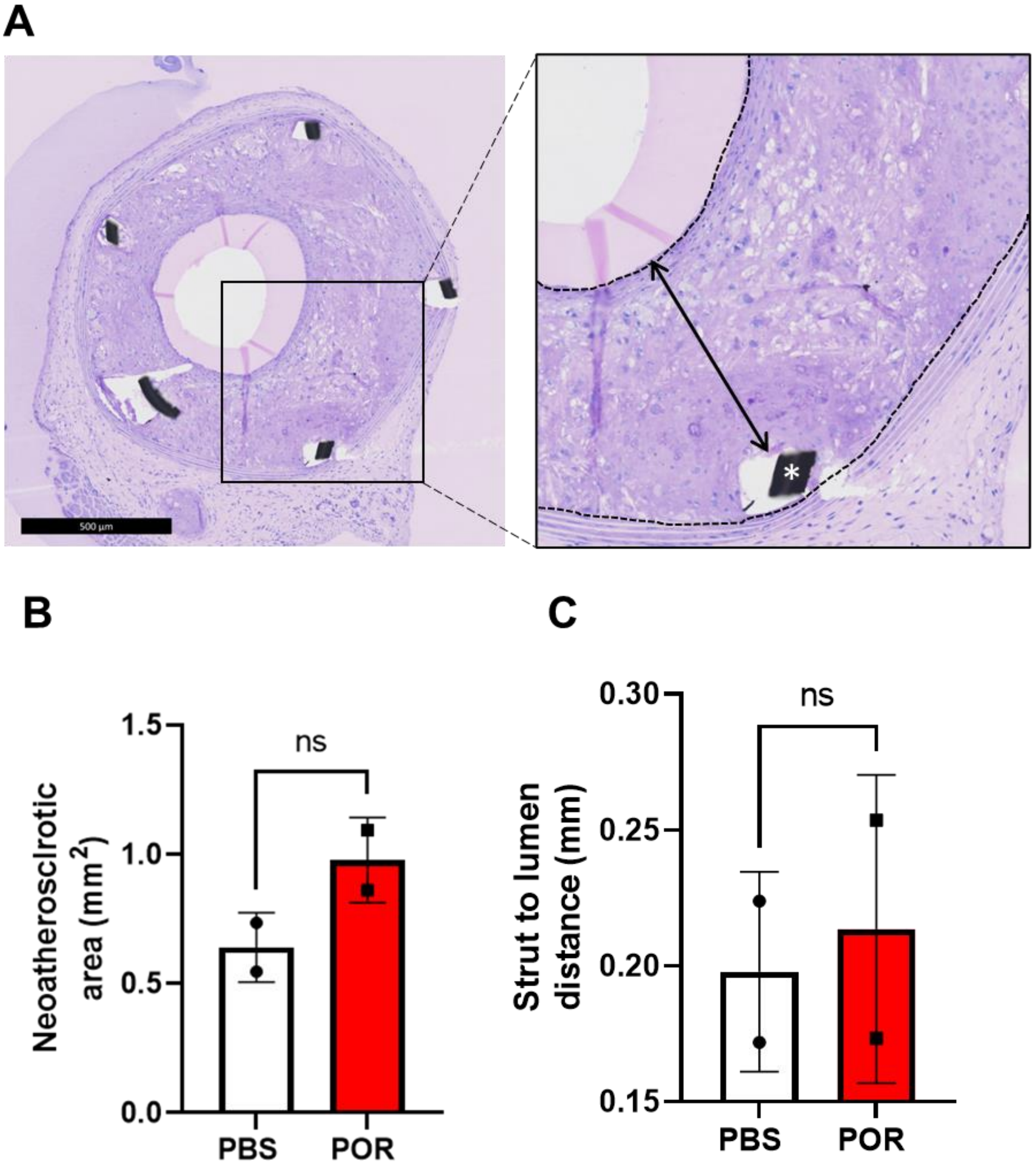

D

	Patent aortas (PBS & POR combined)
Neoatherosclerotic area (mm^2)	0.8096±0.23
Strut to lumen distance (mm)	0.2056±0.040

Figure legend 6.4: No change in neoatherosclerotic area and strut to lumen distance between PBS and porphysome treated *Apoe*$^{-/-}$ mice fed a HCD

(**A**) Representative image of stented aorta that maintained patency from PBS group with inset image illustrating stent strut (*) to lumen distance measurement with black arrow and the neoatherosclerotic area measurement indicating the lumen to the inner edge of the internal elastic lamina with black dashed line. For both PBS and porphysome treated mice quantification was made in aortas that were patent at harvest for neointimal area (**B**) and strut to lumen distance (**C**). Data represents mean ± SD (n=2/group). not-significant (ns) $P>0.05$ vs PBS control by unpaired two-tailed t-test. (**D**) Measurements from B&C were combined, and mean measurements presented for all patent stented aortas. Data represents mean ± SD (n=4). L, Lumen. POR, porphysome. Scale bar = 500 µm.

6.3.4 Stented aortas that maintained patency model some features of in-stent neoatherosclerosis in PBS and porphysome treated groups

Sections from both the PBS and porphysome treatment groups were examined for any morphological features that might be unique to in-stent neoatherosclerosis. We observed a plaque-like phenotype with some cholesterol crystal deposition and foam-like cells (Fig 6.5). A possible fibrous cap was visible at the luminal surface of the neointima, which is a characteristic of an atherosclerotic phenotype (Fig 6.5). However, these features need to be confirmed by further immunohistochemical and histological staining.

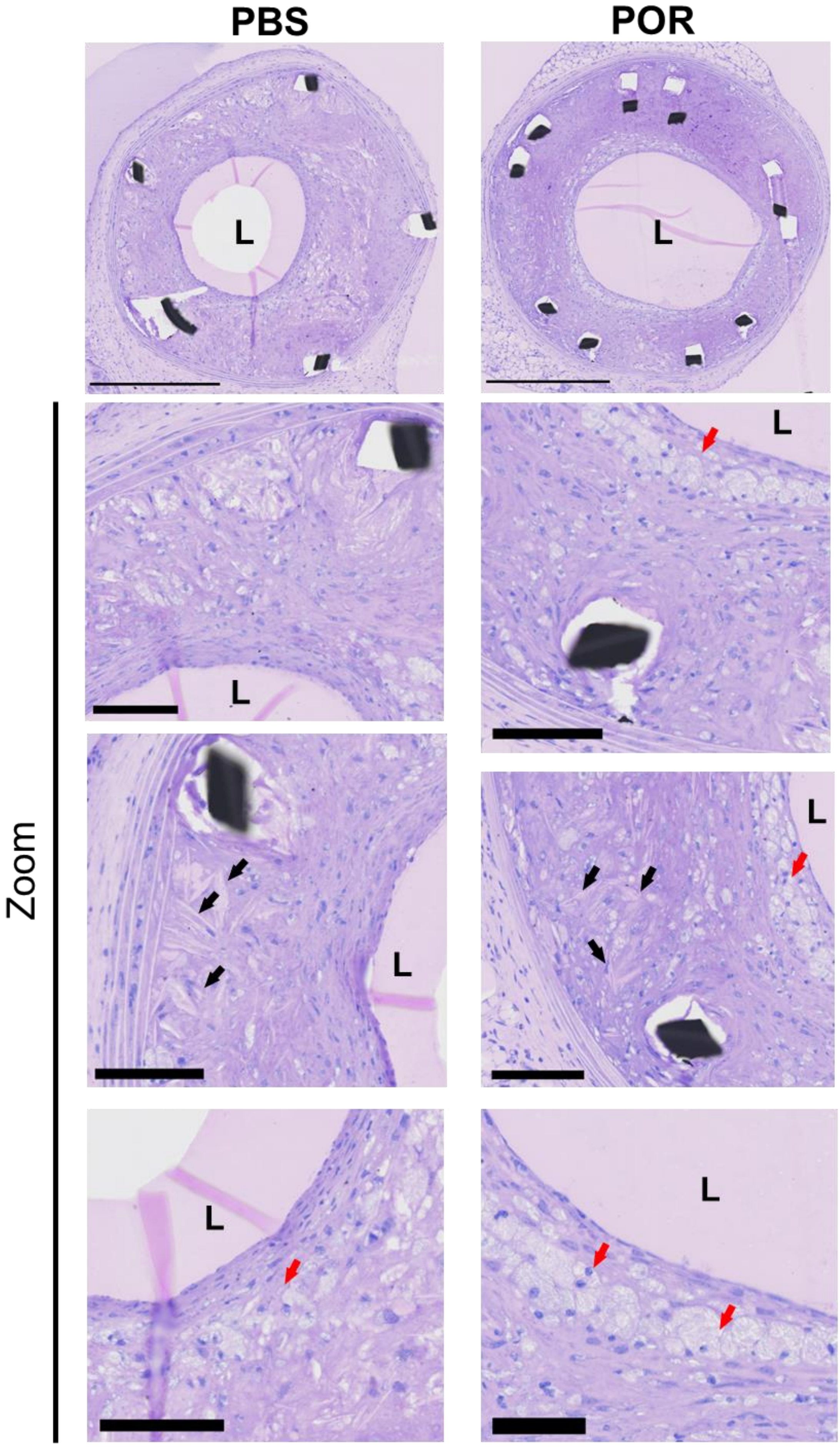
PBS
POR
L
L
L
L
L
L
L
L
Zoom

Figure legend 6.5: Morphological features of neoatherosclerosis in stented aortas from mice fed HCD

Representative images of stented aortas that maintained patency from both the PBS and porphysome treated groups. Zoomed images show some features in-stent atherosclerosis including cholesterol crystal deposition (black arrows) and potentially foam cell macrophages (red arrows). Top row images, Scale bar = 500 µm. Zoomed images, Scale bar = 100 µm. L, Lumen. POR, porphysome.

6.3.5 Grafted aortas with no stent had varied morphological features in *Apoe*$^{-/-}$ mice fed HCD

We included a control mouse the received the carotid interposition grafting surgery with balloon expansion injury but without the inclusion of the stent, followed by HCD. This demonstrated the development of a plaque-like phenotype, with some cholesterol crystal formation in the neointima. However, there was also complete occlusion of the aorta observed in this animal (Fig 6.6).

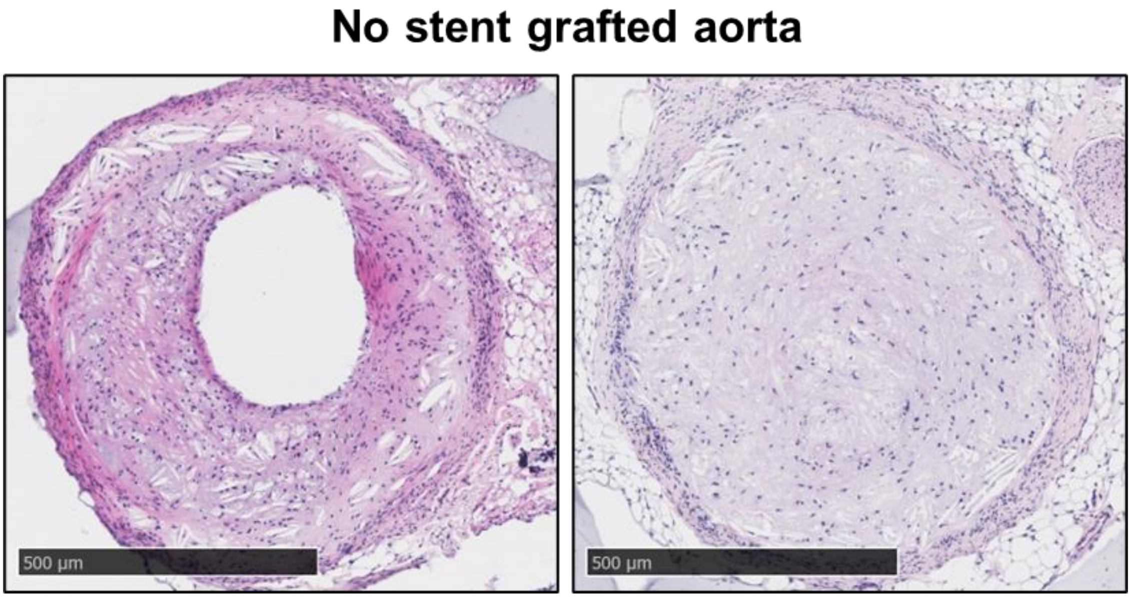
No stent grafted aorta
500 µm
500 µm

Figure legend 6.6: Grafted control aorta with balloon injury but no stent develop plaque-like features in *Apoe*$^{-/-}$ mice fed a HCD

An *Apoe*$^{-/-}$ mouse with a grafted aorta that had balloon catheter injury through balloon expansion but no stent deployment, followed by HCD feeding. Images shown were sectioned at two separate points of the vessel. Scale bar = 500 μm.

6.3.6 Porphysomes could be detected by PET and IVIS fluorescence imaging in mice with implanted stent in HCD fed *Apoe*$^{-/-}$ mice

Like the previous chapters we conducted both PET and IVIS fluorescence imaging in mice to detect the localisation of porphysomes in the in-stent neoatherosclerosis model. One animal is used as an example in Fig 6.7, of which the stented aorta was patent at time of sacrifice. This revealed that the ^{64}Cu-labelled porphysomes could be detected in the right carotid, with a low-mid level activity signal (Fig 6.7A). Furthermore, we could also detect porphysomes at the stent site in the grafted aorta using *ex vivo* IVIS fluorescence imaging of the vascular tree (Fig 6.7B). This could point to the utility of porphysomes to localise to the area of in-stent neoatherosclerotic plaque, but this will require further investigation.

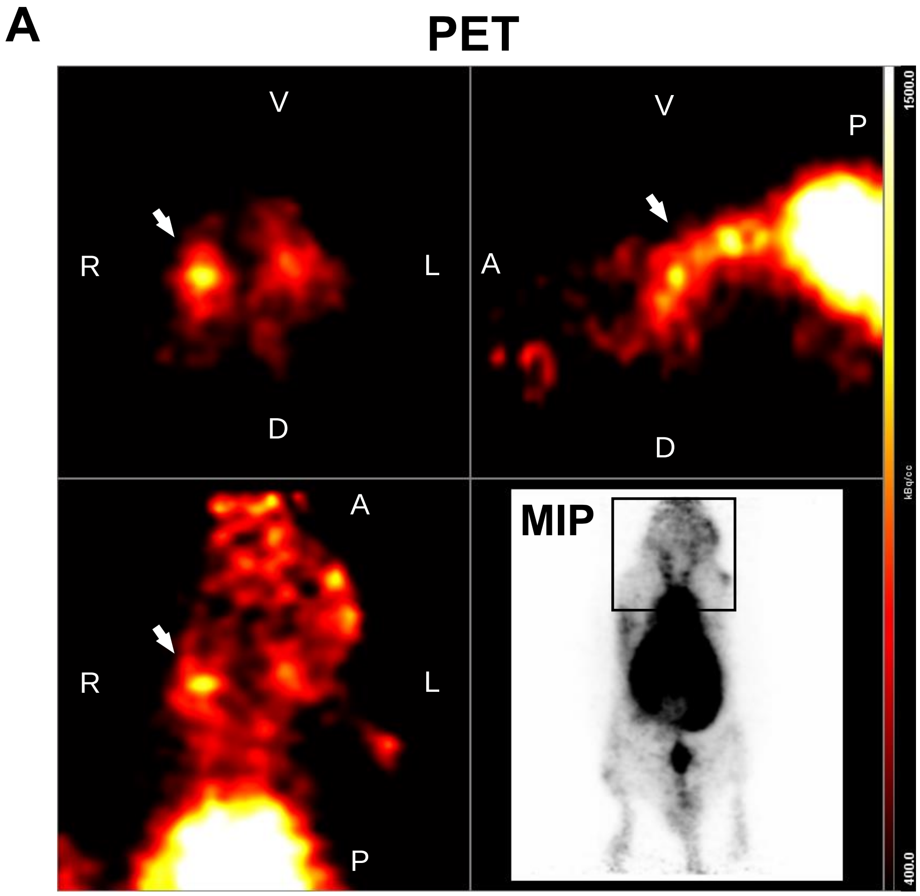
A
PET
V
R
L
D
V
P
A
D
A
R
L
P
MIP
1500.0
kBq/cc
400.0

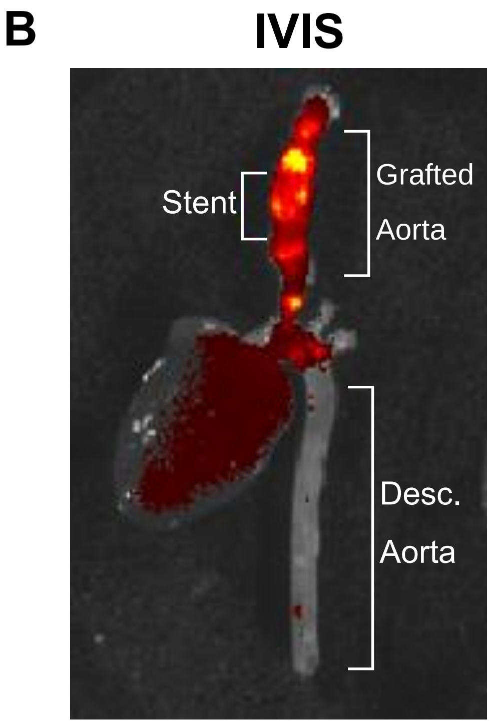
B
IVIS
Stent
Grafted
Aorta
Desc.
Aorta

Figure legend 6.7: Representative images of porphysomes detected in stented aorta graft region with *in vivo* PET and *ex vivo* IVIS fluorescence imaging

(**A**) PET image of mouse with grafted stented aorta in the right carotid region (indicated by white arrow) 6 h post-injection of ^{64}Cu-porphysomes six weeks post-surgery. (**B**) IVIS fluorescence image of the excised vascular tree *ex vivo* 24 h post-injection of porphysomes. The stented aorta in this mouse was patent at sacrifice. V, Ventral; D, Dorsal; R, Right; L, Left; A, Anterior; P, Posterior. Desc., Descending.

6.4 Discussion

Although the introduction of newer generation DES has led to a reduction in both re-stenosis and late thrombotic events, in-stent neoatherosclerosis remains as a contributor to late vascular complications following stent implantation. In-stent neoatherosclerosis is an accelerated form of atherosclerosis that develops over months and years compared to decades for native atherosclerosis. However, the mechanisms that underlie in-stent neoatherosclerosis and why it occurs so rapidly are unknown [37, 43]. This highlights the need for an experimental model that can be used to investigate the molecular and cellular mediators that contribute to in-stent neoatherosclerosis. The study outlined in this chapter has initiated the development of a murine model of in-stent neoatherosclerosis that builds upon a previous in-stent restenosis model [174, 176]. Although we have some evidence of in-stent neoatherosclerosis development in *Apoe*$^{-/-}$ mice following stent implantation, there was a high rate of occlusion in the stented aorta of these mice. This made it difficult to interpret the findings of experiments with porphysomes and indicates that further development is required to refine this model.

There are many reasons why this model of in-stent neoatherosclerosis may have resulted in such a high rate of occlusion in the stented aorta. In this study the overall rate of total occlusion was 66%, which is much higher than was observed in the previous use of the stenting procedure with occlusion rate (from thrombosis) of approx. 16-25% [174, 176]. The carotid interposition grafting surgical procedure was previously used to implant BMS into mice to study neointimal hyperplasia and in-stent restenosis [174, 176]. In this model of in-stent restenosis, the mice remain on a chow diet for 28 days (4 weeks) following surgery. The mice in this study were maintained on a high-cholesterol diet (HCD) for between 42-56 days (6-8 weeks) post-surgery, which is significantly longer than in previous studies. The variation in time on the HCD post-surgery was due to several animals imaged with PET during the post-surgical period and surgical procedures were performed over three weeks on 12 separate surgery days. HCD feeding is established as a method to accelerate the formation of atherosclerosis in *Apoe*$^{-/-}$ mice [148, 175] therefore it is possible that the extended feeding period contributed to the high rate of occlusion observed.

Other contributions to the high rate of occlusion may be attributed to several technical issues encountered during the surgical procedure. The carotid interposition grafting surgery of the stented aorta requires a high level of microsurgical skill greater than that of other small animal surgical procedures. This requires blood flow through the stented section of vessel with successful grafting of the aorta. The procedure requires several challenging steps including the eversion of the carotid over the plastic cuff to enable successful grafting. The diameter of the carotid in mice on average is approx. 0.6 mm [173] which requires the use of vessel dilator forceps with tips only 0.2 mm in size [174, 176]. In addition, the aorta of mice is only on average 0.8 mm in diameter [173], highlights the small scale of the procedure and the skill required. Initially in some mice the blood-flow did not return through the grafted region, which were not included in the experimental part of the study but were all occluded when sectioned (data not shown). The technical issues also contributed to a smaller sample size than was originally planned for, which ideally would have been approximately 12 animals per group. This highlights the need to improve the technical aspects of this model as it could be a factor in the observed rates of excessive occlusion.

From our first experience in developing this model more experimentation appears to be required to determine the optimal period of time for HCD feeding. Improvements in the technical aspects of the surgical procedure would also be desirable. Despite the technically challenging nature of this procedure, it has been performed successfully previously in studies of neointimal hyperplasia and in-stent restenosis [174, 176]. However, the work presented here was the first use of this procedure in a larger scale study as well as the inclusion of HCD and the testing of nanoparticles. Refinement of the procedure and protocol so it can be reproduced reliably in our laboratory without the occlusion seen in the morphology of the stented aortas is of high importance. It must be considered, however, that a significant amount of time and resources are required for this model with the need for personnel that have a high-level of microsurgical skill, an initial limitation that was raised by Ali *et al*. [174].

Other considerations include the balloon catheter expansion of the stent within the aorta, with previous studies using different balloon catheters and inflation pressures that may have influenced the outcome of this study. The nominal pressure to get the balloon (Pantera pro, Biotronik) that was used in this study to a diameter of 1.24 mm was only 8 atm however we decided to use 12 atm to match the pressure used in the most recent study conducted [176] with this balloon (Sprinter legend, Medtronic) requiring 12 atm as the nominal pressure to get to a diameter of 1.2 mm [176]. However, the original study by Ali *et al.* used a 1.25 mm x 13 mm catheter which was only inflated to 8 atm of pressure to get the inner diameter of the stent to 1.25 mm [174]. As the same sized stent was used in this study, alterations in some of these parameters involved in stent expansion could have contributed to the observation of high rates of occlusion by possible overexpansion of the stent and increased vascular damage imposed on the vessel wall. There were some instances of complete perforation of the elastic lamina of the aorta in our study. It has been previously shown that the degree of injury inflicted to the vessel wall during stent expansion is proportional to the amount of restenosis observed [177]. However, the morphology of the occluded aortas appeared to be thrombotic which may also be attributed to the increased injury to the aorta. Only one animal with vessel occlusion had visible red in-stent thrombosis at sacrifice. To address these technical issues, experiments could be conducted to determine the pressure required to expand the stent to an optimal diameter without causing excessive injury to the vessel wall. Previously a vascular injury scoring system has been used to assess the impact of stent expansion which could also be adopted in future to control for variability in vessel injury [174, 177].

There were some promising outcomes from this study, with stented aortas that were patent at harvest appearing to contain lipid-rich regions with some cholesterol crystal deposition observed in the neointima. There was also potential foam cell macrophage accumulation in some areas particularly towards the luminal surface based on morphology reminiscent of foam cells. Given that foam cell macrophage accumulation is an early feature of in-stent neoatherosclerosis this demonstrates that we have modelled some key morphological features [37]. Previously macrophages have been detected in the neointima of *Apoe*$^{-/-}$ mice following stent deployment and chow diet feeding for 28 days [174], so it is highly likely that macrophages would be found in our HCD fed *Apoe*$^{-/-}$ mice. However, we were unable to stain these sections for CD68 to identify macrophages, with several challenges associated with immunohistochemistry of JB-4 resin embedded sections. As JB-4 is a glycol methacrylate resin it cannot be de-plasticised prior to staining procedures meaning that many histological and immunohistochemical stains are unable to penetrate the polymerised plastic in these tissue sections [178]. Despite this we were able to complete some α-SMA staining in the initial optimisation stage, which has been successfully used in JB-4 embedded stented aorta sections previously [176]. This showed that smooth muscle cells were primarily located in both the vessel wall and at the edge of the lumen. This is indicative of smooth muscle cells localising to a fibrous cap which is a feature of atherosclerosis [179].

To compare the neointimal size to previous work, the neointimal area of all aortas that maintained patency was measured. We found that the combined average neointimal/ neoatherosclerotic area of these patent stented aortas from *Apoe*$^{-/-}$ mice was 0.8096 mm^2 after HCD feeding for 44-56 days. In contrast Ali *et al.* [174] found that the average neointimal area for restenosis after 28 days on chow diet was only 0.26 mm^2 in C57Bl/6 mice and increased by 30% in *Apoe*$^{-/-}$ mice (approx. 0.34 mm^2). Although this data is from a past study, this indicates that the HCD and a longer post-surgical period contributed to an observed increase in neointimal area. Not only was the size of the neointima different to the previous studies but had a different morphology, with a more atherosclerosis-like phenotype compared to animals only maintained on chow diet for 28 days [174, 176]. However, this will require direct chow and HCD feeding comparisons to confirm these observations. In addition, it would be ideal to perform a larger study to confirm the reproducibility of the morphological features as the sample size presented here is too small to conduct robust statistical analysis.

We were able to generate some PET and IVIS fluorescence imaging of the stented aorta region in the recipient mice. Fluorescence *ex vivo* imaging revealed some evidence of porphysome localisation to the stented region. The ^{64}Cu-porphysome PET imaging did show activity in the right carotid region, where the stented aorta was grafted, but this was not a particularly strong signal. This may require further investigation to determine if porphysome uptake is specific in the neoatherosclerotic area. Histological analysis of porphyrin-lipid fluorescence in the neoatherosclerotic region could also be quantified in future. The processing steps for resin-embedding may have unwanted effects on the fluorescent properties of the porphyrin-lipid in the tissue, so alternative histological methods may also have to be investigated.

General limitations of the histological analysis of stented aorta samples include the requirement to be embedded into a hard resin rather than OCT or paraffin which are unable to support the metal stent struts during the sectioning process [178]. Therefore, resin embedding is required to support the metal struts and preserve the morphology of the stented aorta sections especially at the stent strut-tissue interface to enable visualisation of vascular responses to stent implantation [180]. There are other types of resin, such as methyl methacrylate (e.g Technovit 9100), that are available for use that can be de-plasticised and are therefore compatible with a wider variety of histological and immunohistochemical stains [174, 178, 180]. However, JB-4 has been the most successful resin used previously by our group so was used for embedding all stented vessels. In future it may be appropriate to use a methyl methacrylate resin to enable further immunohistochemical analysis of these stented aortas to determine the presence of foam cell macrophages, a characteristic feature of in-stent neoatherosclerosis in the peri-strut and luminal surface regions [37, 43]. There are also other histological features that could be investigated such as collagen or lipid content. Although Oil Red O and other lysochrome stains for lipids can only be used on frozen sections, with paraffin and resin embedding requiring ethanol dehydration which removes lipids from the tissue [181]. This may make it difficult to analyse the lipid deposition in the neointima of stented aortas.

It is also worth considering that mice have many inherent differences in vascular wall structure when compared to humans. Typically, mice have a more prominent internal elastic lamina [173] and the aorta is a more elastic artery than that of the muscular coronary arteries that are subjected to stent implantation in humans [174], which may limit the translation of findings in this model. Moreover, in clinical practice stent implantation is used to expand areas of stenosis caused by native atherosclerosis [7].

Therefore, a limitation of this model is that there would be the lack of underlying atherosclerotic plaque in the aorta, as mice were not given a HCD prior to stent deployment. It could be possible in future to induce atherosclerosis development prior to stent deployment although this may require a long period on HCD as the thoracic aorta typically develops plaque at a slower rate than other vascular sites in *Apoe*$^{-/-}$ mice [148, 152]. This would better reflect stent deployment in humans but may not be necessary as in most cases in-stent neoatherosclerosis does not involve continuation of the underlying atherosclerotic lesion [37, 42].

In-stent neoatherosclerosis is consistently observed earlier in DES as compared to BMS [39, 42, 172], so it would also be appropriate to incorporate DES into this model. Other groups that have observed features of in-stent neoatherosclerosis following stent deployment in rabbits [46, 47] used DES in their studies. Therefore, inclusion of DES in our murine model would be advantageous as it may lead to discovery of novel mediators that may explain the differences between in-stent neoatherosclerosis in BMS and DES.

In the immediate future, an important experiment to conduct would be to include comparison of HCD to chow diet feeding to show that the HCD directly influences the development of histopathological features of in-stent neoatherosclerosis. Another consideration is to conduct a time course study (e.g. 1, 14, 28, 42 days) to track the development of neointimal expansion caused by neoatherosclerosis over time as was done by Ali *et al.* [174]. Other experiments might involve analysis of stented aortas using other molecular and cellular techniques such as RT-qPCR or flow cytometry to complement the histological analysis. This could help to further tease out the cellular composition of the stented aortas and as a viable alternative to immunohistochemistry in resin embedded sections.

Although we were unable to show that this murine in-stent neoatherosclerosis model consistently develops a suitable phenotype there were relevant histological features found in some animals. A major hurdle is the high level of skill in completing the challenging surgical procedures required for this model. Furthermore, there are many opportunities to improve upon this model including modifications of several technical details of the surgical procedure and timing of HCD feeding. Overall, this study provides a stepping stone for future work in the establishment of a murine model of in-stent neoatherosclerosis that has the potential to be an important future preclinical testing platform for next generation stent technologies and anti-atherosclerotic drugs.

CHAPTER 7
General Discussion

7.1 General Discussion

Cardiovascular disease (CVD) is the leading cause of morbidity and mortality worldwide, manifesting as a heavy health and societal burden [1]. Atherosclerosis, the major underlying cause of CVD, involves the deposition of lipid-rich plaques within the arteries. Despite the wide-spread adoption of strategies to minimise cardiovascular risk including the use of lipid-lowering interventions, blood pressure management, smoking cessation and other lifestyle modifications, there is still residual risk even in healthy individuals [13]. Therefore, novel strategies to improve the existing treatment and detection of atherosclerosis are needed. Nanotechnologies have recently emerged as a novel way to improve the efficacy of current CVD treatments and diagnostics. The use of nanotechnology can improve the overall pharmacokinetic profile of therapeutic and diagnostic agents to reduce systemic and off-target effects by improving the specific delivery to targeted regions. In atherosclerosis, macrophages accumulate in lesions where they are involved in key processes such as lipid metabolism, inflammation and efferocytosis that influence plaque progression. Therefore, macrophages are a desirable target for nanoparticle-based interventions in atherosclerotic CVD.

Nanotechnology also enables the synthesis of multi-functional nanoparticles that can combine both therapeutic and diagnostic components to produce a nanoparticle that is “theranostic”. A nanoparticle that could both reduce atherosclerosis progression whilst able to be monitored non-invasively to assess the extent of atherosclerotic disease progression would be highly valuable for management of CVD.

Porphysomes are nanoparticles that contain a unique porphyrin-lipid conjugate that is compatible with both fluorescence and PET imaging, enabling multimodal imaging capabilities [85, 89]. ApoA-I-linked porphysomes, that contain an apoA-I mimetic peptide R4F, were assessed in both *in vitro* and *in vivo* models relevant to atherosclerotic CVD. These HDL-mimetic porphysomes were predicted to target plaque macrophages via interaction of the R4F peptide with the scavenger receptor SR-BI [89, 90] which may also be therapeutically anti-atherosclerotic based on previous studies of HDL [63, 117-120]. Therefore, this thesis has investigated the use of apoA-I porphysome nanoparticles as a potential theranostic agent for atherosclerotic CVD.

As shown in Chapter 3 we discovered that apoA-I-porphysomes were able to efflux cholesterol, reduce expression of several key inflammatory cytokines and were detected in cultured macrophages *in vitro*. This is significant as it appears that porphysomes have mimicked some of the beneficial functionality of HDL *in vitro*. As well as this, we could detect the uptake of apoA-I-linked porphysomes *in vitro* within macrophages which is important as it confirmed the potential of porphysomes to be used to detect macrophages *in vivo*.

One of the most significant findings *in vitro* was that the apoA-I linked porphysomes were able to drastically reduce the expression of IL-1β mRNA and protein following inflammatory stimulation of macrophages. Agents that can inhibit IL-1β have already been investigated in CVD with the Canakinumab anti-IL-1β antibody showing a reduction in recurrent cardiovascular events in those with a previous MI, proving that anti-inflammatory therapy is effective in CVD [73]. However, it is unclear how effective porphysomes will perform as an anti-inflammatory nanoparticle. Although the expression of another pro-inflammatory cytokine, CCL5, was significantly reduced by porphysome treatment, CCL2 was increased. These findings were from an *in vitro* setting, highlighting the need to further investigate the overall impact of porphysomes beyond macrophages *in vitro*. Mechanistically, the release of IL-18 and IL-1β is attributed to NLRP3 inflammasome activation which has been implicated in driving plaque progression [130, 132, 182]. We found porphysomes inhibited the transcription factor p65-NFκB, that activates inflammasome assembly, and suppressed components of the inflammasome complex. This suggests that NLRP3 inflammasome inhibition is important in the anti-inflammatory effects of porphysomes.

A key discovery made in Chapter 3 was the excellent uptake of porphysomes into cultured macrophages which could be demonstrated by fluorescence microscopy. This uptake is likely to be via scavenger receptor SR-BI [183], which is the cellular target of the R4F-peptide contained in the outer shell of porphysomes [90]. Due to the scavenging nature of macrophages, this uptake may also have been at least in part via passive non-specific mechanisms. Whilst, highly expressed on plaque macrophages, specifically targeting macrophages via SR-BI may have some limitations as it is expressed on other cell types including hepatocytes and endothelial cells [24]. Despite this, direct interaction with SR-BI has been shown to improve the cytosolic delivery of nanoparticle cargo [90] which would be a key consideration if porphysomes were to be used as a carrier for a therapeutic agent in future.

ApoA-I-porphysomes were also able to induce cholesterol efflux in macrophages. This has implications for the potential of porphysomes to improve the removal of cholesterol from plaque macrophages by reverse cholesterol transport to inhibit atherosclerosis progression [184]. To add to these findings, we observed that the anti-inflammatory effects of porphysomes were not entirely linked to cholesterol efflux from macrophages when compared to MβCD-induced passive cholesterol efflux. This showed that the apoA-I porphysomes were able to demonstrate a greater inhibition of inflammation as compared to MβCD. This suggests that apoA-I porphysomes may act to exert anti-inflammatory effects via cholesterol efflux dependent and independent mechanisms, which are similar to that of endogenous HDL [59, 118]. Overall, the *in vitro* findings from Chapter 3 indicate that apoA-I-linked porphysomes have multi-functional effects on macrophages by reducing inflammation and promoting cholesterol efflux.

The findings from Chapter 3 are summarised in Fig 7.1 which describes the properties of apoA-I-linked porphysomes observed in macrophages *in vitro* highlighting some of the knowledge gaps that remain and require further investigation.

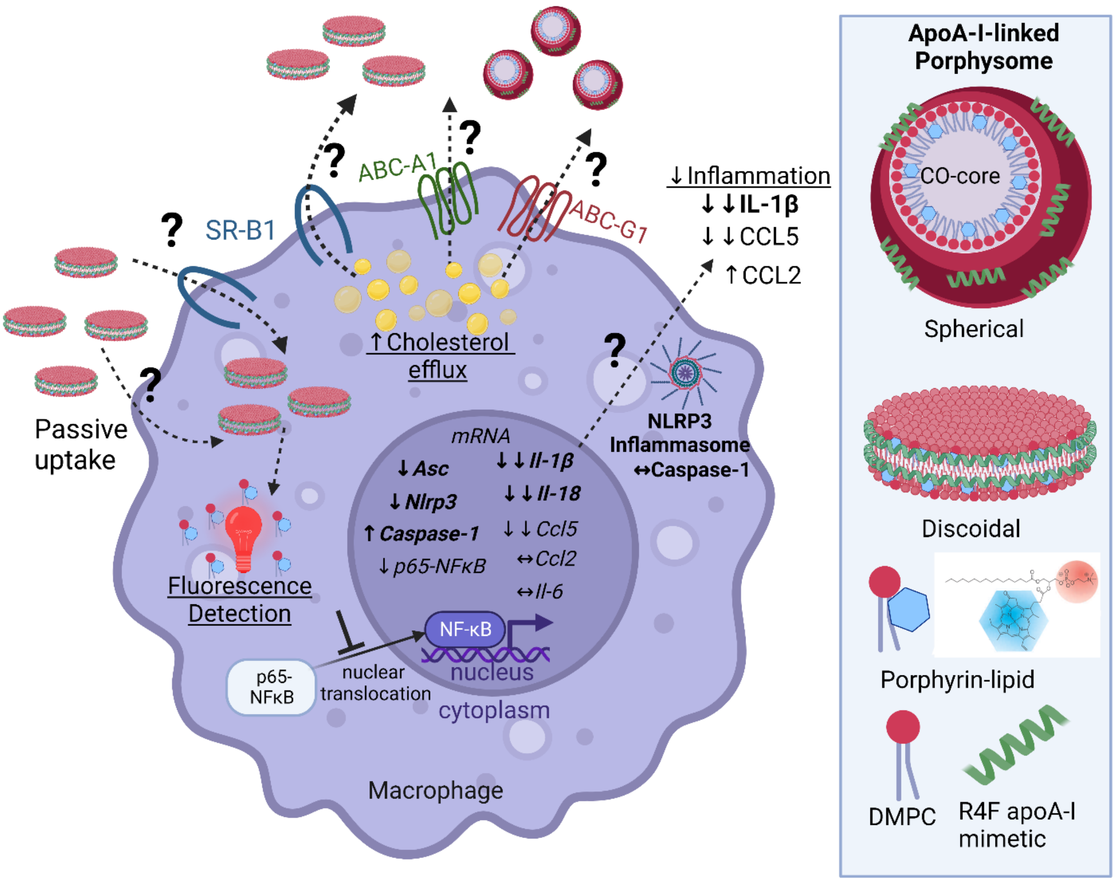
?
SR-B1
ABC-A1
ABC-G1
Passive uptake
↑Cholesterol efflux
↓Inflammation
↓↓IL-1β
↓↓CCL5
↑CCL2
NLRP3 Inflammasome
↔Caspase-1
mRNA
↓Asc
↓Nlrp3
↑Caspase-1
↓p65-NFκB
↓↓Il-1β
↓↓Il-18
↓↓Ccl5
↔Ccl2
↔Il-6
Fluorescence Detection
p65-NFκB
nuclear translocation
NF-κB
nucleus
cytoplasm
Macrophage
ApoA-I-linked Porphysome
CO-core
Spherical
Discoidal
Porphyrin-lipid
DMPC
R4F apoA-I mimetic

Figure legend 7.1: Diagram summarising the therapeutic and diagnostic properties of apoA-I-linked porphysome nanoparticles in macrophages *in vitro.*

Findings from Chapter 3 of this thesis. Diagram illustrates nanoparticle structure of apoA-I-linked porphysome nanoparticles synthesized with porphyrin-lipid conjugate, DMPC (1,2-Dimyristoyl-sn-glycero-3-phosphocholine) and R4F apoA-I mimetic peptide in both discoidal and spherical forms. Spherical form has a CO (cholesteryl oleate) core. Discoidal apoA-I-linked porphysomes (30 mol %) were internalised by macrophages detected by the fluorescence signal from the porphyrin-lipid however the exact route of uptake is unclear but could be via SR-BI mediated or passive mechanisms. Both discoidal and spherical forms increased cholesterol efflux hypothesized to be via interactions with SR-BI, ABCA1 or ABCG1. ApoA-I-linked porphysomes led to an overall decrease in expression of inflammatory genes (e.g cytokines IL-1β and CCL5) which could be explained by inhibition of the nuclear translocation of p65 subunit of NFκB. There was an observed decrease in expression of some components of the **NLRP3 inflammasome (in bold)**, but it is unclear if inhibition of the inflammasome is the underlying mechanism of the observed anti-inflammatory properties.

↔ = no change. ↓ = decrease. ↑ = increase. Created with BioRender.com

There are limitations to relying on interpretation of results from *in vitro* experiments alone, especially in drawing conclusions about atherosclerosis. Porphysomes were therefore tested on *in vivo* models of atherosclerosis, in *Apoe*$^{-/-}$ mice. The aim of these experiments was to assess whether the properties that we observed *in vitro* would translate to an *in vivo* atherosclerosis model.

Chapter 4 and 5 found that apoA-I-linked porphysomes localise to and can be detected at sites of atherosclerosis *in vivo.* This was demonstrated at sites of stable atherosclerosis (Chapter 4) detected using the fluorescent porphyrin-lipid primarily in the aortic sinus (fluorescence microscopy), aortic arch (IVIS imaging) and heart region (PET imaging). This uptake was verified by quantitative methods (γ-counting) in the heart and aorta. Further quantification using flow cytometric analysis also confirmed that the fluorescent porphyrin lipid could be robustly detected in aortic cells, particularly in aortic macrophages. In agreement with these findings, Chapter 5 shows detection of the fluorescent porphyrin-lipid in the unstable plaque using fluorescence microscopy in the carotid of mice with tandem stenosis induced plaque instability. However, PET/ IVIS imaging of the carotid region in these mice did not reveal any specific detection in the unstable plaque region. In both models, porphysomes were detected in CD68^{+} macrophages in the plaque region using florescence microscopy, indicating uptake in plaque macrophages. Overall, this data shows that apoA-I-porphysomes can be detected in regions of plaque deposition *in vivo*, but this is not specific to stable or unstable plaque. This is unsurprising as porphysomes target macrophages that are common to both stable and unstable plaque.

When comparing these findings to previous studies of porphyrin-lipid based nanoparticles, this is the first study in which this type of nanoparticle has been applied to atherosclerotic disease models. This is an advancement towards developing porphysomes for applications in CVD. Only one other CVD-related application has been reported with folate-conjugated porphysomes. These porphysomes were found to track to macrophages at the site of infarction in the ischemia/reperfusion MI model, as detected using non-invasive FMT and PET/CT imaging [113]. This was not, however, tested in a model of atherosclerotic plaque as used in the studies of this thesis. The apoA-I-linked porphysomes in this thesis contain an apoA-I mimetic peptide, which is most closely related to the testing of HDL-mimetic nanoparticles for their accumulation and detection in atherosclerotic plaque [54, 58, 185, 186]. Overall this thesis provides evidence that apoA-I porphysomes have the capacity to detect plaque deposition *in vivo* and this is in keeping with previous work into the development of HDL mimetic nanoparticles to localise to and detect atherosclerosis.

This thesis aimed to investigate the potential therapeutic properties of apoA-I-porphysomes on atherosclerosis progression *in vivo* (Chapter 4 and 5). In Chapter 4, we assessed the changes in stable plaque size and composition in the aortic sinus by histology, which revealed apoA-I-porphysomes had no effect on plaque size, collagen, lipid, macrophage or smooth muscle cell content. Further quantitative measures (flow cytometry) also supported these findings, as apoA-I-porphysomes did not induce significant widespread cellular changes in the aortas of these mice. However, there were some indications of a non-significant reduction in aortic macrophage content, particularly M2 macrophages. In Chapter 5, in the tandem stenosis model of unstable plaque, infusions of apoA-I-porphysomes did, however, have a modest effect on plaque size in which there was a significant reduction in area in the mid-section of Segment I. The same histological changes for stable plaque were also measured in unstable plaque which revealed no changes except that apoA-I-porphysomes reduced collagen content. It is also interesting that we saw some decreases in plaque size and collagen content only in the unstable plaque, which indicates that the apoA-I porphysomes may have different effects on unstable plaque compared to stable plaque. Typically collagen is associated with stabilisation of plaque, reducing the risk of plaque rupture [165]. This indicates that apoA-I-porphysomes may reduce plaque stability.

Although *in vitro* apoA-I-porphysomes were extremely effective at promoting cholesterol efflux and reducing inflammation in macrophages, their effects on plaque *in vivo* were relatively modest.

It is possible that *in vivo* the plaque is not impacted by inhibition of pro-inflammatory cytokines such as IL-1β or cholesterol efflux at the timepoint that we examined which was a later stage of atherosclerosis progression. This may come down to timing of treatment, as HDL and apoA-I based therapies that are known to be involved in cholesterol efflux and reverse cholesterol transport have not been shown to be highly effective clinically [59, 184]. This has been partially explained by preclinical experimentation that indicates that apoA-I treatment only has beneficial therapeutic effects in the early stages of atherosclerosis in HCD fed *Apoe*$^{-/-}$ mice and not in the later stages [149]. Currently our group is assessing the effect of these apoA-I-porphysomes at an earlier timepoint of plaque development with a shorter duration of HCD feeding (6 weeks) in *Apoe*$^{-/-}$ mice with extensive flow cytometric and histological analysis to determine if the timing of nanoparticle administration is important for therapeutic effects to be observed *in vivo*.

There are some considerations to be taken into account when interpreting the results from the *in vivo* experiments conducted in this thesis. The “therapeutic” nanoparticles that were administered either three times per week or on alternate days were synthesised without porphyrin-lipid (R4F-HDL mimetic NPs). The reasoning behind this decision was the requirement for repeated injections over several weeks that would not require the imaging component of the particles and required a higher dose of the R4F apoA-I mimetic peptide to achieve 40mg/kg which has been used for apoA-I previously in *Apoe*$^{-/-}$ mice [149, 176]. In addition, the imaging studies to determine the localisation of the nanoparticles *in vivo* with fluorescence and PET imaging was conducted with particles that contained the highest porphyrin-lipid content (30 mol %). Based on these differences between the composition of these nanoparticles, the distribution of the 30 mol %- porphyrin-lipid NPs cannot be directly extrapolated to the distribution of the R4F-HDL mimetic NPs. In addition, the administration route was different for both nanoparticles, with the R4F-HDL mimetic NPs administered via intraperitoneal injection whereas the 30 mol %-porphyrin-lipid NPs administered by both intraperitoneal and intravenous injection for IVIS and PET imaging respectively. Ideally only a single route of administration would have been used to provide consistency as there are differences in distribution observed in intraperitoneal vs intravenous routes [187], with increased plaque uptake of labelled-HDL NPs administered by intraperitoneal injection shown previously [188]. Regardless of how the experimental design was implemented, the use of R4F-HDL mimetic nanoparticles with a higher R4F concentration was implemented in an effort to increase the likelihood of demonstrating an anti-atherosclerotic effect *in vivo.*

One of the unexpected observations in both the stable and unstable atherosclerosis experiments was the significant change in bodyweight in the porphysome treated *Apoe*$^{-/-}$ mice as compared to the PBS control (Chapter 4 and 5). This presented as a reduction in the average bodyweight after 4-5 weeks following the initiation of the R4F-HDL mimetic nanoparticles. This has been seen in experiments that manipulate apoA-I in mice [160] and administration of the apoA-I mimetic L-4F (reverse peptide of R4F) [189] have also reduced bodyweight in mice. Whether this effect of the R4F-HDL mimetic on body weight is beneficial, however, is currently unclear. Another interesting and unexpected finding was that plasma triglycerides were significantly lowered by apoA-I-porphysomes in mice with unstable plaque but not stable plaque. This could be attributed to the surgical intervention or the result of a higher frequency of administration of the apoA-I porphysomes in the unstable cohort which were given on alternate days compared to three times weekly in the stable cohort. It is possible that the increased frequency of the apoA-I porphysome administration in the unstable cohort may have resulted in increased clearance of circulating triglyceride-rich lipoproteins like very low-density lipoproteins (VLDL). Although this was an unexpected finding, this could be beneficial as lower levels of triglycerides are associated with a lower risk of CVD [169, 190].

We did not assess any effect of the administration of these particles on any other organs such as the liver or spleen in these mice. Previously, porphyrin-lipid based nanoparticles [85, 89] have been shown to be generally well tolerated in mice with no significant toxicity reported. However, this thesis describes the use of the R4F-HDL mimetic particles that have a much higher concentration of the R4F-peptide administered at a relatively high concentration in mice (40mg/kg) over a longer period which has not been assessed for toxicity. ApoA-I protein has previously been administered safely in *Apoe*$^{-/-}$ mice at a concentration of 40mg/kg [63, 149, 176], but it is unclear whether the activity of the apoA-I mimetic R4F in these nanoparticles, a short peptide of only 18 aa, is equivalent to the full length apoA-I protein [100]. Furthermore, these nanoparticles were administered by intraperitoneal injection which is known to produce a different pharmacokinetic release profile as compared to intravenous administration [187], which is the route that has been used previously for both apoA-I [149] and porphyrin-lipid based nanoparticles in mice [85, 89, 99, 113]. However, despite this we did not see any evidence of significant off-target toxicity *in vivo*, with animals maintaining general health throughout the study course.

The in-stent neoatherosclerosis model described in Chapter 6 remains as a work in progress. As discussed in Chapter 6, most of the stented aortas did not retain patency which limited the utility of the model in these experiments to assess robust changes in neoatherosclerosis following porphysome treatment. Despite this we discovered in the stented aortas that maintained patency, neointimal features that modelled in-stent neoatherosclerosis. Some of these morphological features included evidence of foam cells, cholesterol crystals within a necrotic core and a fibrous cap. Although we were unable to confirm whether the observed foam cells were macrophages, the presence of macrophage foam cells is an early feature of in-stent neoatherosclerosis [37, 43]. Therefore, this procedure requires further work to improve the reliability and consistency as an in-stent neoatherosclerosis model. If this were to be successfully established, it would be a first in mice and an important addition to the currently available murine models of plaque development [46, 47].

In future, the use of drug eluting stents (DES) could be an important addition to this model, to investigate differences in biological responses compared to bare metal stents (BMS), which may reveal mechanisms to explain why in-stent neoatherosclerosis is observed earlier in DES than BMS [39, 172]. Although applying the DES polymer coating onto the 2.5 x 0.6 mm stainless-steel BMS used in the murine stenting procedure, to the best of our knowledge, has not been attempted previously. However other coatings have been successfully applied such as a plasma activated coating to immobilise apoA-I protein to the stainless-steel surface [191]. An anti-thrombotic hyperbranched polyglycerol (HPG) coating [192, 193] has also been successfully applied and is currently under investigation *in vivo* by our collaborators (unpublished). It is therefore likely that the polymer coating used to make DES [29] could also be applied to these small-sized stents.

In terms of future directions of the use of porphysomes in the in-stent neoatherosclerosis model, there are some options. Clinical studies have revealed that in-stent neoatherosclerosis consists of foam cell macrophages [37, 42, 43], which are distinctive in regions of plaque rupture in patients with very late stent thrombosis (VLST) [194]. We would predict that the utility of porphysomes might be to localise to areas of macrophage deposition within areas of in-stent neoatherosclerosis *in vivo* for imaging purposes. However, the major challenge of reducing in-stent neoatherosclerosis may be in further improvements of stent biocompatibility, as endothelial dysfunction is thought to be a key factor in promoting progression of in-stent neoatherosclerosis [30]. While DES reduce in-stent restenosis by neointimal hyperplasia, primarily by inhibiting the proliferation and migration of medial smooth muscle cells, they also reduce the rate of re-endothelialisation [29]. This is thought to explain the delayed emergence of in-stent neoatherosclerosis leading to late vascular complications attributed to plaque rupture and in-stent thrombosis [195]. To improve upon currently used stents for PCI is of high importance which could be aided by a better understanding of the mechanisms that underlie in-stent neoatherosclerosis. Nanotechnologies like porphysomes could be used in future for targeted delivery of therapies and for diagnostic purposes to assist detection of macrophage accumulation.

Overall, the data presented in this thesis suggests that apoA-I-porphysomes warrant further investigation as a theranostic agent for atherosclerotic cardiovascular disease. The multi-modal imaging of regions of plaque deposition in atherosclerosis models, especially data that suggests uptake by plaque macrophages *in vivo,* supports the hypothesis that porphysomes are suitable for applications in atherosclerotic CVD.

Although our ambitions to successfully test porphysomes in a model of in-stent neoatherosclerosis were not realised, this still provides a starting point for future studies. The findings from Chapters 3-5 are summarised in Fig 7.2.

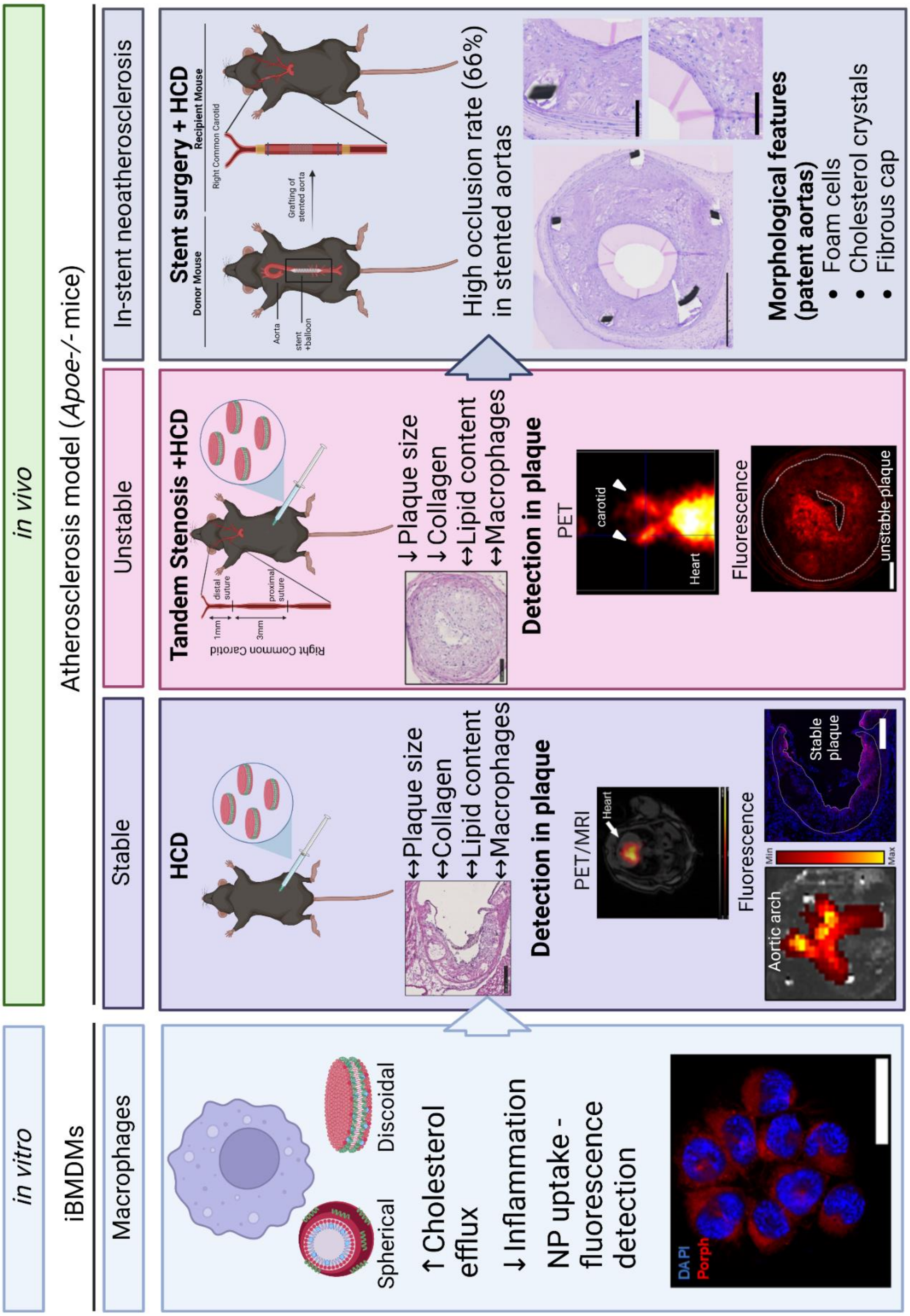
in vitro
iBMDMs
Macrophages
Spherical
Discoidal
↑Cholesterol efflux
↓Inflammation
NP uptake - fluorescence detection
DAPI
Porph
in vivo
Atherosclerosis model (Apoe-/- mice)
Stable
HCD
↔Plaque size
↔Collagen
↔Lipid content
↔Macrophages
Detection in plaque
PET/MRI
Heart
Fluorescence
Aortic arch
Min
Max
Stable plaque
Unstable
Tandem Stenosis +HCD
Right Common Carotid
1mm
3mm
distal suture
proximal suture
↓Plaque size
↓Collagen
↔Lipid content
↔Macrophages
Detection in plaque
PET
carotid
Heart
Fluorescence
unstable plaque
In-stent neoatherosclerosis
Stent surgery + HCD
Donor Mouse
Recipient Mouse
Aorta
stent +balloon
Grafting of stented aorta
Right Common Carotid
High occlusion rate (66%) in stented aortas
Morphological features (patent aortas)
Foam cells
Cholesterol crystals
Fibrous cap

Figure legend 7.2: Summary of the work described in Chapters 3-6 of this thesis representing the some of the theranostic properties of apoA-I-linked porphysomes in atherosclerosis

Figure summarizes the key results of this thesis. Initial *in vitro* studies (Chapter 3), *in vivo* studies in stable (Chapter 4) and unstable (Chapter 5) atherosclerosis, and in-stent neoatherosclerosis model development (Chapter 6). The apoA-I-linked porphysomes were able to increase cholesterol efflux, decrease inflammation and could be detected in macrophages *in vitro*. The apoA-I-linked porphysomes localise to atherosclerotic plaque *in vivo* and can be detected in regions of plaque deposition with both PET and florescence imaging. The apoA-I-linked porphysomes did not lead to robust changes in the size or composition in either stable or unstable plaque. The in-stent neoatherosclerosis model had a high occlusion rate but revealed some relevant morphological features in aortas that maintained patency.

↔ = no change. ↓ = decrease. ↑ = increase

7.2 Future directions

There are several key areas where an improved study design may have provided more information as to the efficacy of porphysomes as a diagnostic *in vivo.* Small animal imaging of radionuclides in small animal models of atherosclerosis, such as that attempted with porphysomes, is a challenge. This can be attributed to the fact that many of the sites of atherosclerosis deposition in mice are small in size and are on the edge of the resolution that PET imaging can decipher [51].

The bulk of the previous work on porphysome imaging with PET has been in tumour models in mice [89, 91], with tumour lesions much larger than atherosclerotic plaque in the vasculature of mice. In addition, there are typically very few target cells, including macrophages, located within the plaque. This makes imaging of atherosclerosis in preclinical mouse models relatively challenging. Therefore, it may be worth considering a larger animal model such as porcine models that may make imaging more translatable and overcome some of the limitations of small animal imaging [8, 51]. Porphysomes have already been shown to be safe at higher concentrations in mice [85], therefore moving onto larger animals should be possible. We could detect apoA-I-porphysomes at the site of atherosclerotic plaque *in vivo*, therefore it is worth further investigating the PET imaging capabilities for non-invasive imaging.

Furthermore, an aspect of nanoparticle imaging that was not investigated in this thesis was the use of *in vivo* NIR fluorescence (NIRF) imaging in live mice. This can be achieved with fluorescence molecular tomography (FMT), a three-dimensional imaging modality that can be used to non-invasively image the distribution of fluorescent probes *in vivo* with high sensitivity and without the use of radiation [8, 196]. We did not have access to equipment with this specific capability, but FMT has been previously used to detect porphyrin-lipid based nanoparticles *in vivo* [89, 113]. While FMT in small animal preclinical studies can be used to successfully detect fluorescent probe localisation with a high degree of sensitivity *in vivo,* this kind of technology has a limited range of penetration to a maximum depth of ~5 cm [8]. Although the fluorescence detection of porphyrin-lipid is within the NIR range and is compatible with this imaging modality, it would not be feasible for use in structures of clinical interest such as the coronary arteries in humans. A way to translate the use of fluorescence imaging of nanoparticles, like porphysomes, might be using intravascular catheter imaging. There is ongoing work within our group and collaborators that specialise in the engineering of ultrathin multimodal intravascular catheters for the detection of atherosclerosis *in vivo* [197]. These catheters are ultrathin to enable improvements in performance but also provide compatibility in small preclinical animal models for further research and development [198]. This type of catheter been used for OCT imaging with the capacity to detect fluorescence which have potential to improve characterisation of plaque morphology [197, 199]. Currently porphysome nanoparticles are being investigated in our group for detection within atherosclerotic plaque in mice with this ultrathin intravascular catheter technology. This may provide a feasible option to translate the use of fluorescence imaging of porphysomes *in vivo* in a clinical setting.

The work presented in this thesis demonstrated a lack of therapeutic impact by apoA-I porphysomes on atherosclerosis *in vivo.* However, we did demonstrate evidence that the apoA-I-porphysomes are taken up by plaque macrophages and could be detected in atherosclerotic plaque. Therefore, a future direction for this work could be to load porphysomes with another established therapeutic agent to assess whether this can improve targeting of the therapy to the atherosclerotic plaque *in vivo*. It would be hypothesised that encapsulation of an anti-atherosclerotic agent would combine targeting of the therapeutic cargo with the multi-modal imaging capabilities of the porphyrin-lipid as a theranostic approach to atherosclerosis. Porphysome nanoparticles were designed with the capacity to be loaded with a drug within the inner core. In the case of the HDL-like porphyrin-lipid nanoparticles, the NIR fluorescent dye DiR-BoA has been previously used to assess delivery of cargo within the nanoparticle core [89, 126]. Initially drug delivery to atherosclerotic plaque can be assessed using DiR-BoA as it is detected fluorescently at a different wavelength to the porphyrin-lipid [89].

We would propose that the choice of therapeutic cargo would ideally be an agent that has shown previously to inhibit atherosclerosis *in vivo*. For example, previous work has shown that incorporation of a statin (simvastatin) within an HDL coating (S-HDL) was able to improve the anti-atherosclerotic effects of the statin by reducing macrophage accumulation [54, 79]. As the apoA-I-porphysomes are HDL-like in structure, incorporating a statin as cargo might be the appropriate first step for this approach.

Another candidate for drug-loading, colchicine, is a potent anti-inflammatory drug recently repurposed for CVD. Colchicine is reported to act as an anti-inflammatory agent by targeting the NLRP3 inflammasome and reducing IL-1β cytokine release [132]. The COLCOT study demonstrated that low-dose colchicine in patients with a recent MI could significantly reduce risk of ischemic cardiovascular events [200]. However, the immunosuppressive effects of systemic colchicine administration may be a limitation to widespread use [200]. Encapsulation of colchicine in apoA-I-porphysomes could reduce some of these systemic effects and target directly to plaque macrophages. There is also a recent example of calcium carbonate nanoparticles used to improve the cardioprotective effects of colchicine in an MI model [201].

In addition to small molecule drugs, another type of cargo that could be used to boost therapeutic capacity could be siRNAs for RNA interference (RNAi) within plaque macrophages. This has been done previously with other types of nanoparticles in atherosclerosis using siRNAs targeting monocyte recruitment [202] and efferocytosis [57]. In addition, similar HDL-mimetic nanoparticles constructed with the R4F peptide, incorporated cholesterol conjugated siRNAs as cargo. This enabled the delivery of a *Bcl2* siRNA to therapeutically target prostate cancer tumours by promoting targeted apoptosis [203]. Therefore, RNAi is another potential option for atherosclerosis therapy with apoA-I porphysomes.

Another way to improve the therapeutic properties of apoA-I porphysomes is the potential for applications of photodynamic therapy (PDT) in atherosclerosis. PDT involves the specific induction of apoptosis in target cells induced by photosensitisers exposed to light. For atherosclerosis, the aim of PDT is to reduce macrophage content, inflammation and improve plaque stabilization by inducing apoptosis at the lesion site [204, 205]. As porphyrin is a photosensitiser and produces highly reactive singlet oxygen, it is able to produce the ROS that contribute to apoptotic processes that underlie PDT [86]. Previously, porphyrin-lipid nanoparticles have been shown to facilitate PDT in murine cancer models [89, 91]. Generally, there are concerns about the phototoxicity of some of the compounds used for PDT that may cause significant side effects when administered systemically. However, porphyrin-lipid based nanoparticles have been shown to have activatable PDT limited only to the region of uptake [85, 89, 91] this may avoid some of these non-specific side effects of other photosensitisers and could be used to target plaque macrophages in future. Other examples of PDT compatible nanoparticles that have targeted macrophages in atherosclerosis are by specific activation by cathepsin-B protease activity [206] and accumulation of dextran-coated iron oxide (CLIO) nanoparticles [207]. However, some of the limitations of this technique include the difficulty of light reaching the atherosclerotic areas that require PDT such as the coronary arteries. So, PDT is envisioned as a therapy that might complement intravascular procedures like PCI or intravascular imaging like OCT. Therefore, PDT using apoA-I porphysomes might be an appropriate option for an intervention of native atherosclerotic lesions but also could be an option as a way to therapeutically target in-stent neoatherosclerosis by improving stabilisation and preventing plaque rupture [204]. Potentially PDT could also be combined with intravascular fluorescence imaging using the novel ultrathin catheter system as a light source [197, 199].

Overall, these strategies might improve the therapeutic effectiveness of apoA-I-porphysomes rather than solely relying upon the action of the properties of the R4F peptide in the porphysome backbone, which may reflect the difficulties in translating apoA-I/HDL-based therapies *in vivo*. Of course, these experiments would have to be tested further in preclinical models and are beyond the scope of this thesis but do provide a future direction for the project which may improve the potential for clinical translation, especially if apoA-I porphysomes are to be considered theranostic.

Although there is still extensive preclinical testing that is required before porphysomes are used in a clinical setting, it is worth discussing the potential translational prospects as a theranostic agent. In terms of the translation of porphysomes as a potential diagnostic agent, this would have to be considered in terms of the overall properties of porphysomes in the imaging of atherosclerosis. As discussed, the lack of significant therapeutic changes in atherosclerosis in *Apoe*$^{-/-}$ mice requires further investigation into the development of a porphysome nanoparticle that has robust therapeutic effects *in vivo*. Furthermore, the studies in this thesis were only in murine models, with large animal studies a possibility to demonstrate feasibility to moving the technology to clinical applications. There is a definite potential for porphysome nanoparticles as a theranostic for atherosclerotic CVD, however there are significant hurdles that include balancing of both therapeutic and diagnostic properties. This includes optimising methods to assess these properties to ascertain the ideal dosage and timing of administration. Ideally the therapeutic and diagnostic actions of the nanoparticles would be contained within one nanoparticle formulation, which could be boosted by additional therapeutics as discussed.

One key consideration would be how porphysome nanoparticles are anticipated to work in a clinical setting. The use of radionuclides (e.g ^{64}Cu) with PET imaging introduces the potential exposure of patients to radiation [8]. This also requires the availability of an on-site facility to produce the appropriate radionuclides. If these nanoparticles were to be administered in a clinical setting, they might be prescribed for PET imaging of atherosclerotic lesions and then subsequently administered over time to provide a therapeutic option. Porphysomes could be used to deliver therapeutic cargo and over time could also be used to track atherosclerotic plaque progression over time, which some of the *in vivo* PET imaging data in this thesis suggests could be possible (Chapter 4) but will require further investigation. The obvious benefits of such an approach would be the ability to only require a single nanoparticle to be tested for both aspects of imaging and therapy [208]. The distinctive advantage of porphyrin-lipid based nanoparticles are the multifunctional properties within a single organic nanoparticle [85, 151]. The porphyrin-lipid in these particles provides the ability for multimodal imaging by fluorescence and PET modalities with other capacity for targeted therapy such as PDT. The loadable core also means these particles can be modified to load therapies, so they have potential for specific drug delivery. Despite the porphyrin-lipid nanoparticle structure possessing a relatively simple design they integrate multiple properties that make them a promising nanoparticle for theranostic applications [96].

Of other approaches to theranostic nanoparticles are currently in an early stage of development, with most only in the preclinical phase [208]. Overall, very few nanoparticle-based formulations have been progressed to human trials [55]. One example is the administration of liposome-based particles loaded with anti-inflammatory prednisolone. Although the nanoparticles did localise to human plaque macrophages *in vivo* this did not lead to detectable anti-inflammatory effects [77]. Furthermore, CER-001 a discoidal pre-β HDL mimetic had little effect on reduction or regression of atherosclerosis in patients [209-211] but Zirconium-89 (^{89}Zr) labelled CER-001 could target atherosclerotic plaque with detection by PET imaging [185]. This further highlights the utility of HDL-mimetic particles to localise to atherosclerotic plaque [58] rather than acting as a standalone therapy. Therefore HDL-mimetics, like apoA-I-porphysomes, might have greater utility as a nanocarrier of therapeutic cargo rather than as a therapeutic agent alone.

To conclude, this thesis has explored apoA-I-porphysomes as a potential theranostic nanoparticle in atherosclerotic CVD. Although there is still a large amount of investigation that is required to further assess the efficacy of porphysomes as a theranostic for atherosclerotic disease, the work presented here is novel and represents the first preclinical studies investigating apoA-I-linked porphysomes in atherosclerosis. Furthermore, the data generated from this thesis will provide guidance on further investigations of porphysome nanoparticles as a theranostic agent for atherosclerotic CVD.

References

1. *World Health Organisation, Cardiovascular diseases (CVDs)*. 2021 11 June 2021; Available from: https://www.who.int/en/news-room/fact-sheets/detail/cardiovascular-diseases-(cvds).
2. Libby, P., et al., *Atherosclerosis.* Nature Reviews Disease Primers, 2019. **5**(1): p. 56.
3. Lusis, A.J., *Atherosclerosis.* Nature, 2000. **407**(6801): p. 233-241.
4. Hansson, G.K., *Inflammation, Atherosclerosis, and Coronary Artery Disease.* New England Journal of Medicine, 2005. **352**(16): p. 1685-1695.
5. Hansson, G.K. and A. Hermansson, *The immune system in atherosclerosis.* Nature Immunology, 2011. **12**(3): p. 204-212.
6. Libby, P., *Interleukin-1 Beta as a Target for Atherosclerosis Therapy: Biological Basis of CANTOS and Beyond.* Journal of the American College of Cardiology, 2017. **70**(18): p. 2278-2289.
7. Byrne, R.A., M. Joner, and A. Kastrati, *Stent thrombosis and restenosis: what have we learned and where are we going? The Andreas Grüntzig Lecture ESC 2014.* European Heart Journal, 2015. **36**(47): p. 3320-3331.
8. Mulder, W.J., et al., *Imaging and nanomedicine in inflammatory atherosclerosis.* Sci Transl Med, 2014. **6**(239): p. 239sr1.
9. Skajaa, T., et al., *High-density lipoprotein-based contrast agents for multimodal imaging of atherosclerosis.* Arterioscler Thromb Vasc Biol, 2010. **30**(2): p. 169-76.
10. Fernández-Friera, L., et al., *Normal LDL-Cholesterol Levels Are Associated With Subclinical Atherosclerosis in the Absence of Risk Factors.* Journal of the American College of Cardiology, 2017. **70**(24): p. 2979-2991.
11. Marieb, E. and K. Hoehn, *Human Anatomy and Physiology, EBook, Global Edition*. 2018, Harlow, UNITED KINGDOM: Pearson Education, Limited.
12. Standring, S., N. Anand, and R. Tunstall, *Gray's anatomy : the anatomical basis of clinical practice*. Forty-second edition. ed. Anatomy : the anatomical basis of clinical practice. 2021, New York: Elsevier.
13. Libby, P., *The changing landscape of atherosclerosis.* Nature, 2021. **592**(7855): p. 524-533.
14. Bentzon, J.F., et al., *Mechanisms of Plaque Formation and Rupture.* Circulation Research, 2014. **114**(12): p. 1852-1866.
15. Fahed, A.C. and I.-K. Jang, *Plaque erosion and acute coronary syndromes: phenotype, molecular characteristics and future directions.* Nature Reviews Cardiology, 2021. **18**(10): p. 724-734.
16. Kolte, D., P. Libby, and I.-K. Jang, *New Insights Into Plaque Erosion as a Mechanism of Acute Coronary Syndromes.* JAMA, 2021. **325**(11): p. 1043-1044.
17. Zhang, C., M. Yang, and A.C. Ericsson, *Function of Macrophages in Disease: Current Understanding on Molecular Mechanisms.* Frontiers in Immunology, 2021. **12**.
18. Moore, K.J., F.J. Sheedy, and E.A. Fisher, *Macrophages in atherosclerosis: a dynamic balance.* Nature Reviews Immunology, 2013. **13**(10): p. 709-721.
19. Lin, P., et al., *Macrophage Plasticity and Atherosclerosis Therapy.* Frontiers in Molecular Biosciences, 2021. **8**.

20. Bobryshev, Y.V., et al., *Macrophages and Their Role in Atherosclerosis: Pathophysiology and Transcriptome Analysis.* BioMed research international, 2016. **2016**: p. 9582430-9582430.
21. Leitinger, N. and I.G. Schulman, *Phenotypic Polarization of Macrophages in Atherosclerosis.* Arteriosclerosis, Thrombosis, and Vascular Biology, 2013. **33**(6): p. 1120-1126.
22. Barrett, T.J., *Macrophages in Atherosclerosis Regression.* Arterioscler Thromb Vasc Biol, 2020. **40**(1): p. 20-33.
23. Chistiakov, D.A., Y.V. Bobryshev, and A.N. Orekhov, *Macrophage-mediated cholesterol handling in atherosclerosis.* Journal of Cellular and Molecular Medicine, 2016. **20**(1): p. 17-28.
24. Linton, M.F., et al., *SR-BI: A Multifunctional Receptor in Cholesterol Homeostasis and Atherosclerosis.* Trends in endocrinology and metabolism: TEM, 2017. **28**(6): p. 461-472.
25. Nguyen, M.T., et al., *Inflammation as a Therapeutic Target in Atherosclerosis.* Journal of Clinical Medicine, 2019. **8**(8).
26. Cochain, C. and A. Zernecke, *Macrophages in vascular inflammation and atherosclerosis.* Pflügers Archiv - European Journal of Physiology, 2017. **469**(3): p. 485-499.
27. Moustapha, A. and H.V. Anderson, *Revascularization interventions for ischemic heart disease.* Current opinion in cardiology, 2000. **15**(6): p. 463-471.
28. Carson, J.L., et al., *Diabetes mellitus increases short-term mortality and morbidity in patients undergoing coronary artery bypass graft surgery.* Journal of the American College of Cardiology, 2002. **40**(3): p. 418-423.
29. Torii, S., et al., *Drug-eluting coronary stents: insights from preclinical and pathology studies.* Nature Reviews Cardiology, 2020. **17**(1): p. 37-51.
30. Ravindran, D., et al., *The multiple roles of chemokines in the mechanisms of stent biocompatibility.* Cardiovascular Research, 2021. **117**(11): p. 2299-2308.
31. Buccheri, S. and D. Capodanno, *Bioabsorbable stents: only bad news?* European Heart Journal Supplements, 2019. **21**(Supplement_B): p. B28-B30.
32. Serruys, P.W., et al., *Comparison of an everolimus-eluting bioresorbable scaffold with an everolimus-eluting metallic stent for the treatment of coronary artery stenosis (ABSORB II): a 3 year, randomised, controlled, single-blind, multicentre clinical trial.* The Lancet, 2016. **388**(10059): p. 2479-2491.
33. Lipinski, M.J., et al., *Scaffold Thrombosis After Percutaneous Coronary Intervention With ABSORB Bioresorbable Vascular Scaffold: A Systematic Review and Meta-Analysis.* JACC: Cardiovascular Interventions, 2016. **9**(1): p. 12-24.
34. Ni, L., et al., *Bioresorbable vascular stents and drug-eluting stents in treatment of coronary heart disease: a meta-analysis.* Journal of Cardiothoracic Surgery, 2020. **15**(1): p. 26.
35. Cutlip, D.E., et al., *Clinical end points in coronary stent trials: a case for standardized definitions.* Circulation, 2007. **115**(17): p. 2344-51.
36. Torrado, J., et al., *Restenosis, Stent Thrombosis, and Bleeding Complications: Navigating Between Scylla and Charybdis.* Journal of the American College of Cardiology, 2018. **71**(15): p. 1676-1695.
37. Otsuka, F., et al., *Neoatherosclerosis: overview of histopathologic findings and implications for intravascular imaging assessment.* European Heart Journal, 2015. **36**(32): p. 2147-2159.

38. Lenz, T., et al., *Are we curing one evil with another? A translational approach targeting the role of neoatherosclerosis in late stent failure.* European Heart Journal Supplements, 2020. **22**(Supplement_C): p. C15-C25.
39. Yonetsu, T., et al., *Comparison of Incidence and Time Course of Neoatherosclerosis Between Bare Metal Stents and Drug-Eluting Stents Using Optical Coherence Tomography.* The American Journal of Cardiology, 2012. **110**(7): p. 933-939.
40. Andreou, I. and P.H. Stone, *In-Stent Atherosclerosis at a Crossroads.* Circulation, 2016. **134**(19): p. 1413-1415.
41. Hong, M.-K. and S.-Y. Lee, *In-Stent Neoatherosclerosis and Very Late Stent Thrombosis.* JACC: Cardiovascular Interventions, 2018. **11**(14): p. 1351-1353.
42. Nakazawa, G., et al., *The pathology of neoatherosclerosis in human coronary implants bare-metal and drug-eluting stents.* J Am Coll Cardiol, 2011. **57**(11): p. 1314-22.
43. Romero Maria, E., et al., *Neoatherosclerosis From a Pathologist's Point of View.* Arteriosclerosis, Thrombosis, and Vascular Biology, 2015. **35**(10): p. e43-e49.
44. Taniwaki, M., et al., *The association between in-stent neoatherosclerosis and native coronary artery disease progression: a long-term angiographic and optical coherence tomography cohort study.* European Heart Journal, 2015. **36**(32): p. 2167-2176.
45. Nakano, M., et al., *Human autopsy study of drug-eluting stents restenosis: histomorphological predictors and neointimal characteristics.* European Heart Journal, 2013. **34**(42): p. 3304-3313.
46. Nakazawa, G., et al., *Comparison of Vascular Responses Following New-Generation Biodegradable and Durable Polymer-Based Drug-Eluting Stent Implantation in an Atherosclerotic Rabbit Iliac Artery Model.* Journal of the American Heart Association, 2016. **5**(10): p. e003803.
47. Nicol, P., et al., *Assessment of a pro-healing stent in an animal model of early neoatherosclerosis.* Scientific Reports, 2020. **10**(1): p. 8227.
48. Zhang, R., et al., *Effects of Methotrexate in a Rabbit Model of In-Stent Neoatherosclerosis: An Optical Coherence Tomography Study.* Scientific Reports, 2016. **6**(1): p. 33657.
49. Tarkin, J.M., et al., *Imaging Atherosclerosis.* Circulation Research, 2016. **118**(4): p. 750-769.
50. Lobatto, M.E., et al., *Multimodal Clinical Imaging To Longitudinally Assess a Nanomedical Anti-Inflammatory Treatment in Experimental Atherosclerosis.* Molecular Pharmaceutics, 2010. **7**(6): p. 2020-2029.
51. Meester, E.J., et al., *Perspectives on Small Animal Radionuclide Imaging; Considerations and Advances in Atherosclerosis.* Frontiers in Medicine, 2019. **6**.
52. Nahrendorf, M., et al., *Nanoparticle PET-CT Imaging of Macrophages in Inflammatory Atherosclerosis.* Circulation, 2008. **117**(3): p. 379-387.
53. Beldman, T.J., et al., *Hyaluronan Nanoparticles Selectively Target Plaque-Associated Macrophages and Improve Plaque Stability in Atherosclerosis.* ACS Nano, 2017. **11**(6): p. 5785-5799.
54. Duivenvoorden, R., et al., *A statin-loaded reconstituted high-density lipoprotein nanoparticle inhibits atherosclerotic plaque inflammation.* Nat Commun, 2014. **5**: p. 3065.

55. Chen, W., et al., *Macrophage-targeted nanomedicine for the diagnosis and treatment of atherosclerosis.* Nature Reviews Cardiology, 2021.
56. Flores, A.M., et al., *Pro-efferocytic nanoparticles are specifically taken up by lesional macrophages and prevent atherosclerosis.* Nature Nanotechnology, 2020. **15**(2): p. 154-161.
57. Tao, W., et al., *siRNA nanoparticles targeting CaMKIIγ in lesional macrophages improve atherosclerotic plaque stability in mice.* Sci Transl Med, 2020. **12**(553).
58. Chen, J., et al., *High density lipoprotein mimicking nanoparticles for atherosclerosis.* Nano Convergence, 2020. **7**(1): p. 6.
59. Rohatgi, A., et al., *HDL in the 21st Century: A Multifunctional Roadmap for Future HDL Research.* Circulation, 2021. **143**(23): p. 2293-2309.
60. Gordon, T., et al., *High density lipoprotein as a protective factor against coronary heart disease. The Framingham Study.* Am J Med, 1977. **62**(5): p. 707-14.
61. Mineo, C. and P.W. Shaul, *Novel biological functions of high-density lipoprotein cholesterol.* Circulation research, 2012. **111**(8): p. 1079-1090.
62. Barter, P.J., P.W. Baker, and K.A. Rye, *Effect of high-density lipoproteins on the expression of adhesion molecules in endothelial cells.* Curr Opin Lipidol, 2002. **13**(3): p. 285-8.
63. Bursill, C.A., et al., *High-density lipoproteins suppress chemokines and chemokine receptors in vitro and in vivo.* Arterioscler Thromb Vasc Biol, 2010. **30**(9): p. 1773-8.
64. Rong, J.X., et al., *Elevating high-density lipoprotein cholesterol in apolipoprotein E-deficient mice remodels advanced atherosclerotic lesions by decreasing macrophage and increasing smooth muscle cell content.* Circulation, 2001. **104**(20): p. 2447-52.
65. Feuerborn, R., et al., *High density lipoprotein (HDL)-associated sphingosine 1-phosphate (S1P) inhibits macrophage apoptosis by stimulating STAT3 activity and survivin expression.* Atherosclerosis, 2017. **257**: p. 29-37.
66. Mackness, M.I., et al., *Protection of low-density lipoprotein against oxidative modification by high-density lipoprotein associated paraoxonase.* Atherosclerosis, 1993. **104**(1): p. 129-135.
67. Li, D., et al., *Inhibition of Arterial Thrombus Formation by ApoA1 Milano.* Arteriosclerosis, Thrombosis, and Vascular Biology, 1999. **19**(2): p. 378-383.
68. Barter, P.J., et al., *Effects of torcetrapib in patients at high risk for coronary events.* The New England journal of medicine, 2007. **357**(21): p. 2109-22.
69. Schwartz, G.G., et al., *Effects of dalcetrapib in patients with a recent acute coronary syndrome.* The New England journal of medicine, 2012. **367**(22): p. 2089-99.
70. Nicholls, S.J., et al., *Effects of the CETP inhibitor evacetrapib administered as monotherapy or in combination with statins on HDL and LDL cholesterol: a randomized controlled trial.* Jama, 2011. **306**(19): p. 2099-109.
71. Boden, W.E., et al., *Niacin in patients with low HDL cholesterol levels receiving intensive statin therapy.* N Engl J Med, 2011. **365**(24): p. 2255-67.
72. Jiang, C., et al., *Dynamically enhancing plaque targeting via a positive feedback loop using multifunctional biomimetic nanoparticles for plaque regression.* Journal of Controlled Release, 2019. **308**: p. 71-85.

73. Ridker, P.M., et al., *Antiinflammatory Therapy with Canakinumab for Atherosclerotic Disease.* New England Journal of Medicine, 2017. **377**(12): p. 1119-1131.
74. Duivenvoorden, R., et al., *Nanoimmunotherapy to treat ischaemic heart disease.* Nature Reviews Cardiology, 2019. **16**(1): p. 21-32.
75. Flores, A.M., et al., *Nanoparticle Therapy for Vascular Diseases.* Arteriosclerosis, Thrombosis, and Vascular Biology, 2019. **39**(4): p. 635-646.
76. Binderup, T., et al., *Imaging-assisted nanoimmunotherapy for atherosclerosis in multiple species.* Science Translational Medicine, 2019. **11**(506): p. eaaw7736.
77. van der Valk, F.M., et al., *Prednisolone-containing liposomes accumulate in human atherosclerotic macrophages upon intravenous administration.* Nanomedicine, 2015. **11**(5): p. 1039-46.
78. Chen, W., et al., *Collagen-specific peptide conjugated HDL nanoparticles as MRI contrast agent to evaluate compositional changes in atherosclerotic plaque regression.* JACC Cardiovasc Imaging, 2013. **6**(3): p. 373-84.
79. Tang, J., et al., *Inhibiting macrophage proliferation suppresses atherosclerotic plaque inflammation.* Science advances, 2015. **1**(3): p. e1400223.
80. Lameijer, M., et al., *Efficacy and safety assessment of a TRAF6-targeted nanoimmunotherapy in atherosclerotic mice and non-human primates.* Nat Biomed Eng, 2018. **2**(5): p. 279-292.
81. Lewis, D.R., et al., *Nanotherapeutics for inhibition of atherogenesis and modulation of inflammation in atherosclerotic plaques.* Cardiovascular Research, 2015. **109**(2): p. 283-293.
82. Lameijer, M., et al., *Efficacy and safety assessment of a TRAF6-targeted nanoimmunotherapy in atherosclerotic mice and non-human primates.* Nature Biomedical Engineering, 2018. **2**(5): p. 279-292.
83. Sanchez-Gaytan, B.L., et al., *HDL-mimetic PLGA nanoparticle to target atherosclerosis plaque macrophages.* Bioconjug Chem, 2015. **26**(3): p. 443-51.
84. Nandwana, V., et al., *High-Density Lipoprotein-like Magnetic Nanostructures (HDL-MNS): Theranostic Agents for Cardiovascular Disease.* Chemistry of Materials, 2017. **29**(5): p. 2276-2282.
85. Lovell, J.F., et al., *Porphysome nanovesicles generated by porphyrin bilayers for use as multimodal biophotonic contrast agents.* Nature Materials, 2011. **10**: p. 324.
86. Rajora, M.A., J.W.H. Lou, and G. Zheng, *Advancing porphyrin's biomedical utility via supramolecular chemistry.* Chemical Society Reviews, 2017. **46**(21): p. 6433-6469.
87. Liu, T.W., et al., *Intrinsically Copper-64-Labeled Organic Nanoparticles as Radiotracers.* Angewandte Chemie International Edition, 2012. **51**(52): p. 13128-13131.
88. Liu, T.W., et al., *Inherently Multimodal Nanoparticle-Driven Tracking and Real-Time Delineation of Orthotopic Prostate Tumors and Micrometastases.* ACS Nano, 2013. **7**(5): p. 4221-4232.
89. Cui, L., et al., *A PEGylation-Free Biomimetic Porphyrin Nanoplatform for Personalized Cancer Theranostics.* ACS Nano, 2015. **9**(4): p. 4484-95.
90. Lin, Q., et al., *Imaging the cytosolic drug delivery mechanism of HDL-like nanoparticles.* Pharm Res, 2014. **31**(6): p. 1438-49.
91. Muhanna, N., et al., *Multimodal Image-Guided Surgical and Photodynamic Interventions in Head and Neck Cancer: From Primary Tumor to Metastatic Drainage.* Clin Cancer Res, 2016. **22**(4): p. 961-70.

92. Pasut, G. and F.M. Veronese, *State of the art in PEGylation: The great versatility achieved after forty years of research.* Journal of Controlled Release, 2012. **161**(2): p. 461-472.
93. Verhoef, J.J.F. and T.J. Anchordoquy, *Questioning the Use of PEGylation for Drug Delivery.* Drug delivery and translational research, 2013. **3**(6): p. 499-503.
94. Amoozgar, Z. and Y. Yeo, *Recent advances in stealth coating of nanoparticle drug delivery systems.* WIREs Nanomedicine and Nanobiotechnology, 2012. **4**(2): p. 219-233.
95. Huynh, E. and G. Zheng, *Porphysome nanotechnology: A paradigm shift in lipid-based supramolecular structures.* Nano Today, 2014. **9**(2): p. 212-222.
96. Huynh, E. and G. Zheng, *Engineering multifunctional nanoparticles: all-in-one versus one-for-all.* WIREs Nanomedicine and Nanobiotechnology, 2013. **5**(3): p. 250-265.
97. Philp, L., et al., *Use of Porphysomes to detect primary tumour, lymph node metastases, intra-abdominal metastases and as a tool for image-guided lymphadenectomy: proof of concept in endometrial cancer.* Theranostics, 2019. **9**(9): p. 2727-2738.
98. Muhanna, N., et al., *Multimodal Nanoparticle for Primary Tumor Delineation and Lymphatic Metastasis Mapping in a Head-and-Neck Cancer Rabbit Model.* Advanced Healthcare Materials, 2015. **4**(14): p. 2164-2169.
99. Rajora, M.A., et al., *Tailored theranostic apolipoprotein E3 porphyrin-lipid nanoparticles target glioblastoma* Chemical Science, 2017. **8**(8): p. 5371-5384.
100. Wolska, A., et al., *Apolipoprotein Mimetic Peptides: Potential New Therapies for Cardiovascular Diseases.* Cells, 2021. **10**(3).
101. Navab, M., et al., *Oral Administration of an Apo A-I Mimetic Peptide Synthesized From D-Amino Acids Dramatically Reduces Atherosclerosis in Mice Independent of Plasma Cholesterol.* Circulation, 2002. **105**(3): p. 290-292.
102. Qin, S., et al., *Reverse D4F, an Apolipoprotein-AI Mimetic Peptide, Inhibits Atherosclerosis in ApoE-null Mice.* Journal of Cardiovascular Pharmacology and Therapeutics, 2012. **17**(3): p. 334-343.
103. Sanchez-Gaytan, B.L., et al., *HDL-Mimetic PLGA Nanoparticle To Target Atherosclerosis Plaque Macrophages.* Bioconjugate Chemistry, 2015. **26**(3): p. 443-451.
104. Marrache, S. and S. Dhar, *Biodegradable synthetic high-density lipoprotein nanoparticles for atherosclerosis.* Proceedings of the National Academy of Sciences, 2013. **110**(23): p. 9445.
105. Rajora, M.A. and G. Zheng, *Targeting SR-BI for Cancer Diagnostics, Imaging and Therapy.* Frontiers in Pharmacology, 2016. **7**.
106. Rodrigueza, W.V., et al., *Mechanism of Scavenger Receptor Class B Type I-mediated Selective Uptake of Cholesteryl Esters from High Density Lipoprotein to Adrenal Cells *.* Journal of Biological Chemistry, 1999. **274**(29): p. 20344-20350.
107. Tapia-Vieyra, J.V., B. Delgado-Coello, and J. Mas-Oliva, *Atherosclerosis and Cancer; A Resemblance with Far-reaching Implications.* Arch Med Res, 2017. **48**(1): p. 12-26.
108. DiRenzo, D., G.K. Owens, and N.J. Leeper, *"Attack of the Clones": Commonalities Between Cancer and Atherosclerosis.* Circ Res, 2017. **120**(4): p. 624-626.
109. Ross, J.S., et al., *Atherosclerosis and Cancer.* Annals of the New York Academy of Sciences, 2001. **947**(1): p. 271-293.

110. Hu, G., et al., *Nanoparticles Targeting Macrophages as Potential Clinical Therapeutic Agents Against Cancer and Inflammation.* 2019. **10**(1998).

111. Jinnouchi, H., et al., *Diversity of macrophage phenotypes and responses in atherosclerosis.* Cellular and Molecular Life Sciences, 2020. **77**(10): p. 1919-1932.

112. Shen, W.-J., S. Azhar, and F.B. Kraemer, *SR-B1: A Unique Multifunctional Receptor for Cholesterol Influx and Efflux.* Annual review of physiology, 2018. **80**: p. 95-116.

113. Ni, N.C., et al., *Non-invasive Macrophage Tracking Using Novel Porphysome Nanoparticles in the Post-myocardial Infarction Murine Heart.* Mol Imaging Biol, 2016. **18**(4): p. 557-68.

114. Chen, Y.C., et al., *A novel mouse model of atherosclerotic plaque instability for drug testing and mechanistic/therapeutic discoveries using gene and microRNA expression profiling.* Circ Res, 2013. **113**(3): p. 252-65.

115. Bäck, M., et al., *Inflammation and its resolution in atherosclerosis: mediators and therapeutic opportunities.* Nature Reviews Cardiology, 2019. **16**(7): p. 389-406.

116. Weissleder, R., M. Nahrendorf, and M.J. Pittet, *Imaging macrophages with nanoparticles.* Nature Materials, 2014. **13**(2): p. 125-138.

117. van der Vorst, E.P., et al., *High-density lipoproteins suppress chemokine expression and proliferation in human vascular smooth muscle cells.* FASEB J, 2013. **27**(4): p. 1413-25.

118. Fotakis, P., et al., *Anti-Inflammatory Effects of HDL (High-Density Lipoprotein) in Macrophages Predominate Over Proinflammatory Effects in Atherosclerotic Plaques.* Arteriosclerosis, Thrombosis, and Vascular Biology, 2019. **39**(12): p. e253-e272.

119. Suzuki, M., et al., *High-Density Lipoprotein Suppresses the Type I Interferon Response, a Family of Potent Antiviral Immunoregulators, in Macrophages Challenged With Lipopolysaccharide.* Circulation, 2010. **122**(19): p. 1919-1927.

120. van der Vorst, E.P.C., et al., *High-Density Lipoproteins Exert Pro-inflammatory Effects on Macrophages via Passive Cholesterol Depletion and PKC-NF-κB/STAT1-IRF1 Signaling.* Cell Metabolism, 2017. **25**(1): p. 197-207.

121. Dowling, J.K., et al., *The Single Nucleotide Polymorphism Mal-D96N Mice Provide New Insights into Functionality of Mal in TLR Immune Responses.* The Journal of Immunology, 2019. **202**(8): p. 2384.

122. De Nardo, D., D.V. Kalvakolanu, and E. Latz, *Immortalization of Murine Bone Marrow-Derived Macrophages.* Methods Mol Biol, 2018. **1784**: p. 35-49.

123. Sei, Y.J., et al., *Detecting the functional complexities between high-density lipoprotein mimetics.* Biomaterials, 2018. **170**: p. 58-69.

124. Keene, D., et al., *Effect on cardiovascular risk of high density lipoprotein targeted drug treatments niacin, fibrates, and CETP inhibitors: meta-analysis of randomised controlled trials including 117 411 patients.* BMJ : British Medical Journal, 2014. **349**: p. g4379.

125. van der Vorst, E.P.C., et al., *HDL and macrophages: explaining the clinical failures and advancing HDL-based therapeutics in cardiovascular diseases?* Expert Review of Cardiovascular Therapy, 2017. **15**(5): p. 343-344.

126. Zhang, Z., et al., *HDL-Mimicking Peptide–Lipid Nanoparticles with Improved Tumor Targeting.* Small, 2010. **6**(3): p. 430-437.

127. Melchior, J.T., et al., *A consensus model of human apolipoprotein A-I in its monomeric and lipid-free state.* Nature Structural & Molecular Biology, 2017. **24**(12): p. 1093-1099.
128. Song, G.J., et al., *SR-BI mediates high density lipoprotein (HDL)-induced anti-inflammatory effect in macrophages.* Biochemical and Biophysical Research Communications, 2015. **457**(1): p. 112-118.
129. Moore, K.J. and I. Tabas, *Macrophages in the pathogenesis of atherosclerosis.* Cell, 2011. **145**(3): p. 341-355.
130. Swanson, K.V., M. Deng, and J.P.Y. Ting, *The NLRP3 inflammasome: molecular activation and regulation to therapeutics.* Nature Reviews Immunology, 2019. **19**(8): p. 477-489.
131. Gaidt, Moritz M., et al., *Human Monocytes Engage an Alternative Inflammasome Pathway.* Immunity, 2016. **44**(4): p. 833-846.
132. Martínez, G.J., D.S. Celermajer, and S. Patel, *The NLRP3 inflammasome and the emerging role of colchicine to inhibit atherosclerosis-associated inflammation.* Atherosclerosis, 2018. **269**: p. 262-271.
133. Grebe, A., F. Hoss, and E. Latz, *NLRP3 Inflammasome and the IL-1 Pathway in Atherosclerosis.* Circulation Research, 2018. **122**(12): p. 1722-1740.
134. Westerterp, M., et al., *Cholesterol Efflux Pathways Suppress Inflammasome Activation, NETosis, and Atherogenesis.* Circulation, 2018. **138**(9): p. 898-912.
135. Noels, H., C. Weber, and R.R. Koenen, *Chemokines as Therapeutic Targets in Cardiovascular Disease.* Arteriosclerosis, Thrombosis, and Vascular Biology, 2019. **39**(4): p. 583-592.
136. Groenen, A.G., et al., *Cholesterol efflux pathways, inflammation, and atherosclerosis.* Critical Reviews in Biochemistry and Molecular Biology, 2021. **56**(4): p. 426-439.
137. Liu, T., et al., *NF-κB signaling in inflammation.* Signal transduction and targeted therapy, 2017. **2**: p. 17023.
138. Perkins, N.D., *Integrating cell-signalling pathways with NF-κB and IKK function.* Nature Reviews Molecular Cell Biology, 2007. **8**(1): p. 49-62.
139. Kilsdonk, E.P.C., et al., *Cellular Cholesterol Efflux Mediated by Cyclodextrins *.* Journal of Biological Chemistry, 1995. **270**(29): p. 17250-17256.
140. Rye, K.-A. and P.J. Barter, *Cardioprotective functions of HDLs<sup>1</sup>.* Journal of Lipid Research, 2014. **55**(2): p. 168-179.
141. Desforges, J.F.M.D., D.J.M.D.P. Gordon, and B.M.M.D.F. Rifkind, *Current Concepts: High-Density Lipoprotein -- The Clinical Implications of Recent Studies.* The New England Journal of Medicine, 1989. **321**(19): p. 1311-1316.
142. Donahue, N.D., H. Acar, and S. Wilhelm, *Concepts of nanoparticle cellular uptake, intracellular trafficking, and kinetics in nanomedicine.* Advanced Drug Delivery Reviews, 2019. **143**: p. 68-96.
143. Gustafson, H.H., et al., *Nanoparticle uptake: The phagocyte problem.* Nano Today, 2015. **10**(4): p. 487-510.
144. Cormode, D.P., et al., *An ApoA-I Mimetic Peptide High-Density-Lipoprotein-Based MRI Contrast Agent for Atherosclerotic Plaque Composition Detection.* Small, 2008. **4**(9): p. 1437-1444.
145. Cormode, D.P., et al., *Nanocrystal core high-density lipoproteins: A multimodality contrast agent platform.* Nano Lett, 2008. **8**(11): p. 3715-23.
146. Nakashima, Y., et al., *ApoE-deficient mice develop lesions of all phases of atherosclerosis throughout the arterial tree.* Arteriosclerosis and Thrombosis: A Journal of Vascular Biology, 1994. **14**(1): p. 133-140.

147. Getz, G.S. and C.A. Reardon, *ApoE knockout and knockin mice: the history of their contribution to the understanding of atherogenesis.* J Lipid Res, 2016. **57**(5): p. 758-66.
148. Gisterå, A., et al., *Animal Models of Atherosclerosis–Supportive Notes and Tricks of the Trade.* Circulation Research, 2022. **130**(12): p. 1869-1887.
149. Morton, J., et al., *Strikingly Different Atheroprotective Effects of Apolipoprotein A-I in Early- Versus Late-Stage Atherosclerosis.* JACC: Basic to Translational Science, 2018. **3**(2): p. 187.
150. Willemsen, L. and M.P.J. de Winther, *Macrophage subsets in atherosclerosis as defined by single-cell technologies.* The Journal of Pathology, 2020. **250**(5): p. 705-714.
151. Huynh, E. and G. Zheng, *Organic Biophotonic Nanoparticles: Porphysomes and Beyond.* IEEE Journal of Selected Topics in Quantum Electronics, 2014. **20**(3): p. 27-34.
152. VanderLaan, P.A., C.A. Reardon, and G.S. Getz, *Site Specificity of Atherosclerosis.* Arteriosclerosis, Thrombosis, and Vascular Biology, 2004. **24**(1): p. 12-22.
153. Paigen, B., et al., *Quantitative assessment of atherosclerotic lesions in mice.* Atherosclerosis, 1987. **68**(3): p. 231-240.
154. Schierwagen, R., et al., *Seven weeks of Western diet in apolipoprotein-E-deficient mice induce metabolic syndrome and non-alcoholic steatohepatitis with liver fibrosis.* Scientific Reports, 2015. **5**(1): p. 12931.
155. Schulz, D., et al., *In-Depth Characterization of Monocyte-Derived Macrophages using a Mass Cytometry-Based Phagocytosis Assay.* Scientific Reports, 2019. **9**(1): p. 1925.
156. Beldman, T.J., et al., *Nanoparticle-Aided Characterization of Arterial Endothelial Architecture during Atherosclerosis Progression and Metabolic Therapy.* ACS Nano, 2019. **13**(12): p. 13759-13774.
157. Kanthi, Y., A. de la Zerda, and B.R. Smith, *Nanotherapeutic Shots through the Heart of Plaque.* ACS Nano, 2020. **14**(2): p. 1236-1242.
158. Kagadis, G.C., et al., *Handbook of Small Animal Imaging : Preclinical Imaging, Therapy, and Applications*. 2016, Baton Rouge, UNITED STATES: Taylor & Francis Group.
159. Cochain, C., et al., *Single-Cell RNA-Seq Reveals the Transcriptional Landscape and Heterogeneity of Aortic Macrophages in Murine Atherosclerosis.* Circulation Research, 2018. **122**(12): p. 1661-1674.
160. Wei, H., et al., *Modulation of adipose tissue lipolysis and body weight by high-density lipoproteins in mice.* Nutrition & Diabetes, 2014. **4**(2): p. e108-e108.
161. Ahmed, M., et al., *Molecular Imaging of Inflammation in a Mouse Model of Atherosclerosis Using a Zirconium-89-Labeled Probe.* International journal of nanomedicine, 2020. **15**: p. 6137-6152.
162. Noonan, J., A. Bobik, and K. Peter, *The tandem stenosis mouse model: Towards understanding, imaging, and preventing atherosclerotic plaque instability and rupture.* British Journal of Pharmacology, 2022. **179**(5): p. 979-997.
163. Searle, A.K., et al., *Pharmacological Inhibition of Factor XIIa Attenuates Abdominal Aortic Aneurysm, Reduces Atherosclerosis, and Stabilizes Atherosclerotic Plaques.* Thromb Haemost, 2022. **122**(02): p. 196-207.
164. Htun, N.M., et al., *Near-infrared autofluorescence induced by intraplaque hemorrhage and heme degradation as marker for high-risk atherosclerotic plaques.* Nature communications, 2017. **8**(1): p. 75-75.

165. Libby, P., *Collagenases and cracks in the plaque.* The Journal of Clinical Investigation, 2013. **123**(8): p. 3201-3203.
166. Michel, J.-B., et al., *Intraplaque haemorrhages as the trigger of plaque vulnerability.* European Heart Journal, 2011. **32**(16): p. 1977-1985.
167. Koenig, W. and N. Khuseyinova, *Biomarkers of Atherosclerotic Plaque Instability and Rupture.* Arteriosclerosis, Thrombosis, and Vascular Biology, 2007. **27**(1): p. 15-26.
168. Namiki, M., et al., *Local Overexpression of Monocyte Chemoattractant Protein-1 at Vessel Wall Induces Infiltration of Macrophages and Formation of Atherosclerotic Lesion.* Arteriosclerosis, Thrombosis, and Vascular Biology, 2002. **22**(1): p. 115-120.
169. Talayero, B.G. and F.M. Sacks, *The Role of Triglycerides in Atherosclerosis.* Current Cardiology Reports, 2011. **13**(6): p. 544.
170. Rashid, I., et al., *Myeloperoxidase is a potential molecular imaging and therapeutic target for the identification and stabilization of high-risk atherosclerotic plaque.* European Heart Journal, 2018. **39**(35): p. 3301-3310.
171. Rittié, L., *Method for Picrosirius Red-Polarization Detection of Collagen Fibers in Tissue Sections.* Methods Mol Biol, 2017. **1627**: p. 395-407.
172. Ali, Z.A., et al., *Increased Thin-Cap Neoatheroma and Periprocedural Myocardial Infarction in Drug-Eluting Stent Restenosis.* Circulation: Cardiovascular Interventions, 2013. **6**(5): p. 507-517.
173. Ebert, M.L.A., et al., *Animal Models of Neointimal Hyperplasia and Restenosis: Species-Specific Differences and Implications for Translational Research.* JACC: Basic to Translational Science, 2021. **6**(11): p. 900-917.
174. Ali, Z.A., et al., *Increased in-stent stenosis in ApoE knockout mice: insights from a novel mouse model of balloon angioplasty and stenting.* Arteriosclerosis, thrombosis, and vascular biology, 2007. **27**(4): p. 833-40.
175. Getz, G.S. and C.A. Reardon, *Diet and Murine Atherosclerosis.* Arteriosclerosis, Thrombosis, and Vascular Biology, 2006. **26**(2): p. 242-249.
176. Vanags, L.Z., et al., *Apolipoprotein A-I Reduces In-Stent Restenosis and Platelet Activation and Alters Neointimal Cellular Phenotype.* JACC: Basic to Translational Science, 2018. **3**(2): p. 200.
177. Schwartz, R.S., et al., *Restenosis and the proportional neointimal response to coronary artery injury: Results in a porcine model.* Journal of the American College of Cardiology, 1992. **19**(2): p. 267-274.
178. Stirling, J.W. and A.E. Woods, *8 - Resin (plastic) embedding for microscopy and tissue analysis*, in *Bancroft's Theory and Practice of Histological Techniques (Eighth Edition)*, S.K. Suvarna, C. Layton, and J.D. Bancroft, Editors. 2019, Elsevier. p. 96-113.
179. Bennett, M.R., S. Sinha, and G.K. Owens, *Vascular Smooth Muscle Cells in Atherosclerosis.* Circulation research, 2016. **118**(4): p. 692-702.
180. Rippstein, P., et al., *Comparison of Processing and Sectioning Methodologies for Arteries Containing Metallic Stents.* Journal of Histochemistry & Cytochemistry, 2006. **54**(6): p. 673-681.
181. Mehlem, A., et al., *Imaging of neutral lipids by oil red O for analyzing the metabolic status in health and disease.* Nature Protocols, 2013. **8**(6): p. 1149-1154.
182. Baldrighi, M., Z. Mallat, and X. Li, *NLRP3 inflammasome pathways in atherosclerosis.* Atherosclerosis, 2017. **267**: p. 127-138.

183. Ji, Y., et al., *Scavenger Receptor BI Promotes High Density Lipoprotein-mediated Cellular Cholesterol Efflux **. Journal of Biological Chemistry, 1997. **272**(34): p. 20982-20985.
184. Ouimet, M., T.J. Barrett, and E.A. Fisher, *HDL and Reverse Cholesterol Transport.* Circulation Research, 2019. **124**(10): p. 1505-1518.
185. Zheng, K.H., et al., *HDL mimetic CER-001 targets atherosclerotic plaques in patients.* Atherosclerosis, 2016. **251**: p. 381-388.
186. Tang, J., et al., *Immune cell screening of a nanoparticle library improves atherosclerosis therapy.* Proceedings of the National Academy of Sciences, 2016. **113**(44): p. E6731-E6740.
187. Turner, P.V., et al., *Administration of substances to laboratory animals: routes of administration and factors to consider.* Journal of the American Association for Laboratory Animal Science : JAALAS, 2011. **50**(5): p. 600-613.
188. Jung, C., et al., *Intraperitoneal Injection Improves the Uptake of Nanoparticle-Labeled High-Density Lipoprotein to Atherosclerotic Plaques Compared With Intravenous Injection.* Circulation: Cardiovascular Imaging, 2014. **7**(2): p. 303-311.
189. Peterson, S.J., et al., *L-4F treatment reduces adiposity, increases adiponectin levels, and improves insulin sensitivity in obese mice **. Journal of Lipid Research, 2008. **49**(8): p. 1658-1669.
190. Nordestgaard, B.G., *Triglyceride-Rich Lipoproteins and Atherosclerotic Cardiovascular Disease.* Circulation Research, 2016. **118**(4): p. 547-563.
191. Vanags, L.Z., et al., *Plasma activated coating immobilizes apolipoprotein A-I to stainless steel surfaces in its bioactive form and enhances biocompatibility.* Nanomedicine: Nanotechnology, Biology and Medicine, 2017. **13**(7): p. 2141-2150.
192. Burzava, A.L.S., et al., *Surface-Grafted Hyperbranched Polyglycerol Coating: Varying Extents of Fouling Resistance across a Range of Proteins and Cells.* ACS Applied Bio Materials, 2020. **3**(6): p. 3718-3730.
193. Moore, E., et al., *Patterning and Biofunctionalization of Antifouling Hyperbranched Polyglycerol Coatings.* Biomacromolecules, 2014. **15**(7): p. 2735-2743.
194. Joner, M., et al., *Neoatherosclerosis in Patients With Coronary Stent Thrombosis.* JACC: Cardiovascular Interventions, 2018. **11**(14): p. 1340-1350.
195. Cui, Y., et al., *Neoatherosclerosis after Drug-Eluting Stent Implantation: Roles and Mechanisms.* Oxidative Medicine and Cellular Longevity, 2016. **2016**: p. 5924234.
196. Stuker, F., J. Ripoll, and M. Rudin, *Fluorescence Molecular Tomography: Principles and Potential for Pharmaceutical Research.* Pharmaceutics, 2011. **3**(2): p. 229-274.
197. Li, J., et al., *Multimodality Intravascular Imaging of High-Risk Coronary Plaque.* JACC: Cardiovascular Imaging, 2022. **15**(1): p. 145-159.
198. Li, J., et al., *Ultrathin monolithic 3D printed optical coherence tomography endoscopy for preclinical and clinical use.* Light: Science & Applications, 2020. **9**(1): p. 124.
199. Li, J., et al., *3D-Printed Micro Lens-in-Lens for In Vivo Multimodal Microendoscopy.* Small, 2022. **18**(17): p. 2107032.
200. Tardif, J.-C., et al., *Efficacy and Safety of Low-Dose Colchicine after Myocardial Infarction.* New England Journal of Medicine, 2019. **381**(26): p. 2497-2505.

201. Wang, L., et al., *Colchicine-Containing Nanoparticles Attenuates Acute Myocardial Infarction Injury by Inhibiting Inflammation.* Cardiovascular Drugs and Therapy, 2021.
202. Leuschner, F., et al., *Therapeutic siRNA silencing in inflammatory monocytes in mice.* Nature Biotechnology, 2011. **29**(11): p. 1005-1010.
203. Lin, Q., et al., *Nanoparticle-enabled, image-guided treatment planning of target specific RNAi therapeutics in an orthotopic prostate cancer model.* Small, 2014. **10**(15): p. 3072-82.
204. Jain, M., et al., *Photodynamic therapy for the treatment of atherosclerotic plaque: Lost in translation?* Cardiovascular Therapeutics, 2017. **35**(2): p. e12238.
205. Waksman, R., et al., *PhotoPoint Photodynamic Therapy Promotes Stabilization of Atherosclerotic Plaques and Inhibits Plaque Progression.* Journal of the American College of Cardiology, 2008. **52**(12): p. 1024-1032.
206. Shon, S.-M., et al., *Photodynamic Therapy Using a Protease-Mediated Theranostic Agent Reduces Cathepsin-B Activity in Mouse Atheromata In Vivo.* Arteriosclerosis, Thrombosis, and Vascular Biology, 2013. **33**(6): p. 1360-1365.
207. McCarthy, J.R., et al., *A Light-Activated Theranostic Nanoagent for Targeted Macrophage Ablation in Inflammatory Atherosclerosis.* Small, 2010. **6**(18): p. 2041-2049.
208. Zhang, Y., et al., *Treatment of atherosclerotic plaque: perspectives on theranostics.* 2019. **71**(7): p. 1029-1043.
209. Tardif, J.-C., et al., *Effects of the high-density lipoprotein mimetic agent CER-001 on coronary atherosclerosis in patients with acute coronary syndromes: a randomized trial†.* European Heart Journal, 2014. **35**(46): p. 3277-3286.
210. Nicholls, S.J., et al., *Effect of Serial Infusions of CER-001, a Pre-β High-Density Lipoprotein Mimetic, on Coronary Atherosclerosis in Patients Following Acute Coronary Syndromes in the CER-001 Atherosclerosis Regression Acute Coronary Syndrome Trial: A Randomized Clinical Trial.* JAMA Cardiology, 2018. **3**(9): p. 815-822.
211. Zheng, K.H., et al., *No benefit of HDL mimetic CER-001 on carotid atherosclerosis in patients with genetically determined very low HDL levels.* Atherosclerosis, 2020. **311**: p. 13-19.